

Doctor thesis

**Spectroscopy of ${}_{\Lambda}^{28}\text{Al}$, ${}_{\Lambda}^{12}\text{B}$ and ${}_{\Lambda}^7\text{He}$
by the $(e, e'K^+)$ Reaction**

Department of Physics, School of Science,
Tohoku University

Akihiko Matsumura

2009

Abstract

Hypernuclear spectroscopy by the $(e, e'K^+)$ reaction is one of the powerful tools to investigate precise structures of hypernuclei and to study ΛN interaction. The second generation hypernuclear experiment at Jefferson Laboratory Hall C, E01-011 experiment, was successfully performed in 2005, introducing the following two novel experimental improvements based on the first pilot experiment performed in 2000.

1) The High resolution and large acceptance Kaon Spectrometer (HKS) which was specialized for the hypernuclear experiment was newly constructed and installed. The HKS was designed to obtain the momentum resolution of 2×10^{-4} ($\Delta p/p$) for a central momentum of 1.2 GeV/ c and to have a large acceptance of 16 msr with the splitter magnet which deflects a kaon and a scattered electron at very forward angles to the opposite directions. 2) The detection angle of scattered electrons was optimized to suppress a huge electron background from Bremsstrahlung and Møller scattering which had been main background for the electron spectrometer in the first generation experiment. The scattered electron spectrometer was vertically tilted by 8 degree (Tilt method). Thanks to these new configurations, both the energy resolution and the hypernuclear yield were significantly improved and spectroscopic studies were performed for various hypernuclei. The achieved energy resolution of ~ 500 keV (FWHM) is the best resolution among hypernuclear reaction spectroscopy.

The missing mass scale was calibrated with the well-known masses of Λ/Σ^0 hyperons with a CH_2 target. Systematic errors of the absolute mass scale and its linearity were carefully evaluated from the detailed Monte Carlo simulation.

Missing mass spectrum of a typical p -shell hypernucleus, ${}^{12}_{\Lambda}\text{B}$, was obtained and two major peaks were interpreted as the states with a Λ hyperon bound in s and p orbits. Obtained binding energies and cross sections for these states agree with the results of the first pioneering experiment, E89-009, and the shell model predictions.

By the $(e, e'K^+)$ reaction, the first sd -shell hypernucleus, ${}^{28}_{\Lambda}\text{Al}$, was successfully measured thanks to the HKS and the Tilt method. Two prominent peaks were interpreted as corresponding to states that a Λ hyperon bound in s and p orbits, respectively. It was found that the obtained binding energy of -17.57 ± 0.02 (stat.) ± 0.24 (sys.) MeV for the ground state was bound deeper than that of the mirror symmetric hypernucleus, ${}^{28}_{\Lambda}\text{Si}$, and shell model calculation. The success of ${}^{28}_{\Lambda}\text{Al}$ spectroscopy is a gateway to heavier mass hypernuclear spectroscopy with electron beam.

A neutron-rich hypernucleus, ${}^7_{\Lambda}\text{He}$, was also studied with sufficient statistics. The binding energy of the ground state was determined as -5.68 ± 0.03 (stat.) ± 0.22 (sys.) MeV reliably for the first time. This result provides new information on charge symmetry breaking effect in the ΛN interaction.

Contents

1	Introduction	1
1.1	Λ hypernucleus	1
1.2	History	2
1.3	Λ single particle potential	3
1.4	Hypernuclear spectroscopy by the $(e, e'K^+)$ reaction	4
1.5	Purpose of the present study	8
2	Experiment	10
2.1	Overview	10
2.1.1	Accelerator	10
2.2	Kinematics	12
2.3	The first Λ hypernuclear spectroscopy with electron beam	13
2.4	Overview of E01-011 experiment	17
2.4.1	Optimization of the experimental condition	17
2.4.2	Setup	17
2.4.3	Large acceptance and High resolution Kaon Spectrometer (HKS)	21
2.4.4	Tilt method for scattered electron	22
2.4.5	Expected energy resolution and singles rate	25
2.4.6	Trigger	27
2.4.7	DAQ	31
2.4.8	Data summary	35
3	Detectors	40
3.1	Introduction	40
3.2	Detector design	41
3.2.1	HKS drift chamber (HDC)	41
3.2.2	HKS scintillation counters (HTOF)	43
3.2.3	HKS Aerogel Cherenkov counters (AC)	44
3.2.4	HKS Water Cherenkov counters (WC)	44
3.2.5	ENGE Drift Chamber (EDC)	45
3.2.6	ENGE Hodoscope (EHODO)	47
3.3	Performance study of the EDC at LNS	49
3.3.1	Plateau curve	49
3.3.2	Setup of beam test	49
3.3.3	Analysis and result	49

3.4	Performance test at KEK	54
3.4.1	Setup	54
3.4.2	Analysis and result	54
4	Analysis	57
4.1	Overview	57
4.2	HKS analysis	57
4.2.1	HKS drift chamber (HDC)	57
4.2.2	HTOF	58
4.2.3	Cherenkov counters	59
4.2.4	K^+ selection	60
4.3	ENGE analysis	64
4.3.1	EDC	64
4.3.2	EHODO	64
4.4	Coincidence	66
4.5	Missing mass	68
4.6	Transfer matrices calibration	68
4.6.1	Momentum matrices calibration	69
4.6.2	Scattering angle matrices calibration	70
4.6.3	Missing mass spectrum of Λ/Σ^0	73
4.7	Background estimation by mixed event analysis	74
4.8	Linearity, mass scale	75
4.9	Cross section	79
4.9.1	Acceptance	80
4.9.2	Number of virtual photons	84
4.9.3	Correction factors	85
4.10	Systematic errors	96
4.10.1	Systematic errors for cross sections	96
4.10.2	Systematic errors for binding energies	96
5	Results and Discussion	99
5.1	Mass spectrum	99
5.2	Systematic errors for cross sections	104
5.3	Discussion	112
5.3.1	Spectroscopy of $^{12}_{\Lambda}\text{B}$	112
5.3.2	Spectroscopy of $^{28}_{\Lambda}\text{Al}$	121
5.3.3	Spectroscopy of $^7_{\Lambda}\text{He}$	127
6	Summary and conclusion	133
A	Mass values	139
B	Spectroscopic factor	141
C	Isotopically enriched ^{28}Si target	144

D	List of the data point of ${}_{\Lambda}^{12}\text{B}$	146
E	List of the data point of ${}_{\Lambda}^{28}\text{Al}$	149
F	List of the data point of ${}_{\Lambda}^7\text{He}$	151

List of Tables

2.1	Kinematics of the E01-011 experiment	12
2.2	Energy resolution of E89-009 experiment	14
2.3	Typical strangeness production channels and thresholds	18
2.4	Q1 and Q2 parameters	21
2.5	Dipole magnet parameters	22
2.6	ENGE singles rate with or without Tilt method	24
2.7	Experimental configuration of E01-011	26
2.8	Expected energy resolution for each target	26
2.9	Expected singles rate	27
2.10	Typical trigger rate for ENGE, HKS and Coincidence	33
2.11	Specification of F1 TDC	34
2.12	Data acquisition settings	38
2.13	Run summary	39
3.1	Parameters of HDC	43
3.2	HTOF parameters	44
3.3	Specification of drift chamber	47
3.4	Position and angular resolution of drift chamber	52
4.1	Fitting results of Λ and Σ^0	73
4.2	Summary of Blind analysis result	78
4.3	List of the experimental efficiencies and factors and its typical values.	80
4.4	Kinematics conditions for solid angle calculation	84
4.5	Summary of number of kaons for each data set	89
4.6	Summary of AC cut efficiencies for each data set	90
4.7	Summary of WC cut efficiencies for each data set	91
4.8	Summary of β cut efficiencies for each data set	92
4.9	Property of the HKS materials for kaon absorption factor estimation	94
4.10	Summary of absorption factor for each target	95
4.11	K^+ decay channels	95
4.12	A summary of systematic errors for cross sections of ${}_{\Lambda}^{12}\text{B}$	97
4.13	A summary of systematic errors for cross sections of ${}_{\Lambda}^{28}\text{Al}$ and ${}_{\Lambda}^7\text{He}$	97
4.14	A summary of systematic errors for binding energies of ${}_{\Lambda}^{12}\text{B}$	97
4.15	A summary of systematic errors for binding energies of ${}_{\Lambda}^{28}\text{Al}$ and ${}_{\Lambda}^7\text{He}$	98
5.1	Data set for ${}^{12}\text{C}$, ${}^{28}\text{Si}$, and ${}^7\text{Li}$ target	100

5.2	Change of the cross sections when the linear background is assumed in the fitting	107
5.3	Obtained binding energies, widths and cross sections for p_{Λ} of ${}^{12}_{\Lambda}\text{B}$ fitted by three Gaussians	109
5.4	Obtained binding energies, widths and cross sections for p_{Λ} of ${}^{12}_{\Lambda}\text{B}$ fitted by a single Gaussians	109
5.5	Obtained binding energies, widths and cross sections for p_{Λ} of ${}^{28}_{\Lambda}\text{Al}$ fitted by three Gaussians	111
5.6	Obtained binding energies and widths for ${}^{12}_{\Lambda}\text{B}$ spectrum	112
5.7	Obtained cross sections for ${}^{12}_{\Lambda}\text{B}$ spectrum	112
5.8	Kinematic comparison between hypernuclear spectroscopy experiments at JLab	114
5.9	Comparison of excitation energies and widths of ${}^{12}_{\Lambda}\text{B}$	115
5.10	Excitation energies and cross sections of ${}^{12}_{\Lambda}\text{C}$	118
5.11	Comparison of experimental results with theoretical calculation for ${}^{12}_{\Lambda}\text{B}$	119
5.12	Obtained binding energies and widths for ${}^{28}_{\Lambda}\text{Al}$ spectrum	122
5.13	Obtained cross sections for ${}^{28}_{\Lambda}\text{Al}$ spectrum	123
5.14	Excitation energies and cross sections of ${}^{28}_{\Lambda}\text{Si}$	124
5.15	Comparison of experimental results with theoretical calculation for ${}^{28}_{\Lambda}\text{Al}$	126
5.16	Obtained binding energy and width for the ${}^7_{\Lambda}\text{He}$ spectrum	127
5.17	Results of the fitting for ${}^7_{\Lambda}\text{He}$ spectrum	128
5.18	Comparison of experimental results with theoretical calculation for ${}^7_{\Lambda}\text{He}$	131
A.1	Particle masses	139
A.2	Nuclear masses	140
B.1	Relative spectroscopic factor of proton pickup reaction for ${}^{28}\text{Si}$	141
B.2	Relative spectroscopic factor of proton pickup reaction for ${}^{12}\text{C}$	141
B.3	Relative spectroscopic factor of proton pickup reaction for ${}^7\text{Li}$	142
D.1	List of the data point of the ${}^{12}_{\Lambda}\text{B}$ spectrum	146
E.1	List of the data point of the ${}^{28}_{\Lambda}\text{Al}$ spectrum	149
F.1	List of the data point of the ${}^7_{\Lambda}\text{He}$ spectrum	151

List of Figures

1.1	A hypernuclear chart	3
1.2	Mass dependence of a Λ hyperon binding energy	5
1.3	Schematic diagram of the $(e, e'K^+)$ reaction	6
1.4	Kinematics of the $(e, e'K^+)$ reaction	6
2.1	Schematic of CEBAF	11
2.2	Hall C beam line	11
2.3	Scattered angle dependence of electron associated with virtual photon	13
2.4	Scattered angle distribution for kaon of $^{12}\text{C}(e, e'K^+)_{\Lambda}^{11}\text{B}$ reaction	14
2.5	Excitation energy spectrum of $_{\Lambda}^{12}\text{B}$ obtained at E89-009	15
2.6	Angular distribution of scattered electron from Bremsstrahlung and associated with virtual photon	16
2.7	Elementary cross section of $p(\gamma, K^+)_{\Lambda}$ reaction	18
2.8	Setup of E01-011 experiment	19
2.9	Schematic and field map comparison of the splitter magnet	20
2.10	Schematic view of ENGE magnet	23
2.11	Figure of merit (FoM) for scattered electron	24
2.12	Schematic drawing of Tilt method	25
2.13	Schematic view of grouping trigger	28
2.14	Front and top view of the TUL-8040	29
2.15	HKS trigger logic	29
2.16	The Trigger Supervisor (TS) logic	30
2.17	A flowchart of CODA	31
2.18	Data acquisition rate performance	32
2.19	Picture of F1 TDC	34
2.20	Picture of a target ladder	35
2.21	Beam position at CH_2 target with raster	36
3.1	Schematic top view of HKS detector package	41
3.2	Schematic view of scattered electron spectrometer	42
3.3	HDC wire layout and coordinate system	42
3.4	Schematic view of HTOF1X	43
3.5	Schematic view of HTOF1Y	44
3.6	Schematic view of AC	45
3.7	Schematic view of WC	46
3.8	Wire configuration of drift chamber	48

3.9	Schematic view of hodoscopes	48
3.10	Singles rates of the drift chamber	49
3.11	Experimental setup at LNS	50
3.12	Typical drift time of drift chamber	51
3.13	Correlation between the drift time and the drift distance	51
3.14	Position resolution of each layer	52
3.15	Voltage dependence on detection efficiency of each layer	53
3.16	Schematic view of the performance test at KEK-PS T1 beamline . . .	54
3.17	Correlation between the number of photoelectrons for WC and TOF distribution for 1.2 GeV/ c particles	55
3.18	TOF resolution of EHODO for 1.2 GeV/ c π^+	56
4.1	The flowchart of analysis	58
4.2	Typical drift time and drift distance of HDC	59
4.3	Residual of HDC	59
4.4	TOF spectrum by HTOF	60
4.5	Number of photoelectrons of aerogel cherenkov counter	61
4.6	Correlation between aerogel cherenkov and β	61
4.7	Number of photoelectrons of water cherenkov counter	62
4.8	Correlation between water cherenkov and β	62
4.9	Run dependence of N.P.E of WC for proton	63
4.10	β spectrum w/ or w/o cherenkov cut	63
4.11	Typical drift time and drift distance of EDC	64
4.12	Scatter plot of drift distance vs. drift time of EDC	65
4.13	Typical residual of EDC	65
4.14	TOF measured by EHODO	66
4.15	Coincidence time spectrum	67
4.16	Flowchart of optics calibration	69
4.17	χ_{pos}^2 and χ_{wid}^2 as a function of V_{kin}	71
4.18	Difference of V_{kin} corresponding to minimum χ_{pos}^2 and χ_{wid}^2 at each iteration step	71
4.19	Sieve slit and collimator for ENGE and HKS	72
4.20	Missing mass spectrum of $p(e, e'K^+)\Lambda/\Sigma^0$	73
4.21	Mixed event analysis procedure	74
4.22	Background comparison	75
4.23	Blind analysis result for $^{12}\text{B}_\Lambda$	77
4.24	Background contamination as a function of S/N	78
4.25	Mass difference between Blind analysis results and assumed values . .	79
4.26	Correlation between θ_{K^+} and ϕ_{K^+}	81
4.27	Correlation between x'_{K^+} and y'_{K^+}	81
4.28	Correlation between $\theta_{e'}$ and $\phi_{e'}$	82
4.29	Correlation between $x'_{e'}$ and $y'_{e'}$	82
4.30	Calculated momentum correlation between a scattered electron and a kaon	83
4.31	Momentum dependence of the solid angle for each spectrometer . . .	84

4.32	The virtual photon flux $\Gamma(\omega)$	85
4.33	Schematic drawing of tracking efficiency estimation	87
4.34	Tracking efficiency of each drift chamber	88
4.35	β_{TOF} - β_K distribution without any offline cut	88
4.36	Kaon survival ratio as a function of AC offline cut	90
4.37	Kaon survival ratio as a function of WC offline cut	91
4.38	Kaon survival ratio as a function of β offline cut	92
4.39	Computer live time factor	96
5.1	Missing mass spectrum for ${}^{12}_{\Lambda}\text{B}$ with counts on the vertical scale . . .	100
5.2	Missing mass spectrum for ${}^{28}_{\Lambda}\text{Al}$ with counts on the vertical scale . . .	101
5.3	Missing mass spectrum for ${}^7_{\Lambda}\text{He}$ with counts on the vertical scale . . .	101
5.4	Missing mass spectrum for ${}^{12}_{\Lambda}\text{B}$ with the vertical scale of differential cross section	102
5.5	Missing mass spectrum for ${}^{28}_{\Lambda}\text{Al}$ with the vertical scale of differential cross section	103
5.6	Missing mass spectrum for ${}^7_{\Lambda}\text{He}$ with the vertical scale of differential cross section	103
5.7	Estimation of a side tail	104
5.8	Fitting of the ${}^{12}_{\Lambda}\text{B}$ when the linear background is assumed for each peak.	105
5.9	Fitting of the ${}^{28}_{\Lambda}\text{Al}$ when the linear background is assumed for each peak.	106
5.10	Fitting of the ${}^7_{\Lambda}\text{He}$ when the linear background is assumed for each peak.	106
5.11	Fitting p_{Λ} of ${}^{12}_{\Lambda}\text{B}$ with three Gaussians	108
5.12	Fitting p_{Λ} of ${}^{12}_{\Lambda}\text{B}$ with a single Gaussians	109
5.13	Fitting p_{Λ} of ${}^{28}_{\Lambda}\text{Al}$ with three Gaussians	110
5.14	Missing mass spectrum for ${}^{12}_{\Lambda}\text{B}$	113
5.15	Missing mass spectrum for ${}^{12}_{\Lambda}\text{B}$	114
5.16	Missing mass spectrum for ${}^{12}_{\Lambda}\text{B}$ obtained in E89-009 experiment . . .	115
5.17	Missing mass spectrum for ${}^{12}_{\Lambda}\text{B}$ obtained in E94-107 experiment . . .	116
5.18	Missing mass spectrum for ${}^{12}_{\Lambda}\text{C}$ spectrum by (π^+, K^+) reaction	117
5.19	Level scheme of ${}^{12}_{\Lambda}\text{B}$, ${}^{12}_{\Lambda}\text{C}$ and their core nuclei	118
5.20	Missing mass spectrum of ${}^{12}_{\Lambda}\text{B}$ with theoretical calculations	120
5.21	Missing mass spectrum for ${}^{28}_{\Lambda}\text{Al}$	121
5.22	Missing mass spectrum for ${}^{28}_{\Lambda}\text{Al}$	122
5.23	Missing mass spectrum for ${}^{28}_{\Lambda}\text{Si}$ spectrum by (π^+, K^+) reaction	123
5.24	Level scheme of ${}^{28}_{\Lambda}\text{Al}$, ${}^{28}_{\Lambda}\text{Si}$ and their core nuclei	124
5.25	Shell model calculation of ${}^{28}_{\Lambda}\text{Al}$ with DWIA	125
5.26	Missing mass spectrum of ${}^{28}_{\Lambda}\text{Al}$ with theoretical calculations	126
5.27	Emulsion data of ${}^7_{\Lambda}\text{He}$	127
5.28	Missing mass spectrum for ${}^7_{\Lambda}\text{He}$	128
5.29	Missing mass spectrum for ${}^7_{\Lambda}\text{He}$	129
5.30	Comparison of the binding energy of ${}^7_{\Lambda}\text{He}$ with those of ${}^7_{\Lambda}\text{Li}(T=1)$ and ${}^7_{\Lambda}\text{Be}$	130

5.31	The same as Fig. 5.30 but plotted in the energy from $\alpha+\Lambda+N+N$	131
5.32	Missing mass spectrum of ${}^7_\Lambda\text{He}$ with theoretical calculations	132
6.1	Updated Mass dependence of a Λ hyperon binding energy	134
B.1	Spectroscopic factor of proton pickup for ${}^{28}\text{Si}$	142
B.2	Spectroscopic factor of proton pickup for ${}^{12}\text{C}$	143
B.3	Spectroscopic factor of proton pickup for ${}^7\text{Li}$	143
C.1	Schematic process for the preparation of enriched ${}^{28}\text{Si}$ target	145

Chapter 1

Introduction

1.1 Λ hypernucleus

A hypernucleus consists of nucleon(s) (proton(s) and neutron(s)) and one or more hyperon(s), such as Λ , Σ^0 and Ξ . Especially, a hypernucleus which contains one Λ particle is called as a Λ hypernucleus. Since a Λ particle has one strange quark, it is free from Pauli blocking from other nucleons. Therefore, a Λ particle can be a probe to investigate the interior structure of a hypernucleus and also provides us new information on hyperon-nucleon (YN) interaction as a extended baryon-baryon interaction.

Because Λ hypernuclear production in direct interaction converts a nucleon into a Λ particle, most states are excited as nucleon-hole Λ -particle states. Spreading widths of these states (Γ_Λ) were calculated to be less than a few 100 keV [1] [2]. This is much narrower than the width of nucleon deep hole states (Γ_N). In the case of ^{40}Ca , it was predicted that $\Gamma_\Lambda(1s \text{ or } 0d)/\Gamma_N(0s) < 0.03 - 0.07$, for example. This is because 1) Λ with 0 isospin excites only isoscalar mode, 2) ΛN interaction is weaker than the NN interaction, 3) no exchange term is required and 4) excitation energies are different. Therefore spectroscopic studies of deeply bound Λ hypernuclear states can be possible and have been successfully undertaken.

YN and YY scattering data will provide us direct information on YN and YY interactions. However, these kinds of experiments are very difficult due to the short lifetimes of hyperons ($\sim 10^{-10}$ s) and there are a few scattering data so far. Therefore, the following procedure plays an important role in the study of YN and YY interactions,

1. Accurate calculation of hypernuclear structure based on YN and YY interaction models
2. Compare experimental data with calculated results
3. The difference in 2. will suggest some modification to the YN and YY interaction models.

Assuming that a Λ hypernuclear wave function can be decomposed into those of a core nucleus and a Λ hyperon, the hypernuclear Hamiltonian is expressed as [3]

$$H = H_{Core} + t_{\Lambda} + \Sigma v_{\Lambda N}^{\text{effective}} \quad (1.1)$$

Here, H_{Core} is the Hamiltonian for the nucleus core and t_{Λ} is the kinetic energy of the Λ hyperon. $v_{\Lambda N}^{\text{effective}}$ represents the effective ΛN interaction. The effective interaction can be constructed via a G-matrix calculation, starting from the two-body interaction in free space.

The Nijmegen model is one of the major interaction models which is based on One Boson Exchange (OBE) model [4]. The Nijmegen potential has been obtained from phenomenological fits to the scattering data using SU(3) with broken symmetry and available hypernuclear data.

1.2 History

The first Λ hypernucleus was discovered in 1953 by an emulsion experiment [5]. Subsequent emulsion experiments measured the binding energies of light Λ hypernuclei ($A \leq 16$) from their weak decay. It was found that the Λ potential is about 2/3 of that of the nucleon. However, the experimental data was limited to the binding energies of ground states, and only a few excited states were investigated.

In the 1970s, experiments using counters with K^- beam started at CERN and BNL. After the success of the first experiment by $(K_{\text{stopped}}^-, \pi^-)$ reaction [6], a novel method of the in-flight (K^-, π^-) reaction in an almost recoilless condition was introduced and various hypernuclei including excited states were studied [7–14]. It was confirmed with better precision that the depth of the hypernuclear potential is about 2/3 of the nuclear one and it was found the spin-orbit splittings of Λ single particle orbits are quite small [9, 14]. The first γ -ray spectroscopy by NaI counters was also carried out at CERN [15, 16]. Though hypernuclear spectroscopy with K^- beams was a powerful tool as a first step, the statistics were often poor due to low intensity beams and the energy resolution was not good enough because of limited resolution of spectrometers. In addition, only limited states could be investigated because the (K^-, π^-) reaction is an exoergic reaction and has a small momentum transfer.

From the middle of 1980s, the (π^+, K^+) reaction was employed at the Alternating Gradient Synchrotron (AGS) of BNL [17, 18]. A new experimental facility, the 12 GeV Proton Synchrotron (PS) of KEK, also played a major role in further understanding of hypernuclei [19–23]. In particular, the Superconducting Kaon Spectrometer (SKS) improved both statistics and resolution significantly. The (π^+, K^+) reaction is endoergic and has a large momentum transfer. Therefore various states can be populated by this reaction. Hypernuclei with a wide mass region up to ${}_{\Lambda}^{208}\text{Pb}$ were investigated by the SKS.

In the last decade, new experimental techniques have been developed. One is precision γ -ray measurement from hypernuclei [24]. A large-acceptance germanium detector array (Hyperball) has been constructed and observed hypernuclear γ transitions with a resolution of a few keV. A series of γ -ray spectroscopy experiments

determined the precise level structure for the p-shell mass region and provided us new information on ΛN interaction.

Another technique is the introduction of $(e, e'K^+)$ reaction. The high quality primary electron beam from the CEBAF of the Thomas Jefferson National Accelerator Facility (JLab) makes it possible to obtain a sub-MeV energy resolution in the hypernuclear reaction spectroscopy. The first $(e, e'K^+)$ spectroscopy was performed successfully in 2000 at JLab [25, 26]. $(e, e'K^+)$ hypernuclear reaction spectroscopy can determine the absolute binding energy with a good accuracy by measuring well-known mass particles, such as Λ and Σ^0 , simultaneously for calibration of the mass scale. The cross section of each bound state can be also measured by the this reaction. Therefore, γ -ray spectroscopy and spectroscopy by $(e, e'K^+)$ are complementary, and we can obtain new information on the the structure of Λ hypernuclei and the ΛN interaction by combining these results.

Observed hypernuclei so far are summarized in Fig. 1.1 [3].

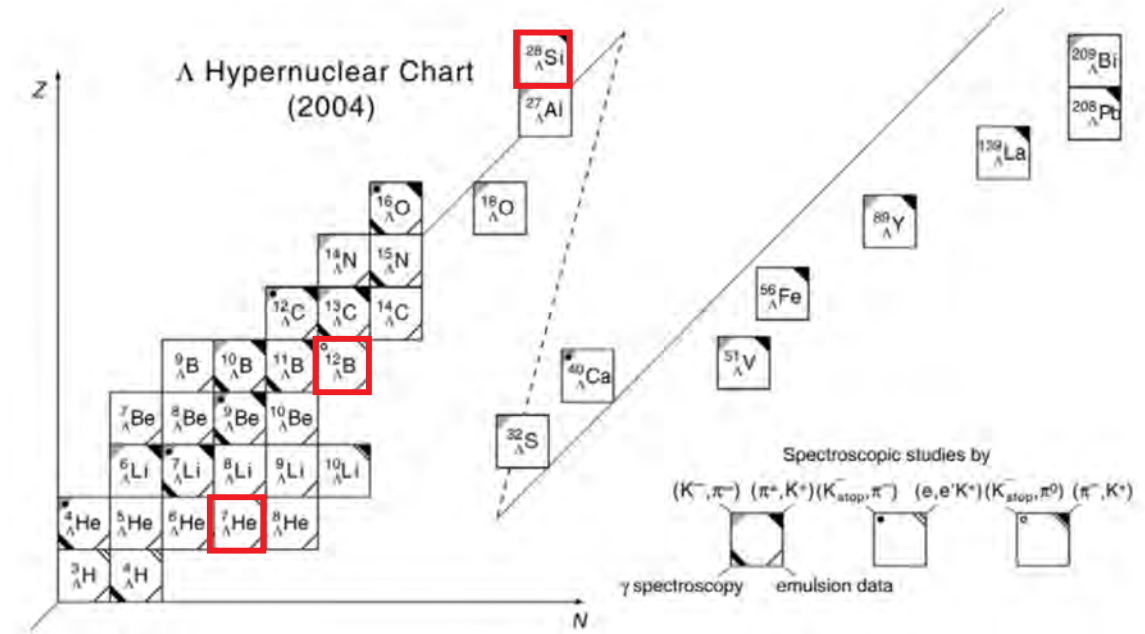


Figure 1.1: A hypernuclear chart [3]. The observed Λ hypernuclei and their experimental methods are shown. Hypernuclei in red boxes are studied in the present thesis.

1.3 Λ single particle potential

Using systematic studies of Λ hypernuclei with a wide mass region by the (K^-, π^-) and (π^+, K^+) reactions, the Λ single particle potential has been investigated. In general, a Λ hypernuclear potential can be expressed by introducing the Woods-Saxon formula as

$$U_{\Lambda} = V_0^{\Lambda} f(r) + V_{LS}^{\Lambda} \left(\frac{\hbar}{m_{\pi} c} \right)^2 \frac{1}{r} \frac{df(r)}{dr} l_s \quad (1.2)$$

$$f(r) = 1/(1 + \exp((r - R)/a)). \quad (1.3)$$

The depth, V_0^{Λ} , and diffuseness, a , were obtained by fitting the measured binding energy data of hypernuclei. Using the systematic study of hypernuclei by the (π^+, K^+) reaction, Hashimoto *et al.* obtained the V_0^{Λ} of -31 MeV with no spin-orbit splitting, which is about 2/3 of the nuclear potential depth for nucleon was consistent with the depth determined by early emulsion data [3, 21, 23].

There have been a number of theoretical discussions on the Λ single-particle potentials. Millener *et al.* discussed the density dependence and non-locality of the Λ nucleus potential (Fig. 1.2) [27]. Yamamoto *et al.* studied the influence of three body ΛNN force and the Λ effective mass in the Skyrme Hartree-Fock approach using the hypernuclear data up to ^{89}Y [28]. The Skyrme Hartree-Fock treatment was extended by Lansky *et al.* taking into account the precise hypernuclear data up to ^{208}Pb by the (π^+, K^+) reaction, and introducing new parameter sets on the basis of the ΛN G -matrix calculations with the $\text{SU}(3)$ -invariant one-boson-exchange potentials [29]. The density dependent relativistic hadron (DDRH) field theory was extended to hypernuclei by Giessen group led by Lenske [30], introducing the vertex scaling factors, R_{σ} and R_{ω} , to obtain the density dependent vertices for the Λ -N model. Later, they improved the DDRH theory, included the new precise hypernuclear measurements by the (π^+, K^+) reaction by Hotchi *et al.* [23]. Their results showed almost half of vertex scaling factors which were evaluated before the precise (π^+, K^+) experiment was performed.

Dover discussed an interesting question, the “distinguishability” of a Λ particle in the nuclear medium [33]. A Λ hyperon is distinguishable from a nucleon at the hadron level since it has the s quark. In a very dense medium, the quarks would be deconfined and the quark picture (“indistinguishability”) might be preferable. It was suggested that the baryon picture and the quark picture of Λ hypernuclear states would yield different mass dependence of absolute Λ binding energies.

So far, the Woods-Saxon potential, which is consistent with the picture of the Λ as a distinguishable particle, provided a good description of Λ single particle potential for existing hypernuclear data as shown in Fig. 1.2. More precise measurements of the Λ hypernuclei with a wide mass region will give new information on the nature of Λ hyperon in a nucleus. The hypernuclear spectroscopy by the $(e, e' K^+)$ reaction could be useful to investigate the structure of hypernucleus with high resolution.

1.4 Hypernuclear spectroscopy by the $(e, e' K^+)$ reaction

The schematic diagram of the $(e, e' K^+)$ reaction is shown in Fig. 1.3. An electron interacts with a target nucleus, emitting a virtual photon which hits a proton in the

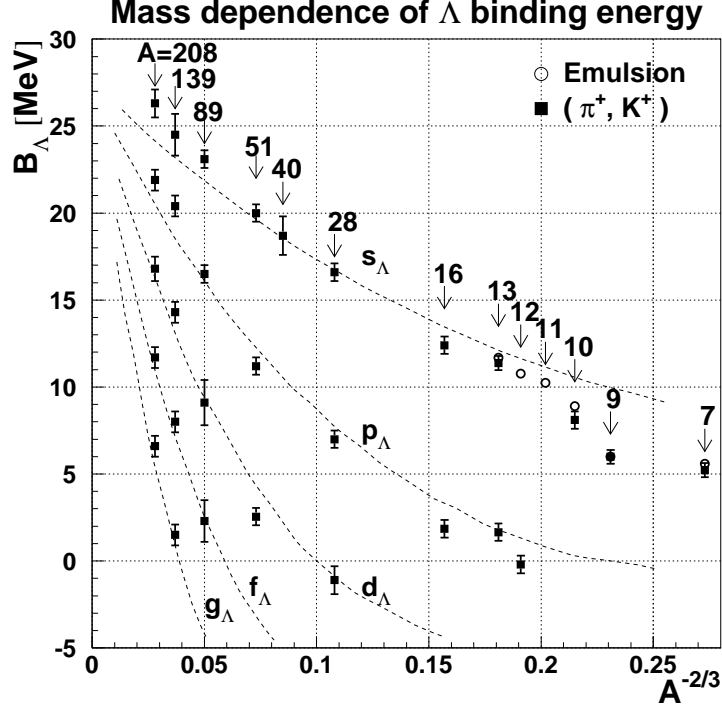


Figure 1.2: Mass dependence of a Λ hyperon binding energy measured by the (π^+, K^+) reaction [3, 18, 21, 23] and the emulsion experiment [31, 32]. The dashed line represents the calculation by a Woods-Saxon potential with a depth of 28 MeV and a radius parameter $r_0 = 1.128 + 0.439 A^{-2/3}$ [27].

target, and a Λ hyperon and a kaon are associatively produced. A Λ hypernucleus is formed when the Λ is bound to the residual nuclear core with the charge of $Z - 1$. Both momenta of the scattered kaon and the scattered electron should be measured simultaneously to obtain the hypernuclear mass with the known incident electron energy.

The elementary amplitudes for the real photon reaction, (γ, K^+) , is practically identical to the one for the electro-production process, $(e, e' K^+)$, at very forward angles of scattered electron. The elementary transition matrix \mathcal{M} for the $\gamma p \rightarrow \Lambda K^+$ can be expressed in terms of four complex amplitudes, spin-independent (f_0) and spin-dependent (g_0, g_1 and g_{-1}) ones, in the laboratory frame [34]

$$\mathcal{M} \equiv \langle \mathbf{k} - \mathbf{p}, \mathbf{p} | t | \mathbf{k}, 0 \rangle_{\text{Lab}} = \epsilon_0(f_0 + g_0\sigma_0) + \epsilon_x(g_1\sigma_1 + g_{-1}\sigma_{-1}) \quad (1.4)$$

where ϵ_x and ϵ_0 denote the unit vectors describing the photon polarization and σ_m is the Pauli spin operator for the baryon. The \mathbf{k} and \mathbf{p} are momentum vectors of photon and kaon, respectively. The differential cross section for the elementary process is given in terms of these amplitudes as

$$\left(\frac{d\sigma}{d\Omega} \right)_{\text{Lab}} = \frac{(2\pi)^4 p^2 E_K E_\gamma E_\Lambda}{k \{ p(E_\Lambda + E_K) - k E_K \cos\theta_K \}} (|f_0|^2 + |g_0|^2 + |g_1|^2 + |g_{-1}|^2) \quad (1.5)$$

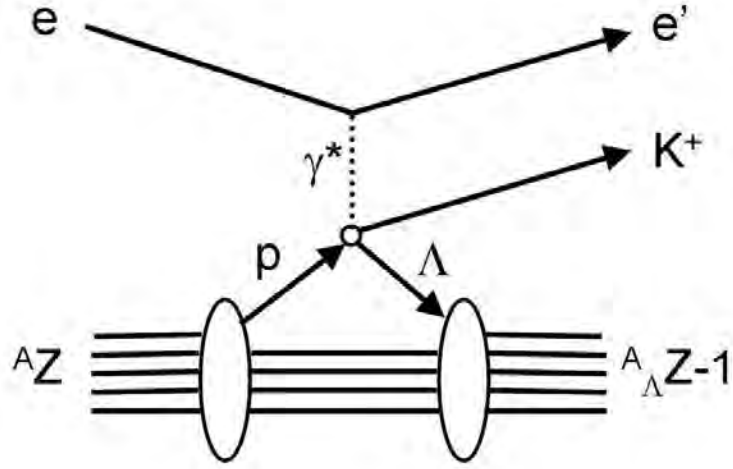


Figure 1.3: Schematic diagram of the $(e, e' K^+)$ reaction.

where the energies, the momenta and the angle are all in the laboratory frame and are described in Fig. 1.4.

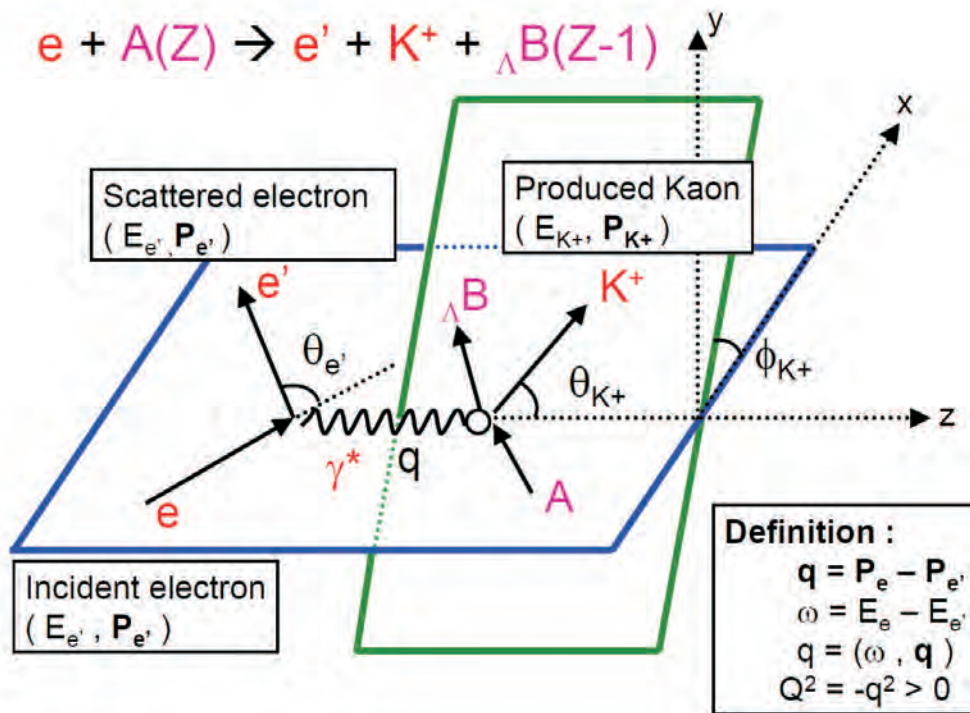


Figure 1.4: Kinematics of the $(e, e' K^+)$ reaction.

Some features of the $(e, e'K^+)$ reaction can be summarized as follows.

1) Large momentum transfer ; the momentum transfer of the $(e, e'K^+)$ reaction is as large as that of the (π^+, K^+) reaction ($\sim 400 \text{ MeV}/c$). Therefore, the recoiling Λ can be bound deeply inside a nucleus. This is an advantage to investigate interior structure for heavier mass nuclei.

2) Electromagnetic interaction ; not only non-spin-flip states but also spin-flip states can be excited because spin-dependent strengths (g_0 , g_1 and g_{-1}) are much larger than the spin-non-flip strength (f_0) [34] (Fig. 2.4). This together with the high momentum transfer gives rise to the selective excitation of hypernuclear high-spin states with unnatural parity.

3) Conversion of proton into Λ ; in contrast to the (K^-, π^-) and (π^+, K^+) reactions, the $(e, e'K^+)$ reaction converts a proton into a Λ . This can populate neutron-rich hypernucleus, such as ${}^7\text{Li}(e, e'K^+){}^7_\Lambda\text{He}$. In general, the same hypernuclei may be produced by the (K^-, π^0) reaction [35], but due to a difference in the spin-flip amplitude the two reactions will afford complementary information on hypernuclear spectroscopy.

Experimentally, the key point of the $(e, e'K^+)$ reaction is the higher resolution attainable than that of mesonic reactions. The high quality primary electron beam enables us to obtain sub-MeV energy resolution [25, 26]. The high intense electron beam also allows us to use thin isotopically enriched target. Moreover, the large acceptances of the spectrometers facilitates the measurement of Λ and Σ^0 hyperons simultaneously. By using their known masses, the absolute mass scale can be calibrated and the binding energy of a Λ hyperon can be determined independently while the emulsion data are used to determine the binding energies in the case of the (π^+, K^+) reaction [3].

On the other hand, there are some experimental difficulties. One is much smaller cross section than the other reactions. While the (K^-, π^-) reaction is the strangeness exchange reaction, the (π^+, K^+) and $(e, e'K^+)$ reactions are associated production reactions, which produce $s\bar{s}$ pair. Moreover, the $(e, e'K^+)$ is induced by electromagnetic interaction while (π^+, K^+) is not. Therefore, the cross section of the $(e, e'K^+)$ is much smaller than that of other two reactions. For example, the cross section of each reaction with ${}^{12}\text{C}$ target is as follows ; $\sim 4 \text{ mb/sr}$ for (K^-, π^-) [12], $\sim 15 \text{ } \mu\text{b/sr}$ for (π^+, K^+) [23], and $\sim 140 \text{ nb/sr}$ for $(e, e'K^+)$, though, we cannot compare them directly because the acceptance and kinematics are different. As far as considering the order of magnitude, the cross section of the $(e, e'K^+)$ reaction is 10^3 times smaller than that of the (K^-, π^-) reaction and 10^2 times smaller than that of the (π^+, K^+) reaction. Another difficulty arises from copious electron background due to high current electron beam.

To overcome these difficulties, we introduced new experimental techniques. The details will be described in the next chapter.

1.5 Purpose of the present study

The purpose of the present study is to carry out the high resolution and high statistic Λ hypernuclear spectroscopy by the $(e, e'K^+)$ reaction with a wide mass region. To perform this, two unique experimental techniques were introduced : High resolution Kaon Spectrometer (HKS) and “Tilt method” for scattered electron. Thanks to these new configurations, the second generation $(e, e'K^+)$ hypernuclear spectroscopy experiment (JLab E01-011) was successfully performed at Jefferson Laboratory with following targets.

$p(e, e'K^+)\Lambda/\Sigma^0$ with CH_2 target

The known masses of Λ and Σ^0 hyperons can be used for the calibration of missing mass scale.

$^{28}\text{Si}(e, e'K^+)_{\Lambda}^{28}\text{Al}$

As discussed in the previous sections, it is very important for further understanding of Λ hyperon's behavior in the nuclear medium to investigate the precise Λ single particle potential in a wide mass region. However, there are only experimental data up to p-shell region by the $(e, e'K^+)$ reaction due to its experimental difficulties. Therefore, it is essential to contrive new experimental configurations for high precision and high statistics hypernuclear investigation. As a first step in studying hypernucleus beyond the p-shell region, $^{28}_{\Lambda}\text{Al}$ hypernucleus on isotopically enriched ^{28}Si target was chosen. The ground state of ^{28}Si has the proton-closed sub shells $[s^4p^{12}(sd)_{pn}^{12}]$ in the sd shell region. The final hypernuclear states are described within the coupled space of the ^{27}Al states and the Λ hyperon orbits (s_{Λ} , p_{Λ} , d_{Λ}). The low-lying energy levels of ^{27}Al are very well reproduced with the full $(sd)^{11}$ shell model [36] and also the proton-pickup spectroscopic factors are in good agreement with the experimental results [37]. The excitation spectrum of $^{28}_{\Lambda}\text{Al}$ can be compared with the mirror symmetric hypernucleus, $^{28}_{\Lambda}\text{Si}$, which has been well studied by the (π^+, K^+) reaction with SKS at KEK [21]. The spectroscopic study of $^{28}\text{Si}(e, e'K^+)_{\Lambda}^{28}\text{Al}$ is the first challenge beyond the p-shell region and will be a breakthrough for further systematic study by the $(e, e'K^+)$ reaction.

$^{12}\text{C}(e, e'K^+)_{\Lambda}^{12}\text{B}$

The precise structure of a typical p-shell hypernucleus, $^{12}_{\Lambda}\text{B}$, can be studied and compared with other experimental data, mirror symmetric hypernucleus, $^{12}_{\Lambda}\text{C}$, which has been used as a reference by the (π^+, K^+) and (K^-, π^-) reaction and theoretical predictions.

$^7\text{Li}(e, e'K^+)_{\Lambda}^7\text{He}$

A neutron-rich hypernucleus, $^7_{\Lambda}\text{He}$, can be measured with high statistics for the first time. The obtained binding energy can be compared with the latest theoretical

calculation based on the cluster model including charge symmetry breaking ΛN interaction.

In this thesis, the overview of E01-011 experiment will be presented in Chapter 2. Chapter 3 will describe the detector R&D. The data analysis including transfer matrix calibration of the spectrometer, efficiency evaluation for the deduction of cross sections, the linearity check of the missing mass scale and the systematic error evaluation will be discussed in Chapter 4. Experimental results will be presented in Chapter 5, comparing with other experimental results and theoretical calculations. The summary and conclusion will be given in Chapter 6.

Chapter 2

Experiment

In this chapter, the overview of experiment for this thesis will be described. Next the kinematics and first hypernuclear spectroscopy with electron beam will be briefly surveyed. Following this, the chapter will conclude with the details of this experiment, such as optimization of experimental conditions, setup, DAQ, data summary and so forth.

2.1 Overview

The hypernuclear spectroscopic experiment by the $(e, e'K^+)$, E01-011 experiment, was successfully carried out at Hall C in Thomas Jefferson National Accelerator Facility (JLab) from June to October, 2005. This experiment investigated the structures of various hypernuclei, such as ${}^7_\Lambda\text{He}$, ${}^{12}_\Lambda\text{B}$ and ${}^{28}_\Lambda\text{Al}$, with high precision and statistics by introducing new experimental techniques. The design of this experiment was based on the pioneering and successful first hypernuclear experiment, E89-009 [25, 26], thus it is called “ Second generation hypernuclear experiment in JLab’s Hall C ”.

2.1.1 Accelerator

The high luminosity electron beam from Continuous Electron Beam Accelerator Facility (CEBAF) is suitable for the hypernuclear spectroscopy by electro-magnetic interaction which has small cross section of hypernuclei production. CEBAF is a five-pass, recirculating, superconducting RF linac designed to provide exceptional beam quality at 6 GeV up to 200 micro amps [38]. The high precision Continuous Wave (CW) electron beam with 100% duty factor from CEBAF is delivered to the three experimental halls, Hall A, Hall B and Hall C (Fig. 2.1). A beam from the injector is accelerated by north and south linac and extracted to independent experimental halls through the use of 499 MHz RF cavities at the beam switch yard. Thus the electron beam has 2 ns bunch structure at the halls.

The Hall C beam line consists of a series of Beam Position Monitors (BPMs), Beam Current Monitors (BCMs), superharps for beam position calibration and an Unser monitor for beam current calibration (Fig. 2.2). A typical beam emittance

was 2×10^{-7} cm·rad with an energy spread of $\Delta E/E \leq 1.0 \times 10^{-9}$ (FWHM) during E01-011. The beam quality is much better than that of meson beams at KEK or BNL where the beam emittance is a few tens cm·rad and energy spread around a few %. Therefore, a direct beam energy measurement was not done and it was assumed that a reaction always occurred at a point on target.

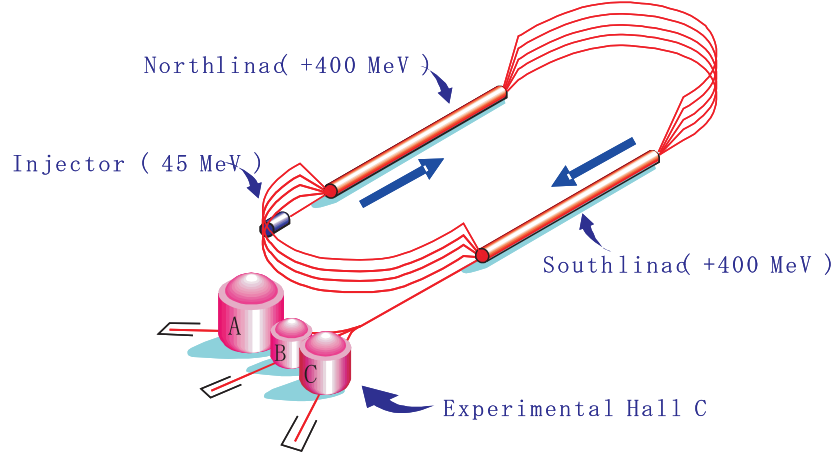


Figure 2.1: Schematic of CEBAF.

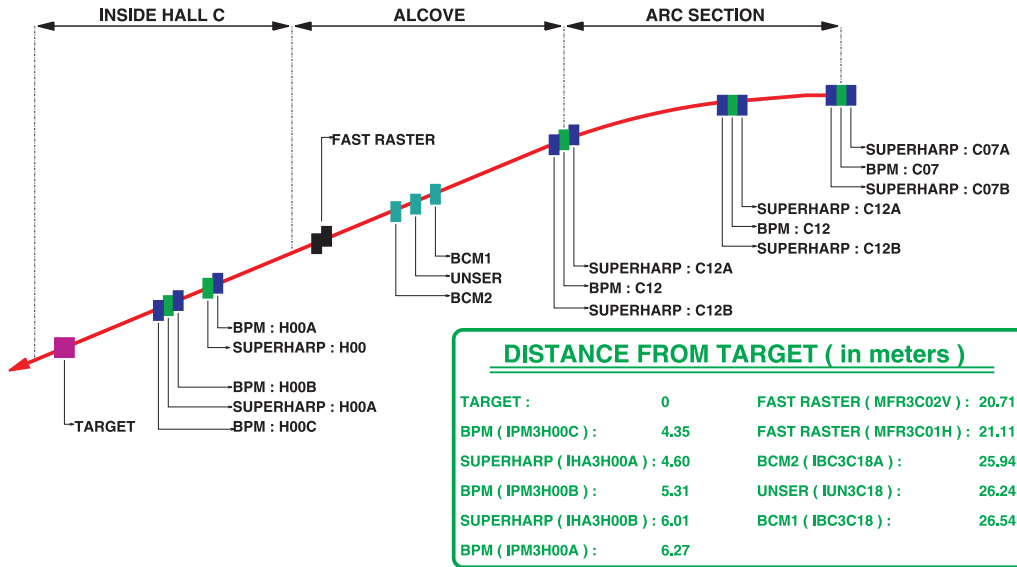


Figure 2.2: Hall C beam line. The target position for E01-011 is about 4.6 m downstream to the normal Hall C target position.

2.2 Kinematics

The triple differential cross section of the elementary process, $p(e, e' K^+) \Lambda$, can be written as [39]

$$\frac{d^3\sigma}{dE_{e'}d\Omega_{e'}d\Omega_K} = \Gamma \left[\frac{d\sigma_T}{d\Omega_K} + \epsilon_L \frac{d\sigma_L}{d\Omega_K} \right] , \quad (2.1)$$

with

$$\Gamma = \frac{\alpha}{4\pi^2} \frac{E_\gamma}{Q^2} \frac{E_{e'}}{E_e} \frac{2}{1-\epsilon} , \quad (2.2)$$

$$E_\gamma = \omega + \frac{Q^2}{2m_p} , \quad (2.3)$$

$$\epsilon = \frac{2E_e^2 E_{e'}^2 \sin^2 \theta_e}{2E_e^2 E_{e'}^2 \sin^2 \theta_e - Q^2 |q|^2} , \quad (2.4)$$

$$\epsilon_L = \frac{Q^2}{\omega^2} \epsilon . \quad (2.5)$$

Here, Γ and E_γ represent the virtual photon flux and energy of real photon, respectively. ϵ and ϵ_L are the longitudinal and transverse photon polarization. α , $\Omega_{e'}$ and Ω_K represent the fine structure constant, solid angle for scattered electrons and solid angle for the kaons. m_p is the mass of a proton. Other parameters are shown in Fig. 1.4.

The scattered angle dependence for scattered electron is shown in Fig. 2.3 and one may notice that it is very forward peaked. The scattered kaon distribution is shown in Fig. 2.4 based on the DWIA calculation by Sotona [40]. The cross section is at maximum at forward angles and both spin-flip and spin-non-flip states are excited in this region. Therefore, both particles should be detected at forward to obtain high hypernuclear yield.

The kinematics of the E01-011 experiment is summarized in Tab. 2.1. Details will be discussed in the following sections.

Beam energy	1.851 GeV
Beam current	30 μ A
Virtual photon energy	1.535 GeV
Central momentum (K^+)	1.2 GeV/ c
Central detection angle (K^+)	7°
Central momentum (e')	0.316 GeV/ c
Central detection angle (e')	4.5°

Table 2.1: Kinematics of the E01-011 experiment

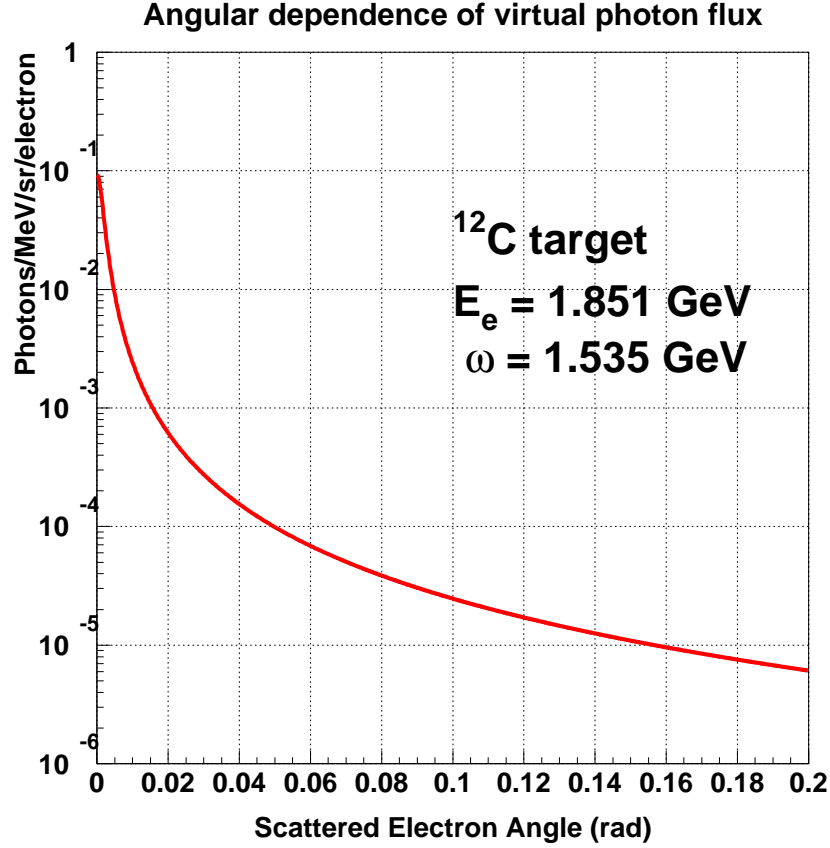


Figure 2.3: Scattered angle dependence of electron associated with virtual photon. The energies of electron beam E_e and virtual photon ω are assumed 1851 MeV and 1580 MeV [39].

2.3 The first Λ hypernuclear spectroscopy with electron beam

The first hypernuclear spectroscopy with electron beam has been carried out in the spring of 2000 in JLab's Hall C (E89-009). The kaon was detected by Short Orbit Spectrometer (SOS) which is the basic equipment of Hall C and the scattered electron was detected by ENGE split-pole spectrometer [41]. As discussed in the previous section, both of the kaon and scattered electron associated with hypernuclear production are emitted in the forward direction. Therefore, both spectrometers have been set up to detect 0 degree emitted particles. E89-009 experiment was executed successfully and obtained the best energy resolution of 0.9 MeV(FWHM) as a hypernuclear reaction spectroscopy at that time.

Though E89-009 experiment has showed a potential of new method to investigate Λ hypernuclei, it has been realized that there has been some space for improvement. One is the huge background contamination of electrons. Scattered electrons from Bremsstrahlung as well as the electrons associated with Λ hypernuclei production,

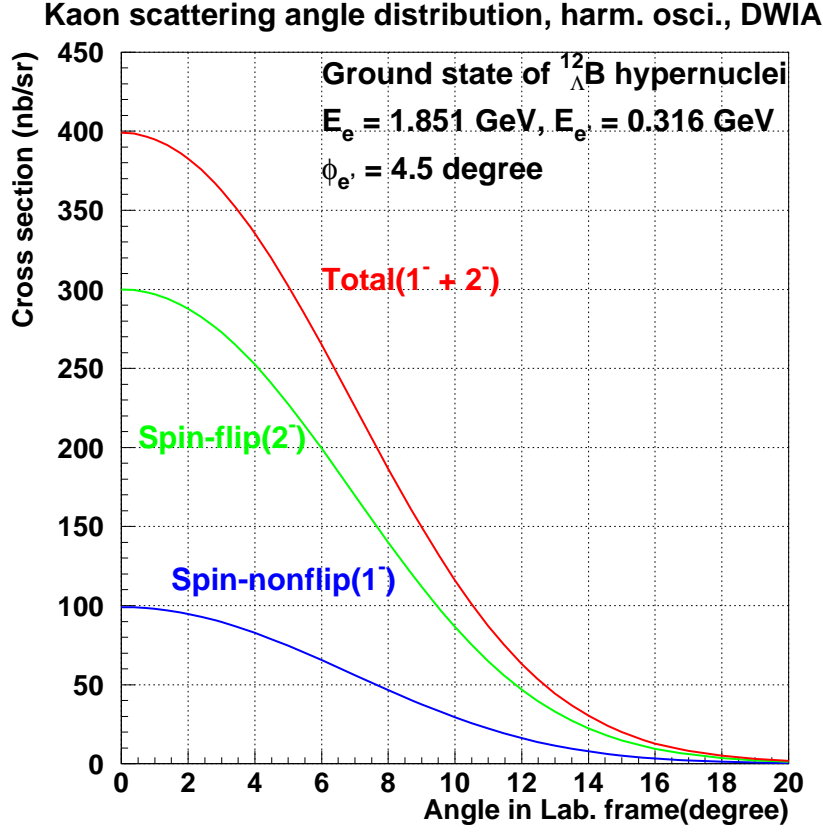


Figure 2.4: Scattered angle distribution for kaon of $^{12}\text{C}(e, e' K^+)_{\Lambda}^{11}\text{B}$ reaction

both peak in the forward sector (Fig. 2.6) [42]. The beam intensity and target thickness had to be limited to keep singles rate of the scattered electron low enough for detectors. Another is that the contribution from SOS resolution had been the largest (Tab. 2.2). The total energy resolution can be improved by introducing a high resolution kaon spectrometer. Furthermore, the new kaon spectrometer should have larger acceptance because the cross section of the electromagnetic hypernuclear production is 100 times lower than the that of hypernuclear production by meson beam [25].

Components	Resolution(keV)
Beam energy	<180
e' momentum	120
K^+ momentum	800
K^+ angle	132
Target thickness	<100
overall	900

Table 2.2: Energy resolution of E89-009 experiment.

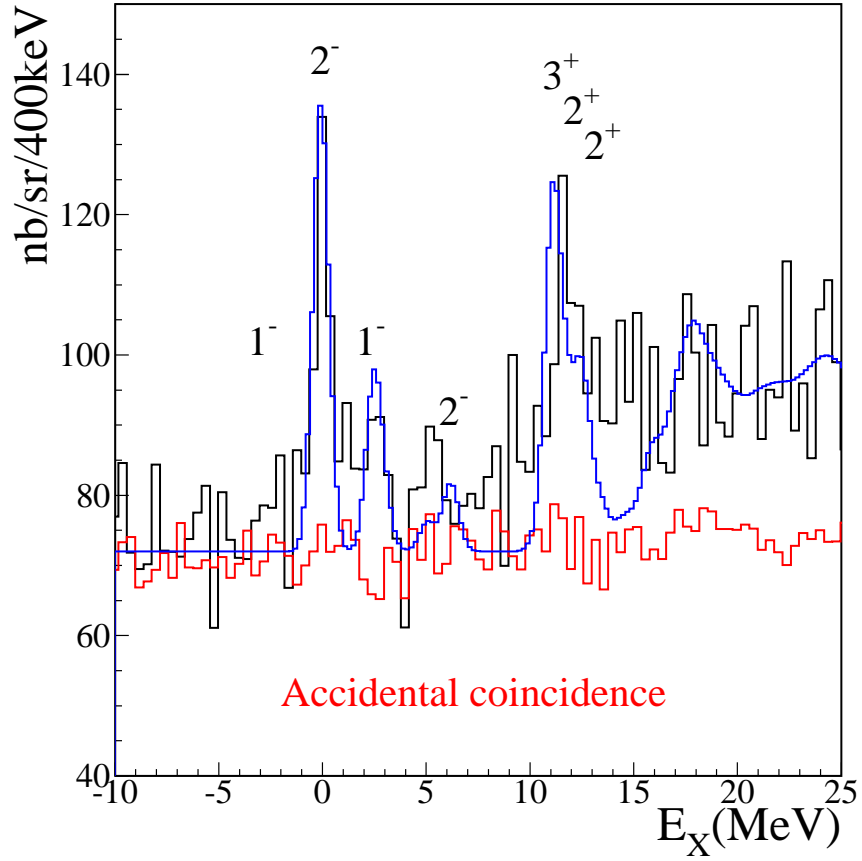


Figure 2.5: Excitation energy spectrum of $^{12}_{\Lambda}\text{B}$ obtained at E89-009. Red line shows the accidental background. Blue line represents the theoretical calculation assumed energy resolution of 900 keV [25].

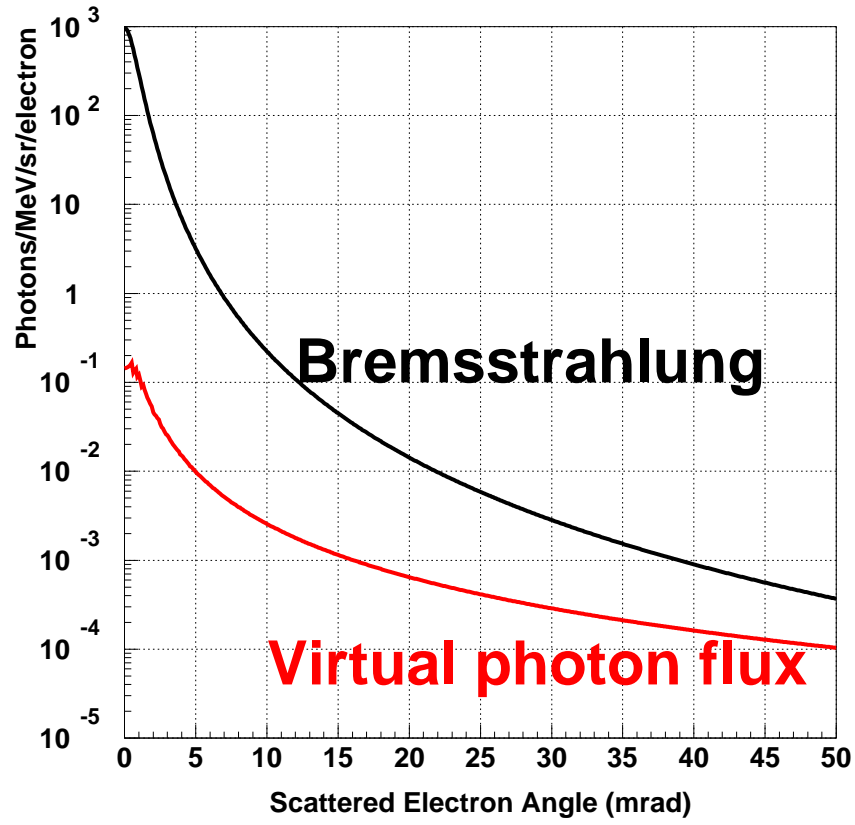


Figure 2.6: Angular distribution of scattered electron from Bremsstrahlung and associated with virtual photon. $E_e=1.851$ GeV and $E_\gamma=1.535$ GeV.

2.4 Overview of E01-011 experiment

The second generation experiment, E01-011 experiment, was successfully carried out at JLab in 2005. To improve both mass resolution and hypernuclear yield simultaneously, two experimental configurations were introduced :

- Large acceptance and high resolution Kaon Spectrometer (HKS),
- New experimental configuration to suppress scattered electron background.

The details will be discussed later.

2.4.1 Optimization of the experimental condition

The experimental conditions have been optimized based on the following conditions.

1. Both scattered electron associated with virtual photon and kaons have forward peak (Fig. 2.3, Fig. 2.4). Therefore, two particles should be detected as forward as possible to obtain high hypernuclear yield rate. The splitter magnet is necessary to separate and measure particles of opposite charge simultaneously scattered forward.
2. The cross section of $p(\gamma, K^+)\Lambda$ reaction is almost maximum and constant around photon energy, E_γ , from 1.1 GeV to 1.5 GeV (Fig. 2.7) [43].
3. Though the hypernuclear yield is augmented with higher beam energy, other strangeness production channels also open (Tab. 2.3) and they will be background sources. Therefore, the energy of incident electron should keep as low as possible. This is also advantage from the point of particle identification and energy resolution.
4. The momentum of kaons was optimized at 1.2 GeV/ c from above conditions and the resolution was aimed at 2×10^{-4} (FWHM) which corresponds to about 230 keV energy resolution in hypernuclear spectra.
5. The electron spectrometer should have a momentum resolution of 4×10^{-4} (FWHM), matching that of the kaon spectrometer. Because the momentum of scattered electron is lower than that of kaons, the required momentum resolution is relaxed compared with that for kaon spectrometer.

2.4.2 Setup

The setup of this experiment consists of three parts (Fig. 2.8).

- Splitter magnet
- Large acceptance and High resolution Kaon Spectrometer (HKS)

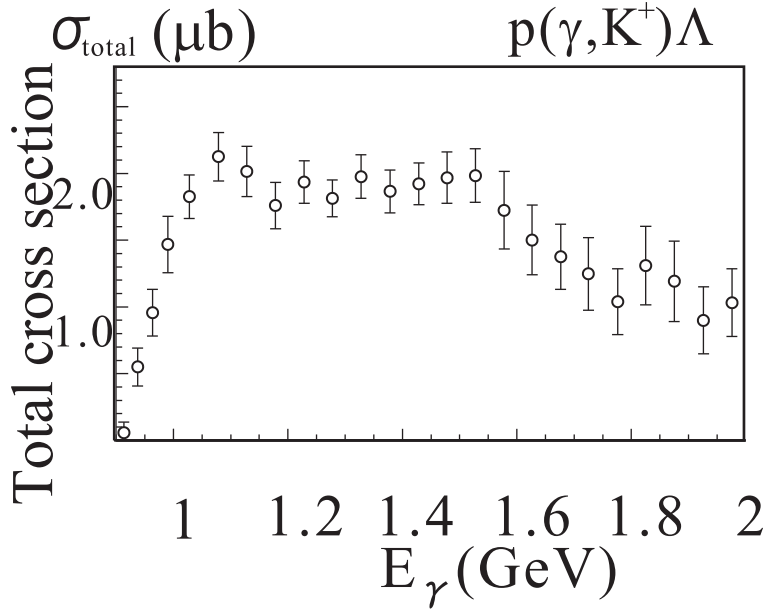


Figure 2.7: Elementary cross section of $p(\gamma, K^+)\Lambda$ reaction. x-axis and y-axis represent the photon energy, E_γ , and total cross section, respectively [43].

Reaction	Threshold(MeV)
$\gamma p \rightarrow K\Lambda$	911
$\gamma p \rightarrow K\Sigma^0$	1046
$\gamma p \rightarrow K\Lambda(1405)$	1452
$\gamma p \rightarrow K^*(892)\Lambda$	1679

Table 2.3: Typical strangeness production channels and thresholds.

- Scattered electron spectrometer

The incident electron beam of 1.851 GeV hits the target housed in the vacuum chamber placed in the splitter magnet. The scattered kaon and electron are separated according to their electric charge by the splitter magnet for the measurements at forward angles. Following the splitter magnet, kaons are measured by newly constructed HKS and electrons by ENGE spectrometer.

Splitter magnet

The splitter magnet bends the electron and kaon to the opposite directions in order to detect them with two independent spectrometers at small scattered angles. This magnet is a normal conducting dipole magnet with a gap of 15.24 cm. A target chamber attached to the target ladder is installed into the gap.

The magnetic field on the mid-plane of the splitter magnet was measured by a hall probe before the experiment. Figure 2.9 (a) shows a measurement point marked as a

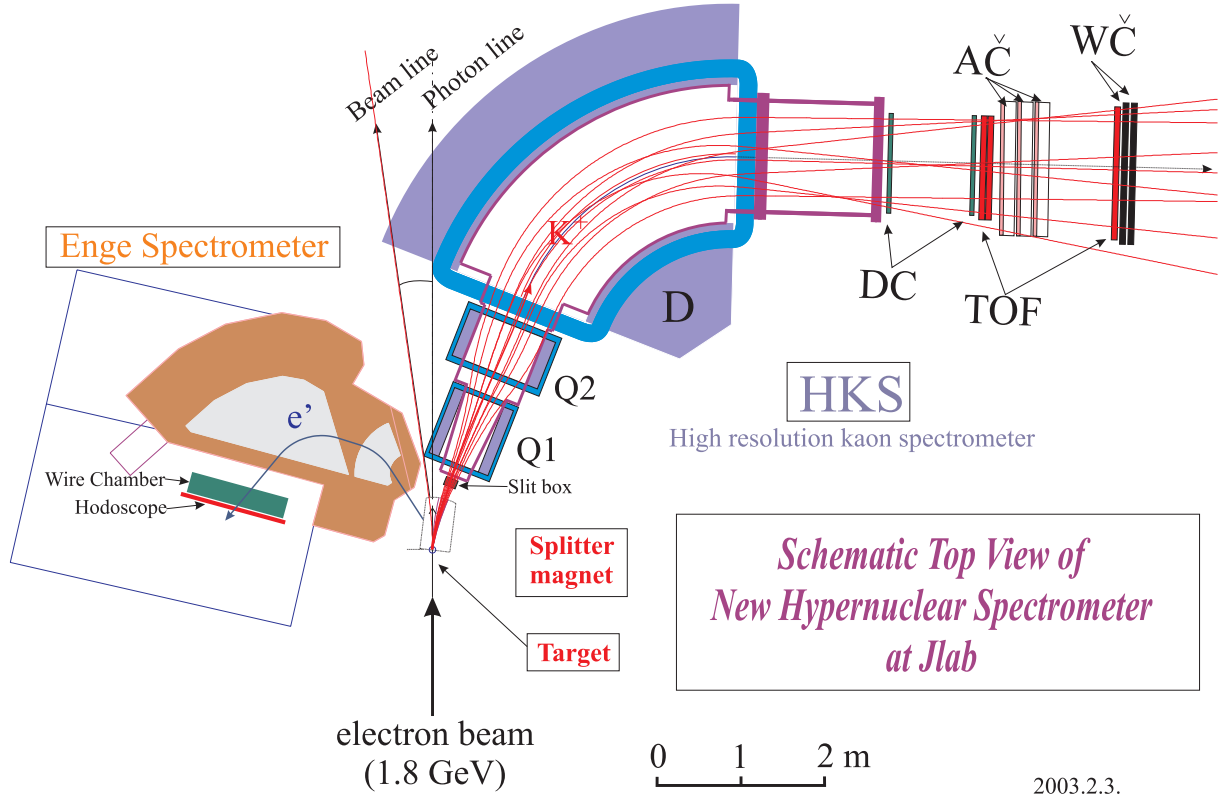
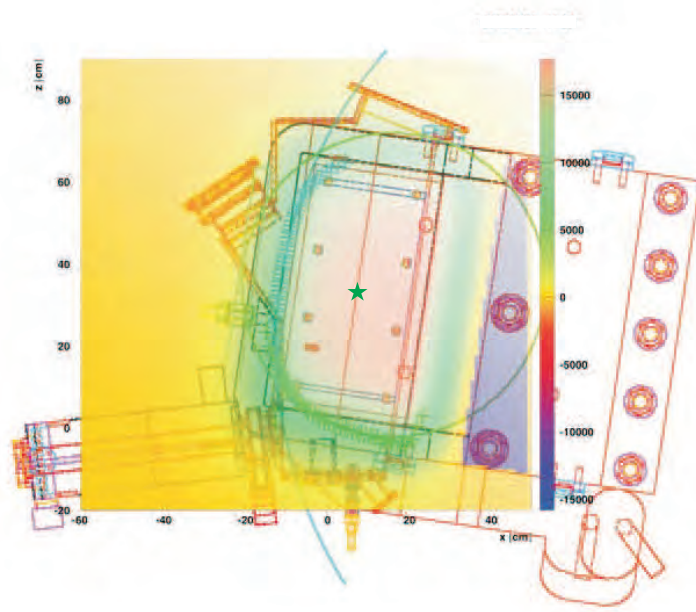
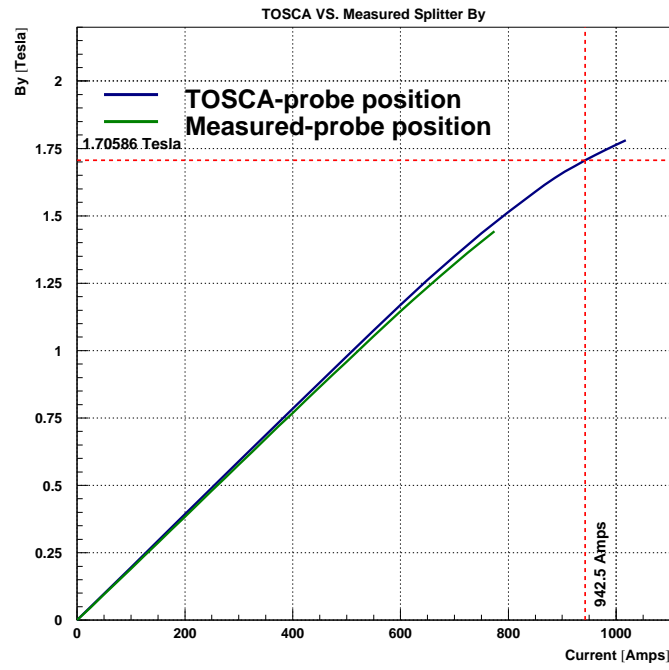


Figure 2.8: Setup of E01-011 experiment. For a kaon side, coordinates represent a positive x being to the beam left, a positive y top and a positive z beam direction while a positive x being to the beam right, a positive y bottom and a positive z beam direction for a scattered electron.

star and (b) represents the measured magnetic field as a function of current overlaid on the result of the 3D finite element calculation by TOSCA. In this measurement, the current could not increase over 780 A due to the limited power. Therefore, the central magnetic field of splitter for an initial transfer matrix evaluation was deduced by the calculation result of TOSCA.



(a) Schematic drawing of the splitter magnet



(b) Measured and calculated magnetic field

Figure 2.9: Schematic drawing of the splitter magnet (a). Magnetic field on the mid-plane of the splitter magnet (marked with *star* in the (a)) is measured and compared with a TOSCA calculation (b).

2.4.3 Large acceptance and High resolution Kaon Spectrometer (HKS)

The positive particles will be detected by the large acceptance and High-resolution Kaon Spectrometer (HKS) which was newly constructed for this experiment. The HKS consists of two quadrupole magnets (Q1, Q2), one dipole magnets (D) and the detectors. All magnets are normal conducting. Parameters of each magnet are listed in Tab.2.4 and Tab.2.5.

Item	Q1	Q2
Bore radius (mm)	120	145
Pole length (mm)	840	600
Max. magnetomotive force (A turns)	224000	144000
Number of turns	256	320
Conductor size	8×8 ($\phi 6$ hole)	13.5×11.5 ($\phi 6.3$ hole)
Coil Winding	Double Pancake Winding	Solenoid Winding
Field Gradient (T/m)	6.6	4.2
Max. Current (A)	875	450
Resistance (m Ω)	181 (@55 °C)	119 (@45 °C)
Cooling Water Flow rate (l/m)	49.6	17.3
Pressure drop (MPa)	0.36	0.38
Number of Coolant circuits	16	8
Total Magnet Weight (ton*)	8.2	10.5

*metric ton.

Table 2.4: Q1 and Q2 parameters

This spectrometer was designed to have short orbit to reduce the number of kaon decay. The designed energy resolution is 2.0×10^{-4} (FWHM) and the acceptance with splitter magnet is 16 msr. This has more than three times larger acceptance than the kaon spectrometer which used at the previous experiment (5 msr). The HKS is installed to detect particles with the scattered angle from 1° to 13° because excessive background of positrons scattered at very forward angle. The particles are measured by following detectors. Details of detectors will be described in the next chapter.

HKS drift chamber (HDC)

The particle trajectory is measured by the two sets of drift chambers (HDCs) which are mounted directly on the HKS dipole magnet. By combining with spectrometer optics information, the momentum and scattered angle at target are reconstructed.

Item	D	
Pole gap height (mm)	200	
Pole length (mm)	1560	
Max. Ampere turns (A turns)	291840	
Number of turns	256	
Conductor size	22 × 22 (ϕ 12 hole)	
Max. Field (T)	1.53	
Max. Current (A)	1140	
Resistance (@47.5 °C) (m Ω)	145	
	Gap side	Yoke Side
Cooling Water Flow rate (l/m)	66.3	68.8
Pressure drop (MPa)	0.32	0.35
Number of Coolant circuits	8	8
Total Magnet Weight (ton*)	210	

*metric ton.

Table 2.5: Dipole magnet parameters

HKS scintillation counters (HTOF)

HKS scintillation counters determine the trigger timing and measure the time of flight (TOF) of particles.

HKS Aerogel Cherenkov counters (AC)

To suppress the pions in HKS at both online and offline levels, three layers of silica Aerogel Cherenkov counters (AC) are installed.

HKS Water Cherenkov counters (WC)

Two layers of Water Cherenkov counters (WC) are installed for the suppression of the protons at both online and offline levels.

2.4.4 Tilt method for scattered electron

The scattered electron spectrometer consists of ENGE magnet (Fig. 2.10) and detectors. ENGE magnet constructed by Enge in 1960's has normal conducting separated pole pieces (split-pole type magnet) and designed to obtain two-directional focusing over the full momentum range of $p_{max}/p_{min} \approx 2.8$ (energy range $E_{max}/E_{min} \approx 8$) [41]. Therefore, this spectrometer is so-called hardware spectrometer which measure the momentum from the horizontal position on the focal plane. In E89-009, only the horizontal position has been measured by silicon strip detector and momentum resolution of 5×10^{-4} (FWHM) for the central momentum of 0.3 GeV/c has been obtained. For E01-011, the magnet is tilted about 8 degrees vertically to suppress a huge amount of scattered electron (Tilt method).

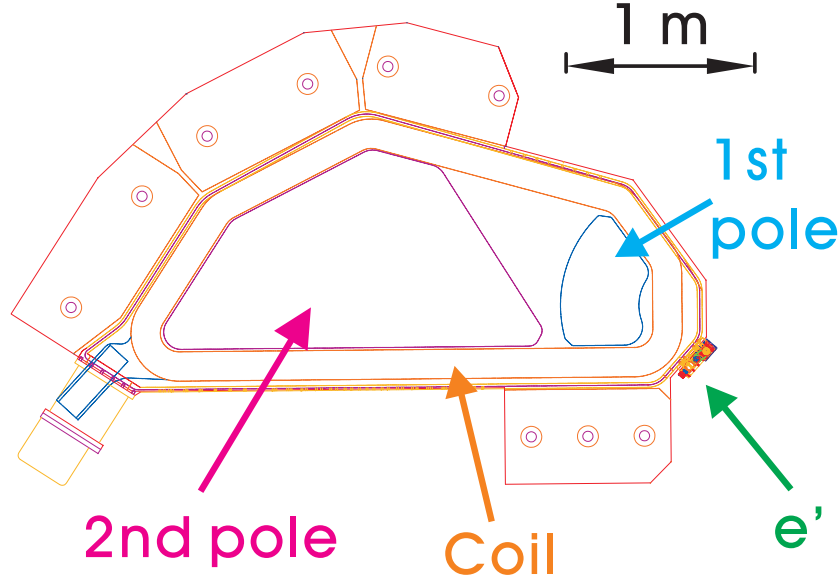


Figure 2.10: Schematic view of ENGE magnet.

As already discussed, 0-degree scattered electrons had been measured in the previous experiment since the virtual photon flux is maximum at forward angles. However, the electrons from Bremsstrahlung also has forward peak and had caused a huge background. Therefore, both the target thickness and beam intensity had been confined to keep singles rates under operation limit of detectors. Because the angular distributions for Bremsstrahlung and virtual photon associated electron are different, the signal to noise (S/N) ratio can be optimized at larger detection angle (Fig. 2.6). On the other hand, the singles rate in total drops down significantly. Thus we can increase the luminosity by using a thicker target and higher beam intensity. This is a principle of the Tilt method.

The Møller scattering electron should be taken into account for the decision of detection angle. Since Møller scattering is two electrons' elastic scattering, a scattered angle is determined uniquely with a given momentum, for example, the ENGE acceptance. The tilt angle was optimized by optical code, RAYTRACE, and Monte Carlo simulation GEANT. The result is shown in Fig. 2.11. Here, singles rate from each process is shown as a function of ENGE tilt angle. A figure of merit (FoM) is defined as $FoM = S/N^{1/2}$, where S is virtual photon rate and N is the sum of Bremsstrahlung and Møller. As a result, the ENGE magnet was vertically tilted by 8 degree because we used the splitter magnet which has horizontal dispersion plane (Fig. 2.12).

Introducing this new technique, we were able to use about 5 times thicker target and 50 times higher beam intensity than the previous experiment. Even though the luminosity was more than 200 times higher, the singles rate for scattered electron was kept 100 times lower (Tab 2.6). Therefore, the statistics and S/N ration were drastically improved and it made possible to take data for beyond p-shell hypernuclei.

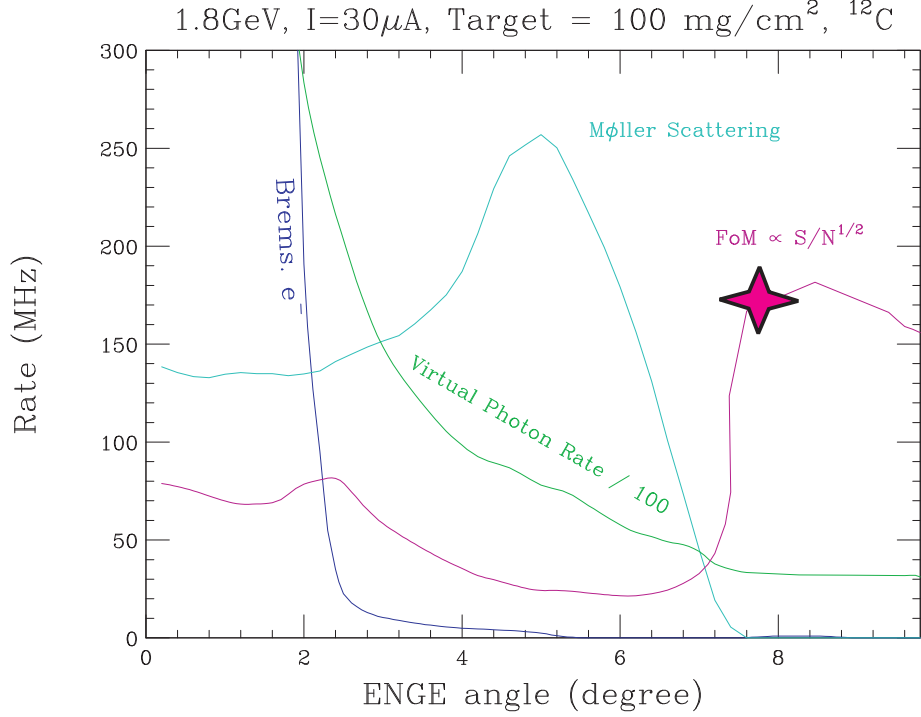


Figure 2.11: Figure of merit (FoM) for scattered electron. The singles rate of each process is represented as a function of tilt angle. FoM is defined as $S/N^{1/2}$, where S is virtual photon rate and N is the sum of Bremsstrahlung and Møller. FoM and virtual photon rate is multiplied by arbitrary factors.

Experiment	Target thickness ^{12}C , [mg/cm^2]	Beam current [μA]	ENGE singles rate [MHz]
E89-009 (w/o Tilt method)	22	0.66	200
E01-011 (w/ Tilt method)	100	30	1.3

Table 2.6: ENGE singles rate with or without Tilt method.

ENGE honeycomb drift chamber (EDC)

A trajectory of scattered electron was measured by a honeycomb-cell type drift chamber (EDC) mounted on the exit of ENGE magnet. Details of EDC are described in the next chapter.

ENGE hodoscope (EHODO)

For the measurement of TOF, an array of scintillation counters (EHODO) were installed behind the EDC. These counters were used for the trigger of scattered electron too. The EHODO consisted of two layers, with each layer composed of 25 counters. Details are represented in the next chapter.

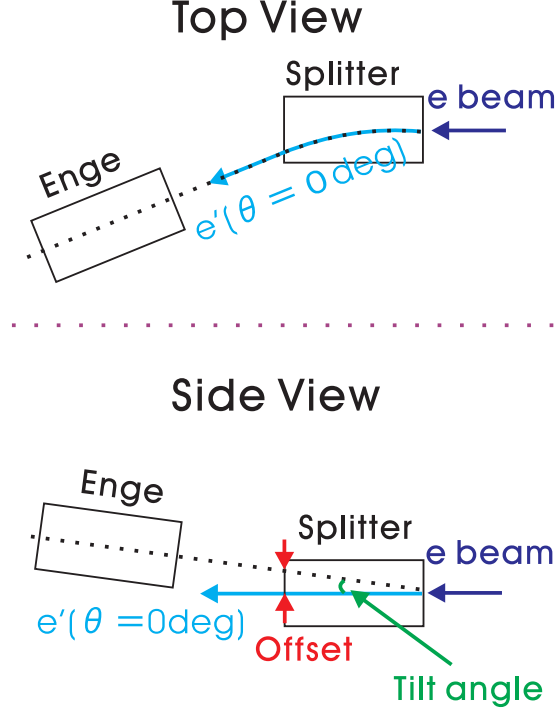


Figure 2.12: Schematic drawing of Tilt method. The ENGE magnet is vertically tilted because the splitter has horizontal dispersion plane.

The experimental configuration of E01-011 is summarized in Tab. 2.7.

2.4.5 Expected energy resolution and singles rate

The expected energy resolution for each target is summarized in Tab. 2.8. The momentum resolution of HKS/ENGE were estimated by GEANT/RAYTRACE including detector resolution and multiple scattering effect. They corresponds to missing mass resolution of 230 keV (FWHM) for HKS and 120 keV (FWHM) for ENGE. The uncertainty of K^+ emission angle is dominant in kinematic broadening. This depends on the target mass number. The momentum loss and spread in target were calculated with Vavilov distribution which reduced to the Landau distribution in the thinner absorber and to a Gaussian form in the thicker absorber [44]. Overall energy resolution were expected to be around 400 keV.

The expected singles rates with 100 mg/cm² target thickness and 30 μ A beam current are summarized in Tab. 2.9. The pion and proton rates in HKS were calculated based on EPC code [45]. They were normalized by the results of the previous experiment. Quasi-free kaon production cross section was assumed to scale as $A^{0.8}$. The index of 0.8 was taken from the effective proton numbers of the $^{12}\text{C}(\gamma, K^+)$ reaction [46]. Positron rate in HKS was evaluated with the GEANT. Because HKS is set to avoid 0 degree, no positrons passed through the dipole. Electron rate

Beam condition	
Energy	1.851 GeV
Stability	$< 1 \times 10^{-4}$
Configuration	Splitter magnet + HKS(QQD) + ENGE spectrometer
kaons spectrometer (HKS)	
Configuration	QQD
Central momentum	1.2 GeV/c
Momentum acceptance	$\pm 12.5\%$
Momentum resolution	2×10^{-4} (FWHM)
Acceptance (w/ splitter)	16 msr
Detection angle	7°
Angular acceptance	$1^\circ - 13^\circ$
ENGE spectrometer	
Central momentum	0.316 GeV/c
Momentum acceptance	$\pm 30\%$
Momentum resolution	4×10^{-4} (FWHM)
Tilt angle*	7.75°
Angular acceptance	$3.7^\circ - 5.7^\circ$

Table 2.7: Experimental configuration of E01-011.

* Due to the fringe field of ENGE magnet, the tilt angle should be larger than angular acceptance limit.

Item	Contribution to the mass resolution (keV,FWHM)			
	C	Si	V	Y
Target				
HKS momentum($\frac{\Delta p}{p}=2 \times 10^{-4}$)			230	
Beam momentum($\frac{\Delta p}{p}=1 \times 10^{-4}$ at 1.8 GeV/c)			≤ 180	
ENGE momentum			120	
K^+ angle ($\Delta\theta < 3.3$ mrad)	134	56	32	18
Target(100mg/cm ²)	< 180	< 171	< 148	< 138
Overall	≤ 390	≤ 360	≤ 350	≤ 345

Table 2.8: Expected energy resolution for each target.

in ENGE was evaluated by two methods, EGS code and Lightbody's code, which agreed more or less to each other. Pion rate in Enge was calculated based on the EPC code, and normalized by the same factor used for the hadron rates in HKS.

Target	Beam Intensity (μA)	HKS				Enge	
		e^+ rate (kHz)	π^+ rate (kHz)	K^+ rate (kHz)	p rate (kHz)	e^- rate (kHz)	π^- rate (kHz)
^{12}C	30	-	420	0.38	150	1,000	2.8
^{28}Si	30	-	420	0.32	130	1,900	2.8
^{51}V	30	-	410	0.29	120	2,650	3.0

Table 2.9: Expected singles rate, assumed 100 mg/cm² target thickness and 30 μA beam current.

2.4.6 Trigger

The main trigger was made from coincidence between HKS and ENGE. For ENGE side, the trigger was constructed by the coincidence of two layers of EHODO. For HKS side, protons and pions were dominant and background for our experiment. Therefore, they were roughly suppressed at trigger level by WC and AC. More tighter cuts were applied to select kaons at offline analysis. The HKS K^+ trigger was constructed like:

$$\text{HKS } K^+ \text{ trigger} = (\text{HTOF}) \otimes (\overline{\text{AC}}) \otimes (\text{WC}) \quad (2.6)$$

where HTOF, AC and WC are described with \oplus (logical “.OR.”) or \otimes (logical “.AND.”) between each layer as follows.

$$\text{HTOF} = \text{HTOF1X} \otimes \text{HTOF2X} \quad (2.7)$$

$$\text{AC} = \text{AC1} \oplus \text{AC2} \oplus \text{AC3} \quad (2.8)$$

$$\text{WC} = \text{WC1} \otimes \text{WC2} \quad (2.9)$$

Here, the number after AC or WC means the layer of each counters. Furthermore, we applied the grouping trigger to avoid kaon overkill and suppress background particles.

Grouping trigger

Because AC responds for pions, it was included as *VETO* into the trigger. Therefore, kaons could be overkilled if the pion detected at the same time. We introduced the grouping trigger which separated a series of detectors into 6 groups as shown in Fig. 2.13. Because the singles rate of AC decreases, the chance of kaon overkill also decreases. Moreover, this grouping trigger also rejects background particles come from beam dump or directly from target since they have larger angles than the particles from HKS optics. The grouping regions were determined by the detailed GEANT study.

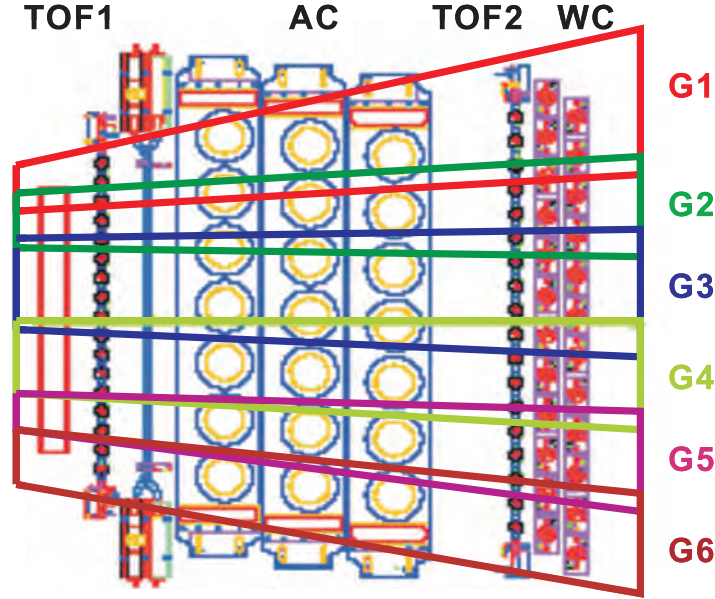


Figure 2.13: Schematic view of grouping trigger.

Tohoku Universal Logic module (TUL-8040)

The grouping trigger is very complicated and requires many more modules and cables in the case of conventional NIM (Nuclear Instruments Modules). Such complex triggers are difficult to construct and modify. Thus we developed a programmable logic module, so called Tohoku Universal Logic model (TUL-8040) (Fig. 2.14). The TUL-8040 has functions which are equivalent to a few tens of NIM modules, and a degree of functional modification is much increased by changing programs. Furthermore, a propagation time in one TUL-8040 module can be suppressed within 50 ns. TUL-8040 mounts ALTERA APEX 20K series of FPGA (Field Programmable Gate Array). FPGA is an extensive programmable logic device, which consists of various numbers of logic gates and flip-flop elements on arrays of which we can modify connections. This series of FPGA have already been utilized in several nuclear experiments at practical level [47, 48].

TUL-8040 has 80 channel inputs (ECL / LVDS 64 ch + NIM 16 ch) and 40 channel outputs (ECL 32ch + NIM 8 ch). Totally 6 TUL-8040 modules were installed for grouping trigger.

Main trigger

Figure 2.15 shows the trigger logic for HKS side after TUL-8040. The trigger timing was always determined by HTOF1X. In addition to HKS K^+ trigger, prescaled triggers for pion $((\text{HTOF}) \otimes (\text{AC}))$ and proton $((\text{HTOF}) \otimes (\overline{\text{AC}}) \otimes (\overline{\text{WC}}))$ were involved as a reference. Each grouping and trigger signal was sent to TDC to identify the trigger type at offline analysis.

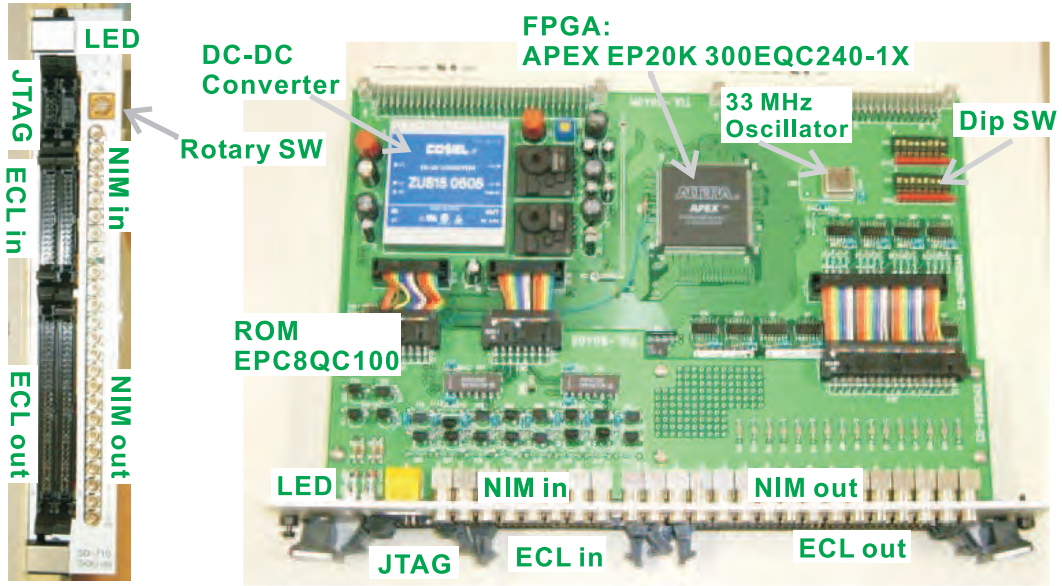


Figure 2.14: Front (*left*) and top (*right*) view of the TUL-8040.

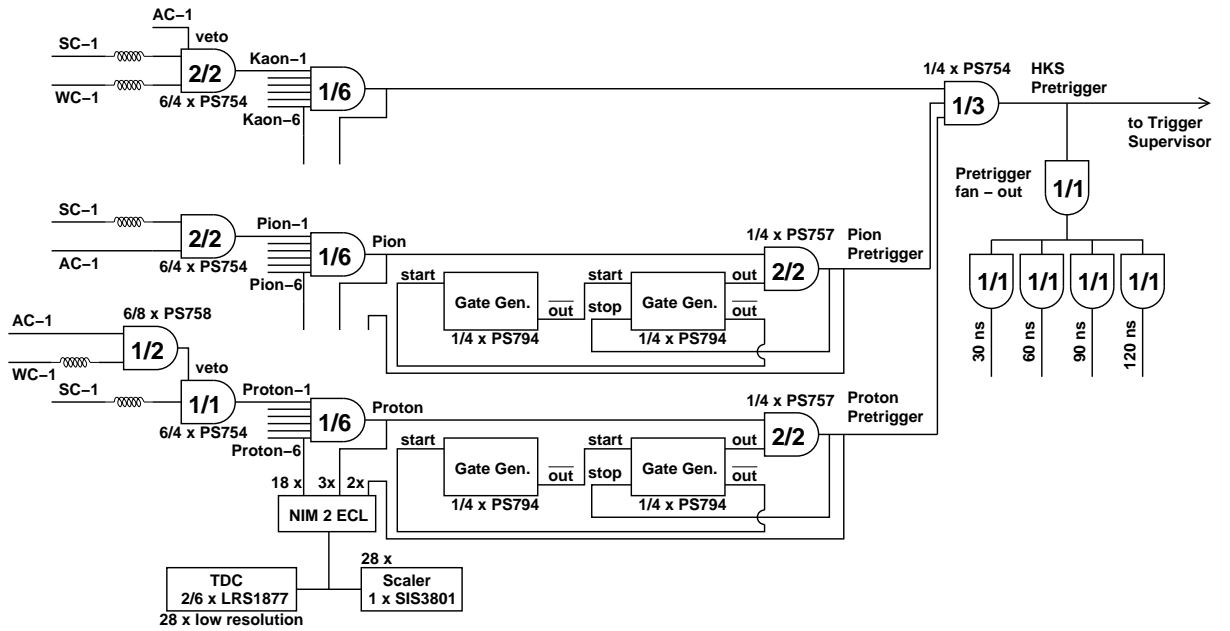


Figure 2.15: HKS trigger logic.

Trigger Supervisor System

The Trigger Supervisor System (TSS) is the link between the experiment specific triggering system and ReadOut Controllers (ROCs) [49]. The trigger system consists of a single Trigger Supervisor module (TS) and a separate interface card for each ROC, which have been developed at JLab. The TS acts as the central control

point for acquisition activity. It accepts and prescales multiple sources of triggers, both physics and calibration types. For example, a thousand pedestal triggers were added at the beginning of each physics run in our experiment. The role of TSS is summarized as follows.

- 1 Accepts and prescales multiple sources of triggers.
- 2 Maintains system busy while an input trigger is being processing.
- 3 Generates signals used for the gating and timing of ROCs.
- 4 Coordinates the actions of multilevel trigger systems.
- 5 Communicates triggering information to the system's ROCs.
- 6 Keeps track of the number of events currently in the ROC buffers.

All triggers are sent to a programmable logic module called 8LM (LeCroy 2365) and controlled by a TS. The TS logic diagram is described in Fig. 2.16. The 8LM receives *TS BUSY*, *TS EN1* or *TS GO* signals and pretriggers. The meanings of each signal are follows: *TS GO* : Run has started, *TS EN1* : Run has started and data taking is enabled, *TS BUSY* : Run has started but data taking is disabled.

The 8LM produces *TRIG* and *PRETRIG* signals, the only difference being whether the *TS BUSY* signal is affected (*TRIG*) or not (*PRETRIG*). All outputs in the 8LM are sent to the scalars and TDCs to be recorded. The 8LM sends the selected *TRIG* signals to the TS, producing a pair long gates (more than 100 μ s). All the ADC and TDC gates are generated by coincidence between the selected *TRIG* signals and the long gate.

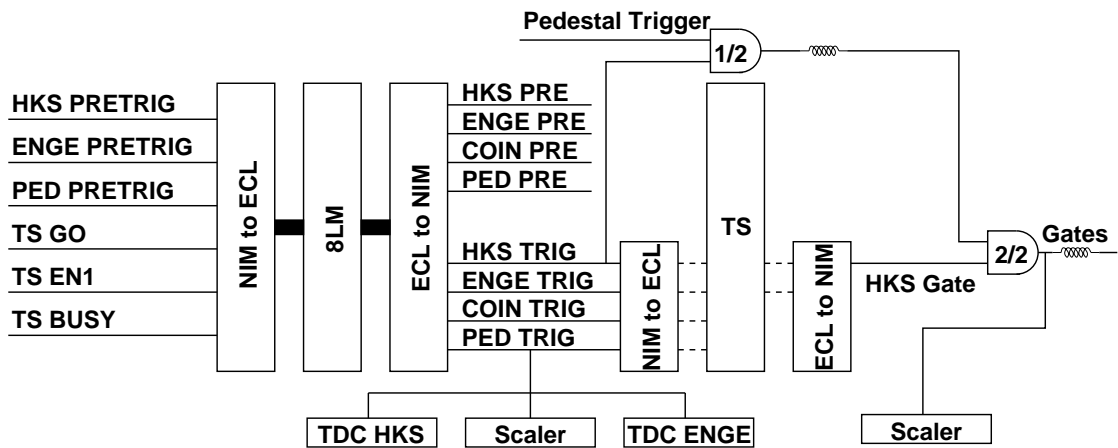


Figure 2.16: Trigger Supervisor (TS) logic.

2.4.7 DAQ

The collected electronic signals were converted to physics data sets written on disks by the CEBAF Online Data Acquisition (CODA) system [50]. General components which consists the CODA system are described in Fig. 2.17.

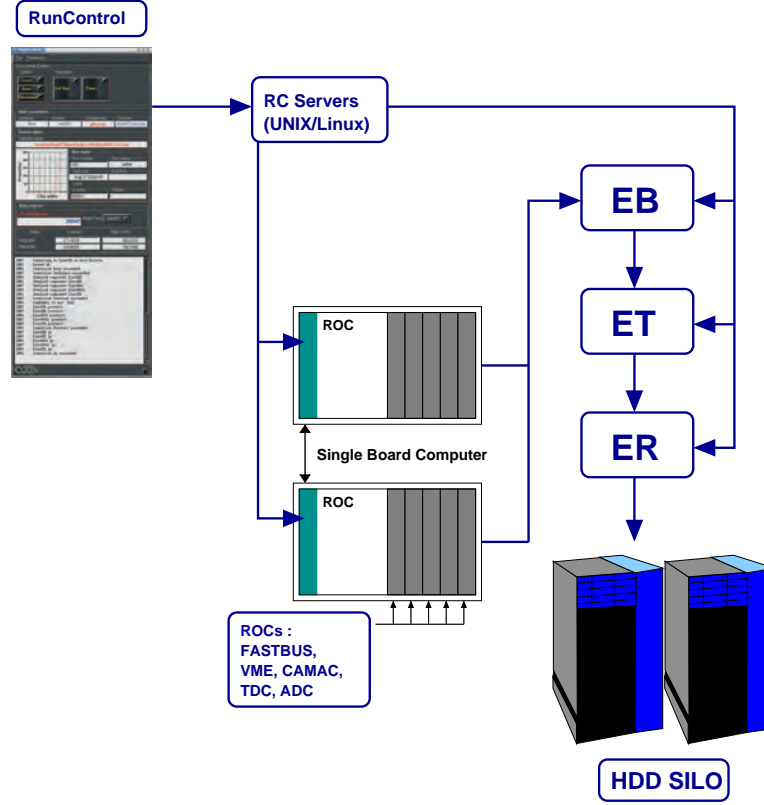


Figure 2.17: A flowchart of CODA.

All signals from HTOF, AC, and WC are sent to a counting house and digitized by FASTBUS TDC or ADC. Time information from drift chambers and EHODO are collected by VME TDC (F1 TDC) at the experimental hall. The information of F1 TDC will be described later. Scaler information is stored temporally in VME scalars. The ROCs read the event data and sent event fragments to the Event Builder (EB). The EB collects data streams from all ROCs indicated by TSS and performs event synchronization.

Combined data fragments by the EB are buffered in Event Transfer (ET). Event size dependency of the ET acceptable event rate is described in Fig. 2.18. As event rate is higher, event size which DAQ processes is decreased, and event rate (coincidence of ENGE and HKS triggers) which is sent to the ET is required to be reduced. Therefore we introduced the Cherenkov counters and grouping triggers in order to suppress the coincidence trigger rate to be less 1 kHz.

Typical event size for E01-011 was 30,000 bytes. Typical ENGE, HKS and coincidence trigger rate for various targets and currents are summarized in Table

2.10. Efficiency of this DAQ data process is estimated as a computer living time efficiency as discussed in Chapter 4.

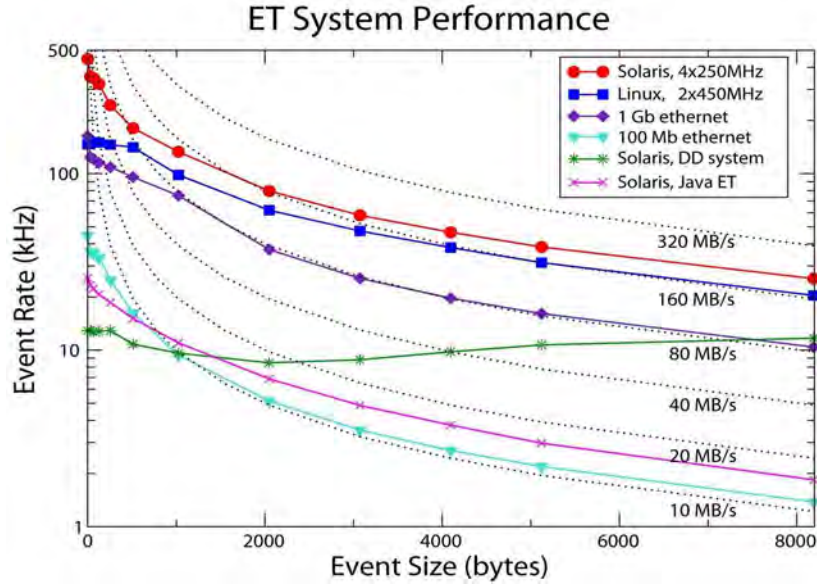


Figure 2.18: CODA DAQ rate performance [50].

The ET distributes data to online monitoring system according to user's requirements, and sends data fragments to Event Recorder (ER). Finally the ER organizes each data fragments into a standard format and writes them to the disks. GB ethernet interfaces connect the various CODA components, and the user controls the data acquisition through a GUI interface. The physics data are stored until the maximum data size set (1 Gbyte/run). Scaler data are stored in every 2 seconds during data taking. Information such as spectrometer settings, accelerator and target status are read out from the CEBAF EPICS database by a script CODA in every 2 - 30 seconds.

F1 TDC

FASTBUS based TDCs have been used at JLab for a long time, but they are no longer available commercially. In addition, they become the limiting factor for dead time and event rates primarily because of longer conversion times in higher rate experiment. Therefore, JLab has designed and developed a new VME based TDC, F1 TDC (Fig. 2.19) [51].

The F1TDC is 6U VME64X slave high resolution multihit TDC. Two kinds of resolution mode are selectable; high-resolution mode up to 60 ps LSB and normal-resolution mode up to 120 ps LSB with a reference clock of 40 MHz. In E01-011, high-resolution mode was applied for EHODO and normal-resolution mode was applied for drift chambers. This was the first full-scale experiment with F1 TDC, and thus, the new data acquisition system with F1 TDC was constructed and combined with existing DAQ. Specification of F1 TDC is summarized in Tab. 2.11

Target	Current [μ A]	HKS [kHz]	ENGE [MHz]	Coin. [kHz]
^6Li	16.0	8.1	1.0	0.29
	20.0	12.2	1.2	0.55
	25.0	20.3	1.5	1.09
^7Li	5.0	1.0	0.3	0.01
	25.0	13.0	1.2	0.69
	28.0	13.8	1.3	0.71
^9Be	19.0	10.1	0.9	0.40
	20.0	13.5	1.1	0.56
	23.7	17.3	1.3	0.79
^{10}B	8.0	1.5	0.4	0.02
	16.0	4.3	0.7	0.12
	30.0	14.2	1.3	0.69
^{12}C	13.0	3.5	0.6	0.09
	26.0	10.1	1.2	0.46
	30.0	14.8	1.4	0.73
^{28}Si	7.0	2.8	0.6	0.55
	13.0	8.4	1.2	0.36
	18.0	16.4	1.7	0.96
^{51}V	14.0	7.5	1.3	0.40
	18.0	15.4	1.8	1.04
^{89}Y	10.0	10.0	1.4	0.52
	13.0	17.5	1.8	1.10
^{208}Pb	0.3	9.9	1.0	0.38
	0.4	9.6	1.0	0.36

Table 2.10: Typical trigger rate for ENGE, HKS and Coincidence.

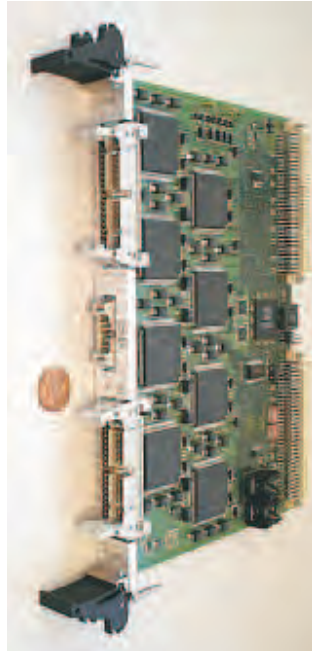


Figure 2.19: Picture of F1 TDC.

<i>Packing</i>	6U VME64X
<i>Inputs</i>	Differential ECL (110 Ohm) 64 channel @ 120 ps LSB 32 channel @ 60 ps LSB
<i>Clock</i>	Differential LVPECL (110 Ohm) - 40 MHz Internal, Front Panel, Back plane
<i>Standard Deviation</i>	Less than 0.9 LSB
<i>Acquisition</i>	Trigger Matching w/ Zero suppression Programmable Trigger Window and Latency
<i>FIFO</i>	1M TDC Data Words
<i>Interface</i>	32-bit VME Block Transfers (>20 Mbyte/s) 64-bit VME Block Transfers (>40 Mbyte/s)
<i>Power</i>	+12V @ 0.5A -12V @ 0.4A 3.3V @ 7.3A 5V @ 1.8A

Table 2.11: Specification of F1 TDC.

2.4.8 Data summary

Data were taken for totally ten targets as listed in Tab. 2.4.8. In the E01-011 experiment, a target is irradiated with high intensity electron beam (up to $30\ \mu\text{A}$) and radiation level around the target increase too high to exchange target. Therefore, an aluminum target ladder (Fig. 2.20), which has six $1.5 \times 1.5\ \text{cm}^2$ holes to hold six targets, was installed. Moving this ladder by remote control, we could change a target without access to the experimental hall.



Figure 2.20: Picture of a target ladder.

The melting point of CH_2 target used for mass scale calibration is low ($\sim 120\ ^\circ\text{C}$) and a high current electron beam with small spot size can easily punch through the target. To avoid this, the Fast Raster system [52] is used to enlarge beam spot size, so-called beam rastering. In the present experiment, the beam spot size for CH_2 target was required to be $5 \times 5\ \text{mm}^2$ (Fig. 2.21).

This beam rastering causes 300 keV mass shift to the missing mass of a Λ , which will give an ambiguity of absolute mass scale. Thus the raster effect is corrected by introducing the raster correction function, $f_{rc}(x_b, y_b)$,

$$X_{tar}^{cor} = f_{rc}(x_b, y_b) + X_{tar}. \quad (2.10)$$

Here X_{tar}^{cor} represents corrected target quantities (emission angle and momentum of a kaon or scattered electron) and X_{tar} target quantities calculated by the transfer

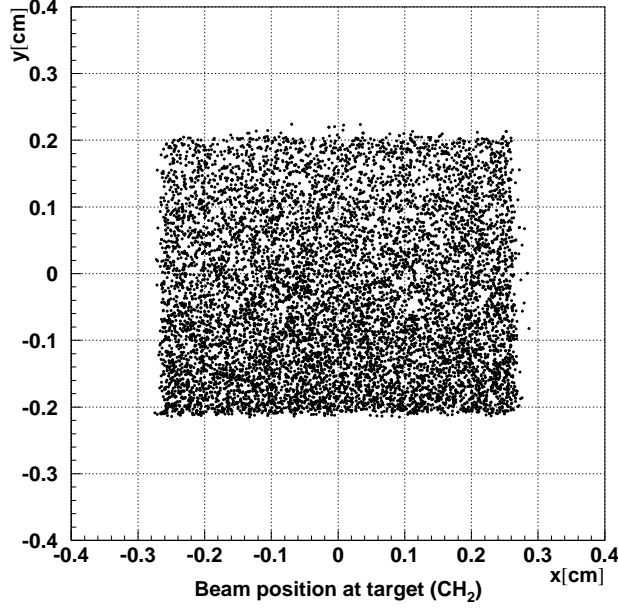


Figure 2.21: Beam position at CH₂ target with raster.

matrix of the spectrometer discussed in Sec. 4.5. The raster correction function can be expressed with the horizontal and vertical beam position, x_b and y_b

$$\begin{aligned}
 f_{rc}(x_b, y_b) = & C_0 x_b + C_1 y_b \\
 & C_2 x_b^2 + C_3 x_b y_b + C_4 y_b^2 \\
 & C_5 x_b^3 + C_6 x_b^2 y_b + C_7 x_b y_b^2 + C_8 y_b^3.
 \end{aligned} \tag{2.11}$$

Here, coefficients, C_x , are derived from a detailed Monte Carlo simulation.

An isotopically enriched target, ²⁸Si, was prepared by using the high intensity vibrational powder plating (HIVIPP) method [53]. A detail of this procedure is shown in Appendix C. Data taking for the ⁵¹V, ⁸⁹Y and ²⁰⁸Pb target was feasibility study for a future experiment. For heavier targets, the high statistics spectroscopy with good S/N ratio becomes more difficult under the present experimental condition since the beam current was limited by the trigger rate. The electron background rate was somehow higher than we expected because the precision of the magnet alignment was not enough. Therefore, more accurate and an improved configuration is necessary for such heavier hypernuclear spectroscopy.

Tab. 2.4.8 shows a summary of E01-011 data taking. During a commissioning run (#1 ~ #4) particle rates on each counter have been investigated and the grouping trigger was not introduced. For the production run (#5 ~ #22), trigger settings of cherenkov counters were changed frequently for rate and trigger study, except #8. HTOF1Y was introduced from #12.

Data set No. (Run No.)	Beam current (Ave.) [μA]	Target	Grouping	Trigger $\text{ENGE} \times \text{HTOF1X} \times \text{HTOF2X} \times \alpha$	Beam charge [mC]
# 1 (55838 - 55864, 55869 - 55910, 56088 - 56163)	2.3	CH_2	OFF	$\alpha = \text{W}\check{\text{C}}(\text{T} \oplus \text{B}) \times \overline{\text{A}\check{\text{C}}}(\text{T} \otimes \text{B})$	247.2
# 2 (55911 - 55921, 56167 - 56228)	16.1	^{12}C	OFF	$\alpha = \text{W}\check{\text{C}}(\text{T} \oplus \text{B}) \times \overline{\text{A}\check{\text{C}}}(\text{T} \otimes \text{B})$	618.5
# 4 (56231 - 56282)	19.7	^{12}C	OFF	$\alpha = \text{W}\check{\text{C}}(\text{T} \otimes \text{B}) \times \overline{\text{A}\check{\text{C}}}(\text{T} \oplus \text{B})$	249.8
# 5 (56283 - 56352, 56629 - 56663, 57203 - 57224, 57318 - 57334)	2.3	CH_2	ON	$\alpha = \text{W}\check{\text{C}}(\text{T} \otimes \text{B}) \times \overline{\text{A}\check{\text{C}}}(\text{T} \oplus \text{B})$	431.8
# 6 (56353 - 56474, 56528 - 56628, 56665 - 57200)	24.4	^{12}C	ON	$\alpha = \text{W}\check{\text{C}}(\text{T} \otimes \text{B}) \times \overline{\text{A}\check{\text{C}}}(\text{T} \oplus \text{B})$	6687.3
# 7 (56476 - 56523, 57225 - 57247, 57270 - 57317, 57335 - 57476, 57482 - 57528)	19.6	^9Be	ON	$\alpha = \text{W}\check{\text{C}}(\text{T} \otimes \text{B}) \times \overline{\text{A}\check{\text{C}}}(\text{T} \oplus \text{B})$	2367.5
# 11 (57547 - 57645, 57683 - 57727)	21.3	^{12}C	ON	$\alpha = \text{W}\check{\text{C}}(\text{T} \otimes \text{B}) \times \overline{\text{A}\check{\text{C}}}(\text{T} \otimes \text{B})$	1129.7
# 12 (57729 - 57830, 58401 - 58409)	21.6	^{12}C	ON	$\alpha = \text{HTOF1Y} \times \text{W}\check{\text{C}}(\text{T} \otimes \text{B})$ $\times \overline{\text{A}\check{\text{C}}}(\text{T} \otimes \text{B})$	661.3
# 13 (57258 - 57265, 57837 - 58394)	12.5	^{28}Si	ON	$\alpha = \text{HTOF1Y} \times \text{W}\check{\text{C}}(\text{T} \otimes \text{B})$ $(\times \overline{\text{A}\check{\text{C}}}(\text{T} \otimes \text{B}))$	2776.6
# 14 (58410 - 58716, 59112 - 59149, 59479 - 59511, 59870 - 59991, 60551 - 60561)	22.4	^{12}C	ON	$\alpha = \text{HTOF1Y} \times \text{W}\check{\text{C}}(\text{T} \oplus \text{B})$ $(\times \overline{\text{A}\check{\text{C}}}(\text{T} \otimes \text{B}))$	4633.1

Data set No. (Run No.)	Beam current (Ave.) [μ A]	Target	Grouping	Trigger ENG E \times HTOF1X \times HTOF2X \times α	Beam charge [mC]
# 15 (58719 - 59109, 59154 - 59315, 59362 - 59478, 59513 - 59750, 59801 - 59868, 59992 - 60019, 60095 - 60168, 60346 - 60394, 60562 - 60622, 60724 - 60756)	12.7	^{28}Si	ON	$\alpha = \text{HTOF1Y} \times \text{WC}(\text{T} \oplus \text{B})$ $(\times \overline{\text{AC}}(\text{T} \otimes \text{B}))$	10555.4
# 16 (59316 - 59360, 59751 - 59800)	18.2	^9Be	ON	$\alpha = \text{HTOF1Y} \times \text{WC}(\text{T} \oplus \text{B})$ $(\times \overline{\text{AC}}(\text{T} \otimes \text{B}))$	1316.3
# 17 (60026 - 60062, 60169 - 60198, 60395 - 60418)	12.4	^{51}V	ON	$\alpha = \text{HTOF1Y} \times \text{WC}(\text{T} \oplus \text{B})$ $(\times \overline{\text{AC}}(\text{T} \otimes \text{B}))$	699.6
# 18 (60063 - 60093, 60199 - 60232, 60421 - 60440)	10.6	^{89}Y	ON	$\alpha = \text{HTOF1Y} \times \text{WC}(\text{T} \oplus \text{B})$ $(\times \overline{\text{AC}}(\text{T} \otimes \text{B}))$	516.0
# 19 (60236 - 60354, 60441 - 60549, 61036 - 61068)	24.9	^7Li	ON	$\alpha = \text{HTOF1Y} \times \text{WC}(\text{T} \oplus \text{B})$ $(\times \overline{\text{AC}}(\text{T} \otimes \text{B}))$	3467.6
# 20 (60623 - 60723, 60757 - 60809, 60963 - 60981, 61015 - 61035)	20.5	^6Li	ON	$\alpha = \text{HTOF1Y} \times \text{WC}(\text{T} \oplus \text{B})$ $(\times \overline{\text{AC}}(\text{T} \otimes \text{B}))$	2273.3
# 21 (60812 - 60961)	26.5	^{10}B	ON	$\alpha = \text{HTOF1Y} \times \text{WC}(\text{T} \oplus \text{B})$ $(\times \overline{\text{AC}}(\text{T} \otimes \text{B}))$	3099.1
# 22 (60982 - 61013)	0.9	^{208}Pb	ON	$\alpha = \text{HTOF1Y} \times \text{WC}(\text{T} \oplus \text{B})$ $(\times \overline{\text{AC}}(\text{T} \otimes \text{B}))$	16.5

Table 2.12: Data acquisition settings. Here, $\text{T} \oplus \text{B}$ ($\text{T} \otimes \text{B}$) represents a .OR. (.AND.) logic of two PMT mounted on Top/Bottom side of each Čerenkov counter.

Target	Thickness [mg/cm ²]	Purity [%]	Total beam charge [mC]	Run time [hours]	Notes
CH ₂	460		679.0	82.2	for mass calibration
⁶ Li	164		2273.3	34.3	
⁷ Li (Nat.)	189	92.4	3467.6	42.3	
⁹ Be	188	99	3683.8	56.9	
¹⁰ B	114	~ 99.9	3099.1	35.1	Isotropically enriched
¹² C (Nat.)	100	98.9	13979.7	190.6	
²⁸ Si	65	~ 99.9	13332.0	331.9	Enriched
⁵¹ V (Nat.)	59.6	99.7	699.6	16.9	Enriched, for feasibility study
⁸⁹ Y	56	99.9	516.0	15.3	for feasibility study
²⁰⁸ Pb(Nat.)	283		16.5	5.7	for feasibility study

Table 2.13: Run summary.

Chapter 3

Detectors

In this chapter, the detailed R&D of detectors for E01-011 experiment will be presented.

3.1 Introduction

As already discussed in Chap. 2, HKS which consists of normal conducting QQD magnets and detectors was newly constructed to achieve momentum resolution of 2×10^{-4} (FWHM) for a kaon. Moreover, a huge amount of proton and pion were expected to be detected in HKS (Tab. 2.9). They need to be suppressed at the trigger level.

The detector package of HKS consists of two sets of planar-type drift chambers for the particle trajectory measurement, three layers of scintillation counters for both of the trigger and time of flight measurement and two kinds of cherenkov counters to suppress pions and protons at both online and offline level. A schematic top view of HKS detector package is shown in Fig. 3.1.

For scattered electron side, the detection angle of scattered electron was optimized and a new configuration of electron arm spectrometer (Tilt method) was introduced to the second generation ($e, e'K^+$) hypernuclear spectroscopy in JLab's Hall C(E01-011) [54, 55]. The E01-011 experiment aimed to achieve an energy resolution of around 400 keV (FWHM), thus the requirement for momentum resolution of scattered electron was 120 keV (FWHM, $\delta p/p = 4 \times 10^{-4}$) (Tab. 2.8).

The electron arm spectrometer in E01-011 consists of ENGE magnet which has been used in E89-009 and detectors. ENGE magnet is the split-pole type magnet and has good focusing power for not only horizontally but also vertically [41]. Therefore, only horizontal position at focal plane was measured in E89-009 and obtained the 5×10^{-4} resolution (FWHM, $\delta p/p$) with a central momentum of 300 MeV/ c .

The Tilt method allows us to take data with more than 200 times higher luminosity. However, it distorts the optical quality because of tilted ENGE magnet in E01-011 and it is essential to measure both position and angle at focal plane. We developed a new drift chamber with honeycomb cell structure in order to measure trajectory of scattered electron with angles distributed from -25° to $+25^\circ$ and a few MHz singles rate. Hodoscopes were also developed for the trigger and the time

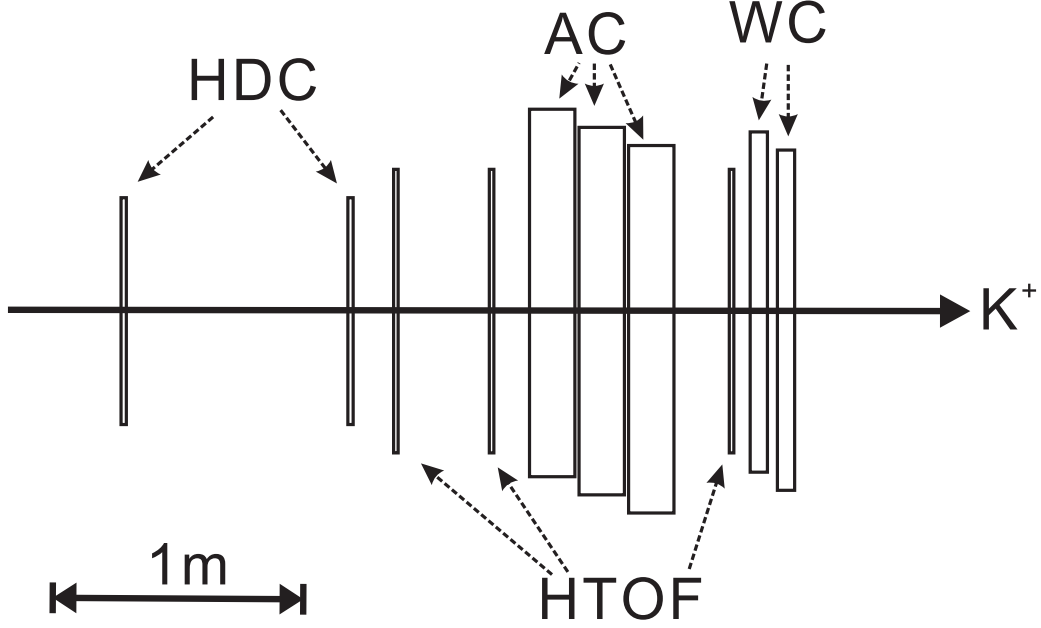


Figure 3.1: Schematic top view of HKS detector package.

of flight (TOF) measurement. These performances were checked with the beam at Laboratory of Nuclear Science (LNS), Tohoku University and 12 GeV-PS, KEK.

The detector package of e' spectrometer consists of drift chamber for tracking, hodoscopes for trigger and the TOF measurement and new readout system with VME-based high resolution TDC. The detector design and performance of each detector from beam test will be described in this chapter.

3.2 Detector design

3.2.1 HKS drift chamber (HDC)

The particle trajectory in HKS is measured by the two sets of drift chambers (HDCs) which are mounted directly on the HKS dipole magnet. By combining with spectrometer optics, the momentum and scattered angle at target are reconstructed.

The distance between HDCs is 1 m. Each HDC contains 6 planes (U, U', X, X', V, V'), therefore there will be 12 planes in total. The U and U' wires have an angle of 60° with respect to wires in X and X' plane, while V and V' wires have an angle of -60° . The effective area of each plane is $122 \times 30 \text{ cm}^2$ and cell size is 0.5 cm. The U', X' and V' planes have offset of half cell with respect to U, X and V planes, respectively, in order to increase the capability to resolve the left-right ambiguity. The layout of HDC is shown in Fig. 3.3. The sense wires are gold plated tungsten with the diameter of $30 \mu\text{m}$ and field wires are beryllium copper with the diameter of $90 \mu\text{m}$. The cathode planes which are double copper coated mylar are inserted between sensitive planes.

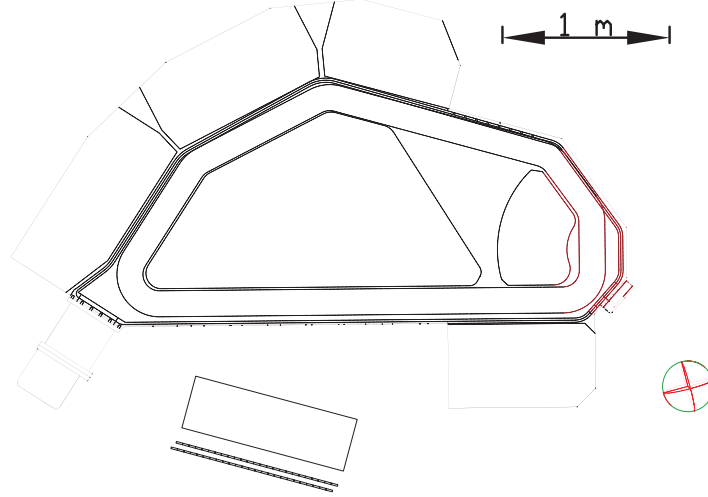


Figure 3.2: Schematic view of electron spectrometer. The spectrometer consists of ENGE magnet and detector package. Electrons are measured by the drift chamber and hodoscopes placed at the exit of magnet. The spectrometer was vertically tilted by 8 degree to improve signal to noise ratio. [54, 55]

The HDCs are filled with Ar-C₂H₆ 50/50 gas. Signals from the sense wires are fed to Nanometric N277L amplifier-discriminator cards which are attached to the frame of HDC. Discriminated ECL signals are sent to VME multihit TDC (F1 TDC, the detail of this module was shown in Sec. 2.4.7). The parameters of HDC are summarized in Tab. 3.1.

HKS DC Coordinate Systems and Wire Orientations (beam's eye view)

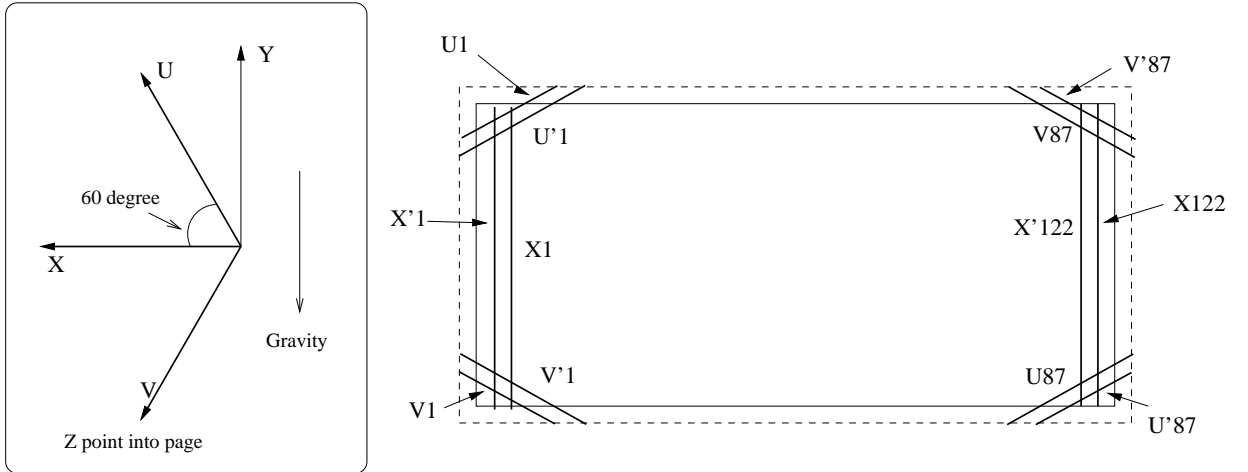


Figure 3.3: HDC wire layout and coordinate system.

Geometrical parameters	
Effective area	$122 \times 30 \text{ cm}^2$
Wire configuration	U, U', X, X', V, V'
Operational parameters	
Operation HV	– 1970 V
Threshold	3 V
Gas content	Ar + C ₂ H ₆ 50/50
Gas pressure	16 psi

Table 3.1: Parameters of HDC

3.2.2 HKS scintillation counters (HTOF)

HKS scintillation counters determine the trigger timing and measure the time of flight (TOF) of particles. There are three sets of hodoscopes, HTOF1X, HTOF1Y and HTOF2X. Each hodoscope consists of Bicron BC408 scintillator, acrylic light guides and Hamamatsu H1949-50 phototubes on both ends. HTOF1X consists of 17 segments of scintillators with an active area of $126.5 \times 30 \text{ cm}^2$ (Fig. 3.4). Similarly, HTOF2X consists of 18 segments, but has wider active area of $171 \times 30 \text{ cm}^2$ to cover dispersing particles at downstream. HTOF1Y consists of 9 vertical segments of scintillators with an active area of $125 \times 31.5 \text{ cm}^2$ (Fig. 3.5).

The distance between HTOF1X and HTOF2X is set to 1.5 m to separate kaons from pions and protons in the momentum region of interest. The parameters of HTOF are summarized in Tab. 3.2.

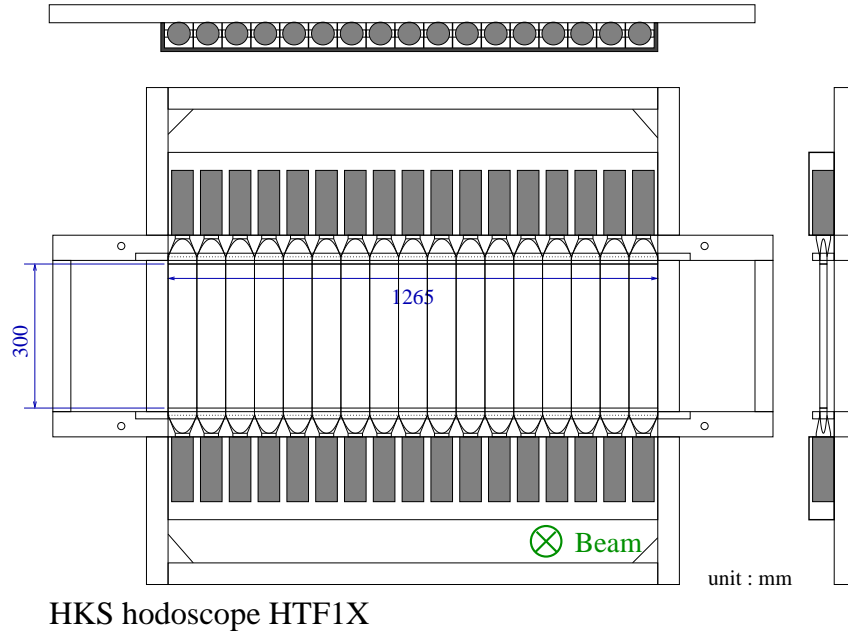


Figure 3.4: Schematic view of HTOF1X.

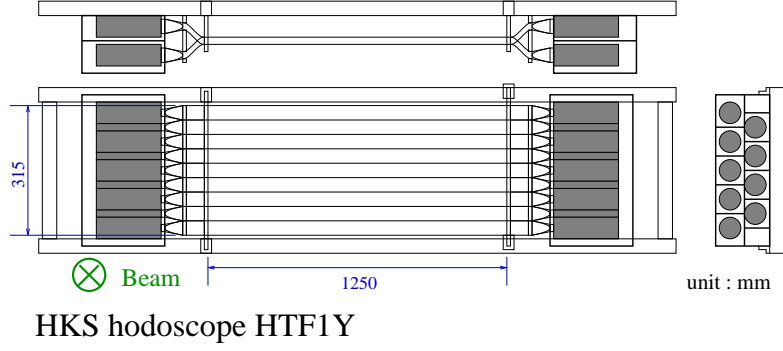


Figure 3.5: Schematic view of HTOF1Y.

Components		
Scintillator	Bicron BC408	
PMT	Hamamatsu H1949-50	
Geometrical parameters		
HTOF1X	$30^H \times 126.5^W \times 2^T \text{cm}^3$	$7.5^W \text{ cm} \times 17\text{-segments}$
HTOF1Y	$31.5^H \times 125^W \times 2^T \text{cm}^3$	$3.5^W \text{ cm} \times 9\text{-segments}$
HTOF2X	$35^H \times 171^W \times 2^T \text{cm}^3$	$9.5^W \text{ cm} \times 18\text{-segments}$
Operational parameters		
Operation HV	$\sim -1800 \text{ V}$	

Table 3.2: HTOF parameters.

3.2.3 HKS Aerogel Cherenkov counters (AC)

To suppress the pions in HKS trigger by a factor of 10^{-4} , three layers of silica Aerogel Cherenkov counters (AC) are installed just behind the HTOF1Y. The AC consists of one diffusion box with an internal volume of $46^H \times 169^W \times 31^T \text{ cm}^3$ (Fig. 3.6), silica aerogel tiles with a refraction index of 1.05 (Matsushita Electric Works SP-50, $11.3^H \times 11.3^W \times 1^T \text{ cm}^3$ for one tile) and phototubes. The interior of box is covered with a Millipore membrane paper (HAHY0010). The box is also optically separated into 7 segments by the Millipore paper to distinguish between multiple tracks and therefore avoid the overkill of kaons. 5 layers of 4 by 2 silica aerogel tiles are placed at the upstream of each segment. The two kind of $5''\phi$ phototubes (Hamamatsu R1250 for the first and second layer, Photonis XP4572B/D1 for the third layer) are mounted on both sides of diffusion box directly. The AC is designed based on a test experiment in KEK-PS [56].

3.2.4 HKS Water Cherenkov counters (WC)

Two layers of Water Cherenkov counters (WC) are placed behind the HTOF2X for the suppression of the protons by a factor of 10^{-4} in the trigger. Each layer has 12 segments. The box is made of white cast acrylic sheet (Mitsubishi Rayon

HKS aerogel Cherenkov Counter

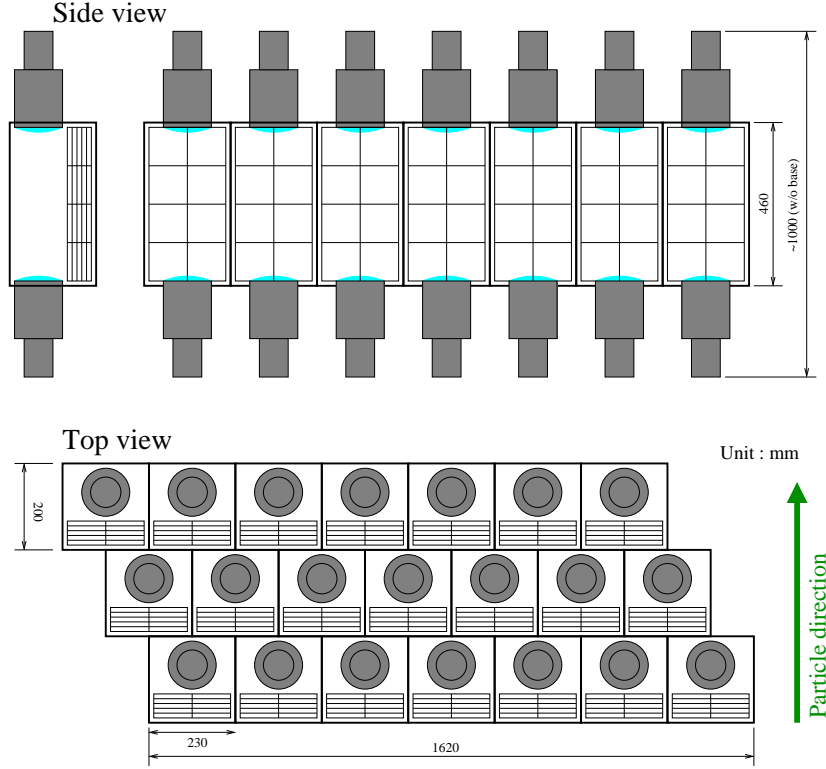


Figure 3.6: Schematic view of AC.

Co., Ltd; Acrylite #402) with the radiation volume of $35^H \times 15^W \times 7.5^T \text{ cm}^3$. Two UVT acrylic windows (Mitsubishi Rayon Co., Ltd; Acrylite #000) viewed from both end by Hamamatsu R329-02 phototubes. The box is refilled with de-ionized water ($\sim 18 \text{ M}\Omega\text{-cm}$) whose refraction index of 1.33 is suitable to distinguish between kaons and protons in the momentum region of interest ($1.05 \sim 1.35 \text{ GeV}/c$). To improve the gain and light emission uniformity, the amino G-salt (Di-pottasium salt of 2-amino-6, 8-naphthalene-disulphonic acid) is dissolved into the water as a wave length shifter ($100 \text{ mg}/l$) [57].

3.2.5 ENGE Drift Chamber (EDC)

The required performance of drift chamber was estimated by a detailed simulation including window material, $\text{Ar} + \text{C}_2\text{H}_6$ gas and multiple scattering. The result showed that the horizontal and vertical resolution on the focal plane should be better than $200 \text{ }\mu\text{m}$ and $300 \text{ }\mu\text{m}$, respectively, and the angular resolution should be better than 1.5 mrad to achieve the momentum resolution of 4×10^{-4} (FWHM, $\delta p/p$) for scattered electron.

Another requirement for the drift chamber is to detect electrons with large incident angle (from -25° to $+25^\circ$) under high singles rate of a few MHz. Therefore, we adopted honeycomb cell structure (side of cell is 0.5 cm) which has good symmetry

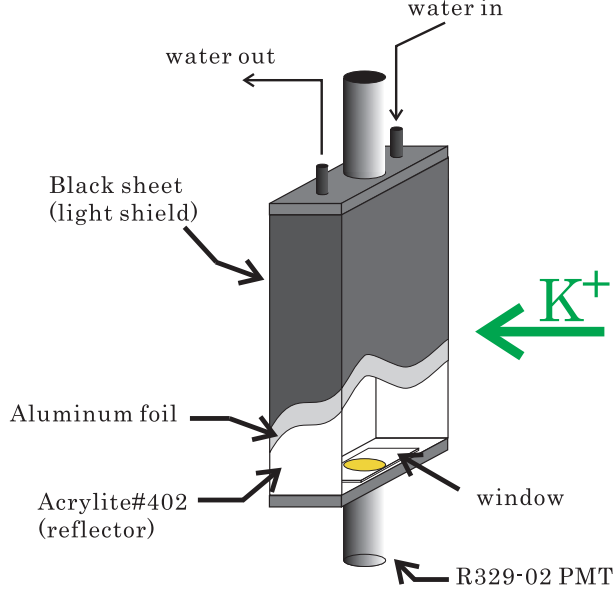


Figure 3.7: Schematic view of WC.

of electric field.

The chamber consists of 10 layers (xx',uu',xx',vv',xx'). The x', u' and v' layer is shifted by half cell from x, u and v, respectively. The uu' and vv' layers are tilted by +30° and -30° with respect to the x. The distance between x and u(v) layer is 7.5 cm and there are shield wire between layers for electrical separation. The chamber box is made of aluminum and feed-throughs are inserted in the drilled holes of 0.248 cm ϕ on the box and glued. In order to stretch wires of u and v layers, holes are tilted by $\pm 30^\circ$ (Fig. 3.8).

The effective area is 100 cm (width) \times 12 cm (height) \times 32 cm (depth) and filled with Ar+C₂H₆ (50% : 50%) gas. Anode and shield wires are connected to ground and operational voltage of cathode wire is optimized as about -2200 V (Sec. 3.3.1). In total, there are 1098 readout channels which are connected to the amplifier discriminators (Nanometric, N277L) mounted on the outside of chamber. N277L card has 16 channels and its power consumption is about 5.5 W per card. Thirty-five N277L cards are mounted on the top of the box (the bottom side also has 35 cards). The total consumption power of one side reached as much as 192.5W. The ventilation air flow V (m³/min) for emitting this power into the air can be estimated as

$$w = \frac{V}{60} \times d \times C \times T_f. \quad (3.1)$$

Here, w , d , C and T_f represent heat out per second by fan, air density, specific heat of air and temperature difference by the performance of fan and surrounding environments, respectively. Assigning $w=192.5$ (J/sec), $d=1.2$ (kg/m³) and $C=1000$ (J/(kg \cdot °C)), one can obtain

$$V = \frac{9.625}{T_f}. \quad (3.2)$$

Assuming the estimation at the minimum, $T_f=1$ ($^{\circ}\text{C}$), ventilation air flow has to be more than $9.6 \text{ m}^3/\text{min}$ to cool the cards. Therefore, the 6 fans are attached on one side of chamber. Since each fan has $2 \text{ m}^3/\text{min}$ ventilation power, the total ventilation air flow is $12 \text{ m}^3/\text{min}$ for one side. The specification of the drift chamber is summarized in Table 3.3.

Effective area	100 cm \times 12 cm \times 32 cm
Number of layer	10(x,x',u,u',x,x',v,v',x,x')
Distance between paired layers	7.5 cm
Side of honeycomb cell	0.5 cm
Tilt angle of u,u',v,v'	$\pm 30^{\circ}$
Window	Aluminized Myler(12.5 μm thick)
Anode wire	gold-plated W (20 $\mu\text{m}\phi$)
Cathode wire	gold-plated Al (80 $\mu\text{m}\phi$)
Amplifier discriminator	Nanometric N277L
readout channel	xx'=672ch uu'=213ch vv'=213ch total=672+213+213=1098ch
Tension of Anode wire	50 gw
Tension of Cathode wire	90 gw
Gas	Ar + C ₂ H ₆ (50 % : 50 %)
Operational voltage	-2200 V

Table 3.3: Specification of drift chamber.

3.2.6 ENGE Hodoscope (EHODO)

Behind the drift chamber, hodoscopes are installed for the purpose of trigger and TOF measurement. The required TOF resolution is about 75 ps (rms) which corresponds to the resolution of hodoscopes of K^+ side [54, 55]

The total singles rate of electron was estimated as 5 MHz. To keep the singles rate of each counter less than 1 MHz, the size of plastic scintillator (BICRON, BC420) was set to 4 cm \times 12 cm \times 1 cm. The UVT acrylic light guides and 3/4" ϕ photomultipliers(PMT) (Hamamatsu, H6612) are attached on both sides of a scintillator (Fig. 3.9). As a glue to attach PMT on light guide, the UV cure plastic adhesive (DYMAX, 3094) is used instead of usual optical cement. The UV adhesive has much shorter cure time upon exposure to UV light (typically a few second) than the optical cement, and thus a assembly of the counter is much easier.

To check the performance of UV adhesive, transmissivity measurement was performed. The result showed the same transmissivity as optical cement in the region

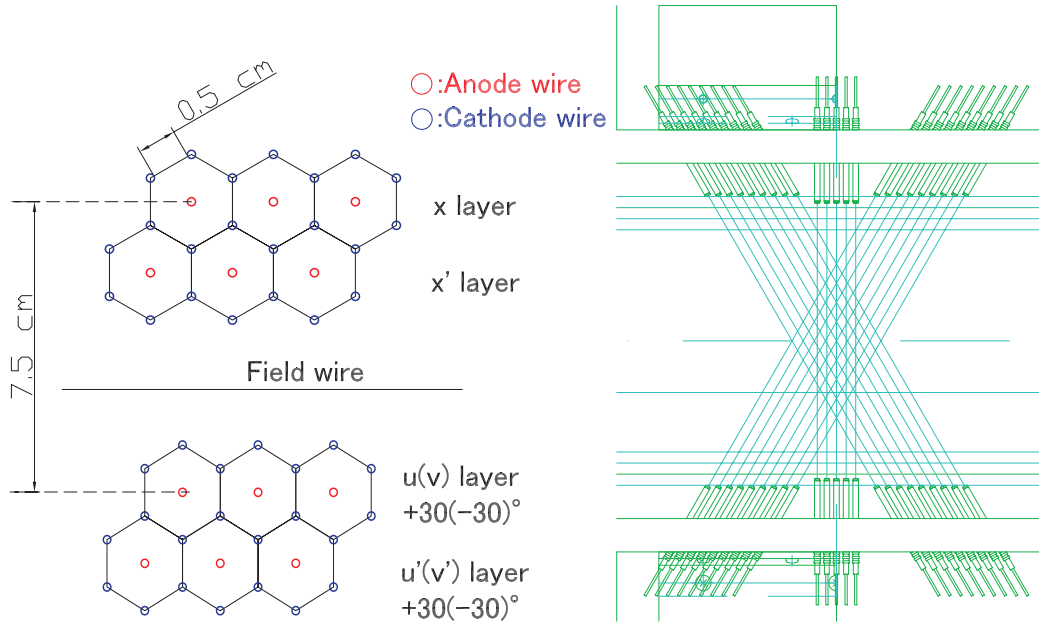


Figure 3.8: Wire configuration of drift chamber.

of visible light which is the most sensitive for H6612 PMT. Additionally, the TOF comparison between UV and optical glue was studied with the same scintillator and PMT. It was confirmed that there was no difference between them.

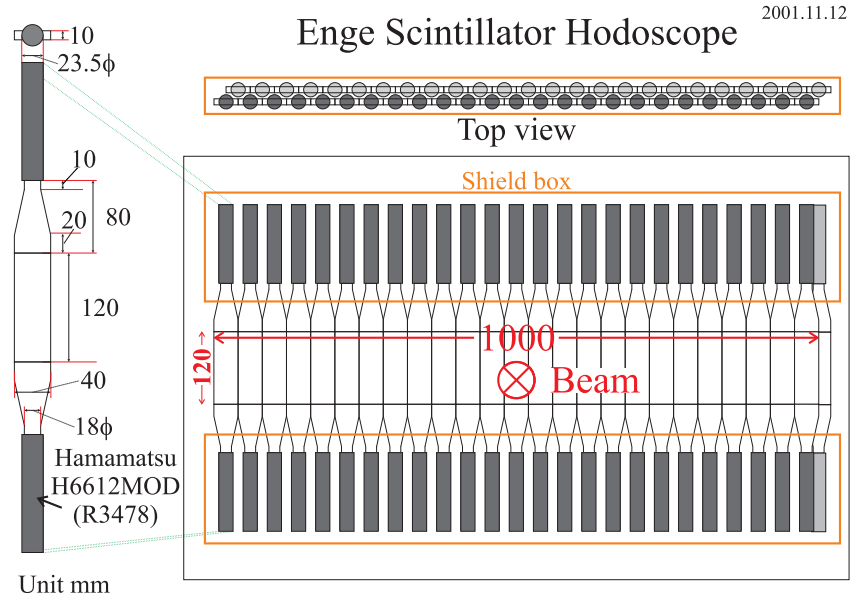


Figure 3.9: Schematic view of hodoscopes. Two layers of hodoscopes were placed behind the drift chamber. Each layer had 25 scintillation counters.

3.3 Performance study of the EDC at LNS

3.3.1 Plateau curve

Figure 3.10 shows the supplied voltage dependence of singles rate checked by ^{90}Sr close to window. We found a clear plateau around -2200V.

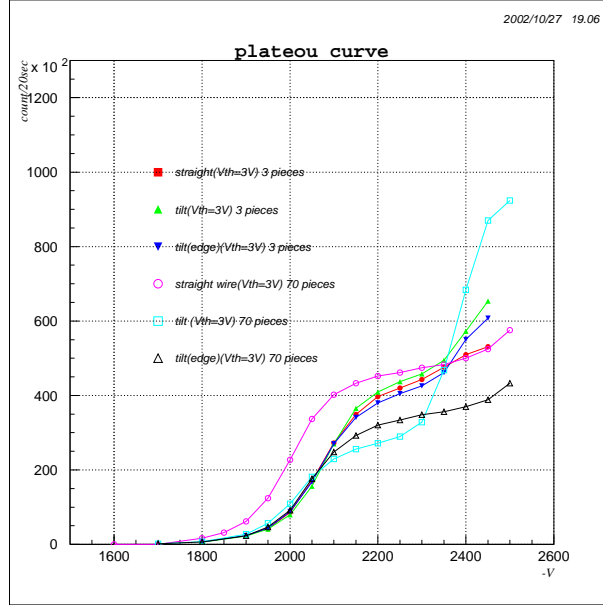


Figure 3.10: Singles rates of the drift chamber with the ^{90}Sr beta source in the function of supplied voltage. Since the distance between the wire and source was not the same, the singles rates were all different.

3.3.2 Setup of beam test

The performance of the drift chamber was studied at LNS. The tagged photon from 1.2 GeV Stretcher-Booster Ring was converted into positron and electron pair by a copper wire of 0.9 mm ϕ in the front of a dipole magnet. The positron and electron were deflected by the dipole magnet and passed through the drift chamber with the momentum from 200 to 400 MeV/ c and the incident angles from 10 to 25°. Two scintillation counters were placed behind the chamber for the trigger. (Fig. 3.11).

3.3.3 Analysis and result

The typical drift time of drift chamber is shown in Fig. 3.12 with supplied voltage of -2200 V. The drift distance is calculated by 3rd order polynomial in drift time. The trajectory of electron is obtained by minimizing following χ^2 ,

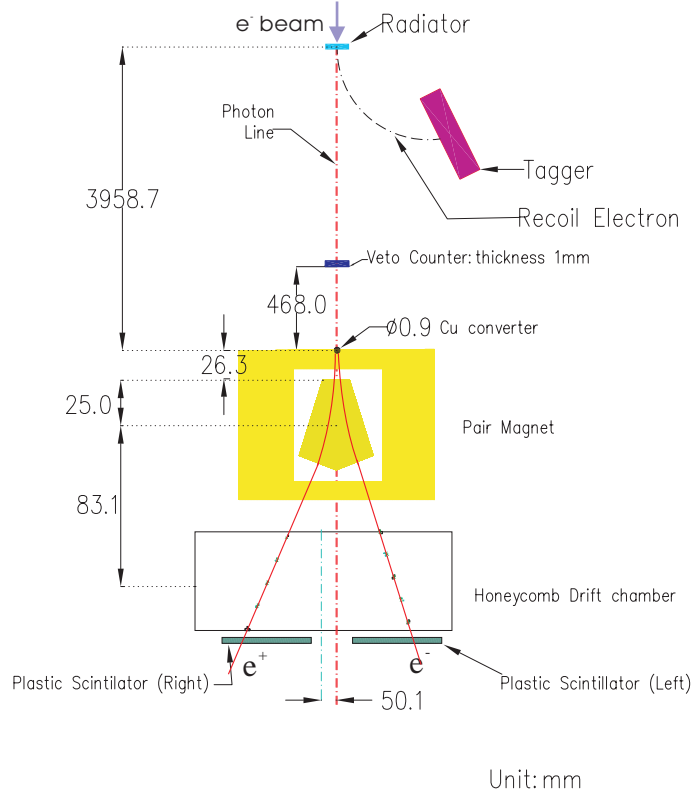


Figure 3.11: Experimental setup at LNS. The tagged photon from accelerator was converted into positron and electron by the copper converter of 0.9 mm ϕ in the front of dipole magnet.

$$\chi^2 = \sum_{i=1}^n w_i (s_i - s(z_i))^2 \quad (3.3)$$

$$w_i = \frac{1}{\sigma_i} \cos \theta_i. \quad (3.4)$$

Here, n , w_i , z_i , σ_i and θ_i represent number of layer, weight of each layer, distance along z-axis (electron direction), assumed position resolution of each layer and incident angle of electron, respectively. s is the distance along s-axis which is orthogonal to the sense wires. Since this chamber has honeycomb cell structure, the drift distance is described as the cylinder around the sense wire. Therefore, the z_i is not constant and fitting is done until the χ^2 will converge. The drift distance is updated in each iteration by fitting the correlation between drift time and drift distance (Fig. 3.13).

The position resolution and efficiency in each plane were given by the following. First of all, the trajectory is calculated by fitting 9 layers except for one layer. Then the efficiency was obtained by searching that the corresponding wire had a hit or not. The position resolution was the difference between trajectory and the position by

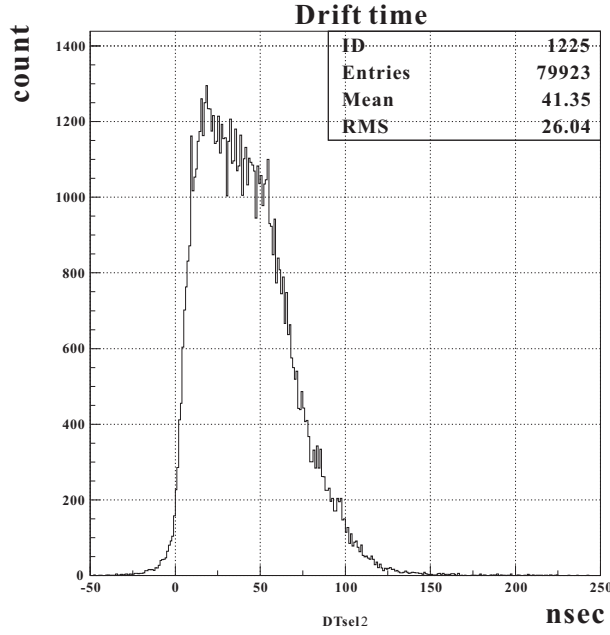


Figure 3.12: Typical drift time of drift chamber.

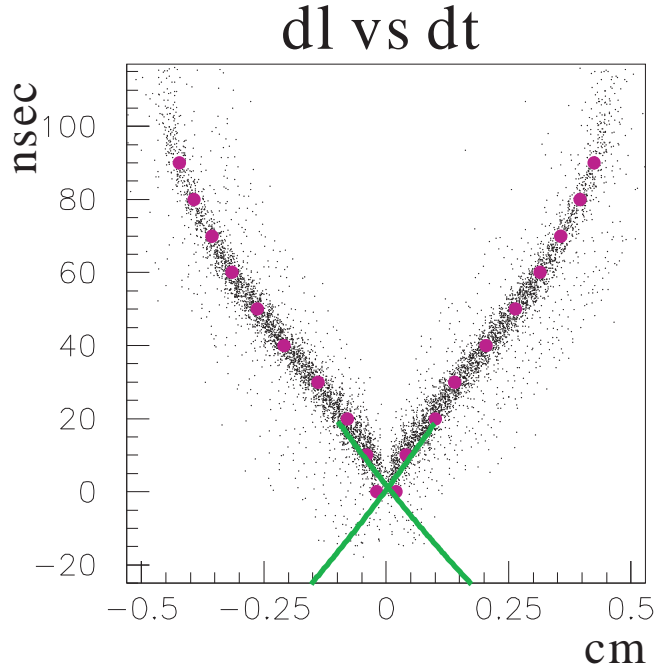


Figure 3.13: Correlation between the drift time and the drift distance. Purple points represent the mean value in each part and are fitted by 3rd order polynomial.

the drift length in expected layer. Figure 3.14 shows the layer dependence of position resolution with -2200 V. On average, we obtained about $230 \mu\text{m}$ position resolution per plane. Supplied voltage and threshold dependence of layer efficiency result were

shown in Fig. 3.15. The threshold of 1 V is equivalent to $1 \mu\text{A}$. The efficiency become almost flat with more than 99% in the region of less than -2100 V for supplied voltage and less than 4 V for threshold. Therefore, the operational voltage were determined to -2200 V for the supplied voltage and 2 V for the threshold.

The position and angular resolution as a drift chamber were defined as following. The trajectories by fitting 10 layers, only x and x' layers and u,u',v, and v' layers were calculated respectively. The horizontal position and angular resolution were defined as the residual between the 10 layers' fitting and x layers' one. Similarly, the vertical resolution was defined as the residual between 10 layers' fitting and u-v layers' fitting. As a result, we obtained $86 \mu\text{m}$ and $210 \mu\text{m}$ for horizontal and vertical position resolution, and 0.7 mrad and 2.8 mrad for horizontal and vertical angular resolution. It was confirmed that there was no dependence of incident angle and momentum of electron and positron.

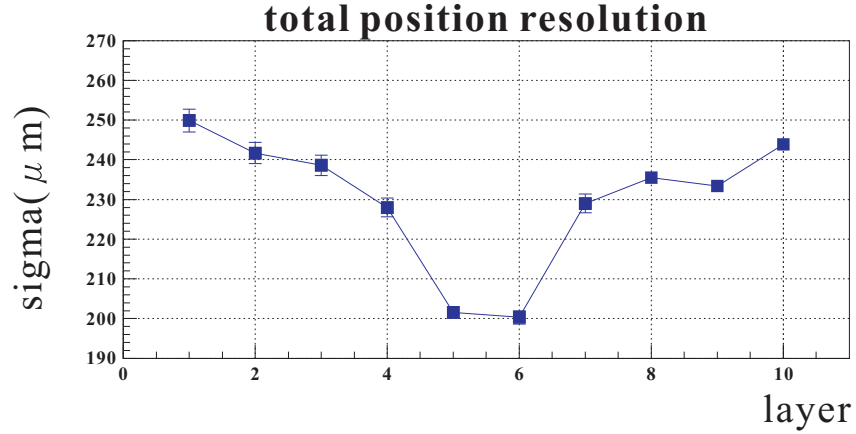


Figure 3.14: Position resolution of each layer.

Position resolution (horizontal : x)	$86 \mu\text{m}$
Position resolution (vertical : y)	$210 \mu\text{m}$
Angular resolution (horizontal : x')	0.7 mrad
Angular resolution (vertical : y')	2.8 mrad

Table 3.4: Position and angular resolution of drift chamber.

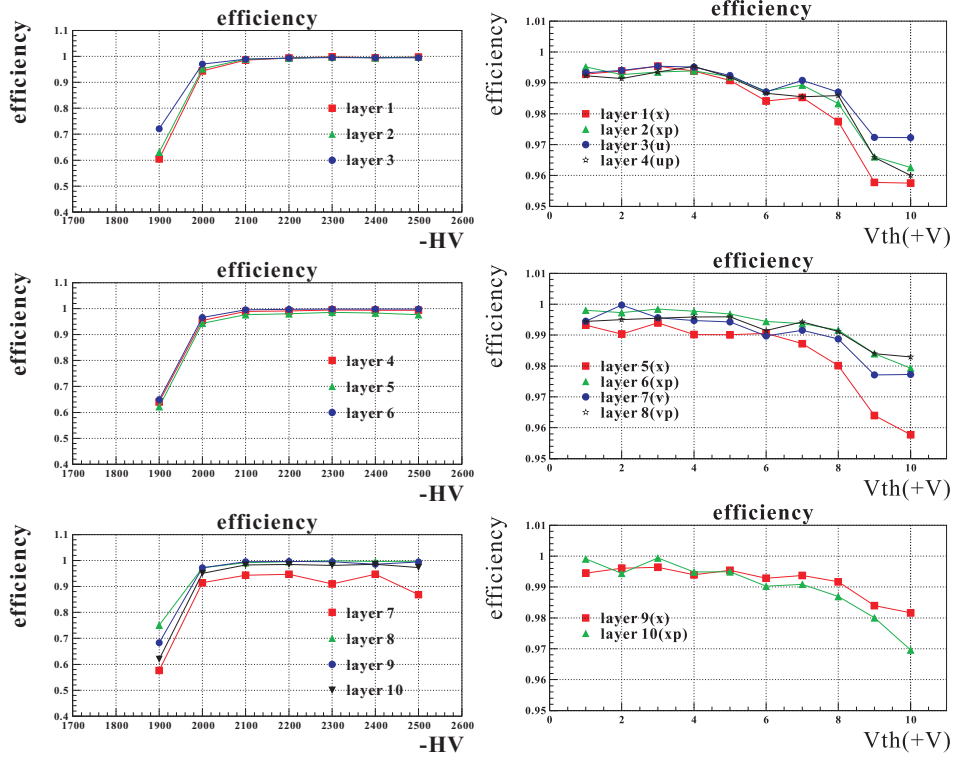


Figure 3.15: Voltage dependence on detection efficiency of each layer.

3.4 Performance test at KEK

3.4.1 Setup

The performances of HTOF, AC, WC and EHODO were studied at KEK 12GeV-PS T1 beam line (T494,T500 and T530 experiment that were beam test for the counters of E01-011). This beam line provided unseparated secondary beam containing pions, kaons and protons. The momentum from 1.05 GeV/ c to 1.35 GeV/ c which is the acceptance of K^+ spectrometer in E01-011 were extracted. The trigger was made by four EHODOs (two in front, two in back). Between the EHODOs, HTOF, AC and WC were placed and used for particle identification (Fig. 3.16).

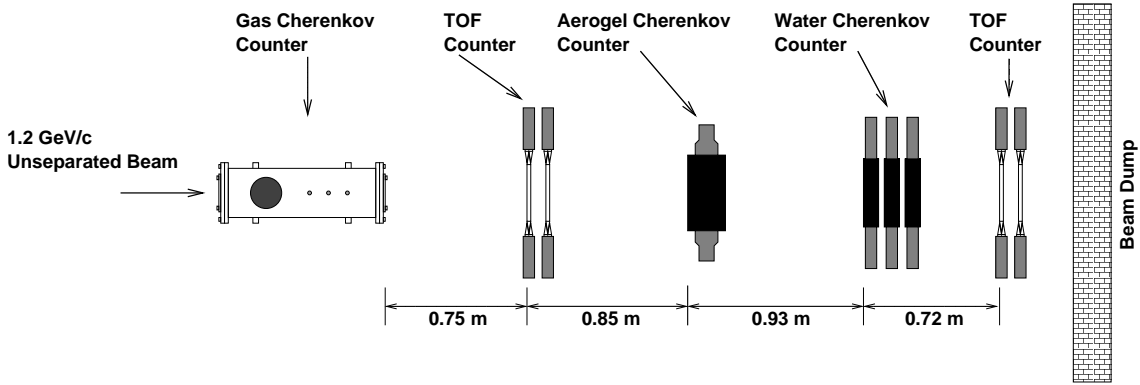


Figure 3.16: Schematic view of the performance test at KEK-PS T1 beamline.

3.4.2 Analysis and result

The particle could be identified easily from the information on TOF and cherenkov counters (Fig. 3.17). From the number of particles, proton suppression ratio of WC was estimated to be 97.7% at a certain threshold level, while the kaon overkill ratio was less than 3%. Therefore the proton suppression ratio can be 7×10^{-4} , considering two layers of WC will be used.

The TOF resolution of EHODOs for 1.2 GeV/ c pion is shown in Fig. 3.18 after slewing correction. As a result, we obtained 99 ps TOF resolution in sigma. Assumed that each counter has same resolution, the timing resolution of each counter was estimated to be 75 ps. For HTOF, the obtained TOF resolution was 77 ps in sigma.

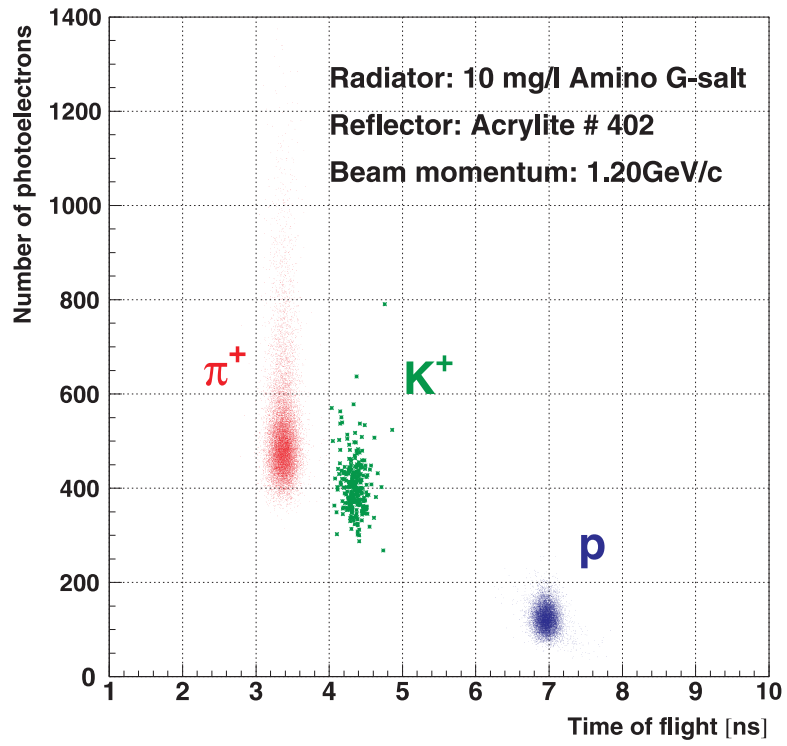


Figure 3.17: Correlation between the number of photoelectrons for WC and TOF distribution for 1.2 GeV/ c particles.

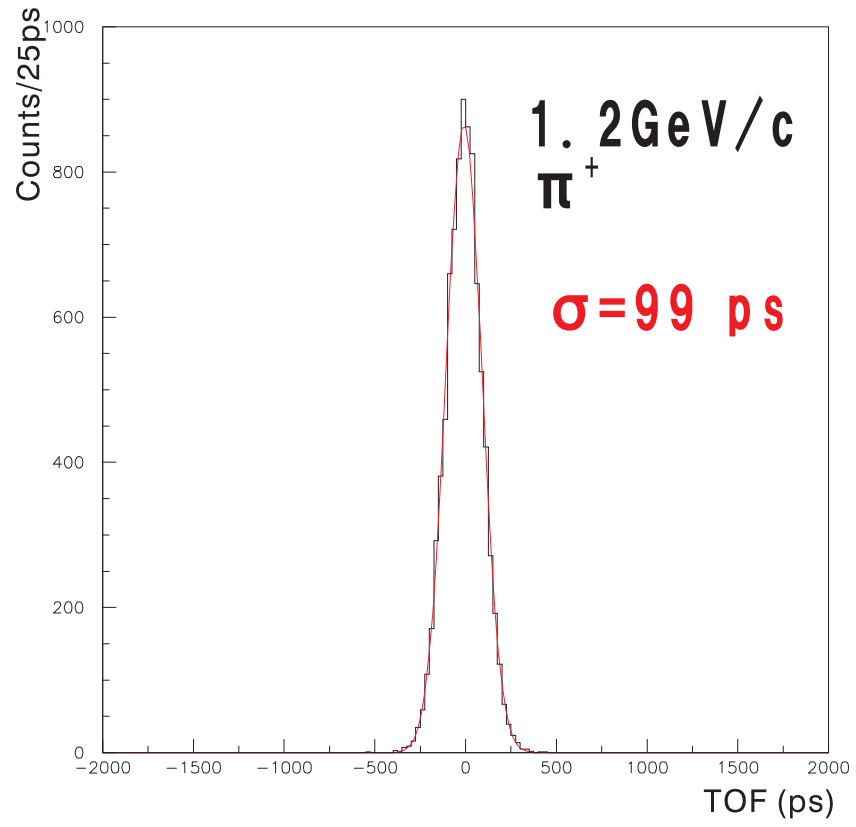


Figure 3.18: TOF resolution of EHODO for $1.2 \text{ GeV}/c \pi^+$.

Chapter 4

Analysis

In this chapter, the E01-011 analysis will be described. Following the representations of each detector's performance, a way to make coincidence between two arms will be shown. The optics tune, missing mass calculation, estimation of systematic errors and efficiencies of detectors will be discussed in this chapter.

4.1 Overview

A flowchart summarizing the E01-011 analysis is shown in Fig. 4.1. Raw data was processed by an analyzer, ENGINE, which is a standard analysis code in JLab Hall C. As a first step, parameters, such as TDC calibration, pulse height correction, numbers of photoelectrons and so on, were determined from experimental data. Then, applying the cut condition to select $(e, e'K^+)$ events, we obtained the reduced ascii data. Because we measured only focal plane quantities, the momentum and emission angle for each particle were calculated by optical matrices of both spectrometers. To calibrate these matrices, the well-known masses of the Λ , Σ^0 and ^{12}B peaks, and sieve slit data were used. The systematic error, which depends on this calibration procedure, was estimated by detailed Monte Carlo simulation. Finally, the efficiencies and acceptances of the spectrometers necessary to derive cross sections were calculated.

4.2 HKS analysis

The performance of each detector in the HKS will be shown here. In addition, a method to select kaons by suppressing background events, such as due to protons and pions, will be introduced.

4.2.1 HKS drift chamber (HDC)

Trajectories of particles were measured by two sets of drift chambers. A typical drift time and drift distance of HDC are shown in Fig. 4.2. Because the HDC is a planar drift chamber, the drift distance was determined to be uniform in a cell size.

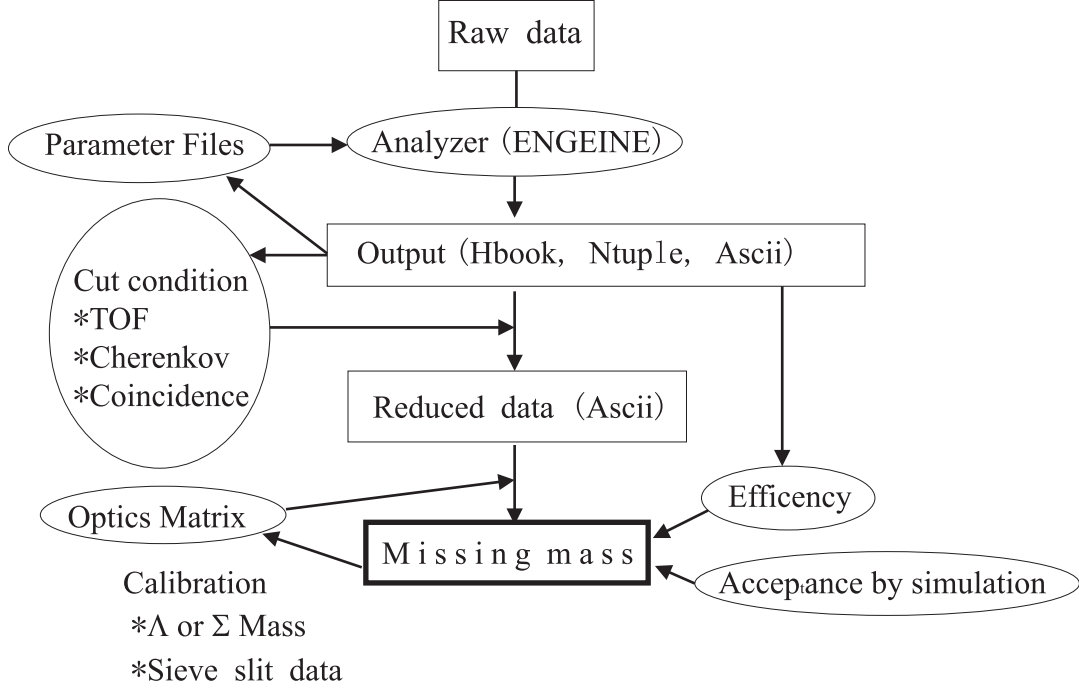


Figure 4.1: The flowchart of analysis.

Over flow events made peaks at ± 0.5 cm in Fig. 4.2. The tracking code required more than 5 plane hits for each chamber, thus a track was obtained with more than 10 planes. Each track was obtained by the least-square method. A typical residual was about $280 \mu\text{m}$ in sigma (Fig. 4.3) and a typical plane efficiency was about 99 %.

Trajectories were extrapolated to the HTOF, AC and WC and the consistency was examined after their analysis.

4.2.2 HTOF

The TOF of particles was measured by HTOF1X and HTOF2X which were separated by a distance of 1.5 m. All raw signals from the PMTs were converted into logic signals by leading edge type discriminators. The pulse height correction was performed with ADC information. A typical TOF resolution was about 160 ps in sigma for $1.2 \text{ GeV}/c \pi^+$ after the correction (Fig. 4.4).

The particle velocity, β_{TOF} , was calculated by TOF and the flight length from the drift chamber analysis. Another velocity quantity, β_K , was introduced in the analysis. β_K was calculated with momentum and mass information as follows:

$$\beta_K = \frac{p}{\sqrt{p^2 + m_K^2}}. \quad (4.1)$$

Here, p represents the particle momentum and the particle is assumed to be a kaon to obtain β_K .

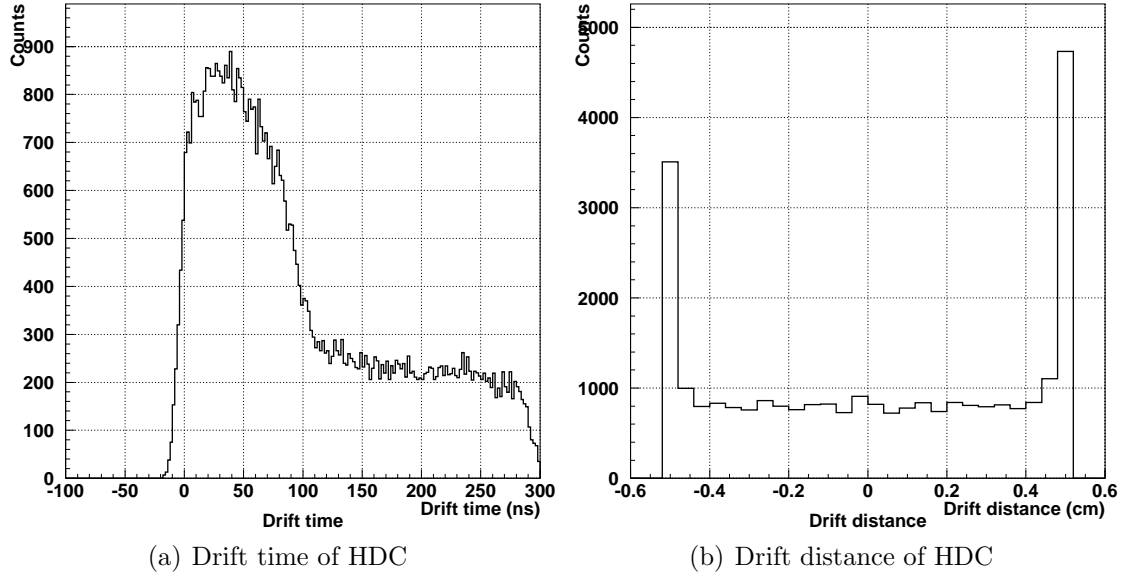


Figure 4.2: Typical drift time and drift distance of HDC.

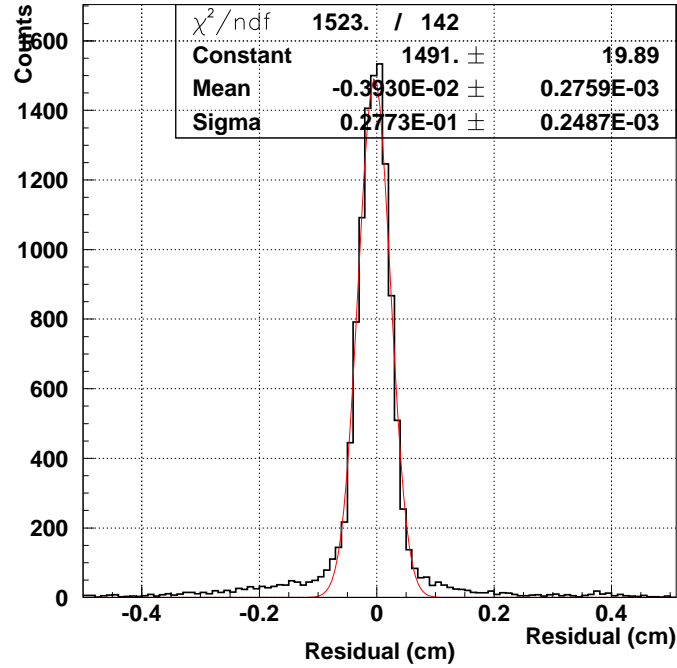


Figure 4.3: Residual of HDC.

4.2.3 Cherenkov counters

Both aerogel and water Cherenkov counters were included in the trigger to suppress pions and protons as discussed in Chap. 2. Their thresholds were set with margins to avoid kaon overkill. Therefore, their information was used for off-line analysis with tighter cut conditions.

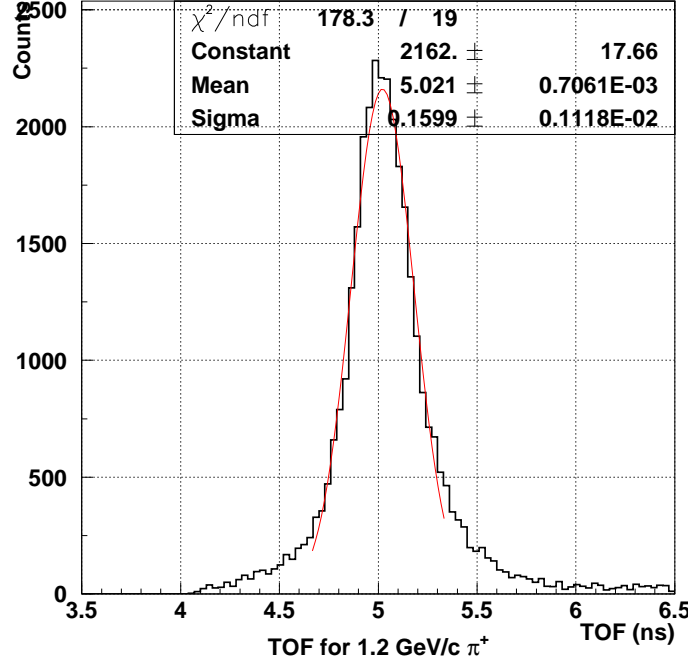


Figure 4.4: TOF spectrum by HTOF.

Raw ADC signals of cherenkov counters converted into number of photoelectrons (N.P.E) with pedestal and one photoelectron information for each PMT:

$$[\text{Number of electrons}] = \frac{[\text{Raw signal}] - [\text{Pedestal}]}{[\text{One photoelectron}] - [\text{Pedestal}]} \quad (4.2)$$

Then, all signals on the particle trajectory were summed. The summed N.P.E. are shown in Fig. 4.5 and 4.7. From the correlation between β and summed N.P.E (Fig. 4.6 and 4.8), all particles were identified clearly.

4.2.4 K^+ selection

Kaons were selected by suppressing pions and protons. Each particle was identified by the β and N.P.E from the cherenkov counters. Because setting parameters such as high voltage and trigger configuration were changed frequently, the threshold for each counter was set period by period.

During experiment, it was found that the gain of the WC decreased gradually (Fig. 4.9). This was caused by radiation damage on the wave length shifter. Therefore, summed N.P.E of the WC was normalized by using the peak of kaon in the offline analysis.

A typical β - β_k distribution is shown in Fig. 4.10. One can see that there are some protons after applying cherenkov cut in the green histogram because rejection power of the WC is not so strong in the high momentum side. Finally, the β cut was applied to select kaons cleanly.

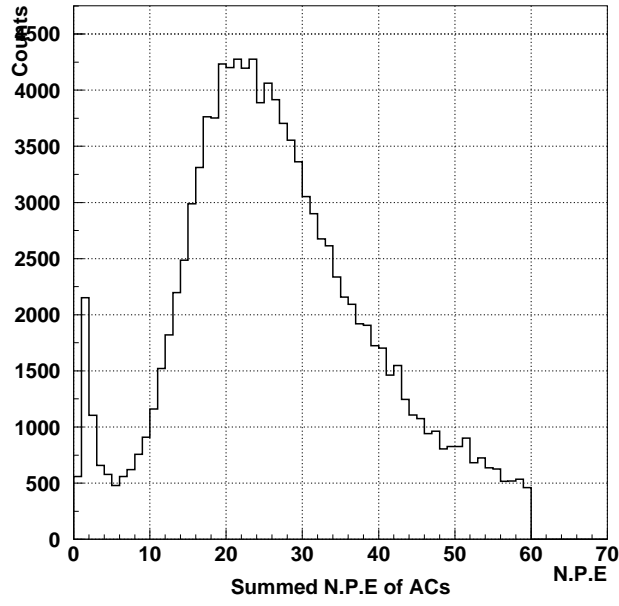


Figure 4.5: Number of photoelectrons of aerogel cherenkov counter.

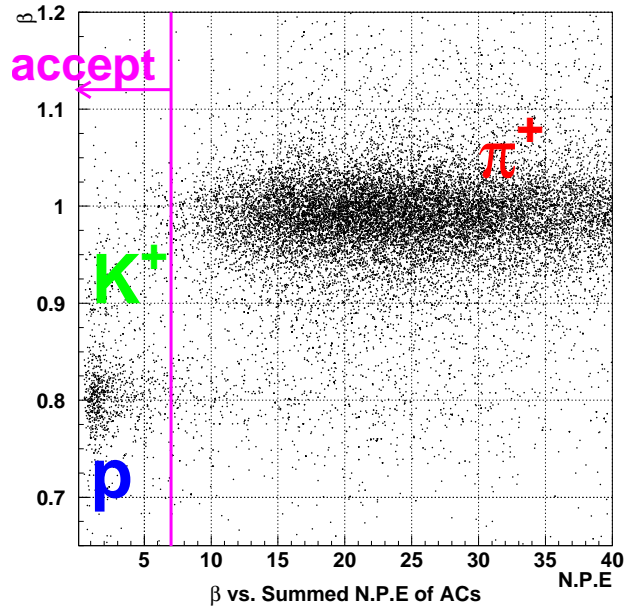


Figure 4.6: Correlation between aerogel cherenkov and β .

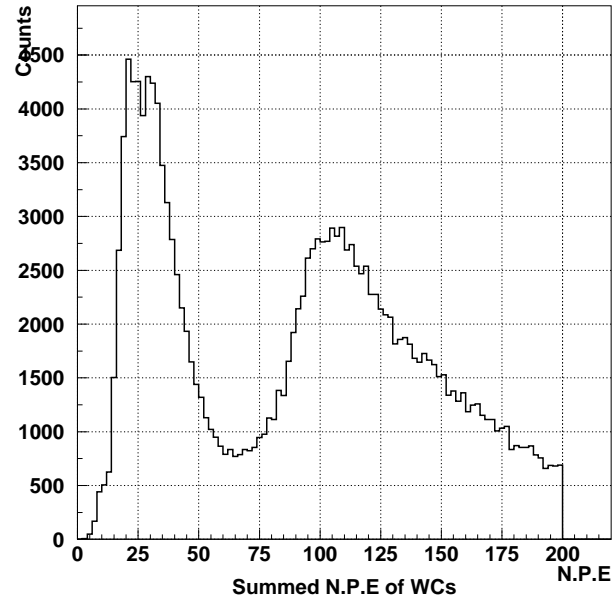


Figure 4.7: Number of photoelectrons of water cherenkov counter.

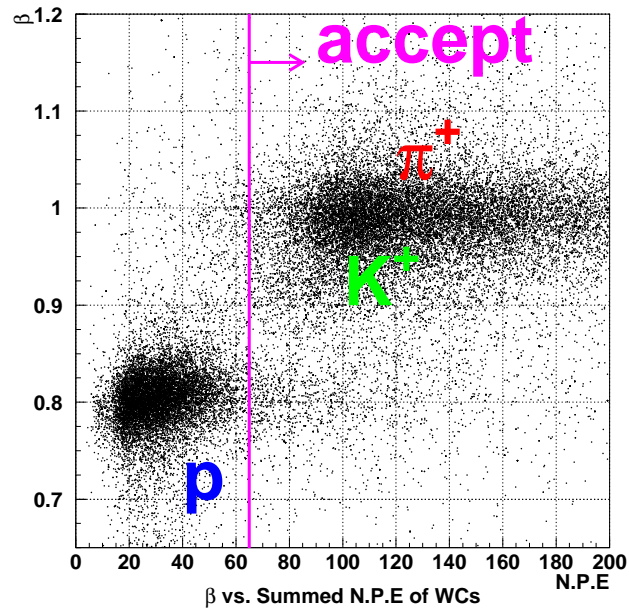


Figure 4.8: Correlation between water cherenkov and β .

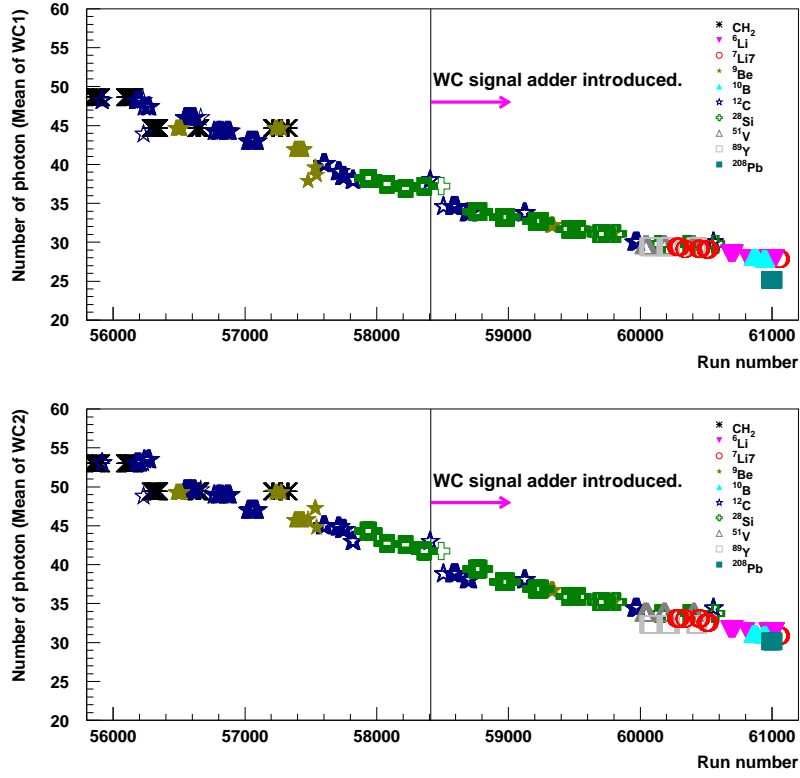


Figure 4.9: Run dependence of N.P.E of WC for proton. Top shows the first layer of WC and bottom shows the second layer.

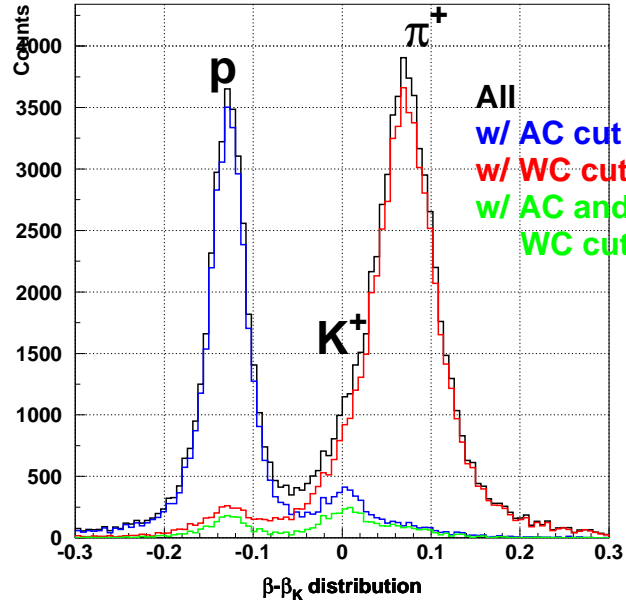


Figure 4.10: Typical β spectrum w/ or w/o cherenkov cut. Black, blue, red and green histograms represent all events, with AC cut, with WC cut and with AC and WC cut, respectively.

4.3 ENGE analysis

Performances for each detectors in ENGE will be shown here.

4.3.1 EDC

Particle trajectories were measured by EDC. Basically, an analysis procedure is the same as shown in Chap. 3. One different point is that the start timing of TDC was always determined by HTOF1X. Because particles has different path lengths for both HKS and ENGE sides, a time zero in the ENGE local is different from that in the HKS. To determine a time zero, a pre-trajectory was calculated from a wire position without considering drift distance. Then, the mean time of EHODOs on the pre-trajectory was defined as the time zero in ENGE local system. Thus, drift time of EDC (Fig. 4.11) was obtained by subtracting ENGE local time zero from raw TDC. A drift distance was calculated by the third order polynomial (Fig. 4.12). A typical plane resolution was about $220 \mu\text{m}$ in sigma (Fig. 4.13) and the plane efficiency was 99%. They are consistent with the results of the beam test shown in the previous chapter.

Trajectories were combined with EHODO information after its analysis.

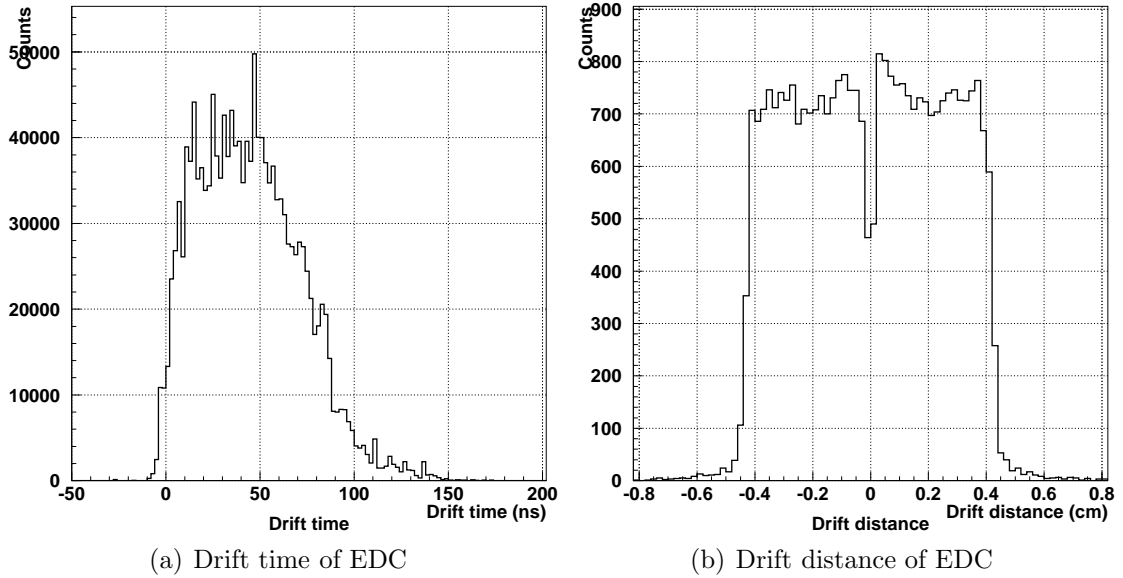


Figure 4.11: Typical drift time and drift distance of EDC.

4.3.2 EHODO

The TOF of scattered electron was measured by two layers of EHODO. A pulse height correction was applied because a leading edge type discriminator was used. A typical TOF resolution was about 190 ps in sigma (Fig. 4.14). A ground noise caused this result which was much worse than the result from the beam test in

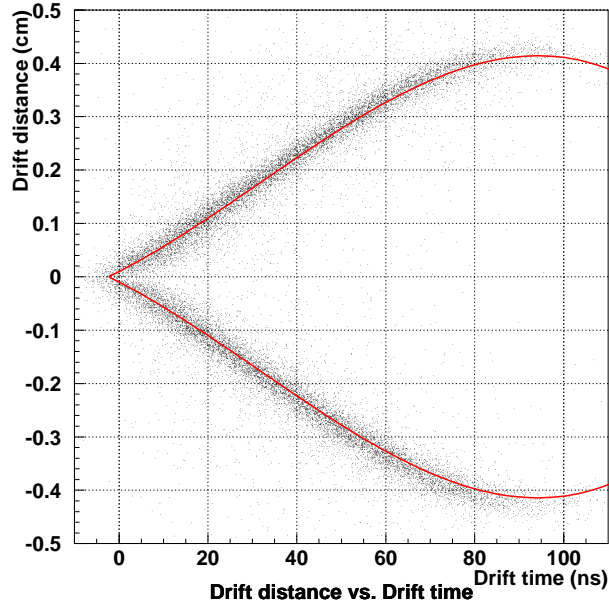


Figure 4.12: Scatter plot of drift distance vs. drift time of EDC. Red line represents the fitting result by a third order polynomial function.

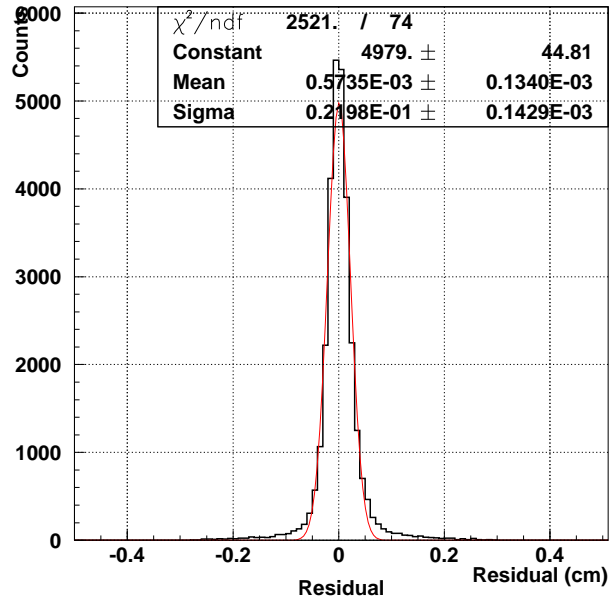


Figure 4.13: Typical residual of EDC.

Chap. 3. However, this caused no serious problem to select $(e, e'K^+)$ since electron beam has 2 ns bunch structure and 190 ps TOF resolution is enough to separate them. The detail will be discussed in the next section.

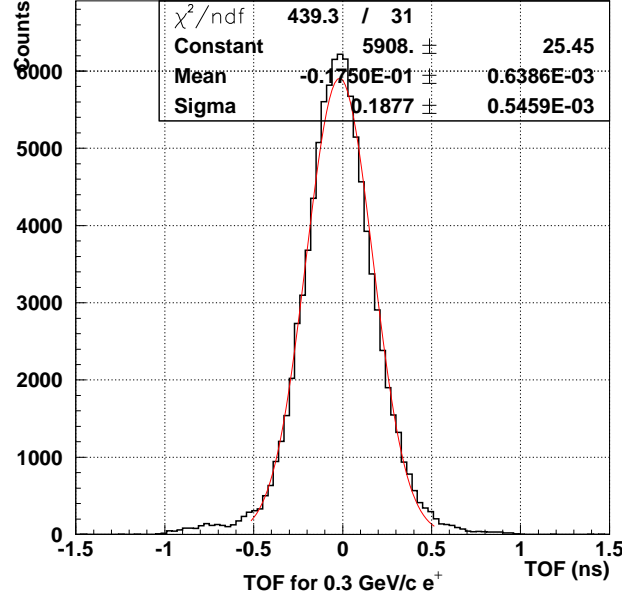


Figure 4.14: TOF measured by EHODO.

4.4 Coincidence

To identify the $(e, e'K^+)$ event, the coincidence time was calculated as:

$$[\text{Coincidence time}] = t_{K^+}^{\text{tar}} - t_{e'}^{\text{tar}} - t^{\text{RF}}. \quad (4.3)$$

Here, $t_{K^+}^{\text{tar}}$ and $t_{e'}^{\text{tar}}$ are target times for each particle. The target time was obtained by subtracting flight time from target to focal plane from focal plane time. Because each particle has different path length which depends its momentum and scattered angle, correction functions with focal plane quantities were introduced.

$$t_{K^+(e')}^{\text{tar}} = t_{K^+(e')}^{\text{fp}} - t_{K^+(e')}^0 - f_{K^+(e')}(x_{fp}, x'_{fp}, y_{fp}, y'_{fp}), \quad (4.4)$$

$$f_{K^+(e')}(x_{fp}, x'_{fp}, y_{fp}, y'_{fp}) = \sum_{\alpha+\beta+\gamma+\eta=1}^2 C_{\text{path}}(\alpha, \beta, \gamma, \eta) x_{fp}^\alpha x_{fp}'^\beta y_{fp}^\gamma y_{fp}'^\eta. \quad (4.5)$$

$t_{K^+(e')}^0$ is flight time of each particle which path through a center of optics and has central momentum. The parameter, C_{path} , is the coefficient of paths length correction function.

t^{RF} in Eq. 4.3 represents radio frequency (RF) timing from the accelerator. Therefore, a beam structure of 2 ns bunch can be seen in the calculated coincidence time (Fig. 4.15). A central peak in Fig. 4.15 contains both $(e, e'K^+)$ events and accidental coincidence between e' and K^+ , while side peaks come from accidental coincidence. Thus, the amount of accidental coincidence in the central peak can be

estimated from neighboring peaks by the mixed event analysis which will be discussed in Sec. 4.7. The red histogram in Fig. 4.15 represents accidental coincidence events.

A path length correction was dominant to the coincidence time resolution of about 1 ns (σ). To identify a bunch where particles come from, both HTOF and EHODO had sufficient TOF resolution.

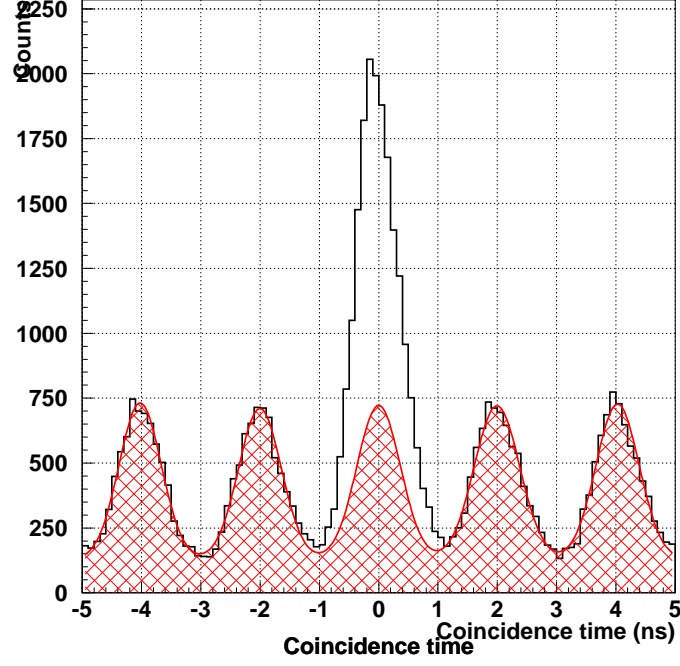


Figure 4.15: Coincidence time spectrum. The red histogram represents accidental background events estimated by mixed event analysis.

4.5 Missing mass

A missing mass of Λ hypernucleus, M_{HY} , can be obtained by solving energy and momentum conservation laws:

$$\begin{cases} E_e + M_A = E_{e'} + E_{K^+} + E_{HY} \\ \mathbf{P}_e = \mathbf{P}_{e'} + \mathbf{P}_{K^+} + \mathbf{P}_{HY}, \end{cases} \quad (4.6)$$

$$\begin{aligned} M_{HY}^2 &= E_{HY}^2 - \mathbf{P}_{HY}^2 \\ &= (E_e + M_A - E_{e'} - E_{K^+})^2 \\ &\quad - (P_e^2 + P_{e'}^2 + P_{K^+}^2 - 2P_e P_{e'} \cos \theta_{ee'} + 2P_{e'} P_{K^+} \cos \theta_{e'K^+} - 2P_{K^+} P_e \cos \theta_{K^+e}). \end{aligned} \quad (4.7)$$

Here, E_{HY} and \mathbf{P}_{HY} are the total energy and momentum vector of a hypernucleus, respectively. Similarly, E_x and \mathbf{P}_x represent the total energy and momentum vector of each particle ($x = e, e', K^+$). M_A is the nuclear mass of the target. $\theta_{ee'}$, $\theta_{e'K^+}$ and θ_{K^+e} are the opening angles between two particles. Because only position and angle at focal plane were measured in this experiment, target quantities (scattering angle and momentum) should be reconstructed with transfer matrices, M_{F2T} , which are described by 6th order polynomials in the present analysis.

$$\begin{aligned} \mathbf{X}_{\text{tar}} &= \begin{pmatrix} x'_{tar} \\ y'_{tar} \\ dp \end{pmatrix} \\ &= M_{F2T} \mathbf{X}_{\text{fp}} \\ &= \sum_{\alpha+\beta+\gamma+\eta=1}^6 C_{F2T}^i(\alpha, \beta, \gamma, \eta) x_{fp}^\alpha x_{fp}'^\beta y_{fp}^\gamma y_{fp}''^\eta. \end{aligned} \quad (4.8)$$

Here, \mathbf{X}_{tar} represents target quantities, scattering angle (x'_{tar} , y'_{tar}) and momentum ($dp = (P_x - P_c)/P_c \times 100$, P_c ; central momentum), and \mathbf{X}_{fp} represent focal plane quantities (x_{fp} , x'_{fp} , y_{fp} and y'_{fp}). An index of i corresponds to each term of the three \mathbf{X}_{tar} components.

4.6 Transfer matrices calibration

In this experiment, the HKS was a new spectrometer and, from the viewpoint of optics, the scattered electron spectrometer was also a new spectrometer because it was tilted vertically and the original optical nature was lost. Therefore, their optics has to be calibrated with the well known masses such as Λ and Σ^0 and sieve slit (SS) data. In this section, the procedure of the optics calibration will be given.

Figure 4.16 shows the flowchart of the optics calibration. As a start point, transfer matrices were extracted from the simulation data. HKS and Splitter parts were simulated by the Monte Carlo simulation, GEANT, with three dimensional field map calculated by TOSCA which applies the finite element method. ENGE optics was calculated by the optics program, RAYTRACE.

Next, the momentum part of M_{F2T} was calibrated by using missing masses. Then, the scattering angle part was updated with SS data. These procedures were iterated till their results converged. In the following subsections, the detail of these calibration procedures will be given.

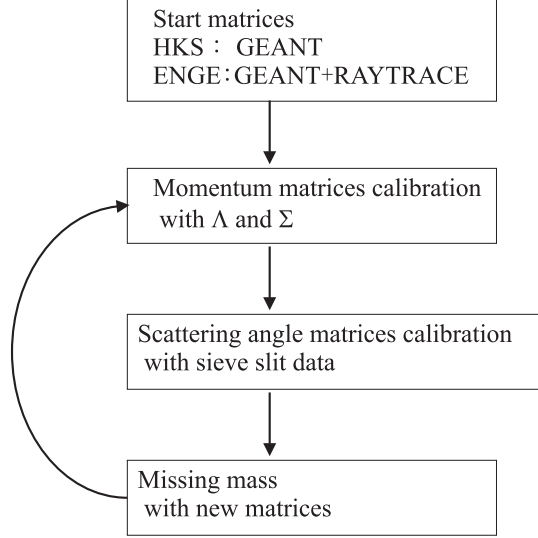


Figure 4.16: Flowchart of optics calibration.

4.6.1 Momentum matrices calibration

Momentum matrices were calibrated with a non-linear least square method. First, Λ and Σ^0 peaks were selected by fitting missing mass spectrum with Gaussian functions. Then minimizing χ^2 defined by Eq. 4.9 for these events, momentum matrices were updated.

$$\chi^2 = \frac{1}{2} \sum_{n=1}^{nevent} w_i \sum_i \left(\frac{M_i^{Calc.} - M_i^{PDG}}{\sigma_i} \right)^2. \quad (4.9)$$

Here, $nevent$ and i represents the number of events and each particle such as Λ and Σ^0 , respectively. w_i is the weight based on the number of events and, at final step of iteration, w_Λ and w_{Σ^0} were chosen to be respectively 2 and 1, considering weight due to the number of event difference. $M_i^{Calc.}$ and M_i^{PDG} are calculated missing mass and published missing mass values from Particle Data Group (PDG) and AME2003 [58].

After iterations of the calibration procedure with Λ and Σ^0 , major hypernuclear states such as ^{12}B ground state and p-shell state became visible. Their states were also included in χ^2 . However, a fixed M_i^{PDG} was not used at all and their mass values were set free.

Kinematics scan

From the study of simulated data, it was found that the offset and the width of missing mass peak depend on kinematics offsets, or central momenta for kaon and electron. To select the best kinematics offsets, we scanned the kinematics setting after momentum calibration. To do so, two parameters, χ_{pos}^2 and χ_{wid}^2 , were defined as

$$\chi_{pos}^2 = w_\Lambda(\mu_\Lambda - M_\Lambda^{PDG})^2 + w_{\Sigma^0}(\mu_{\Sigma^0} - M_{\Sigma^0}^{PDG})^2, \quad (4.10)$$

$$\chi_{wid}^2 = w_\Lambda\sigma_\Lambda^2 + w_{\Sigma^0}\sigma_{\Sigma^0}^2. \quad (4.11)$$

Here, μ_Λ and μ_{Σ^0} are means of Λ and Σ^0 peak. The parameters σ_Λ and σ_{Σ^0} represent widths of Λ and Σ^0 peaks. Naturally, we expect that the correct kinematics parameters will give minimum χ_{pos}^2 and χ_{wid}^2 simultaneously. To see the χ^2 variation as a function of kinematics offsets, a kinematics variable, V_{kin} , was defined as

$$V_{kin} = \Delta E_b - \Delta P_{K+}^0 - \Delta P_{e'}^0. \quad (4.12)$$

Here, ΔE_b , ΔP_{K+}^0 and $\Delta P_{e'}^0$ represent the offset of incident electron beam energy, kaon momentum and scattered electron momentum, respectively. Figure 4.17 shows a typical χ_{pos}^2 and χ_{wid}^2 as a function of V_{kin} with a 50 keV step at the final step of calibration procedure. The error bars represent the error of each χ^2 caused by the fitting error for the hyperon peaks. The minimum of χ_{pos}^2 and χ_{wid}^2 appears at $V_{kin}=-0.125$ and $V_{kin}=-0.075$, respectively, in Fig. 4.17. This difference of V_{kin} gradually reduced by iterative calibration (Fig. 4.18).

4.6.2 Scattering angle matrices calibration

Scattering angles of each particle were calibrated with the SS data. The SS and collimators made of tungsten alloy (Heavimet) were attached at the entrance of ENGE and HKS Q1 magnet. Figure 4.19 shows the figures of the SS and collimators. The ENGE SS plate had 30 holes of 0.5 cm ϕ with a horizontal interval of 2 cm and vertical interval of 1 cm. It also had a $11^w \times 4^h$ cm² collimator and its thickness was 2.54 cm enough to stop 300 MeV/c electron. The HKS SS had 53 slit holes of 0.632 cm ϕ with a horizontal interval of 1.524 cm and vertical interval of 2.032 cm. One of holes had a smaller diameter of 0.316 cm and another hole was completely closed to break the symmetry.

The procedure of scattering angle matrices calibration is listed as following.

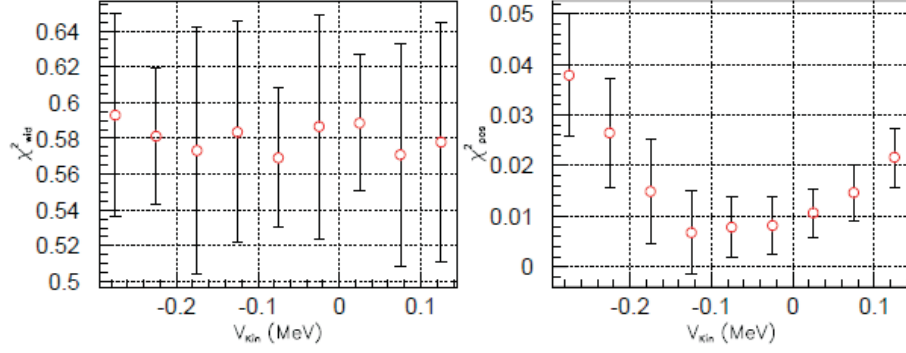


Figure 4.17: χ_{pos}^2 and χ_{wid}^2 as a function of V_{kin} in a 50 keV step at the final step of calibration procedure. The error bars represent the error of each χ^2 caused by the fitting error for the hyperon peaks.

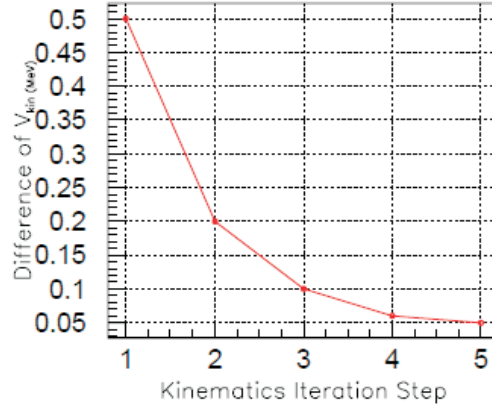
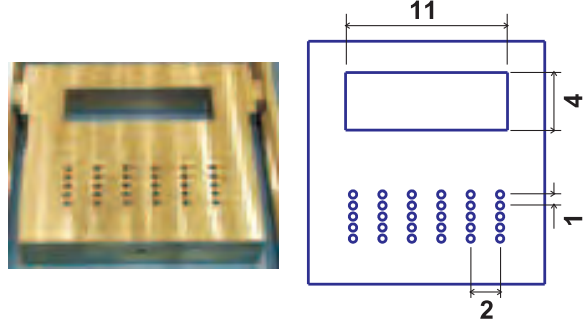
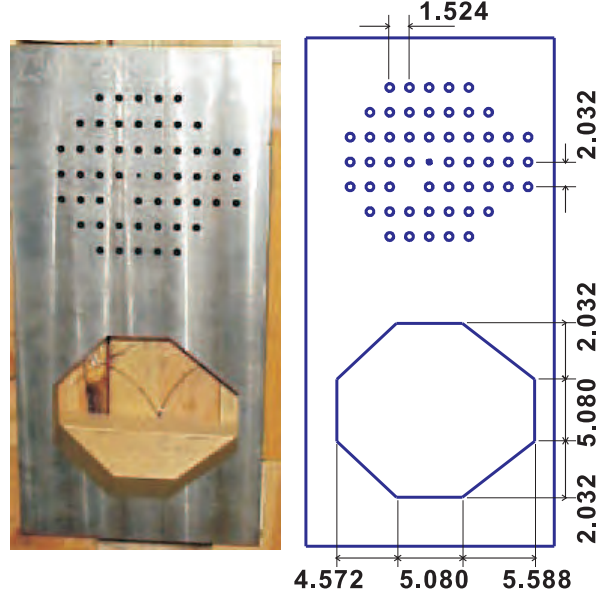


Figure 4.18: Difference of V_{kin} corresponding to minimum χ_{pos}^2 and χ_{wid}^2 at each iteration step.

1. Comparing focal plane distribution of experimental data with that of simulation, sieve slit hole which a particle pathed through was identified for each event.
2. Reconstruct scattering angle at target, $x_{tar}'^{F2T}$ and $y_{tar}'^{F2T}$, with F2T matrices. The momentum of each particle was also calculated.
3. Ideal scattering angle, $x_{tar}'^{S2T}$ and $y_{tar}'^{S2T}$, were calculated from SS hole position, x_{SS} and y_{SS} , and momentum with transfer matrix from SS to target, M_{S2T} . M_{S2T} was extracted from splitter field map calculated by TOSCA.
4. Minimizing χ_{ang}^2 defined by Eq. 4.13, scattering angle part of M_{F2T} was calibrated.



(a) ENGE sieve slit and collimator



(b) HKS sieve slit and collimator

Figure 4.19: Sieve slit and collimator for ENGE and HKS. Unit is cm.

$$\chi_{ang}^2 = \frac{1}{2\sigma^2} \sum_{n=1}^{nevent} \left((x_{tar}'^{F2T} - x_{tar}'^{S2T})^2 + (y_{tar}'^{F2T} - y_{tar}'^{S2T})^2 \right), \quad (4.13)$$

where $x_{tar}'^{F2T}$ and $y_{tar}'^{F2T}$ were calculated by Eq. 4.8 and $x_{tar}'^{S2T}$ and $y_{tar}'^{S2T}$ were calculated by

$$x_{tar}'^{S2T} \text{ (or } y_{tar}'^{S2T} \text{)} = M_{S2T} X_{SS} = \sum_{\alpha+\beta+\gamma=1}^6 C_{S2T}(\alpha, \beta, \gamma) x_{ss}^\alpha y_{ss}^\beta dp^\gamma. \quad (4.14)$$

Here, dp was also calculated by Eq. 4.8

4.6.3 Missing mass spectrum of Λ/Σ^0

Obtained Λ and Σ^0 spectrum with CH_2 target after the matrices calibration is shown in Fig. 4.20. A hatched region represents the accidental background by mixed event analysis (Sec. 4.7). Quasi-free hyperons on ^{12}C of CH_2 can be seen below Λ and Σ^0 . Two peaks are fitted by two Gaussians with the 2nd order polynomial function for background. Obtained missing mass differences ($M_x - M_{\Lambda/\Sigma^0}$) and widths are summarized in Tab. 4.1. Mass differences of Λ and Σ^0 are considered as the systematic error discussed in Sec. 4.8 and 4.10. The widths of their peaks are much broader than the expected resolution for hypernuclei since hyperons are much lighter than hypernuclei and thus kinematical broadening is large.

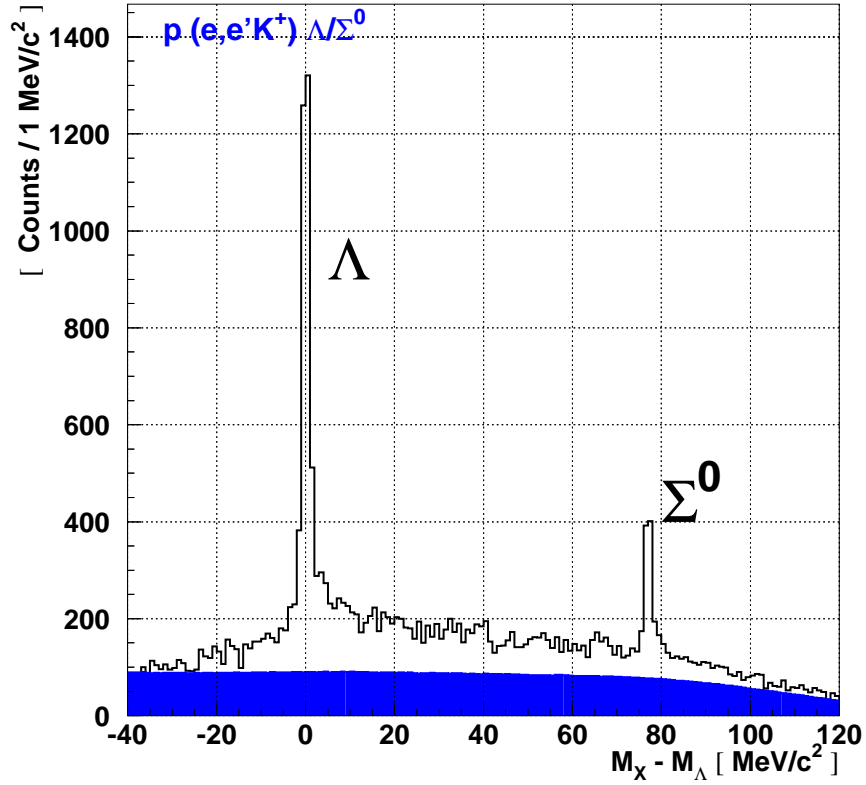


Figure 4.20: Missing mass spectrum of $p(e, e'K^+)\Lambda/\Sigma^0$. A hatched region represents the accidental background by mixed event analysis (Sec. 4.7). There are quasi-free produced hyperons from ^{12}C of CH_2 below Λ and Σ^0 . Errors are statistical only.

Particle	$M_x - M_{\Lambda/\Sigma^0}$ [MeV/ c^2]	FWHM [MeV/ c^2]
Λ	0.09 ± 0.02	1.94 ± 0.45
Σ^0	0.05 ± 0.03	1.87 ± 0.56

Table 4.1: Fitting results of Λ and Σ^0 . Errors are statistical only.

4.7 Background estimation by mixed event analysis

In this experiment, an accidental coincidence between e' and K^+ caused background event. To derive hypernuclear cross sections, this background should be estimated and subtracted from the spectrum. Ordinarily, the accidental background was estimated by averaging side peaks in Fig. 4.15.

To reduce statistical fluctuation of accidental coincidence background, the mixed event analysis which increased statistics by combining e' and K^+ randomly was introduced (Fig. 4.21). These particles were selected from side peaks at -4 and -2 ns in Fig. 4.15, and have information on acceptance of each spectrometer. A side peak at 2 ns in Fig. 4.15 was not included because there remained small amount of $(e, e'\pi^+)$ events which were not included in the accidental coincidence events under the true coincidence events.

In this analysis, the statistics of background event was increased by a factor of 100. Therefore, the statistical fluctuation decreased 10 times lower than the normal background. The red histogram in Fig. 4.22 shows the accidental background.

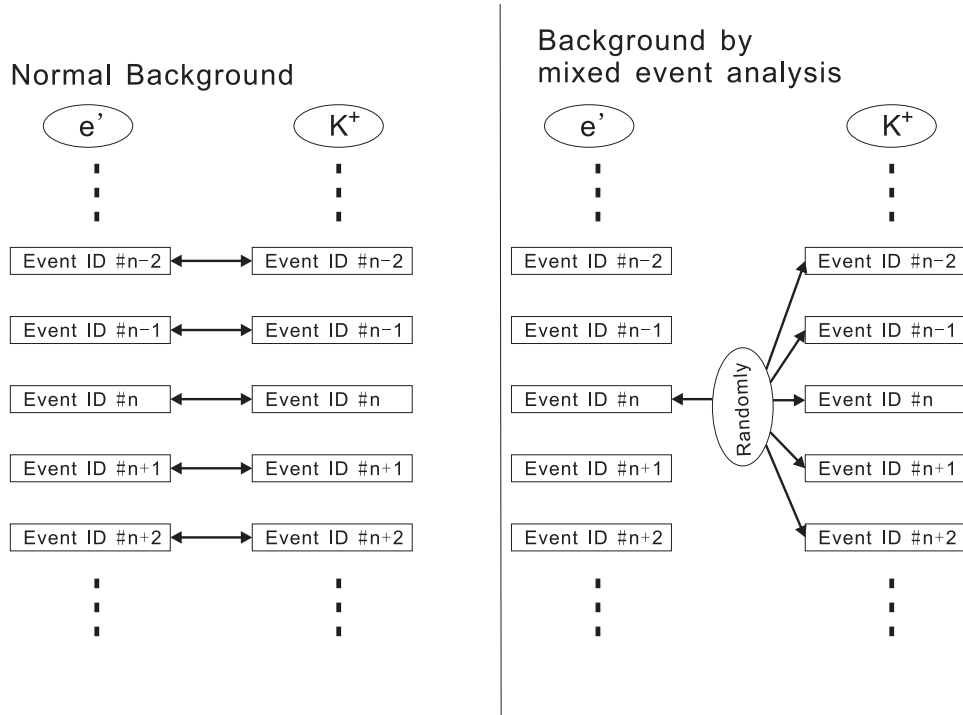


Figure 4.21: Mixed event analysis procedure.

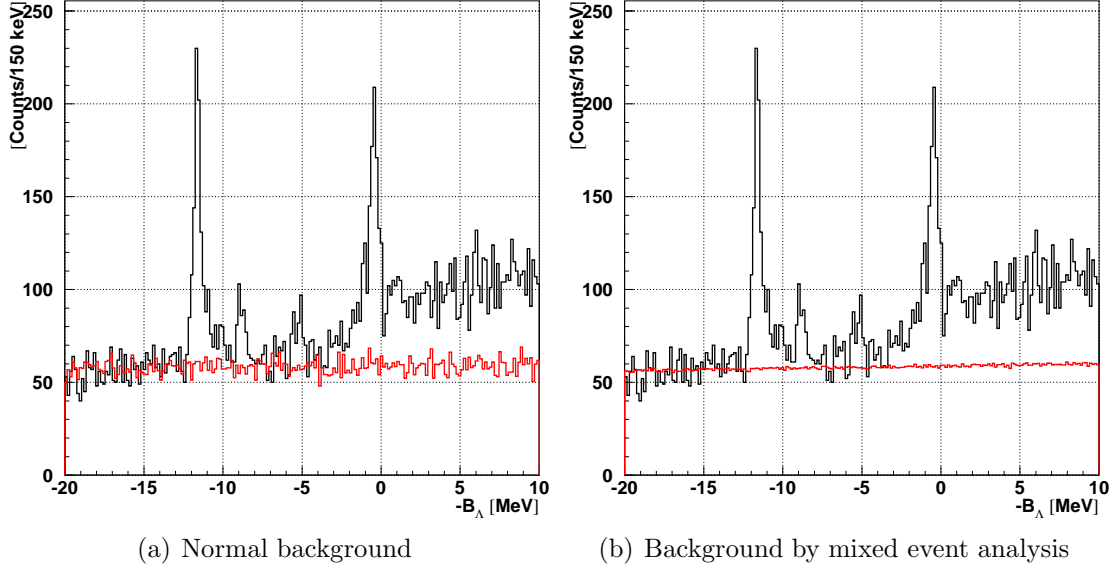


Figure 4.22: ^{12}B spectrum (black) with background (red). The background by mixed event analysis (right) is much smoother than normal background (left) thanks to 100 times higher statistics.

4.8 Linearity, mass scale

As discussed in Sec. 4.6, transfer matrices of two spectrometers were calibrated with experimental data. Accuracies of binding energies and cross sections depending on this calibration procedure were estimated with a help of detailed simulation data as follows (blind analysis of simulated data; Blind analysis);

1. Hyperon and hypernuclear masses were assumed as follows: the published PDG values were used for Λ and Σ^0 hyperons. On the other hand, ^{12}B hypernuclear masses were arbitrary changed from the expected values in the simulation and those values were hidden from the persons who analyzed the data. In this study, four hypernuclear states were applied and their assumed binding energies and yields are shown in Tab. 4.2.
2. Momenta and scattering angles of e' and K^+ at the target were calculated by solving energy and momentum conservation laws.
3. Focal plane quantities for each particle were obtained by detailed Monte Carlo simulation (GEANT3). This simulation included realistic experimental conditions such as detector resolution, beam raster effect, multiple scattering, two-arm coincidence and so on. The realistic magnetic field maps calculated by TOSCA were applied for all magnets. The optics of this simulation was defined as “correct optics”.
4. Changing the magnet positions and field strengths, another data set of focal plane quantities were obtained, and parameters of the “deformed optics” were

derived. This optics was used as a start point of the calibration procedure.

5. Accidental background events were generated by combining independent e' and K^+ events. The number of events and S/N ratio for Λ and Σ^0 hyperons were set to the same level as the experimental result. Similar to the case of masses, those for $^{12}_\Lambda\text{B}$ hypernuclear yields were arbitrarily changed and hidden from analyzers.
6. Starting from the “deformed optics” obtained at 4., the analyzers calibrated the transfer matrices with the same procedures as for the experimental data. After the calibration was done, systematic errors of binding energies and cross sections depended on this calibration procedure were estimated by comparing the results with assumed values at 1.

Figure 4.23 shows the result of the “Blind analysis” for $^{12}_\Lambda\text{B}$. A black histogram represents all events. Because this is simulation data, the accidental background events can be easily distinguished from $(e, e'K^+)$ events. A red histogram represents $(e, e'K^+)$ events after subtracting background and a blue line shows fitting result with four Gaussians and constant background.

The accuracies of the binding energies were estimated by comparing fitting result with the assumed mass values. And those of cross sections were estimated by counting the number of background events included in each hypernuclear state (Contamination). The result of Blind analysis is summarized in Tab. 4.2.

From this study, three kinds of information can be extracted:

$$|\Delta B_\Lambda|$$

The binding energy difference between the assumed value and the fitting result should be included the systematic error of the binding energy.

Contamination

The number of events for each peak can be calculated from the results of fitting. However, it was found that some background events could migrate into the peak region. These misidentified events were defined as a “Contamination” and its ratio was calculated for each peak. Due to these events, the cross section is always overestimated. Therefore, this value should be included in negative systematic error of the cross sections.

Loss

As shown in the red histogram of Fig. 4.23, some true $(e, e'K^+)$ events leaked out to the outside area of the peak. The ratio of a number of the lost events to that of the generated events were defined as the “Loss”. In contrast to the “Contamination”, the ratio of lost events results in the underestimation of the cross sections. Therefore, this effect was included in positive systematic error.

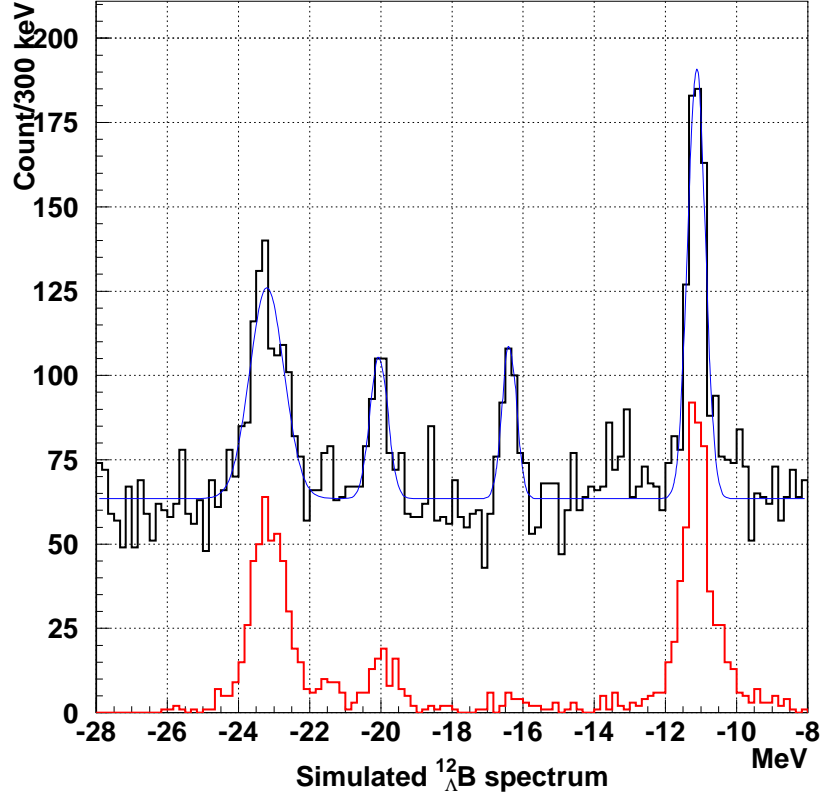


Figure 4.23: Blind analysis result for $^{12}_{\Lambda}\text{B}$. Black histogram represents all artificially generated events. Red histogram shows $(e, e'K^+)$ events after subtracting accidental background. Blue line is the fitting result with four Gaussian and constant background.

In the experimental data a part of “Loss” and “Contamination” effects might be cancelled out. However, the most stringent situation was applied to the current analysis, considering these effects were independent. Results of blind analysis of simulated data are summarized in Tab. 4.2 and plotted as a function of S/N ratio with statistical errors (Fig. 4.24). Since the S/N dependence was found for $|\Delta B_{\Lambda}|$ and “Contamination”, these two systematic errors are individually estimated for observed peaks in real data analysis. On the other hand, the ratio of “Loss” was determined as 30% for all peaks because there was no strong S/N dependence. These values are summarized in Tab. 4.12 and 4.13 of Sec 4.10.

In the calibration of the experimental data analysis, only prominent peaks were taken into account and poor S/N states such as core excited states were excluded because it was hard to be identified. Moreover, some hypernuclear states were placed outside of tuned states in mass scale. Therefore, the mass linearity over the entire acceptance region was also checked from the blind analysis of simulated data, comparing missing masses of background events which were not included in calibration procedures with assumed ones.

Top of Fig. 4.25 shows mass difference between the results of the blind analysis

Assumed values			Blind analysis results				
S/N ratio	B_Λ [MeV]	Yield [counts]	B_Λ [MeV]	Yield [counts]	$ \Delta B_\Lambda $ [MeV]	Contamination [%]	Loss [%]
1.45	11.37	600	11.43	491	0.06	4.4	21.8
0.09	16.31	30	16.70	191	0.39	83.6	4.4
0.27	20.31	100	20.35	142	0.04	42.4	18.2
1.28	23.37	550	23.32	407	0.05	1.5	27.1

Table 4.2: Summary of Blind analysis result.

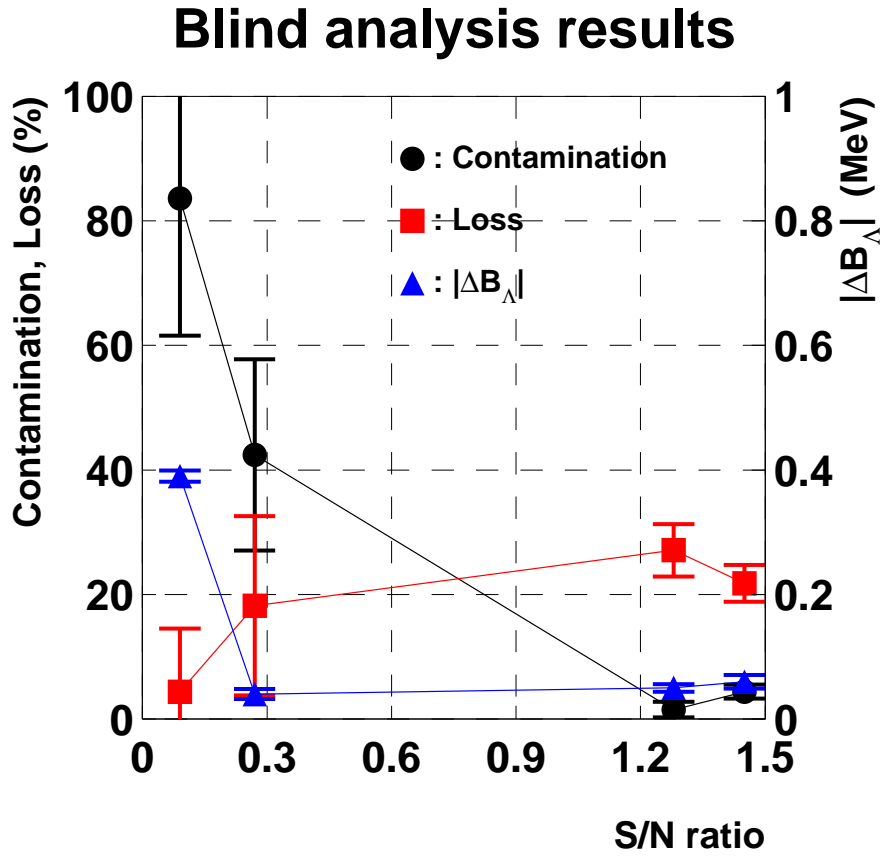


Figure 4.24: Background contamination from the result of Blind analysis as a function of S/N.

of simulated data and assumed values over the entire acceptance region. Bottom shows mass difference as a function of missing mass scale that hypernuclear bound states should be in a negative region. Dots and errors represent the mean and sigma values of Gaussian fitting, respectively. The mean values fluctuate within a hundred keV over the entire acceptance and there is no mass dependence.

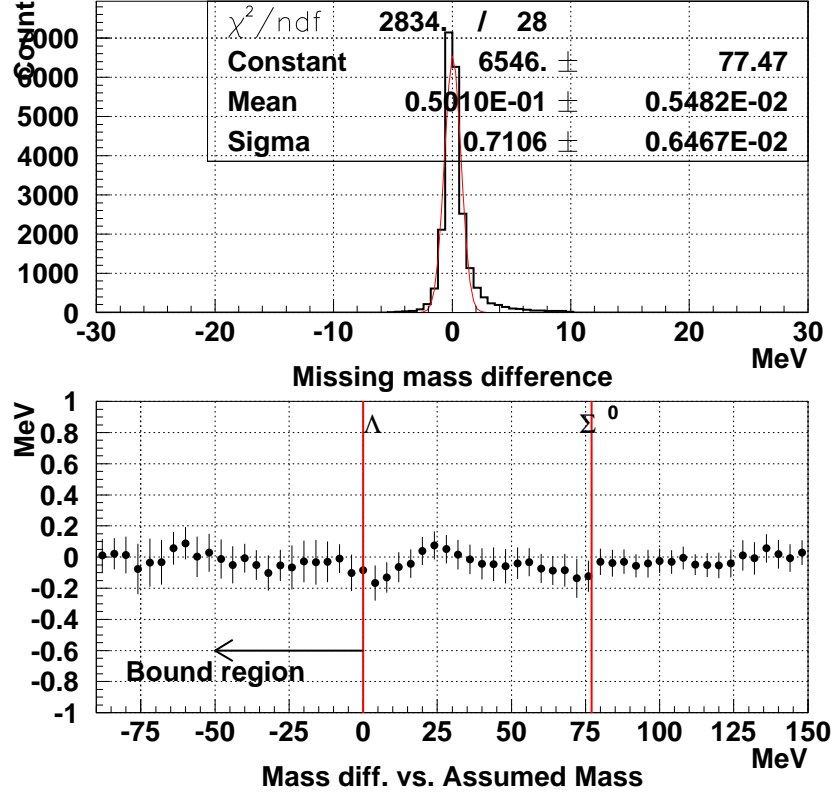


Figure 4.25: Top shows mass difference between Blind analysis results and assumed values over the entire acceptance. Bottom represents mass difference as a function of missing mass scale. Dots and errors represent the mean and sigma values of Gaussian fitting, respectively.

4.9 Cross section

The differential cross section of the (γ^*, K^+) reaction is calculated from the experimental yields divided by the total experimental efficiency:

$$\overline{\left(\frac{d\sigma}{d\Omega}\right)}_{1^\circ-13^\circ} = \frac{1}{N_T} \sum_{i=1}^{N_{HY}} \frac{1}{\epsilon_{total} N_\gamma(P_{e'}) d\Omega_i} \quad (4.15)$$

where $d\Omega$ is the solid angle of HKS, N_T is the number of target nuclei, N_γ is the number of virtual photons, N_{HY} is the yield of hypernucleus and ϵ_{total} is the total experimental efficiency. The total cross section can be obtained by multiplying the differential cross section and the HKS solid angle.

$$\sigma_{1^\circ-13^\circ} = \frac{1}{N_T} \sum_{i=1}^{N_{HY}} \frac{1}{\epsilon_{total} N_\gamma(P_{e'}) d\Omega_i} d\Omega_i. \quad (4.16)$$

The total experimental efficiency is defined as

$$\epsilon_{total} = \epsilon_{htrk} \cdot \epsilon_{etrk} \cdot \epsilon_{AC} \cdot \epsilon_{WC1} \cdot \epsilon_{WC2} \cdot \epsilon_{\beta} \cdot f_{abs} \cdot f_{decay} \cdot f_{comp} \quad (4.17)$$

where the meanings and typical values are summarized in Tab. 4.3.

Factors and efficiencies	Meanings	Typical value and error
ϵ_{htrk}	HKS tracking efficiency	0.961 ± 0.006
ϵ_{etrk}	Enge tracking efficiency	0.881 ± 0.002
ϵ_{AC}	AC cut efficiency	0.957 ± 0.010
ϵ_{WC1}	WC1 cut efficiency	0.954 ± 0.009
ϵ_{WC2}	WC2 cut efficiency	0.950 ± 0.009
ϵ_{β}	$\beta_{TOF}-\beta_{K^+}$ cut efficiency	0.980 ± 0.013
f_{abs}	Kaon absorption factor	0.818 ± 0.005
f_{decay}	Kaon decay factor	0.345 ± 0.001
f_{comp}	Computer live time factor	0.970 ± 0.002
Total		0.197 ± 0.007

Table 4.3: List of the experimental efficiencies and factors and typical values (Data Set ID. #6).

In this section, the detail explanation about how each value was estimated will be discussed.

4.9.1 Acceptance

Reconstructed emission angle correlations at the target point (θ and ϕ with spherical coordinates, x' and y' with orthogonal coordinates) for kaons and scattered electrons are shown from Fig. 4.26 to Fig. 4.29. For a kaon side, coordinates represent a positive x being to the beam left, a positive y top and a positive z beam direction while a positive x being to the beam right, a positive y bottom and a positive z beam direction for a scattered electron (Fig. 2.8). Plotted events in these figures are already selected as $(e, e'K^+)$ events after applying cherenkov and β cut conditions.

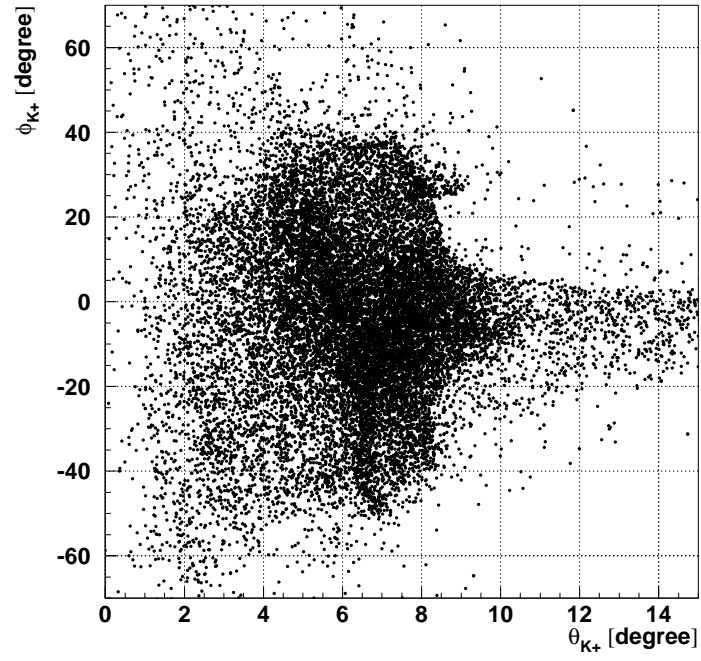


Figure 4.26: Correlation between θ_{K+} and ϕ_{K+} .

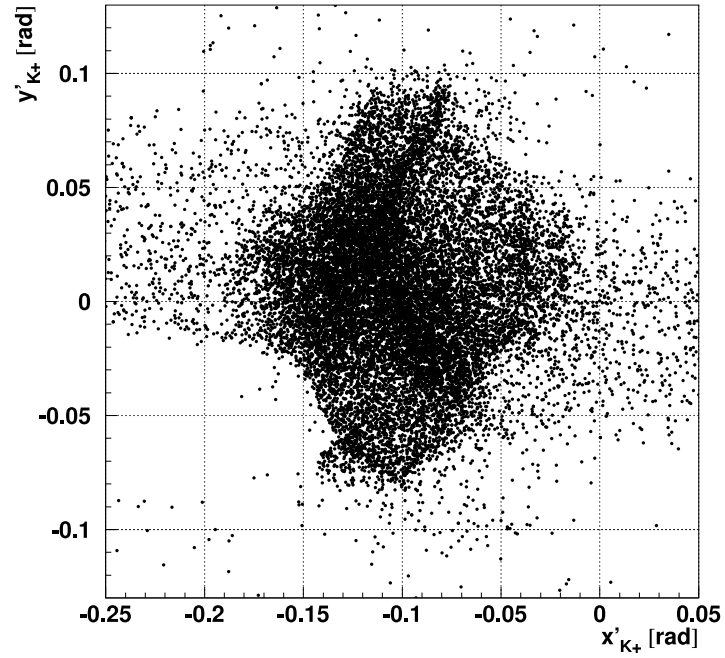


Figure 4.27: Correlation between x'_{K+} and y'_{K+} .

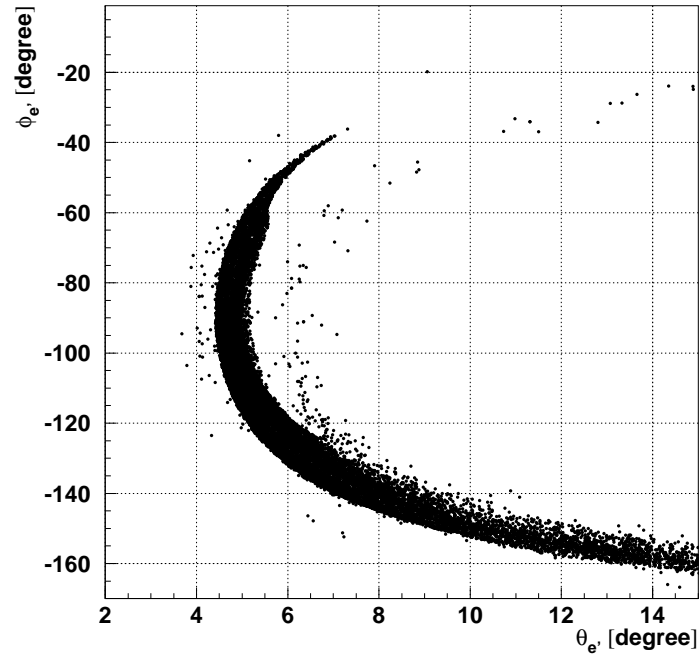


Figure 4.28: Correlation between $\theta_{e'}$ and $\phi_{e'}$.

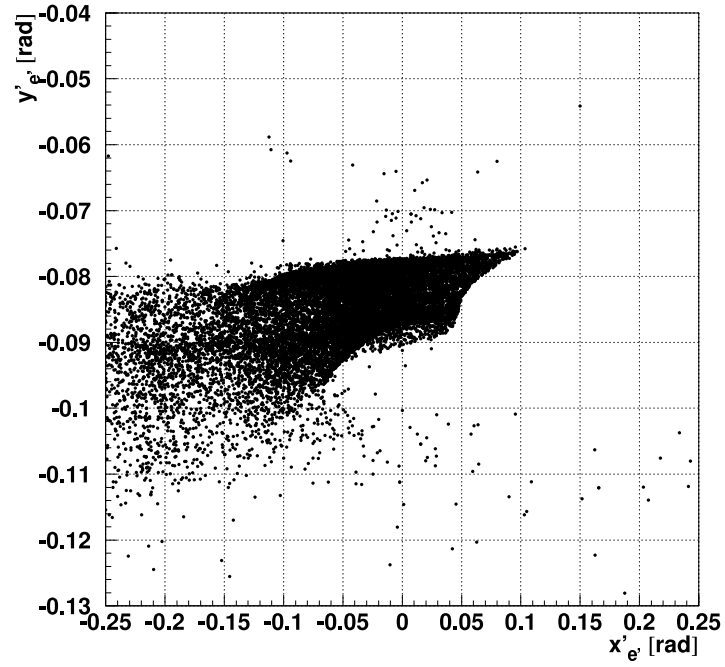


Figure 4.29: Correlation between $x_{e'}$ and $y_{e'}$.

The momentum correlation between the scattered electron and kaon for the Λ , Σ^0 and hypernuclear ground states was calculated as Fig. 4.30, assumed the incident electron beam energy of 1.851 GeV, scattered electron angle of 0.08 rad and scattered kaon angle of 0.12 rad. Binding energies for the ground states of ${}_{\Lambda}^{28}\text{Al}$, ${}_{\Lambda}^{12}\text{B}$ and ${}_{\Lambda}^7\text{He}$ are assumed as -17.00 MeV, -11.37 MeV and -6.00 MeV, respectively. The black box represents the acceptances of spectrometers, which correspond to $0.316 \text{ GeV}/c^2 \pm 30\%$ for scattered electron and $1.2 \text{ GeV}/c^2 \pm 12.5\%$ for kaon.

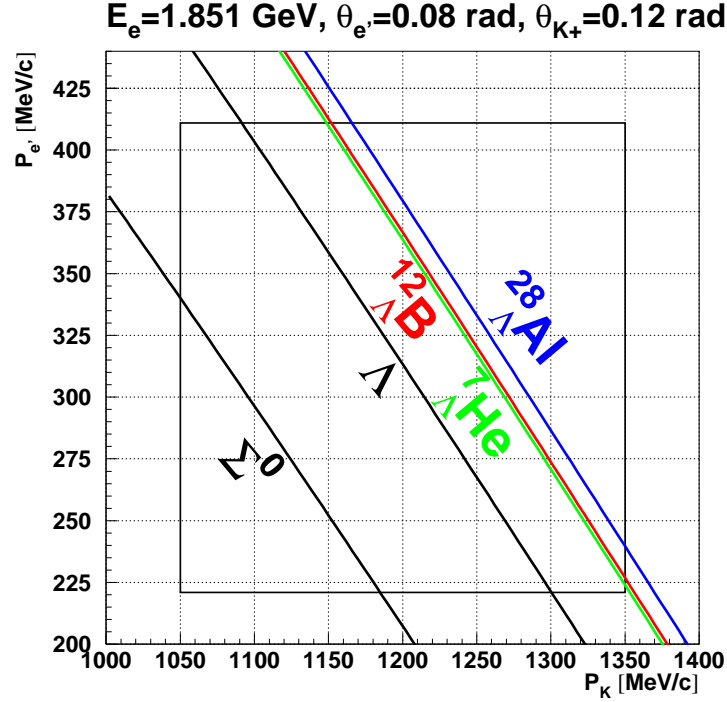


Figure 4.30: Calculated momentum correlation between a scattered electron and a kaon for the Λ , Σ^0 and hypernuclear ground states with $E_e = 1.851 \text{ GeV}$, $\theta_{e'} = 0.08 \text{ rad}$ and $\theta_{K^+} = 0.12 \text{ rad}$. Binding energies for the ground states of ${}_{\Lambda}^{28}\text{Al}$, ${}_{\Lambda}^{12}\text{B}$ and ${}_{\Lambda}^7\text{He}$ are assumed as -17.00 MeV, -11.37 MeV and -6.00 MeV, respectively.

The HKS solid angle acceptance was derived by GEANT calculation with TOSCA magnetic field map. On the other hand, the ENGE part was estimated by a combination of GEANT (Splitter magnet part) and RAYTRACE (ENGE magnet part). The split pole of the ENGE spectrometer is too complicated to be modeled precisely by TOSCA, however, the pole shape is designed and fabricated to realize the optics system described by the optics code, RAYTRACE [41]. Therefore, we applied combined simulation to estimate acceptance for ENGE. Kinematic conditions are summarized in Tab. 4.4.

The momentum dependent solid angle $S(p_i)$ ($i=K^+, e'$) for each spectrometer can be calculated with:

$$S(p_i) = \Delta\Omega \frac{\text{number of accepted event}(p_i)}{\text{number of generated event}(p_i)} \quad (4.18)$$

HKS part	
$\Delta x'_{K^+}$	$-0.27 \text{ rad} < y'_{K^+} < 0.27 \text{ rad}$
$\Delta y'_{K^+}$	$-0.27 \text{ rad} < y'_{K^+} < 0.27 \text{ rad}$
Δp_{K^+}	$950 \text{ MeV}/c < p_{K^+} < 1450 \text{ MeV}/c$
ENGE part	
$\Delta \theta_{e'}$	$0.05 \text{ rad} < \theta < 0.31 \text{ rad}$
$\Delta \phi_{e'}$	$0.0 \text{ rad} < \phi < 2\pi \text{ rad}$
$\Delta p_{e'}$	$188 \text{ MeV}/c < p_{e'} < 507 \text{ MeV}/c$

Table 4.4: Kinematics conditions for solid angle calculation.

where $\Delta\Omega$ represents the solid angle of generated events at target. Figure 4.31 shows the results of acceptance calculation. The statistical error of the simulation was estimated as 1% .

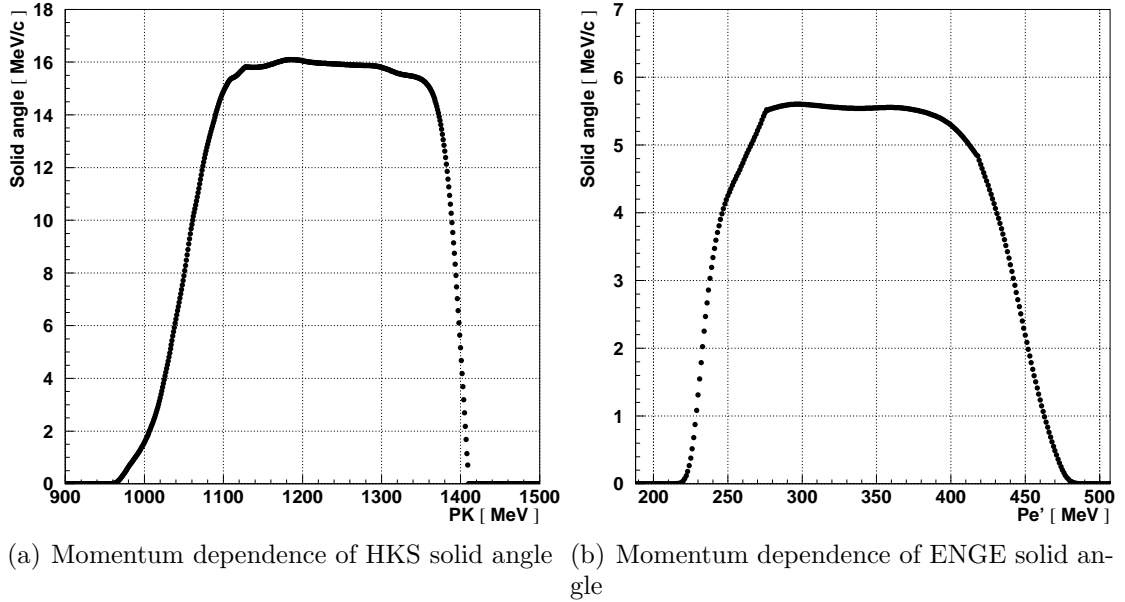


Figure 4.31: Momentum dependence of the solid angle for each spectrometer. HKS solid angle was derived by GEANT and ENGE solid angle was derived by a combination of RAYTRACE and GEANT.

4.9.2 Number of virtual photons

As discussed in Sec. 2.2, the number of virtual photon, N_γ produced at target point can be integrated over virtual photon flux, Γ (Eq. 2.2), all over the acceptance:

$$N_\gamma = \frac{Q}{e} \int \int \Gamma(\omega, \theta_{e'}) \frac{S(P_{e'})}{\Delta\Omega} d\omega d\Omega \quad (4.19)$$

where Q is total charge, e is the elementary charge and ω is the total energy of virtual photon which cover from 1339 MeV to 1604 MeV.

Figure 4.32 shows the momentum dependence of the virtual photon flux $\Gamma(\omega)$ integrated with the e' scattering angle in a unit of [MeV/electron]. Integrating the virtual photon flux $\Gamma(\omega)$ over the virtual photon energy ω , the number of virtual photons per electron was estimated to 4.805×10^{-6} for fixed beam energy of 1.851 GeV.

The beam current monitor was calibrated during the beam time. The systematic error from this measurement is less than 2% . On the other hand, the accuracy of the magnet alignment was estimated to be 0.25 mm. The systematic error from this misalignment was estimated to be 22% . Due to the Tilt method, we measured scattered electron with scattering angle of around 70 mrad where the angular distribution has a large slope (Fig. 2.3). The magnet misalignment is very sensitive to the detection angle. Therefore, this systematic caused by magnetic alignment accuracy is dominant contribution to the entire systematic error of the virtual photon flux.

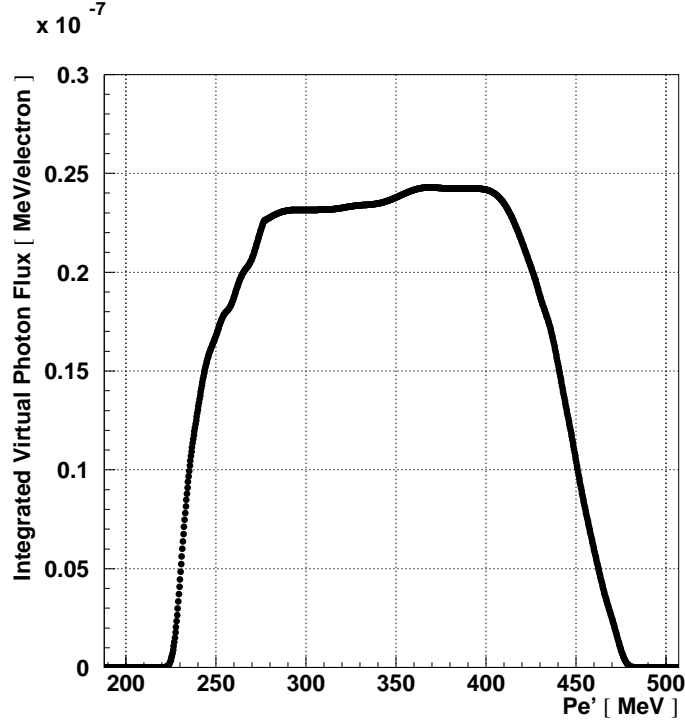


Figure 4.32: The virtual photon flux, $\Gamma(\omega)$, integrated with e' scattering angle $\theta_{e'}$.

4.9.3 Correction factors

Tracking efficiencies (ϵ_{htrk} , ϵ_{etrk})

The HKS tracking efficiency was evaluated from the information of HDCs, HTOF and WC. There were three steps to find track candidates as shown in Fig. 4.33 (a).

- (1) HTOF1X \otimes HTOF2X ($-5 < \Delta\text{CounterID} < 4$)
- (2) HTOF2X \otimes WC1
- (3) HTOF2X \otimes WC2

where $\Delta\text{CounterID}$ represents the difference of counter ID for HTOF1X and HTOF2X. This information was introduced to select particles which go through HKS optics. At step (1), protons which dose not decay in the HKS were chosen by TOF between HTOF1X and HTOF2X. At step (2) and (3), WCs behind a fired HTOF2X were selected. ADC information of WCs was also used to identify protons. Finally, HKS tracking efficiency was evaluated from HDC tracks and tracking candidates.

$$\text{HKS tracking efficiency } (\epsilon_{\text{htrk}}) = \frac{\text{HTOF1X} \otimes \text{HTOF2X} \otimes \text{WC} \otimes \text{HDC tracks}}{\text{HTOF1X} \otimes \text{HTOF2X} \otimes \text{WC}}. \quad (4.20)$$

The averaged HKS tracking efficiency was $92.08 \pm 0.95\%$.

The Enge tracking efficiency was evaluated with a similar way to the HKS one as shown in Fig. 4.33 (b). Tracking candidates were selected by EHODO information with a cut condition:

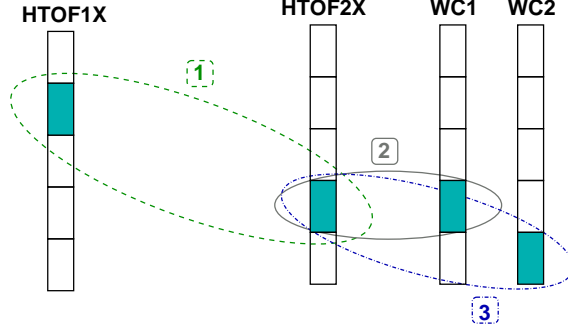
$$|\text{CounterID (EHODO1)} - \text{CounterID (EHODO2)}| \leq 2. \quad (4.21)$$

The Enge tracking efficiency was evaluated requiring EDC tracks as

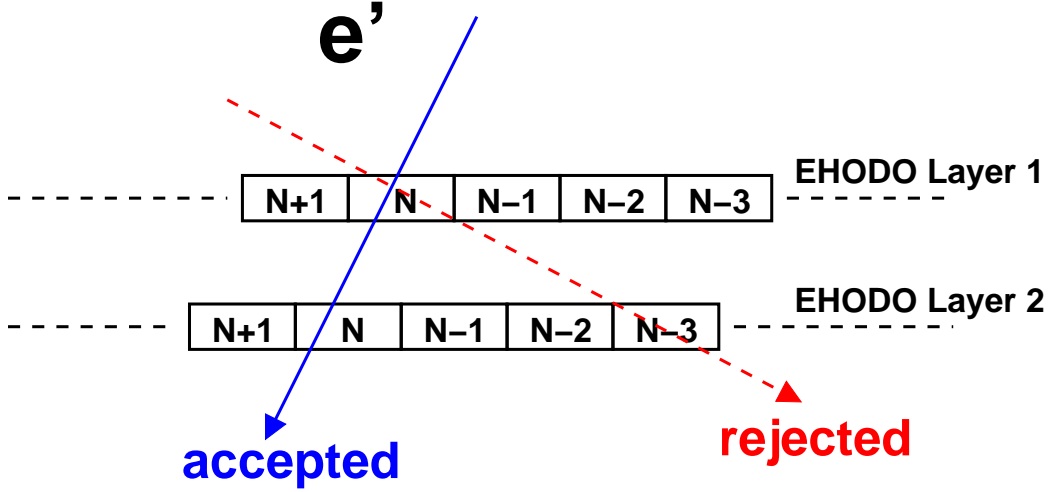
$$\text{Enge tracking efficiency } (\epsilon_{\text{etrk}}) = \frac{\text{EHODO1} \otimes \text{EHODO2} \otimes \text{EDC tracks}}{\text{EHODO1} \otimes \text{EHODO2}}. \quad (4.22)$$

The averaged Enge tracking efficiency was $91.57 \pm 0.26\%$.

The obtained tracking efficiencies for entire run are summarized in Fig. 4.34.



(a) Schematic drawing of HDC tracking



(b) Schematic drawing of EDC tracking

Figure 4.33: Schematic drawing of tracking efficiency estimation.

Cut efficiencies (ϵ_{AC} , ϵ_{WC1} , ϵ_{WC2} , ϵ_{β})

Cut efficiencies were estimated by the ratio of the number of kaons below an each cut condition to that without any cut. The number of kaons was calculated by integrating a Gaussian in Fig. 4.35. Since β_K assumed a particle as kaon and online cherenkov cut was already applied to the data, the pion and the proton distribution was not a Gaussian. Therefore, pions were fitted with a Lorentzian (Eq. 4.23) and protons were fitted with a pseudo-Legit function (Eq. 4.24).

$$y = \frac{c_1}{4(x - c_2)^2 + c_1^2}. \quad (4.23)$$

$$y = c_1 \left[c_2 \frac{2}{\pi} \frac{c_3}{4(x - c_4)^2 + c_3^2} + (1 - c_2) \frac{\sqrt{4 \ln 2}}{\sqrt{\pi} c_3} e^{-\frac{4 \ln 2}{c_3^2} (x - c_4)^2} \right]. \quad (4.24)$$

The number of kaons for each data set is summarized in Tab. 4.5

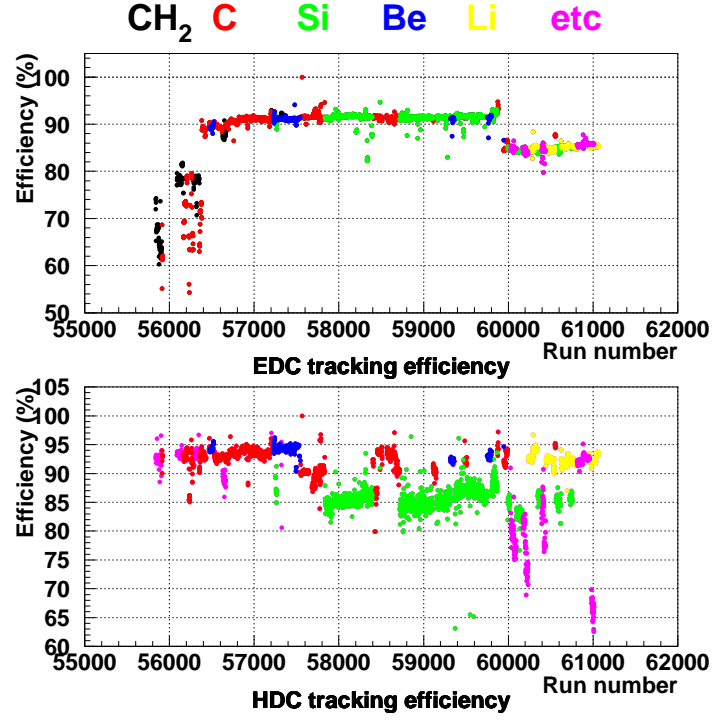


Figure 4.34: Tracking efficiency of each drift chamber as a function of run number.

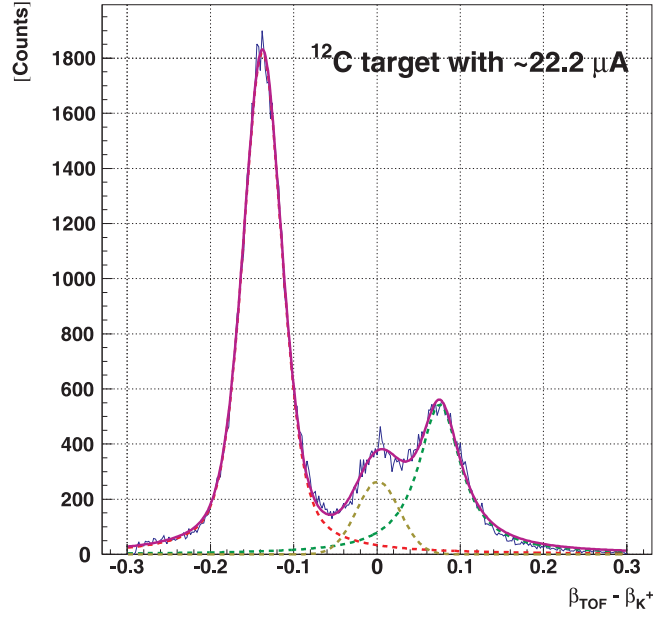


Figure 4.35: $\beta_{\text{TOF}} - \beta_K$ distribution without any offline cherenkov cut.

An offline cherenkov cut was applied to the sum of the number of photoelectrons detected on three or two layers.

Data set No.	Beam current (Ave.) [μ A]	Target	Grouping	Number of kaons	Beam charge [mC]
# 1	2.3	CH ₂	OFF	6839	247.2
# 2	16.1	¹² C	OFF	5289	618.5
# 4	19.7	¹² C	OFF	1331	249.8
# 5	2.3	CH ₂	ON	9697	431.8
# 6	24.4	¹² C	ON	56115	6687.3
# 7	19.6	⁹ Be	ON	31797	2367.5
# 11	21.3	¹² C	ON	14803	1129.7
# 12	21.6	¹² C	ON	5658	661.3
# 13	12.5	²⁸ Si	ON	16092	2531.7
# 14	22.4	¹² C	ON	50251	4633.1
# 15	12.7	²⁸ Si	ON	100449	11156.1
# 16	18.2	⁹ Be	ON	26949	1316.3
# 17	12.4	⁵¹ V	ON	4465	699.6
# 18	10.6	⁸⁹ Y	ON	2310	516.0
# 19	24.9	⁷ Li	ON	72923	3467.6
# 20	20.5	⁶ Li	ON	47658	2273.3
# 21	26.5	¹⁰ B	ON	44865	3099.1

Table 4.5: Summary of number of kaons for each data set. The number of kaons was estimated by the fitting of $\beta_{\text{TOF}} - \beta_K$ distribution.

$$\text{Offline AC threshold} = (\text{AC1} + \text{AC2} + \text{AC3}), \quad (4.25)$$

$$\text{Offline WC threshold} = (\text{WC1} + \text{WC2}). \quad (4.26)$$

Figure 4.36 and 4.37 show typical kaon survival ratios as a function of offline AC and WC thresholds, respectively. Cut efficiencies for each data set are summarized in Tab. 4.6 and 4.7, where errors are statistical only.

Similar to cherenkov cut efficiencies, β cut efficiency (ϵ_β) was evaluated from the number of kaons in Tab. 4.5. A β cut was defined as:

$$\beta \text{ cut} \geq |\beta_{\text{TOF}} - \beta_{K+}|. \quad (4.27)$$

A typical kaon survival ratio is shown as a function of β cut condition in Fig. 4.38. β cut efficiencies for each data set are summarized in Tab. 4.8, where errors are statistical only.

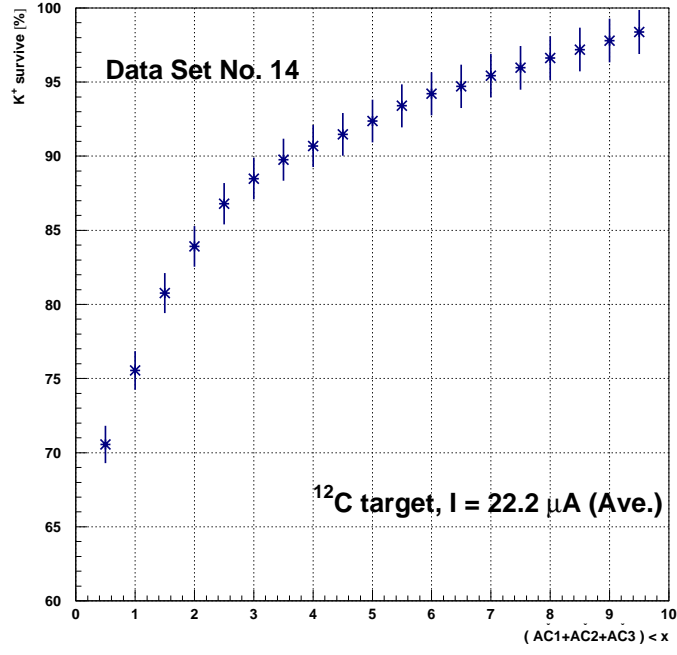


Figure 4.36: Kaon survival ratio as a function of AC offline cut for Data Set # 14.

Data Set No. No.	Beam current (Ave.) [μ A]	Target	Efficiency [%]
# 1	2.3	CH ₂	90.69 \pm 1.15
# 2	16.1	¹² C	90.11 \pm 1.31
# 4	19.7	¹² C	95.56 \pm 2.67
# 5	2.3	CH ₂	95.51 \pm 0.99
# 6	24.4	¹² C	95.90 \pm 1.11
# 7	19.6	⁹ Be	97.15 \pm 1.11
# 11	21.3	¹² C	97.63 \pm 1.62
# 12	21.6	¹² C	95.42 \pm 2.24
# 13	12.5	²⁸ Si	95.64 \pm 2.21
# 14	22.4	¹² C	99.90 \pm 1.19
# 15	12.7	²⁸ Si	95.35 \pm 1.09
# 16	18.2	⁹ Be	95.37 \pm 1.04
# 17	12.4	⁵¹ V	95.13 \pm 1.46
# 18	10.6	⁸⁹ Y	95.28 \pm 2.03
# 19	24.9	⁷ Li	95.34 \pm 1.03
# 20	20.5	⁶ Li	95.50 \pm 0.90
# 21	26.5	¹⁰ B	95.41 \pm 0.93

Table 4.6: Summary of AC cut efficiencies for each data set. Errors are statistical only.

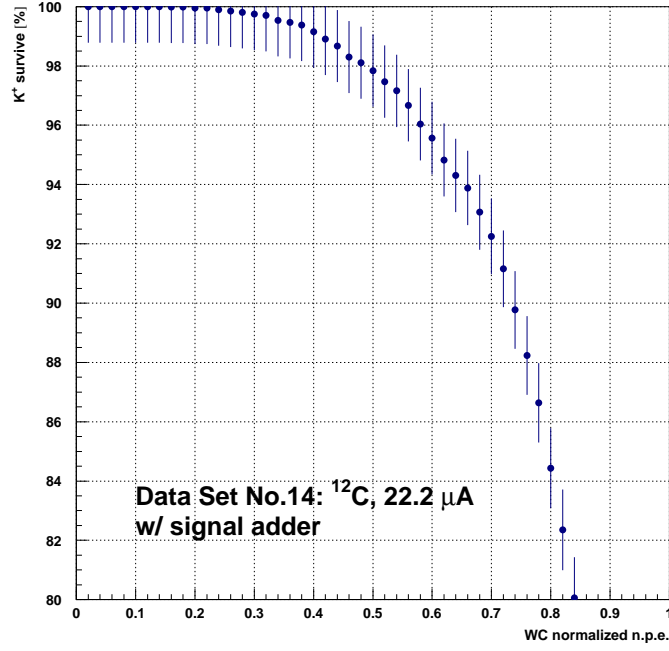


Figure 4.37: Kaon survival ratio as a function of WC offline cut for Data Set # 14.

Data Set No. No.	Beam current (Ave.) [μA]	Target	Efficiency (WC1) [%]	Efficiency (WC2) [%]
# 1	2.3	CH_2	95.27 ± 1.30	95.10 ± 1.30
# 2	16.1	^{12}C	95.41 ± 1.45	95.37 ± 1.46
# 4	19.7	^{12}C	95.24 ± 2.26	95.76 ± 2.28
# 5	2.3	CH_2	95.39 ± 0.84	95.61 ± 0.85
# 6	24.4	^{12}C	95.41 ± 0.95	95.27 ± 0.95
# 7	19.6	^9Be	95.39 ± 0.86	95.12 ± 0.86
# 11	21.3	^{12}C	95.45 ± 1.57	95.25 ± 1.58
# 12	21.6	^{12}C	95.58 ± 1.86	95.43 ± 1.92
# 13	12.5	^{28}Si	95.60 ± 1.72	95.60 ± 1.77
# 14	22.4	^{12}C	95.42 ± 1.21	95.38 ± 1.19
# 15	12.7	^{28}Si	95.38 ± 0.89	95.20 ± 1.10
# 16	18.2	^9Be	95.66 ± 1.07	95.48 ± 1.05
# 17	12.4	^{51}V	95.59 ± 1.42	95.27 ± 1.36
# 18	10.6	^{89}Y	95.44 ± 1.90	95.66 ± 1.84
# 19	24.9	^7Li	95.57 ± 1.09	95.55 ± 1.05
# 20	20.5	^6Li	95.61 ± 0.91	95.41 ± 0.87
# 21	26.5	^{10}B	95.58 ± 0.98	95.30 ± 0.94

Table 4.7: Summary of WC cut efficiencies for each data set. Errors are statistical only.

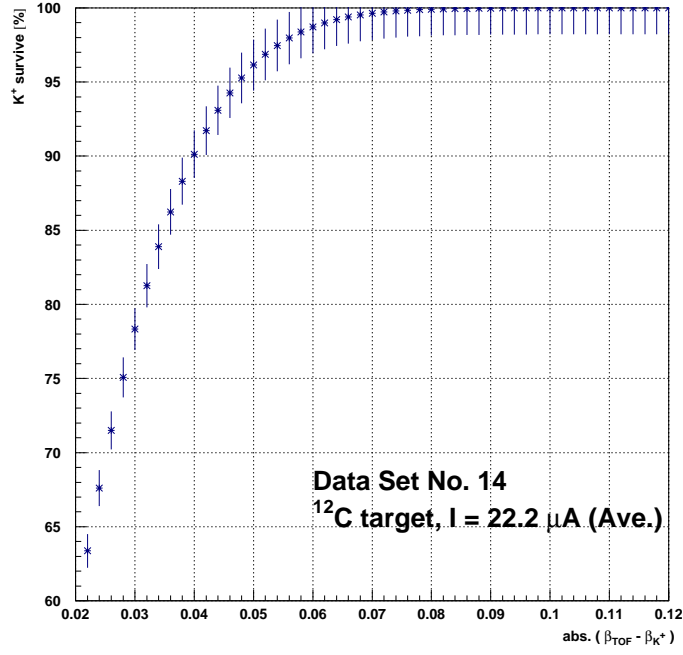


Figure 4.38: Kaon survival ratio as a function of β offline cut for Data Set # 14.

Data set No.	Beam current (Ave.) [μA]	Target	Grouping	Beam charge [mC]	Efficiency [%]
# 1	2.3	CH_2	OFF	247.7	96.53 ± 1.68
# 2	16.1	^{12}C	OFF	626.6	96.58 ± 1.87
# 4	19.7	^{12}C	OFF	255.2	92.30 ± 3.38
# 5	2.3	CH_2	ON	432.9	99.73 ± 1.37
# 6	24.4	^{12}C	ON	6721.5	97.70 ± 1.52
# 7	19.6	^9Be	ON	2400.5	97.63 ± 1.53
# 11	21.3	^{12}C	ON	1133.0	94.75 ± 2.19
# 12	21.6	^{12}C	ON	686.7	99.36 ± 2.99
# 13	12.5	^{28}Si	ON	2804.0	99.09 ± 2.94
# 14	22.4	^{12}C	ON	4662.5	99.42 ± 1.74
# 15	12.7	^{28}Si	ON	11217.4	99.10 ± 1.69
# 16	18.2	^9Be	ON	1321.2	99.37 ± 1.56
# 17	12.4	^{51}V	ON	700.3	98.66 ± 2.30
# 18	10.6	^{89}Y	ON	520.7	97.65 ± 3.07
# 19	24.9	^7Li	ON	3481.5	98.80 ± 1.58
# 20	20.5	^6Li	ON	2276.6	98.94 ± 1.32
# 21	26.5	^{10}B	ON	3105.3	99.07 ± 1.44

Table 4.8: Summary of β cut efficiencies for each data set. Errors are statistical only.

Kaon absorption correction

Some kaons were absorbed in the materials including target, detector and so on and could not be detected. Such events should be taken into account with a kaon absorption correction factor (f_{abs}). This factor was calculated with properties of all materials which kaon passed through. A list of materials for HKS arm are summarized in Tab. 4.9 with their thickness and densities. The kaon absorption reaction rate, $(1-f_{abs})$ can be written as:

$$1 - f_{abs} = \sigma_{inel} \frac{N_A \rho t}{A}, \quad (4.28)$$

where σ_{inel} is the inelastic cross section, N_A is the Avogadro's number, ρ is the material density, and t is the thickness of material. Considering all materials in Tab. 4.9, the $N_A \rho t / A$ amounts to $0.250 \sim 0.252$ [%/mb]

The total cross section and the elastic cross section around $1.05 \text{ GeV}/c < p_{K^+} < 1.35 \text{ GeV}/c$ has been measured as $16.95 \text{ mb} < \sigma_{total} < 19.85 \text{ mb}$ [59–61], and $10.06 < \sigma_{el} < 11.81 \text{ mb}$ [60, 62, 63], respectively. Therefore the inelastic cross section (σ_{inel}) can be expected to be less than 10 mb. The kaon absorption factors depending on target is summarized in Tab. 4.10 where σ_{inel} is fixed as 10 mb. The uncertainty associated with this correction is based only on a measurement accuracy of ~ 1 [mm] for the detector size, which corresponds to 0.01%.

Kaon decay factor

The kaon is an unstable particle with a mean life time $\tau = (1.2385 \pm 0.0024) \times 10^{-8} \text{ sec}$ [64]. Therefore, some of kaons decay before it is detected. The kaon decay factor (f_{decay}) is estimated by a Monte Carlo simulation (GEANT). As a reference, the kaon decay channels and branching ratios are summarized in Tab. 4.11. The kaon decay factor is calculated by a ratio of (A) a number of kaons divided by (B) a number of particles which create trigger. (A) is identified by the last detector in HKS, WC2, and (B) contains not only kaons but also all charged particles from kaon decay.

$$f_{decay} = \frac{\# \text{ of kaons identified by WC}}{\# \text{ of events which create a trigger}} \quad (4.29)$$

The weighted average of the decay factor is estimated to be 34.5%, and its error is dominated by statistical on the calculation as 0.01%.

Material	t [cm]	ρ [g/cm ³]	Notes
Target			
CH ₂	0.5008	0.92	
⁶ Li	0.356	0.46	
⁷ Li	0.350	0.54	
⁹ Be	0.1007	1.848	
¹⁰ B	0.041	2.16	
¹² C	0.0452	2.25	
²⁸ Si	0.0389	2.33	
⁵¹ V	0.01	5.96	
⁸⁹ Y	0.0125	4.478	
Target chamber			
Vacuum ($\sim 2 \times 10^{-5}$ [Torr], 20 [°C])	~ 81	3.2×10^{-11}	
Spectrometer			
Vacuum ($\sim 2 \times 10^{-5}$ [Torr], 20 [°C])	~ 557	3.2×10^{-11}	
Kevlar (C ₁₄ N ₂ O ₂ H ₁₀) exit	0.02	0.74	
Mylar (C ₁₀ O ₄ H ₈) exit	0.0125	1.39	
Detector Hut			
*He bag			Placed between
He gas	100	1.79×10^{-4}	HDC1 & 2
Kapton bag	0.004	1.42	
*HDC1 and 2			
DC Mylar cathode	0.0176	1.39	
Ar/C ₂ H ₆ gas	7.41	0.00154	
Sense wires (W)	0.00008	19.3	
Field wires (W)	0.00034	19.3	
*HTOF1X,1Y and 2X	6	1.032	
*AČ 1,2 and 3			
Paper wall for AČ	1.8	1.42	
Silica aerogel	15	0.2	
*WČ 1 and 2			
Plastic wall for WČ	0.9	1.19	Polymethylmethacrylate
Water	15	1	
*Miscellaneous			
Air	~ 115	0.0012	HDC2 through WČ2
Aluminum foil for light shielding	0.312	2.70	
Plastic sheet for light shielding	1.04	1.30	Polyvinyl-chloride

Table 4.9: Property of the HKS materials. These parameters are used to calculate the kaon absorption factor. For p [Torr], t [°C], air density (ρ) is written as $\rho = 101.325 / \{287.055 \times (273.15 + t)\} \times p / 761.842$ [g/cm³].

DAQ efficiency

The computer live time factor is a ratio of a time interval when the DAQ processes a previous event. The Hall C DAQ processes the events with $\sim 400 \mu\text{s}$ time intervals

Target	K^+ absorption factor
CH ₂	0.9744
⁶ Li	0.9748
⁷ Li	0.9748
⁹ Be	0.9749
¹⁰ B	0.9750
¹² C	0.9750
²⁸ Si	0.9750
⁵¹ V	0.9750
⁸⁹ Y	0.9750

Table 4.10: Summary of absorption factor for each target. K^+ inelastic cross section (σ_{inel}) is fixed as 10 mb.

Decay Modes	Fraction [%]
$\mu^+ \nu_\mu$	63.44 ± 0.14
$\pi^+ \pi^0$	20.92 ± 0.12
$\pi^+ \pi^+ \pi^-$	5.59 ± 0.03
$\pi^0 e^+ \nu_e$	4.98 ± 0.07
$\pi^0 \mu^+ \nu_\mu$	3.32 ± 0.06
$\pi^+ \pi^0 \pi^0$	1.75 ± 0.02

Table 4.11: Summary of K^+ decay channels and fraction [64].

or event rate of ~ 2.5 kHz. The computer live time factor (f_{comp}) is calculated as a ratio of a number of accepted trigger events to that of pre-trigger events which were recorded in scalers for all runs.

$$f_{comp} = \frac{\Sigma \text{ accepted triggers}}{\Sigma \text{ pre-triggers}} \quad (4.30)$$

The beam current was set to keep DAQ efficiency more than 90% during a experiment. Figure 4.39 shows the computer live time factor as a function of run number.

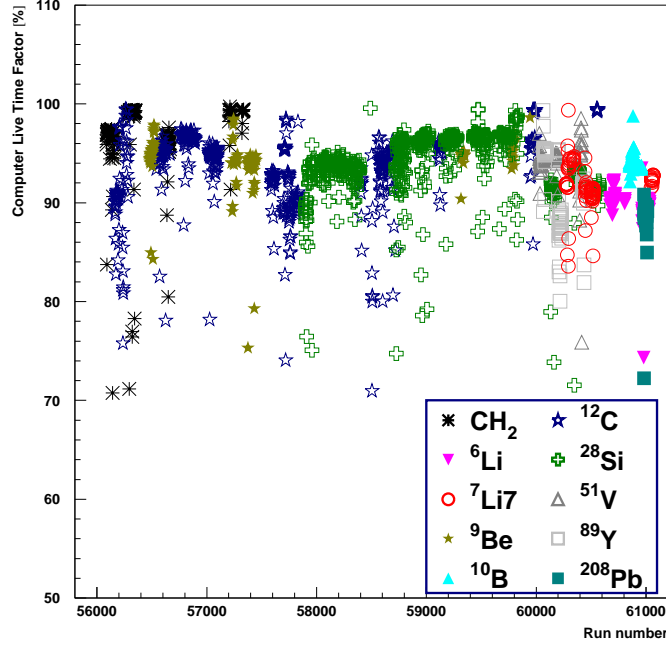


Figure 4.39: Computer live time factor as a function of run number.

4.10 Systematic errors

As discussed in Sec. 4.8, systematic errors due to the present calibration procedure strongly depend on the S/N ratio. Therefore, the total systematic error was individually evaluated for each bound state.

4.10.1 Systematic errors for cross sections

The total systematic errors of the cross section are summarized in Tab. 4.12 and 4.13. The number of events and S/N ratio for each state were estimated from the missing mass spectra shown in the next chapter (Fig. 5.1, 5.2 and 5.3). “Target thickness” was measured by a laser displacement meter. Errors of number of virtual photons and HKS acceptance were discussed in the Sec. 4.9.2 and 4.9.1, respectively. Systematic errors depending on the calibration procedure were evaluated from the results of blind analysis of simulated data discussed in the Sec. 4.8, considering the S/N ratio of each state.

4.10.2 Systematic errors for binding energies

Similar to the cross section, systematic error for the binding energy was evaluated for each bound state. Tab. 4.14 and 4.15 is a summary of the systematic errors for binding energies. Two components, “Kinematics tuning” and “Tuning procedure”, were discussed in Sec. 4.6 and 4.8, respectively. Since these components does NOT guarantee the sign (positive or negative) under the present analysis, the systematic errors for excitation energies were given by the quadratic sum. For example, the

systematic error of ${}^{12}_{\Lambda}\text{B}$ #2 state is calculated as $(0.097^2 + 0.10^2 + 0.090^2 + 0.10^2)^{1/2} = 0.1936$ MeV.

Peak ID	${}^{12}_{\Lambda}\text{B}$ #1	${}^{12}_{\Lambda}\text{B}$ #2	${}^{12}_{\Lambda}\text{B}$ #3	${}^{12}_{\Lambda}\text{B}$ #4
Number of event [counts]	590	180	250	530
S/N	0.96	0.33	0.24	0.69
Target thickness [%]	2	2	2	2
Number of virtual photon [%]	22	22	22	22
HKS acceptance [%]	1	1	1	1
Efficiencies [%]	5	5	5	5
Tuning (Contamination) [−%]	20	60	60	30
Tuning (Loss) [+%]	30	30	30	30

Table 4.12: A summary of systematic errors for cross sections of ${}^{12}_{\Lambda}\text{B}$.

Peak ID	${}^{28}_{\Lambda}\text{Al}$ #1	${}^{28}_{\Lambda}\text{Al}$ #2	${}^{28}_{\Lambda}\text{Al}$ #3	${}^7_{\Lambda}\text{He}$ #1
Number of event [counts]	190	280	54	90
S/N	0.53	0.51	0.15	0.40
Target thickness [%]	5	5	5	5
Number of virtual photon [%]	22	22	22	22
HKS acceptance [%]	1	1	1	1
Efficiencies [%]	5	5	5	5
Tuning (Contamination) [−%]	40	40	90	30
Tuning (Loss) [+%]	30	30	30	30

Table 4.13: A summary of systematic errors for cross sections of ${}^{28}_{\Lambda}\text{Al}$ and ${}^7_{\Lambda}\text{He}$.

Peak ID	${}^{12}_{\Lambda}\text{B}$ #1	${}^{12}_{\Lambda}\text{B}$ #2	${}^{12}_{\Lambda}\text{B}$ #3	${}^{12}_{\Lambda}\text{B}$ #4
Number of event [counts]	590	180	250	800
S/N	0.96	0.33	0.24	0.74
Kinematics tuning [MeV]	0.097	0.090	0.090	0.090
Tuning procedure [MeV]	0.10	0.30	0.30	0.10

Table 4.14: A summary of systematic errors for binding energies of ${}^{12}_{\Lambda}\text{B}$.

Peak ID	$^{28}_{\Lambda}\text{Al}$ #1	$^{28}_{\Lambda}\text{Al}$ #2	$^{28}_{\Lambda}\text{Al}$ #3	$^7_{\Lambda}\text{He}$ #1
Number of event [counts]	190	280	54	90
S/N	0.53	0.51	0.15	0.40
Kinematics tuning [MeV]	0.125	0.101	0.092	0.094
Tuning procedure [MeV]	0.20	0.20	0.30	0.20

Table 4.15: A summary of systematic errors for binding energies of $^{28}_{\Lambda}\text{Al}$ and $^7_{\Lambda}\text{He}$.

Chapter 5

Results and Discussion

In this chapter, missing mass spectra obtained in the E01-011 experiment will be described. Fitting results will be compared with theoretical calculations and discussed.

5.1 Mass spectrum

The missing masses and cross sections were evaluated for the data with natural ^{12}C (^{12}C : 98.9%, ^{13}C : 1.1%), isotopically enriched ^{28}Si , and natural ^7Li (^7Li : 92.4%, ^6Li : 7.6%) targets. Their data sets are summarized in Tab. 5.1. As discussed in Sec. 4.5 missing mass values were calculated with Eq. 4.7. Figures 5.1, 5.2 and 5.3 show the measured hypernuclear mass spectra of $^{12}_{\Lambda}\text{B}$, $^{28}_{\Lambda}\text{Al}$, and $^7_{\Lambda}\text{He}$, respectively. The ordinate represents observed counts, and the abscissa represents the Λ binding energy, $-B_{\Lambda}$, defined as:

$$-B_{\Lambda} = M_{HY} - (M_{\Lambda} + M_A) \quad (5.1)$$

where M_{HY} , M_{Λ} and M_A show the masses of a hypernucleus, a Λ and a core nucleus, respectively. These values are summarized in Appendix A. The accidental background events are shown by the blue histogram with statistical error bars. A detailed explanation of how the accidental background was obtained is explained in Sec. 4.7.

Data set No.	Beam current (Ave.) [μA]	Target	Grouping	Trigger $\text{ENGE} \times \text{HTOF1X} \times \text{HTOF2X} \times \alpha$	Beam charge [mC]
# 2	16.1	^{12}C	OFF	$\alpha = \text{W}\check{\text{C}}(\text{T} \oplus \text{B}) \times \overline{\text{A}\check{\text{C}}}(\text{T} \oplus \text{B})$	618.5
# 4	19.7	^{12}C	OFF	$\alpha = \text{W}\check{\text{C}}(\text{T} \otimes \text{B}) \times \overline{\text{A}\check{\text{C}}}(\text{T} \oplus \text{B})$	249.8
# 6	24.4	^{12}C	ON	$\alpha = \text{W}\check{\text{C}}(\text{T} \otimes \text{B}) \times \overline{\text{A}\check{\text{C}}}(\text{T} \oplus \text{B})$	6687.3
# 11	21.3	^{12}C	ON	$\alpha = \text{W}\check{\text{C}}(\text{T} \otimes \text{B}) \times \overline{\text{A}\check{\text{C}}}(\text{T} \otimes \text{B})$	1129.7
# 12	21.6	^{12}C	ON	$\alpha = \text{HTOF1Y} \times \text{W}\check{\text{C}}(\text{T} \otimes \text{B}) \times \overline{\text{A}\check{\text{C}}}(\text{T} \otimes \text{B})$	661.3
# 13	12.5	^{28}Si	ON	$\alpha = \text{HTOF1Y} \times \text{W}\check{\text{C}}(\text{T} \otimes \text{B}) \times \overline{\text{A}\check{\text{C}}}(\text{T} \otimes \text{B})$	2776.6
# 14	22.4	^{12}C	ON	$\alpha = \text{HTOF1Y} \times \text{W}\check{\text{C}}(\text{T} \oplus \text{B}) \times \overline{\text{A}\check{\text{C}}}(\text{T} \otimes \text{B})$	4633.1
# 15	12.7	^{28}Si	ON	$\alpha = \text{HTOF1Y} \times \text{W}\check{\text{C}}(\text{T} \oplus \text{B}) \times \overline{\text{A}\check{\text{C}}}(\text{T} \otimes \text{B})$	10555.4
# 19	24.9	^7Li	ON	$\alpha = \text{HTOF1Y} \times \text{W}\check{\text{C}}(\text{T} \oplus \text{B}) \times \overline{\text{A}\check{\text{C}}}(\text{T} \otimes \text{B})$	3467.6
Total	-	^{12}C	-	-	13979.7
	-	^{28}Si	-	-	13332.0
	-	^7Li	-	-	3467.6

Table 5.1: Data set for ^{12}C , ^{28}Si , and ^7Li target.

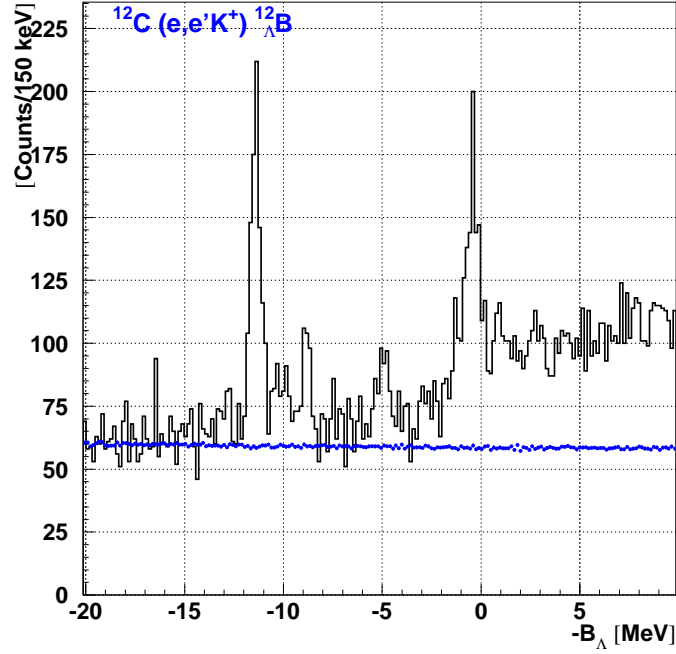


Figure 5.1: Missing mass spectrum for $^{12}_{\Lambda}\text{B}$ with counts on the vertical scale. The blue histogram represents the accidental background estimated by the mixed event analysis.

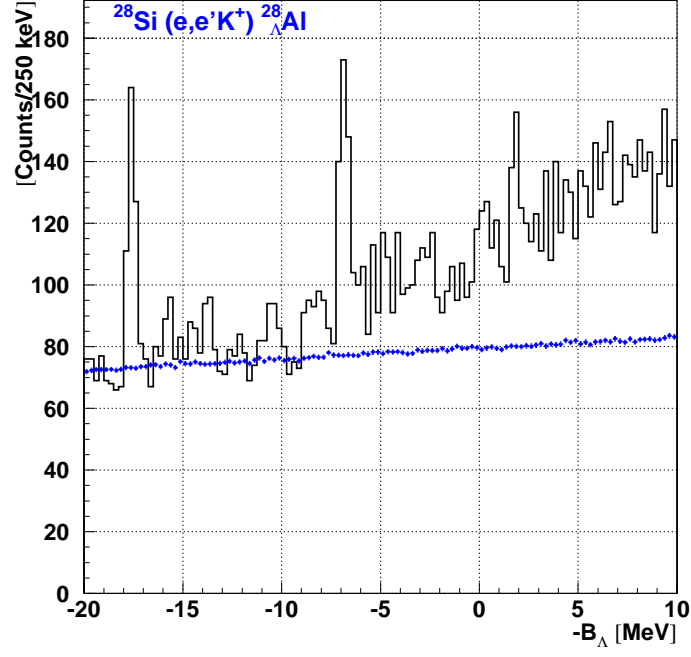


Figure 5.2: Missing mass spectrum for $^{28}_{\Lambda}\text{Al}$ with counts on the vertical scale. The blue histogram represents the accidental background estimated by the mixed event analysis.

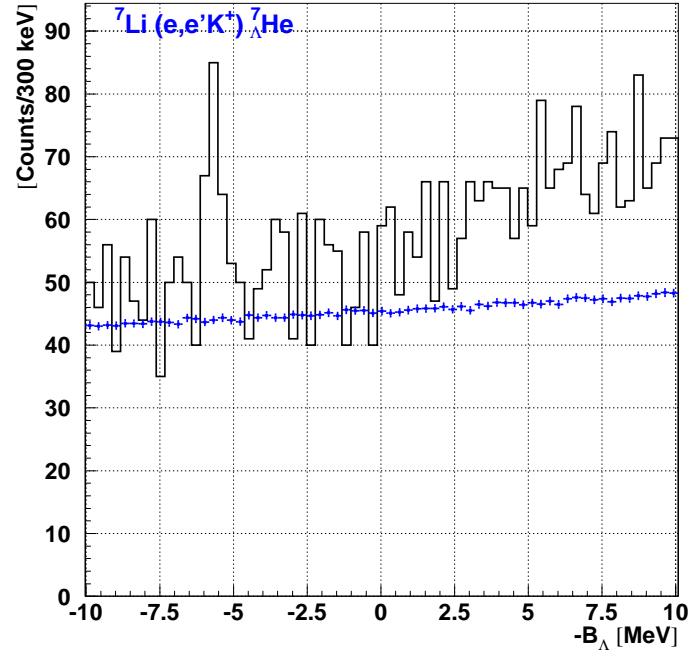


Figure 5.3: Missing mass spectrum for $^7_{\Lambda}\text{He}$ with counts on the vertical scale. The blue histogram represents the accidental background estimated by the mixed event analysis.

The cross section of each hypernucleus is calculated by

$$\overline{\left(\frac{d\sigma}{d\Omega}\right)}_{1^\circ-13^\circ} = \frac{1}{N_T} \sum_{i=1}^{N_{HY}} \frac{1}{\epsilon_{total} N_\gamma(P_{e'}) d\Omega_i}. \quad (5.2)$$

$$\sigma_{1^\circ-13^\circ} = \frac{1}{N_T} \sum_{i=1}^{N_{HY}} \frac{1}{\epsilon_{total} N_\gamma(P_{e'}) d\Omega_i} d\Omega_i. \quad (5.3)$$

Details of Eq. 5.2 and Eq. 5.3 are described in Sec. 4.9. The differential cross section is averaged over the HKS acceptance which covers kaon scattering angles from 1° to 13° . Figures 5.4, 5.5 and 5.6 show missing mass spectra with the y-axis representing the differential cross section. In these figures, the excitation energy of the hypernucleus (Ex), which defines the ground state as zero, is also shown on the top of the figure. The quoted errors are statistical only. Thanks to the mixed event analysis (Sec. 4.7), the statistical fluctuation of accidental background events is much less than of the true coincidence events. Therefore, the statistical error from the accidental background events is almost negligible.

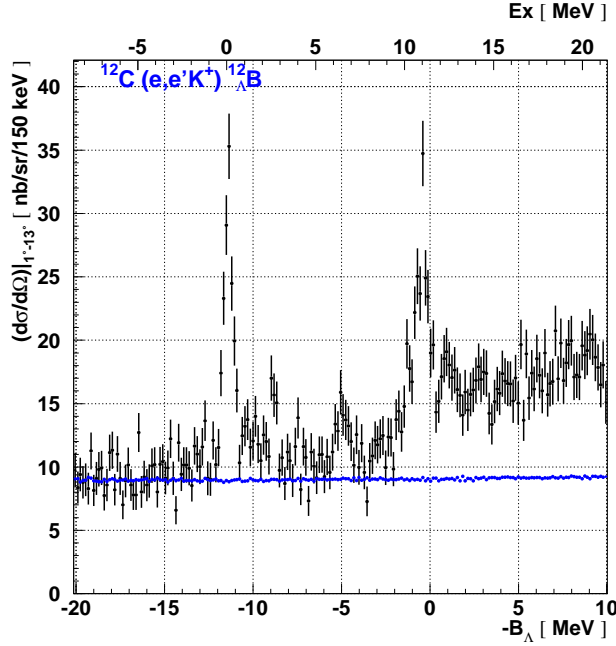


Figure 5.4: Missing mass spectrum for $^{12}_{\Lambda}\text{B}$ with the vertical scale of differential cross section. The blue histogram represents the accidental background estimated by the mixed event analysis. Errors are statistical only.

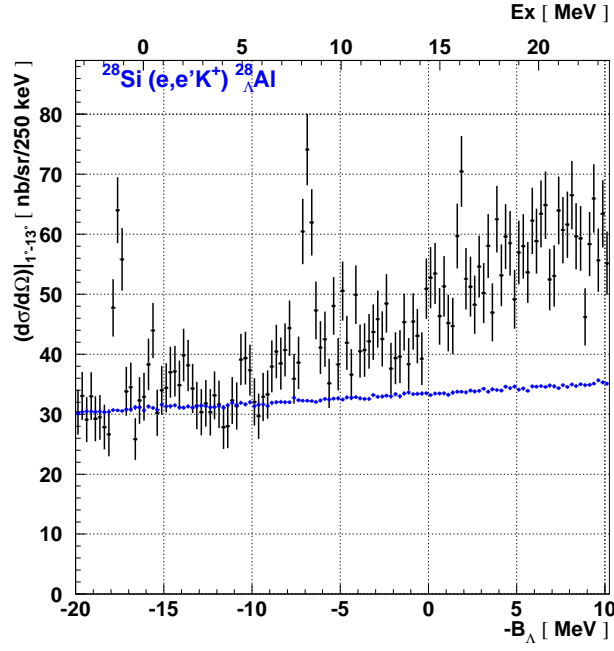


Figure 5.5: Missing mass spectrum for $^{28}_{\Lambda}\text{Al}$ with the vertical scale of differential cross section. The blue histogram represents the accidental background estimated by the mixed event analysis. Errors are statistical only.

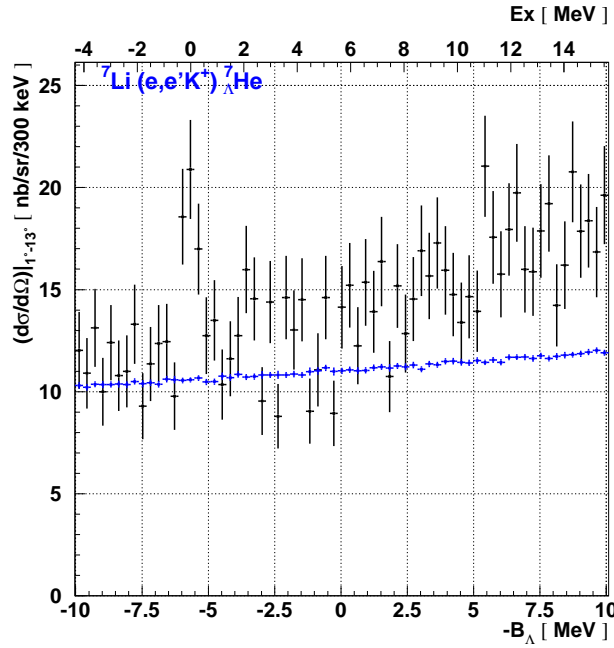


Figure 5.6: Missing mass spectrum for $^7_{\Lambda}\text{He}$ with the vertical scale of differential cross section. The blue histogram represents the accidental background estimated by the mixed event analysis. Errors are statistical only.

5.2 Systematic errors for cross sections

Evaluation of blind analysis result by the experimental data

As discussed in Sec. 4.8, some of the true ($e, e'K^+$) events leaked out to the outside area of the peak during the matrix calibration. For the ${}^{12}_{\Lambda}\text{B}$ ground state, the amount of such “Loss” events is evaluated to be about 30% of the peak (Tab. 4.12). Some events are observed on both sides of the ${}^{12}_{\Lambda}\text{B}$ ground state peak at $-B_{\Lambda} = -11.4$ MeV in Fig. 5.7. The tails are much larger than the radiative tail or energy straggling which were studied by a detailed simulation. According to the theoretical calculation, no state is expected to exist between the ground state ($-B_{\Lambda} \simeq -11.4$ MeV) and the first core excited state ($-B_{\Lambda} \simeq -8.5$ MeV). Therefore, these extra events are most likely due to the “Loss” events of the ground state.

In order to compare the number of the events with the “Loss” from the ground state peak, the number of these events was counted by integrating the green hatched region shown in Fig. 5.7. The result showed that the cross section of this component was 32 nb/sr which corresponds to 32% of the ground state cross section fitted by a Gaussian shown in red line in Fig. 5.7. Considering that a portion of the “Loss” of the first core excited states also contributes to the extra events, the systematic error estimation by the detailed simulation is consistent with this scenario.

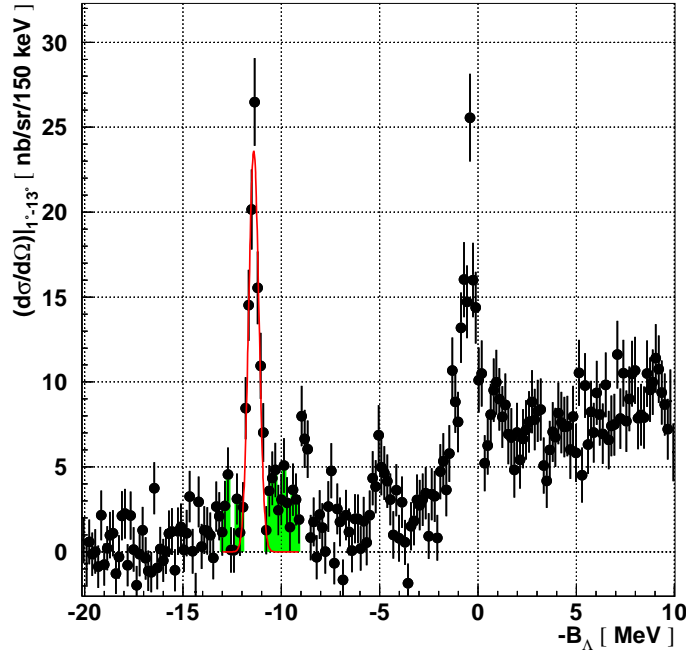


Figure 5.7: Estimation of a side tail for the ground state of ${}^{12}_{\Lambda}\text{B}$. The cross section of the extra events shown in green is 32 nb/sr, which corresponds to 32% of ground state.

Uncertainty of the background estimation

As discussed in Sec. 4.7, the accidental background level was estimated by the mixed event analysis with sufficient statistics. The quasi-free Λ production events ($-B_\Lambda > 0$) were fitted with a function proportional to the square root of the binding energy in this study. However, there may be an uncertainty originating from the distortion of the background shape by unknown reasons. This uncertainty was estimated as follows. The cross section difference for a Λ bound state between the case for the accidental background plus the square root quasi-free shape and the case for the linear background was defined as a $\Delta_{B.G.}$. The $\Delta_{B.G.}$ (assuming the highest background level) was estimated by fitting each bound state with a Gaussian and a linear function shown in red line of Fig. 5.8, 5.9 and 5.10. Here, the width σ of a Gaussian was fixed at the width presented in the next section. Results are summarized in Tab. 5.2 and are smaller than the effect of “Contamination” shown in Tab. 4.12 and in Tab. 4.13. Therefore, these values are treated to be already included in the systematic errors due to the tuning processes.

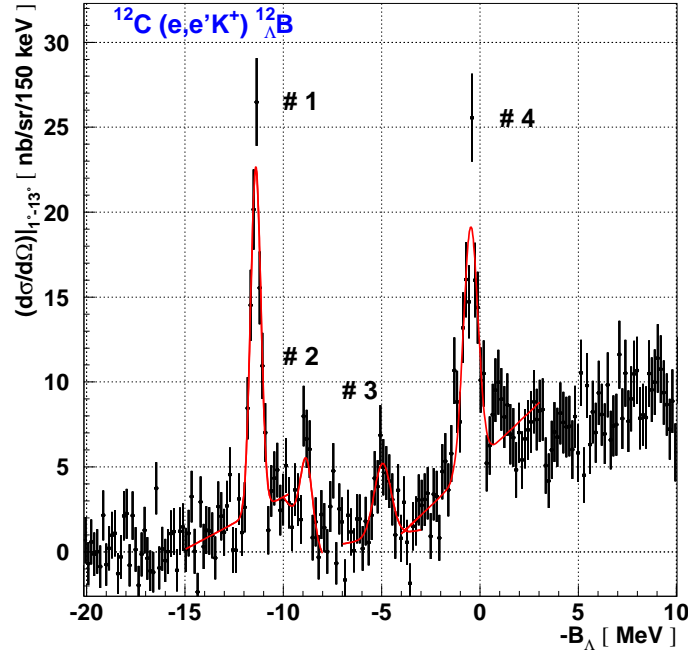


Figure 5.8: Fitting of the $^{12}_\Lambda\text{B}$ when the linear background is assumed for each peak.

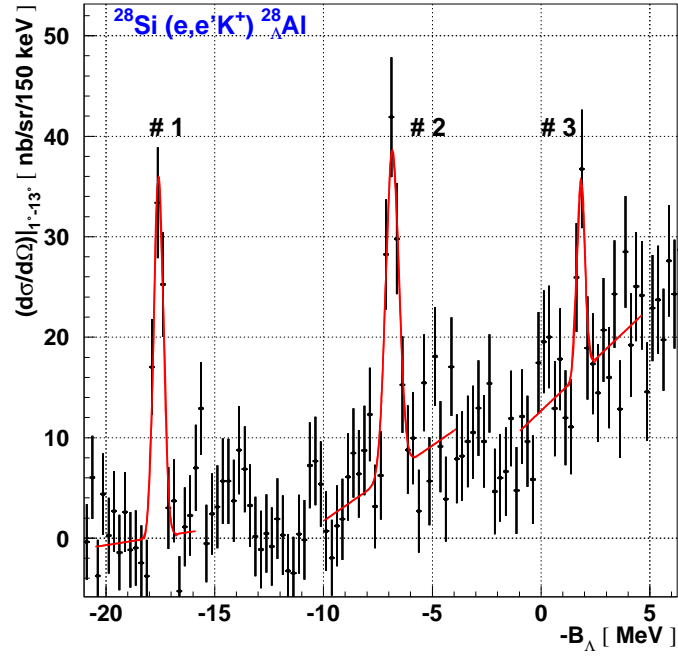


Figure 5.9: Fitting of the $^{28}_{\Lambda}\text{Al}$ when the linear background is assumed for each peak.

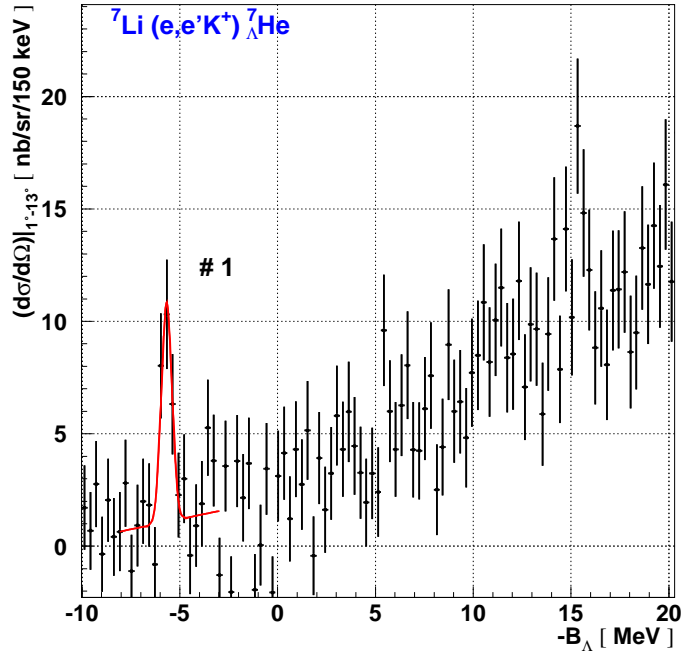


Figure 5.10: Fitting of the $^7_{\Lambda}\text{He}$ when the linear background is assumed for each peak.

Peak ID	$\Delta_{B.G.}$ [nb/sr]
$^{12}_{\Lambda}\text{B}$ #1	-12
$^{12}_{\Lambda}\text{B}$ #2	-10
$^{12}_{\Lambda}\text{B}$ #3	-8
$^{12}_{\Lambda}\text{B}$ #4	-34
$^{28}_{\Lambda}\text{Al}$ #1	-5
$^{28}_{\Lambda}\text{Al}$ #2	-30
$^{28}_{\Lambda}\text{Al}$ #3	-14
$^7_{\Lambda}\text{He}$ #1	-4

Table 5.2: Change of the cross sections when the linear background is assumed in the fitting.

An additional structure is seen beside the # 4 peak in Fig. 5.8. A similar structure was already observed in the other experimental data of $^{12}_{\Lambda}\text{B}$ (Fig. 5.17 [65]). The shell model calculation with DWIA also predicted that some peaks exist around the p_{Λ} peak (Fig. 5.19). In order to estimate the effect on the p_{Λ} peak from this structure, the # 4 peak region was fitted by three Gaussians with free parameters defined as # 4-L, # 4-C and # 4-R in Fig. 5.11. The obtained binding energies, widths and cross sections are summarized in Tab. 5.3. On the other hand, Tab. 5.4 summarized the results of fitting with a single Gaussian (Fig. 5.12), which gives a larger cross section since the side peaks are neglected. As for the p_{Λ} peak (# 4-C in Fig. 5.11 and # 4 in Fig. 5.12), the difference of the binding energies is 0.06 MeV and the difference of the differential cross sections is 28 nb/sr, which are within the errors shown in Tab. 5.4. In the following sections, fitting results by three Gaussians (# 4-C in Tab. 5.3) are applied for discussion on the p_{Λ} state.

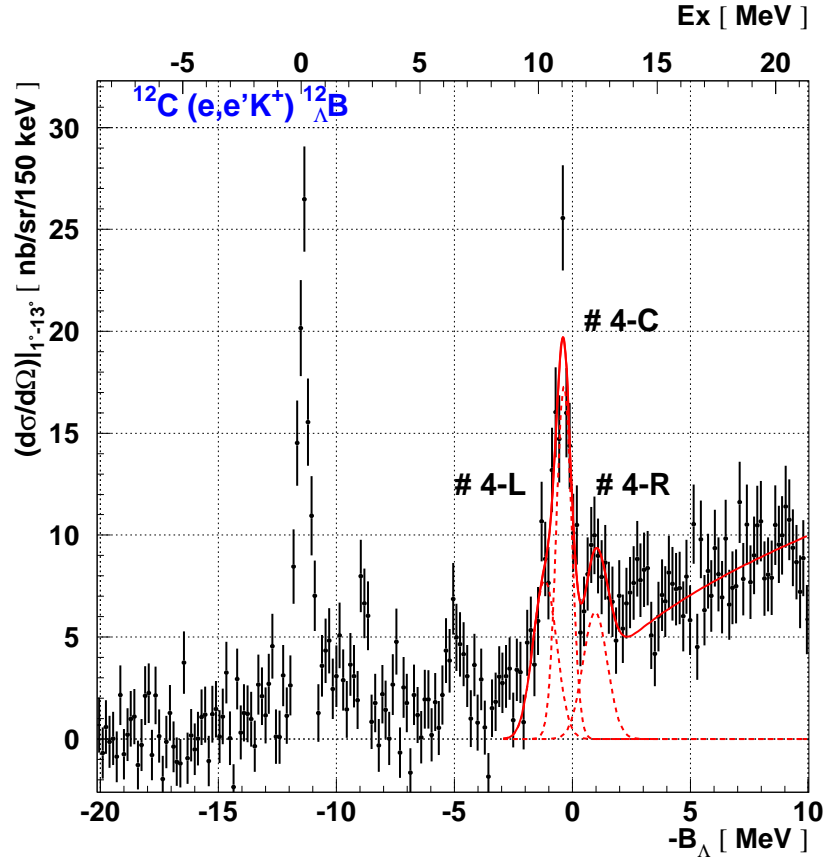


Figure 5.11: Missing mass spectrum for $^{12}_{\Lambda}\text{B}$. The p_{Λ} peak of $^{12}_{\Lambda}\text{B}$ is fitted with three Gaussians. The vertical axis represents the differential cross section.

Peak No.	$-B_\Lambda$ [MeV] \pm (stat.) \pm (sys.)	Ex [MeV] \pm (stat.) \pm (sys.)	FWHM [MeV]	$(\overline{d\sigma/d\Omega}) _{1^\circ-13^\circ}$ [nb/sr] \pm (stat.) \pm (sys.)
# 4-L	$-1.17 \pm 0.03 \pm 0.31$	$10.23 \pm 0.03 \pm 0.34$	1.18 ± 0.12	$65 \pm 3.5^{+24}_{-42}$
# 4-C	$-0.35 \pm 0.01 \pm 0.13$	$11.05 \pm 0.01 \pm 0.19$	0.77 ± 0.07	$94 \pm 4.0^{+35}_{-35}$
# 4-R	$0.97 \pm 0.03 \pm 0.31$	$12.37 \pm 0.03 \pm 0.34$	1.21 ± 0.13	$54 \pm 2.4^{+20}_{-35}$

Table 5.3: Obtained binding energies, widths and cross sections for the p_Λ peak of $^{12}_\Lambda\text{B}$ fitted by three Gaussians (Fig. 5.11).

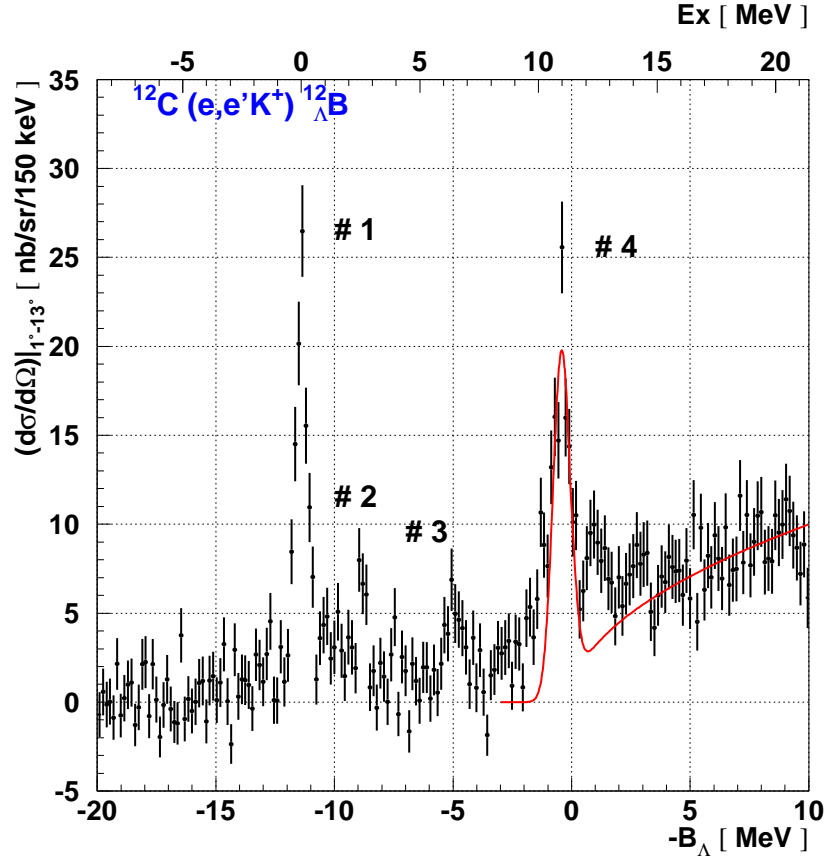


Figure 5.12: Missing mass spectrum for $^{12}_\Lambda\text{B}$. The p_Λ peak of $^{12}_\Lambda\text{B}$ is fitted with a single Gaussian. The vertical axis represents the differential cross section .

Peak No.	$-B_\Lambda$ [MeV] \pm (stat.) \pm (sys.)	Ex [MeV] \pm (stat.) \pm (sys.)	FWHM [MeV]	$(\overline{d\sigma/d\Omega}) _{1^\circ-13^\circ}$ [nb/sr] \pm (stat.) \pm (sys.)
# 4	$-0.41 \pm 0.01 \pm 0.13$	$10.99 \pm 0.01 \pm 0.19$	0.87 ± 0.13	$122 \pm 4.3^{+46}_{-46}$

Table 5.4: Obtained binding energies, widths and cross sections for the p_Λ peak of $^{12}_\Lambda\text{B}$ fitted by a single Gaussians (Fig. 5.12).

Similar to the p_Λ peak of $^{12}_\Lambda\text{B}$, the side peak effect for the p_Λ peak of $^{28}_\Lambda\text{Al}$ was also estimated. Some excited states are expected to exist between major peaks for $^{28}_\Lambda\text{Al}$ (Fig. 5.25). In the $^{28}_\Lambda\text{Al}$ spectrum (Fig. 5.9), a structure can be seen beside # 2. They are fitted by three Gaussians, defined as #2-L, #2-C and #2-R in Fig. 5.13. A width for #2-C is free while widths for other two peaks are assumed to be the same. The results are summarized in Tab. 5.5. In the case of fitting the p_Λ peak with a single Gaussian, the results are summarized in the next section (Tab. 5.12 and Tab. 5.13). Differences for the p_Λ peak between these fitting procedures are 0.03 MeV for the binding energy and 3 nb/sr for the cross section, which are within the systematic errors in Tab. 5.12 and Tab. 5.13. In the present analysis, the binding energy and cross section for p_Λ of $^{28}_\Lambda\text{Al}$ state are evaluated by a single Gaussian fitting.

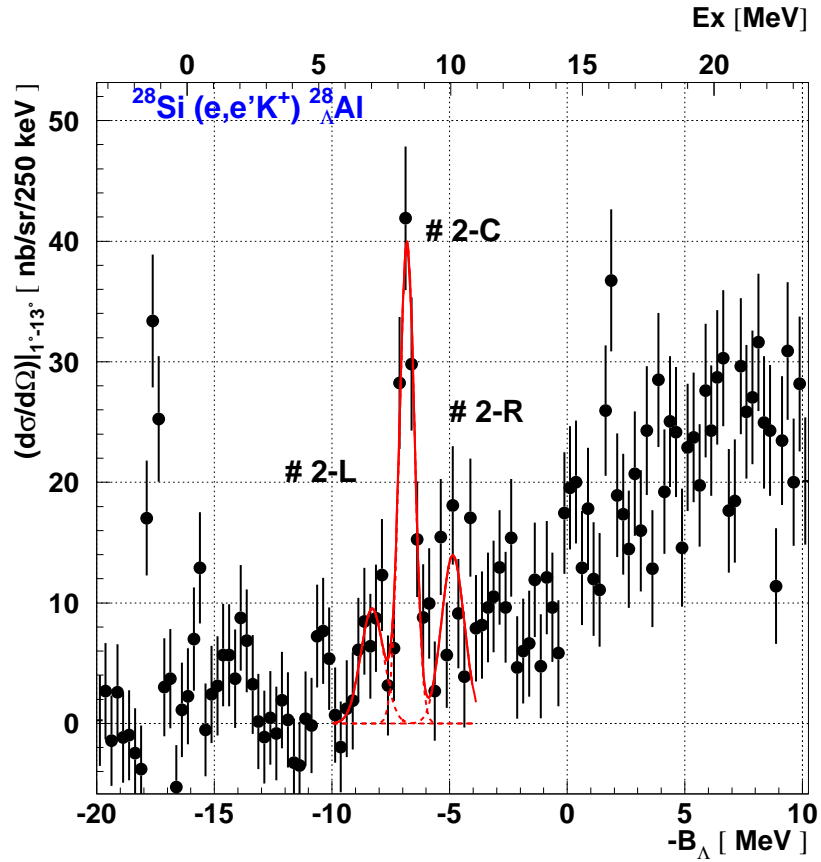


Figure 5.13: Missing mass spectrum for $^{28}_\Lambda\text{Al}$. The p_Λ peak of $^{28}_\Lambda\text{Al}$ state is fitted with three Gaussians. The vertical axis represents the differential cross section .

Peak No.	$-B_\Lambda$ [MeV] \pm (stat.) \pm (sys.)	Ex [MeV] \pm (stat.) \pm (sys.)	FWHM [MeV]	$(d\sigma/d\Omega) _{1^\circ-13^\circ}$ [nb/sr] \pm (stat.) \pm (sys.)
# 2-L	$-8.29 \pm 0.05 \pm 0.32$	$9.28 \pm 0.05 \pm 0.40$	1.15 ± 0.12	$47 \pm 5.0^{+18}_{-44}$
# 2-C	$-6.81 \pm 0.02 \pm 0.32$	$10.76 \pm 0.02 \pm 0.40$	0.75 ± 0.07	$128 \pm 8.5^{+48}_{-59}$
# 2-R	$-4.86 \pm 0.05 \pm 0.32$	$12.71 \pm 0.05 \pm 0.40$	1.15 ± 0.12	$68 \pm 3.4^{+26}_{-63}$

Table 5.5: Obtained binding energies, widths and cross sections for the p_Λ peak of $^{28}_\Lambda\text{Al}$ fitted by three Gaussians (Fig. 5.13).

5.3 Discussion

5.3.1 Spectroscopy of $^{12}_{\Lambda}\text{B}$

Results

In the mass spectrum of $^{12}_{\Lambda}\text{B}$ in Fig. 5.14, two major peaks are observed around $-B_{\Lambda}$ of -11 MeV and -1 MeV. They can be interpreted as having the configuration of one proton-hole and one Λ particle in the s or p orbit : $[(p_{3/2})^{-1}(s_{1/2})_{\Lambda}]$ and $[(p_{3/2})^{-1}(p_{3/2}, p_{1/2})_{\Lambda}]$.

In order to extract the binding energies and the averaged differential cross sections of these peaks, the accidental background level was estimated by fitting the background obtained by mixed event analysis (Sec. 4.7) with a 5th order polynomial function. The quasi-free Λ component at $-B_{\Lambda} > 0$ region was fitted by a function proportional to the square root of $-B_{\Lambda}$. The s_{Λ} state peak was fitted by a single Gaussian while the p_{Λ} state peak was fitted by a Gaussian with two side peaks as discussed in the previous section, after subtracting accidental background (Fig. 5.14). Two core excited state candidates were also fitted by Gaussians. The total cross section for each state was evaluated with a similar procedure (Fig. 5.15). The obtained binding energies and widths are summarized in Tab. 5.6 and cross sections are summarized in Tab. 5.7. The details of systematic errors were discussed in Sec. 4.10 and 5.2.

Peak No.	$-B_{\Lambda}$ [MeV] \pm (stat.) \pm (sys.)	Ex [MeV] \pm (stat.) \pm (sys.)	FWHM [MeV]
# 1	$-11.40 \pm 0.01 \pm 0.14$	0	0.61 ± 0.05
# 2	$-8.89 \pm 0.02 \pm 0.31$	$2.51 \pm 0.02 \pm 0.34$	0.48 ± 0.09
# 3	$-5.00 \pm 0.03 \pm 0.31$	$6.40 \pm 0.03 \pm 0.34$	1.01 ± 0.08
# 4	$-0.35 \pm 0.01 \pm 0.13$	$11.05 \pm 0.01 \pm 0.19$	0.77 ± 0.07

Table 5.6: Obtained binding energies and width for $^{12}_{\Lambda}\text{B}$ spectrum.

Peak No.	$(d\sigma/d\Omega) _{1^{\circ}-13^{\circ}}$ [nb/sr] \pm (stat.) \pm (sys.)	$\sigma_{1^{\circ}-13^{\circ}}$ [nb] \pm (stat.) \pm (sys.)
# 1	$101 \pm 4.2^{+38}_{-31}$	$1.60 \pm 0.07^{+0.60}_{-0.48}$
# 2	$31 \pm 2.3^{+12}_{-20}$	$0.49 \pm 0.04^{+0.18}_{-0.31}$
# 3	$39 \pm 2.5^{+15}_{-25}$	$0.62 \pm 0.04^{+0.23}_{-0.40}$
# 4	$94 \pm 4.0^{+35}_{-35}$	$1.50 \pm 0.07^{+0.56}_{-0.56}$

Table 5.7: Obtained cross sections for $^{12}_{\Lambda}\text{B}$ spectrum. The details of systematic errors are described in Sec. 4.10.

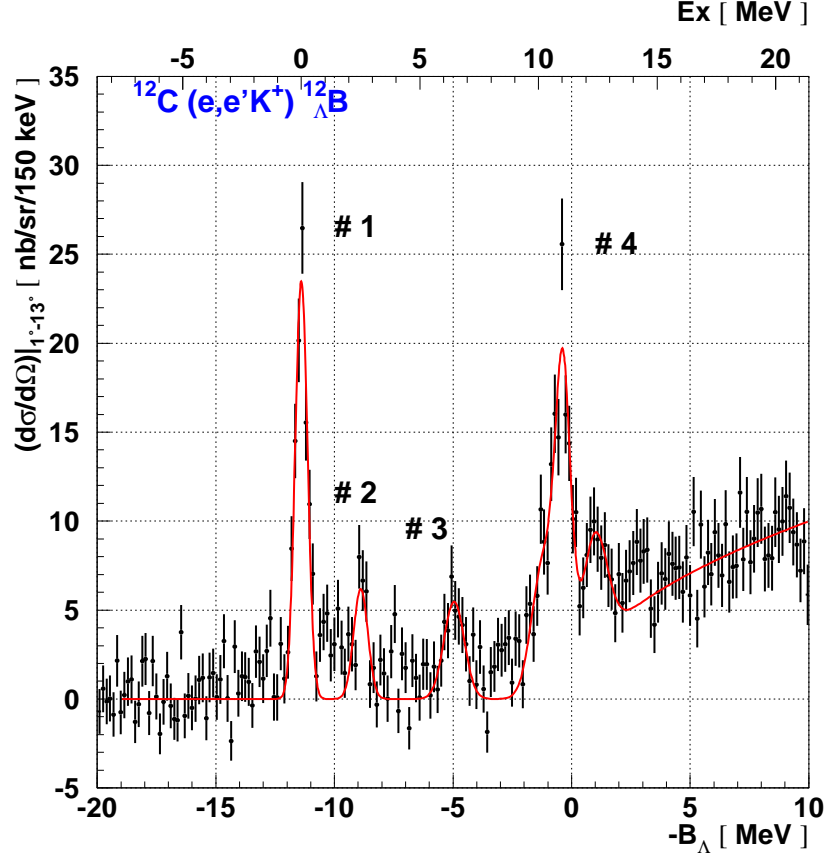


Figure 5.14: Missing mass spectrum for $^{12}_{\Lambda}\text{B}$. The accidental background is estimated by the mixed event analysis. The vertical axis represents the differential cross section

Comparison with other $^{12}_{\Lambda}\text{B}$ data

The observed $^{12}_{\Lambda}\text{B}$ can be compared with other experimental results: one is the first generation hypernuclear spectroscopy experiment at JLab Hall C (E89-009, 2000) [25, 26], as shown in Fig. 5.16, and another is the hypernuclear spectroscopy experiment performed at JLab Hall A (E94-107, 2004) [65], as shown in Fig. 5.17. It should be noted that cross sections cannot be compared directly because the kinematics of those experiments is not the same (Tab. 5.8). The measured excitation energies, binding energies and widths of the two major peaks are summarized in Tab. 5.9.

The obtained binding energy of $-11.40 \pm 0.01 \pm 0.14$ MeV for the ground state in the present study is in good agreement with the E89-009 result of -11.52 ± 0.35 MeV. The excitation energy of the p_{Λ} peak which corresponds to the energy spacing between the s_{Λ} and p_{Λ} states in the present study agrees with the E94-107 result within the error. On the other hand, the width ratio of $\Gamma_{s_{\Lambda}}/\Gamma_{p_{\Lambda}}=0.61/0.87=0.70$ of E01-011 is inconsistent with $\Gamma_{s_{\Lambda}}/\Gamma_{p_{\Lambda}}=1.15/0.67=1.72$ of E94-107. The E94-104 collaboration suggested that this width is attributed to an unresolved spin-doublet

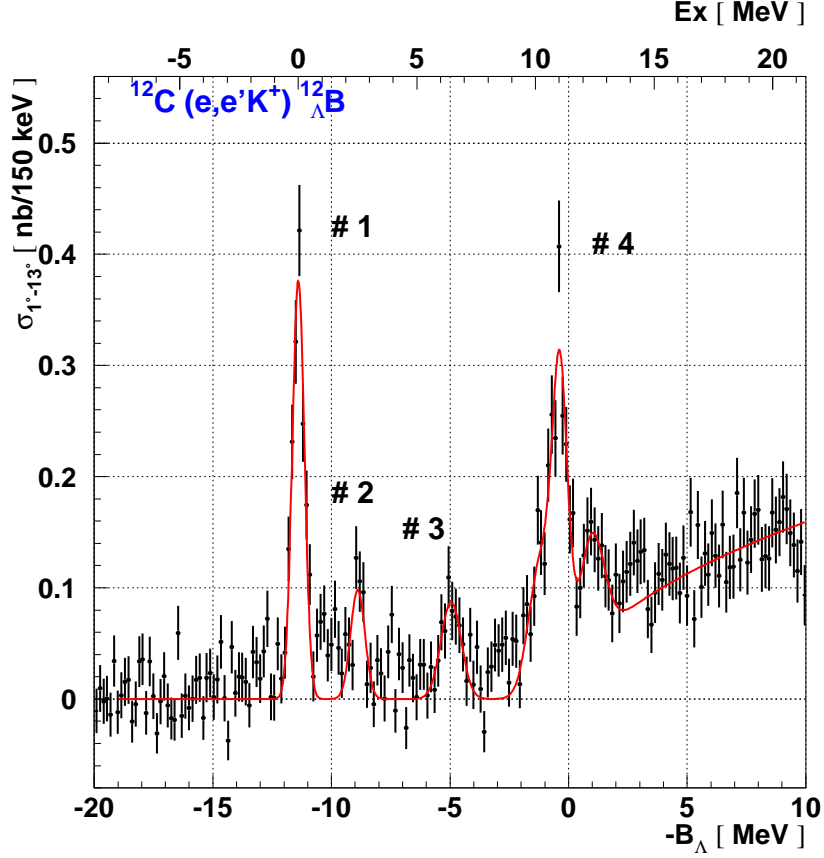


Figure 5.15: Missing mass spectrum for $^{12}_{\Lambda}\text{B}$. The accidental background is estimated by the mixed event analysis. The vertical axis represents the total cross section .

splitting or other unknown structures close to the ground state [65]. Recently, the level space of the ground state doublet of $^{12}_{\Lambda}\text{C}$ was measured by γ -ray spectroscopy to be 163 keV [66]. Assuming the charge symmetry breaking effect is small, the result of the present study is consistent with the result of the γ -ray measurement.

Experiment	E89-009	E94-107	E01-011
Year	2000	2004, 2005	2005
E_{γ} [MeV]	1.5	2.2	1.5
Q^2 [GeV^2]	0.01	0.07	0.01
E_e [GeV]	1.86/1.72	4.02/3.78/3.66	1.85
$P_{e'}$ [GeV/c]	0.28	1.8/1.57/1.44	0.32
$\theta_{e'}$ [degree]	0.0	6.0	4.5
P_{K^+} [GeV/c]	1.2	1.96	1.2
θ_{K^+} [degree]	0.0	6.0	7.0

Table 5.8: Kinematic comparison between hypernuclear spectroscopy experiments at JLab.

Experiment	s_Λ		p_Λ	
	$Ex(-B_\Lambda)$ [MeV] \pm (stat.) \pm (sys.)	Width [MeV] \pm (stat.)	$Ex(-B_\Lambda)$ [MeV] \pm (stat.) \pm (sys.)	Width [MeV] \pm (stat.)
E01-011	0 ($-11.40 \pm 0.01 \pm 0.14$)	0.61 ± 0.05	$11.05 \pm 0.01 \pm 0.19$ ($-0.41 \pm 0.01 \pm 0.13$)	0.87 ± 0.13
E89-009 [25, 26, 67]	0 (-11.52 ± 0.35)	0.75	(-0.49 ± 0.16)	N/A
E94-107 [65]	0	1.15 ± 0.18	10.93 ± 0.03	0.67 ± 0.15

Table 5.9: Comparison of excitation energies and widths of ${}^{12}_\Lambda\text{B}$.

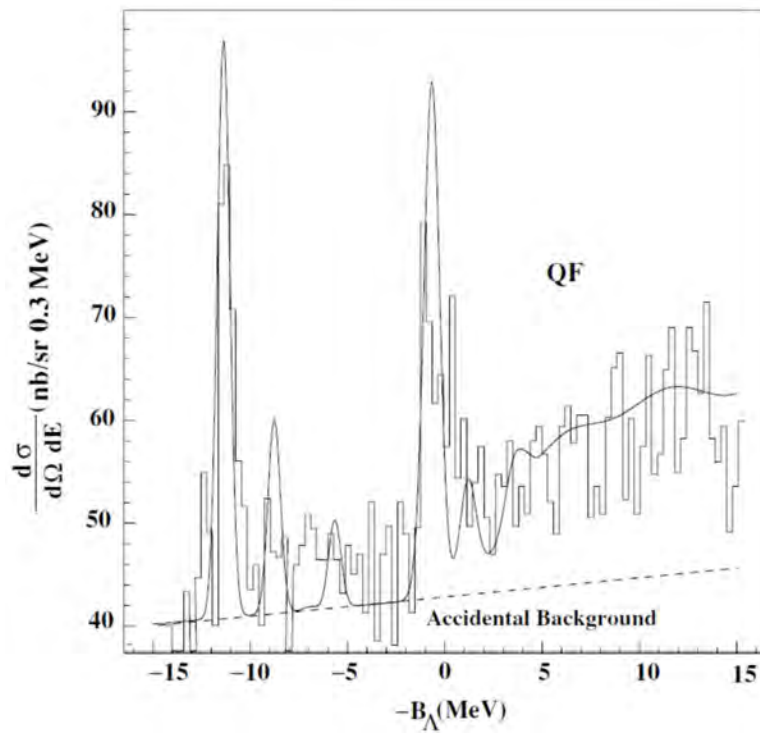


Figure 5.16: Missing mass spectrum for ${}^{12}_\Lambda\text{B}$ obtained in E89-009 experiment [26].

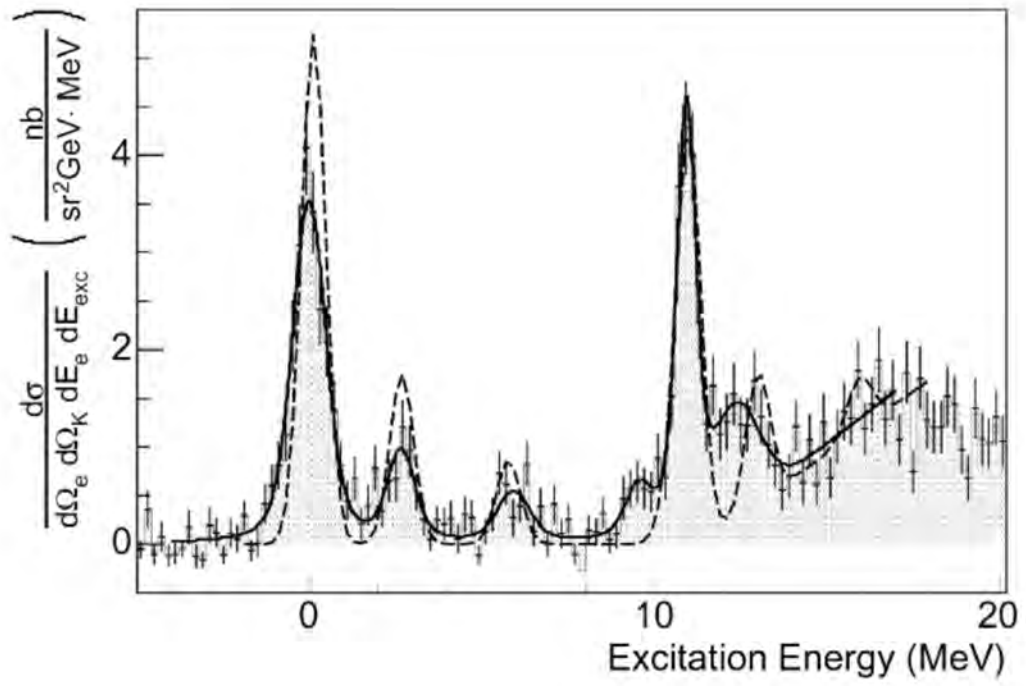


Figure 5.17: Missing mass spectrum for $^{12}_{\Lambda}\text{B}$ obtained in E94-107 experiment [65].

Comparison with mirror symmetric ${}^{12}_{\Lambda}\text{C}$ data

The obtained ${}^{12}_{\Lambda}\text{B}$ spectrum can be compared with a mirror symmetric ${}^{12}_{\Lambda}\text{C}$ spectrum measured by the (π^+, K^+) reaction (KEK E336) [3, 22]. The measured ${}^{12}_{\Lambda}\text{C}$ spectrum is shown in Fig. 5.18 and the obtained excitation energies and cross sections are summarized in Tab. 5.10. Two major peaks assigned as #1 and #4 in Fig. 5.18 can be interpreted as having the configuration of one neutron-hole and one Λ particle in the s or p orbits. The energy spacing of 11.00 ± 0.03 MeV between these two peaks can be compared with the $11.05 \pm 0.01 \pm 0.19$ MeV spacing of ${}^{12}_{\Lambda}\text{B}$. The energy difference of this spacing (0.05 MeV) is smaller than that of theoretical calculation of 0.77 MeV which is evaluated by a weighted average of p_{Λ} states [40, 68]. The level schemes of ${}^{12}_{\Lambda}\text{B}$, ${}^{12}_{\Lambda}\text{C}$ and their core nuclei as well as their theoretical calculations are shown in Fig. 5.19.

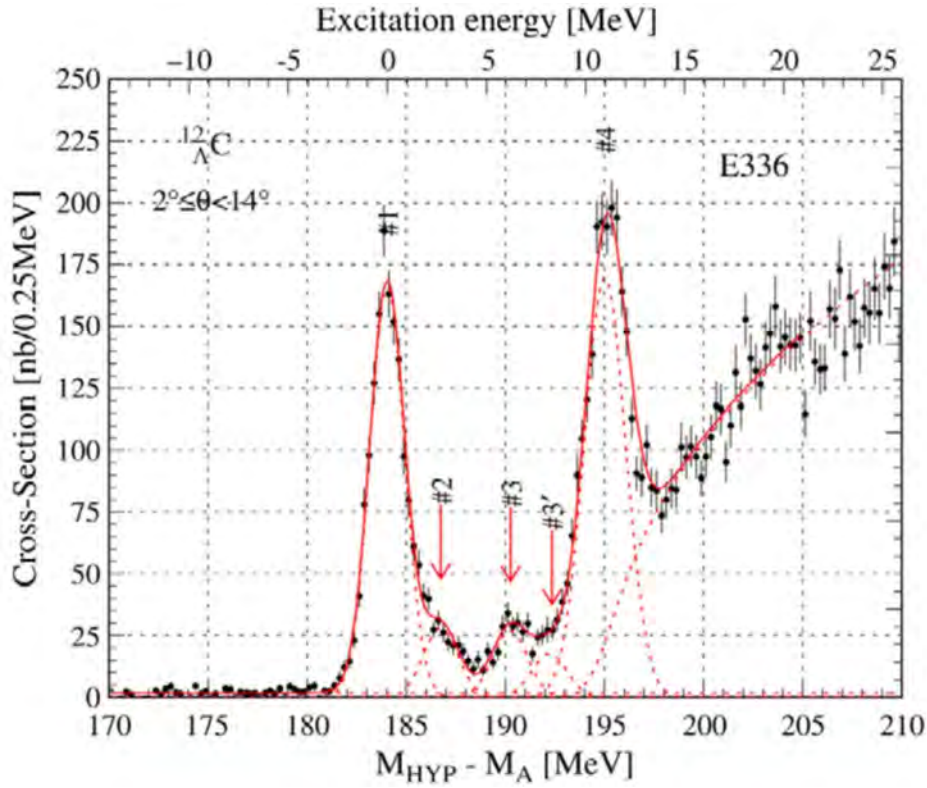


Figure 5.18: Missing mass spectrum of ${}^{12}_{\Lambda}\text{C}$ spectrum by (π^+, K^+) reaction [3, 22].

Peaks	B_Λ or Ex [MeV]	Width (FWHM) [MeV]	Cross sections $\sigma_{2^\circ-14^\circ}$ [μb]
#1	$B_\Lambda=10.80$ (fixed)	1.97 ± 0.03	1.44 ± 0.03
#2	$Ex=2.63 \pm 0.06$	1.97 ± 0.03	0.24 ± 0.02
#3	$Ex=6.09 \pm 0.08$	1.97 ± 0.03	0.23 ± 0.02
#3'	$Ex=8.12 \pm 0.17$	1.97 ± 0.03	0.18 ± 0.02
#4	$Ex=11.00 \pm 0.03$	2.39 ± 0.06	1.81 ± 0.02

Table 5.10: Excitation energies and cross sections of ${}^{12}_\Lambda\text{C}$ [3, 22].

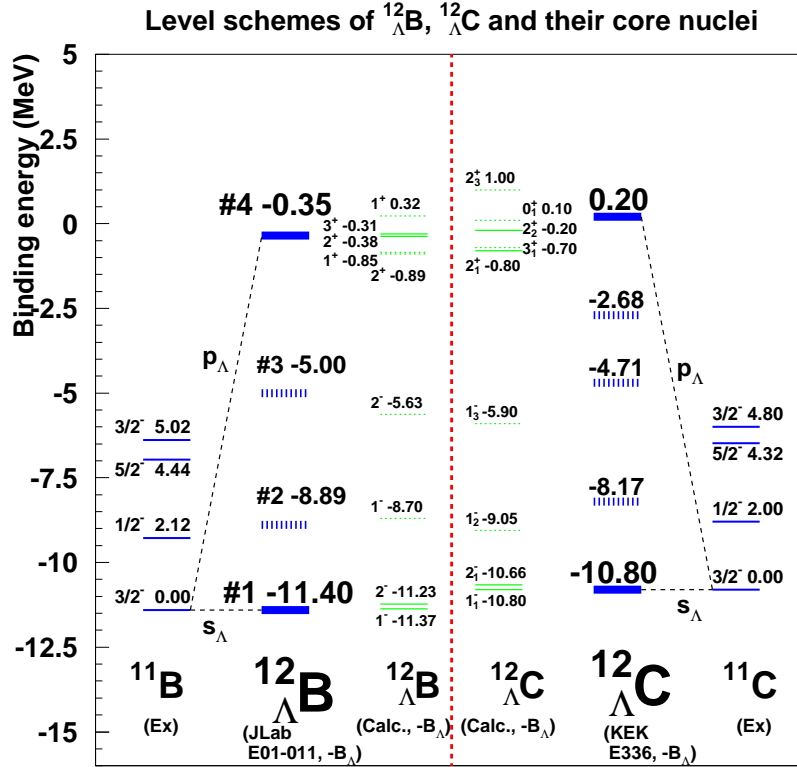


Figure 5.19: Level scheme of ${}^{12}_\Lambda\text{B}$, ${}^{12}_\Lambda\text{C}$ and their core nuclei. The binding energies of ground states for theoretical calculation are adjusted to the emulsion data.

Comparison with theoretical calculations

The production and structure of p -shell Λ hypernuclei were investigated by Itonaga *et al.* [68, 69] with configuration-mixed shell model wave functions which were obtained based on the experimental data from (K^-, π^-) and (π^+, K^+) reactions. They calculated the hypernuclear properties by diagonalizing the Hamiltonian:

$$H = H_N^{(\text{Cohen-Kurath})} + t_\Lambda + \xi \mathbf{l}_\Lambda \cdot \mathbf{s}_\Lambda + \sum_N v_{\Lambda N}, \quad (5.4)$$

where t_Λ is the kinetic energy of a Λ hyperon, $\xi \mathbf{l}_\Lambda \cdot \mathbf{s}_\Lambda$ is the Λ spin-orbit po-

tential, and $v_{\Lambda N}$ is the ΛN interaction. The Cohen-Kurath shell-model Hamiltonian ($H_N^{(\text{Cohen-Kurath})}$) and its wave function [70, 71] are applied to the core-nucleus since spectroscopic factors of the p -shell nuclei are generally well reproduced by the Cohen-Kurath's shell model calculation [71, 72].

For the interaction part, the YNG interaction [73] deduced on the basis of the G-matrix calculation with the Nijmegen soft core model (NSC97f) [74] interaction is used.

The experimental results were compared with theoretical predictions by Sotona *et al.* [40]. They used the DWIA formalism adopting two kinds of elementary production models : Saclay-Lyon A (SLA) [75] and Kaon-MAID (KMAID) [76]. The KMAID model includes four nucleon and two kaon resonances as intermediate state in resonance terms of s-channel and t-channel. The SLA model excludes the nucleon resonances with spin 1/2 and 5/2 and includes one nucleon resonance in s-channel, two kaon resonances in t-channel and four hyperon resonances in u-channel. Cross sections for the virtual photon energies of $1.3 < E_\gamma < 1.6$ GeV and the kaon scattering angle of $1^\circ < \theta_{K^+}^{Lab.} < 13^\circ$, which correspond to the present experimental conditions with a beam energy of $E_\gamma = 1.8$ GeV, are averaged for each theoretical calculation. The results of this study and theoretical predictions are summarized in Tab. 5.11. In Fig. 5.20, the theoretical calculation is overlaid.

For the cross section, the prediction based on the SLA model is preferable for the ground state. As for the p_Λ state, the experimental result agrees with predictions by both models.

	Experimental results		Theoretical prediction			
peak no.	Ex [MeV]	$(d\sigma/d\Omega) _{1^\circ-13^\circ}$ [nb/sr]	J^π	Ex [MeV]	$(d\sigma/d\Omega) _{1^\circ-13^\circ}$ [nb/sr]	
					SLA	KMAID
# 1	0.0	$101 \pm 4.2^{+38}_{-31}$	1 ⁻	0	19.7	20.7
			2 ⁻	0.14	65.7	43.0
# 4	$11.05 \pm 0.01 \pm 0.19$	$94 \pm 4.0^{+35}_{-35}$	2 ⁺	10.99	48.3	38.0
			3 ⁺	11.06	75.3	68.5

Table 5.11: Comparison of obtained excitation energies and cross sections with theoretical calculations for $^{12}_\Lambda\text{B}$ for the virtual photon energies of $1.3 < E_\gamma < 1.6$ GeV corresponding to the present experiment.

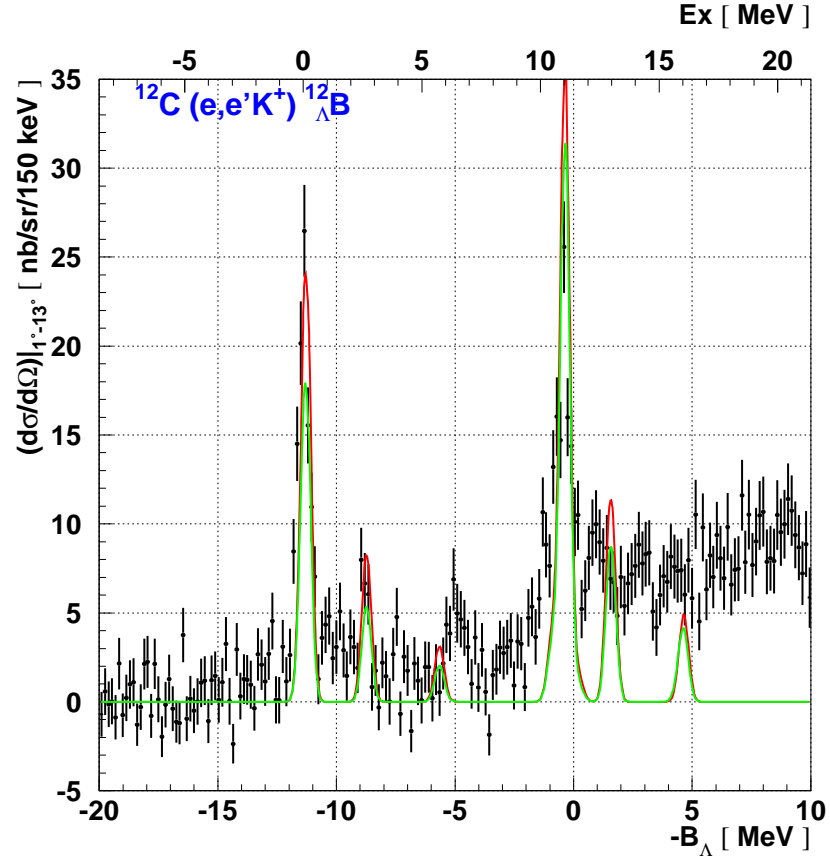


Figure 5.20: Missing mass spectrum of $^{12}_{\Lambda}\text{B}$ with theoretical calculations. Red and green curves represent calculations based on the SLA and KMAID models, respectively, with an energy resolution of 470 keV (FWHM).

5.3.2 Spectroscopy of $^{28}_{\Lambda}\text{Al}$

Results

The first sd -shell hypernuclear spectroscopy experiment by the $(e, e'K^+)$ reaction was successfully performed on the isotopically enriched ^{28}Si target thanks to the tilt method. Three major peaks which can be interpreted as $[(d_{5/2})_p^{-1}(s_{1/2})_{\Lambda}]$, $[(d_{5/2})_p^{-1}(p_{3/2}, p_{1/2})_{\Lambda}]$ and $[(d_{5/2})_p^{-1}(d_{5/2}, d_{3/2})_{\Lambda}]$ states are observed in the mass spectrum of $^{28}_{\Lambda}\text{Al}$. Similar to the $^{12}_{\Lambda}\text{B}$ case, each peak was fitted by a Gaussian after subtracting accidental background (Fig. 5.21 and Fig. 5.22). Fitting results are summarized in Tab. 5.12 and Tab. 5.13.

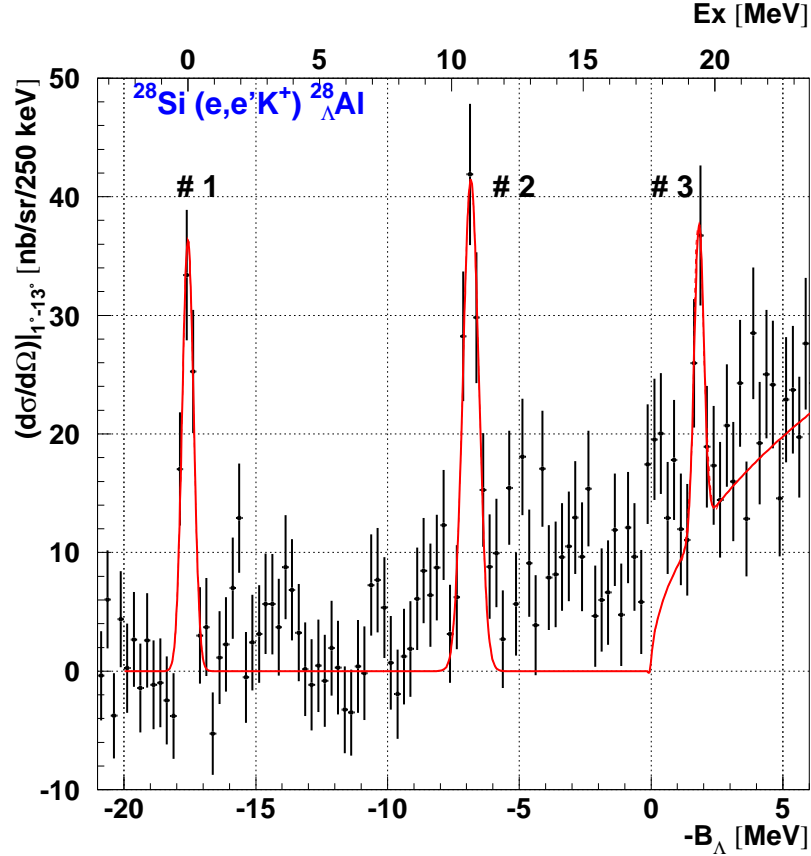


Figure 5.21: Missing mass spectrum for $^{28}_{\Lambda}\text{Al}$. The vertical axis represents the differential cross section.

Comparison with mirror symmetric $^{28}_{\Lambda}\text{Si}$ data

The obtained $^{28}_{\Lambda}\text{Al}$ spectrum can be compared with a mirror symmetric $^{28}_{\Lambda}\text{Si}$ spectrum measured by the (π^+, K^+) reaction on a natural silicon target (^{28}Si : 92.2%, ^{29}Si : 4.7%, ^{30}Si : 3.1%) (KEK E140a) [3, 21]. The measured $^{28}_{\Lambda}\text{Si}$ spectrum is shown in Fig. 5.23 and the excitation energies and cross sections are summarized in Tab. 5.14. The three major peaks, assigned as #1 #3 and #5 in Fig. 5.23, can be

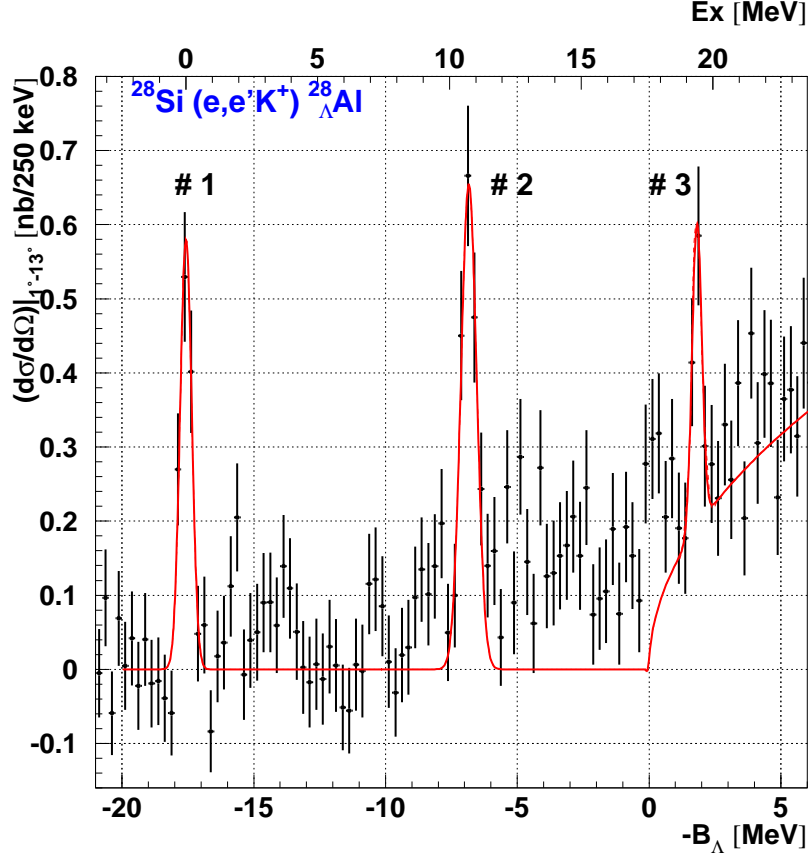


Figure 5.22: Missing mass spectrum for $^{28}_{\Lambda}\text{Al}$. The vertical axis represents the total cross section.

Peak No.	$-B_{\Lambda}$ [MeV] \pm (stat.) \pm (sys.)	Ex [MeV] \pm (stat.) \pm (sys.)	FWHM [MeV]
# 1	$-17.57 \pm 0.02 \pm 0.24$	0	0.52 ± 0.07
# 2	$-6.84 \pm 0.02 \pm 0.22$	$10.73 \pm 0.02 \pm 0.33$	0.70 ± 0.09
# 3	$1.82 \pm 0.03 \pm 0.31$	$19.39 \pm 0.03 \pm 0.39$	0.43 ± 0.13

Table 5.12: Obtained binding energies and widths for $^{28}_{\Lambda}\text{Al}$ spectrum.

interpreted as having configurations of $[(d_{5/2})_n^{-1}(s_{1/2})_{\Lambda}]$, $[(d_{5/2})_n^{-1}(p_{3/2}, p_{1/2})_{\Lambda}]$ and $[(d_{5/2})_n^{-1}(d_{5/2}, d_{3/2})_{\Lambda}]$, respectively. The level scheme of $^{28}_{\Lambda}\text{Al}$, $^{28}_{\Lambda}\text{Si}$ and their core nuclei are presented with their theoretical calculations in Fig. 5.24.

The binding energy of $^{28}_{\Lambda}\text{Al}$ ground state ($-17.57 \pm 0.02 \pm 0.24$ MeV) is 1.0 MeV deeper than that of $^{28}_{\Lambda}\text{Si}$ (16.6 ± 0.2 MeV). The energy spacing between the s_{Λ} and p_{Λ} states of $^{28}_{\Lambda}\text{Al}$ is $10.73 \pm 0.02 \pm 0.33$ MeV, which is 1.1 MeV wider than that of $^{28}_{\Lambda}\text{Si}$. While the energy spacing between the p_{Λ} states and d_{Λ} of $^{28}_{\Lambda}\text{Al}$ is $8.66 \pm 0.03 \pm 0.39$ MeV, which is consistent with that of $^{28}_{\Lambda}\text{Si}$, 8.1 ± 0.8 MeV within error, the

Peak No.	$(d\sigma/d\Omega) _{1^\circ-13^\circ}$ [nb/sr] \pm (stat.) \pm (sys.)	$\sigma_{1^\circ-13^\circ}$ [nb] \pm (stat.) \pm (sys.)
# 1	$79 \pm 5.7^{+30}_{-37}$	$1.28 \pm 0.09^{+0.48}_{-0.59}$
# 2	$125 \pm 7.5^{+47}_{-58}$	$1.96 \pm 0.12^{+0.74}_{-0.91}$
# 3	$47 \pm 6.4^{+18}_{-44}$	$0.76 \pm 0.10^{+0.29}_{-0.71}$

Table 5.13: Obtained cross sections for $^{28}_{\Lambda}\text{Al}$ spectrum. The details of systematic errors are described in Sec. 4.10.

ground state of $^{28}_{\Lambda}\text{Al}$ is bound deeper than that of $^{28}_{\Lambda}\text{Si}$.

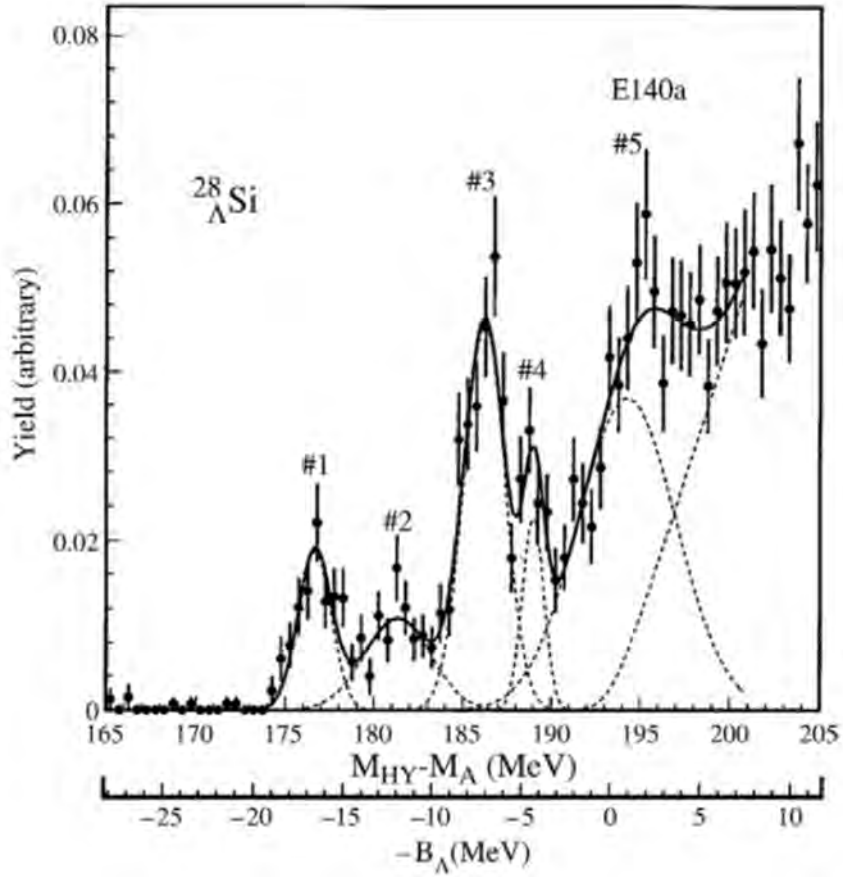


Figure 5.23: Missing mass spectrum of $^{28}_{\Lambda}\text{Si}$ spectrum by (π^+, K^+) reaction [3, 21].

Comparison with theoretical calculations

Recently, a new theoretical calculation based on the shell model was performed for $^{28}_{\Lambda}\text{Al}$ by Motoba and Sotona [37, 40]. They used sophisticated wave functions solved in the $(0d_{5/2}0d_{3/2}1s_{1/2})^{11,12}_{pn}$ full space for $^{27,28}\text{Si}$ in order to calculate the

Peaks	B_Λ or Ex [MeV]	Width (FWHM) [MeV]	Relative yield (arbitrary)
#1	$B_\Lambda=16.6 \pm 0.2$	2.2 (fixed)	0.09 ± 0.01
#2	$Ex=4.7 \pm 0.4$	4.4 ± 1.0	0.10 ± 0.04
#3	$Ex=9.6 \pm 0.2$	2.7 ± 0.3	0.27 ± 0.05
#4	$Ex=12.4 \pm 0.2$	1.4 ± 0.4	0.07 ± 0.04
#5	$Ex=17.7 \pm 0.8$	6.5 ± 1.1	0.51 ± 0.16

Table 5.14: Excitation energies and cross sections of $^{28}_\Lambda\text{Si}$ [3, 22].

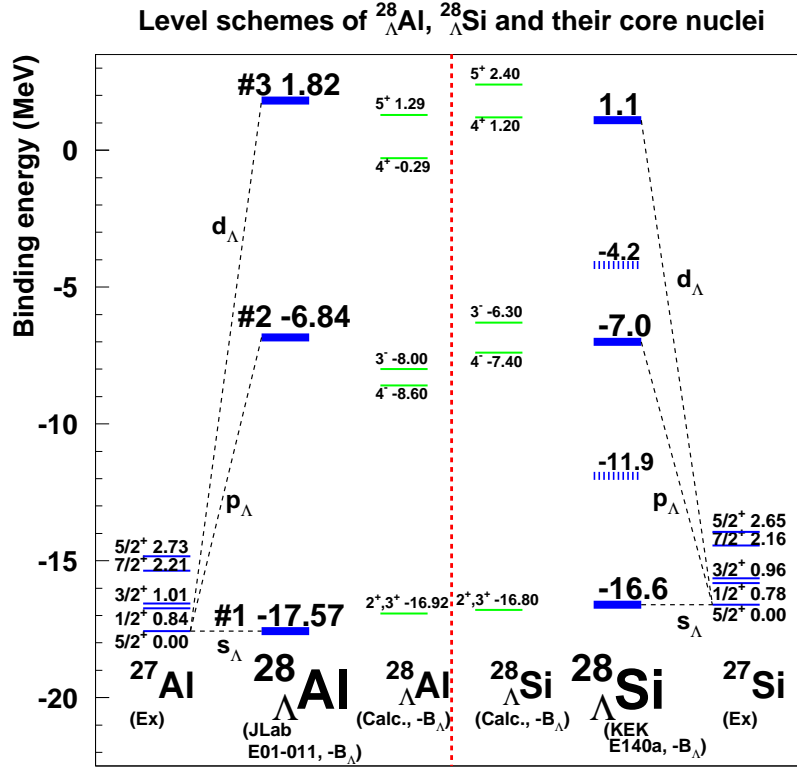


Figure 5.24: Level scheme of $^{28}_\Lambda\text{Al}$, $^{28}_\Lambda\text{Si}$ and their core nuclei.

proton pickup spectroscopic amplitudes. By making use of these values, the cross sections for the $^{28}_\Lambda\text{Si}(\gamma, K^+)^{28}_\Lambda\text{Al}$ reaction were evaluated in DWIA. The kaon distorted partial waves were obtained by solving the Klein-Gordon equation with the optical potential which is proportional to the density distribution of ^{28}Si . They applied the YNG interaction derived from Nijmegen model-D [4]. Figure 5.25 shows the theoretical calculation of $^{28}_\Lambda\text{Al}$ adopting SLA amplitude at $E_\gamma = 1.3$ GeV and $\theta_{K^+} = 3^\circ$, assuming the energy resolution is 0.3 MeV.

The obtained experimental results and theoretical calculations are summarized in Tab. 5.15. Similar to $^{12}_\Lambda\text{B}$, the calculated cross sections were averaged over the experimental conditions. The theoretical calculations are superimposed on the ex-

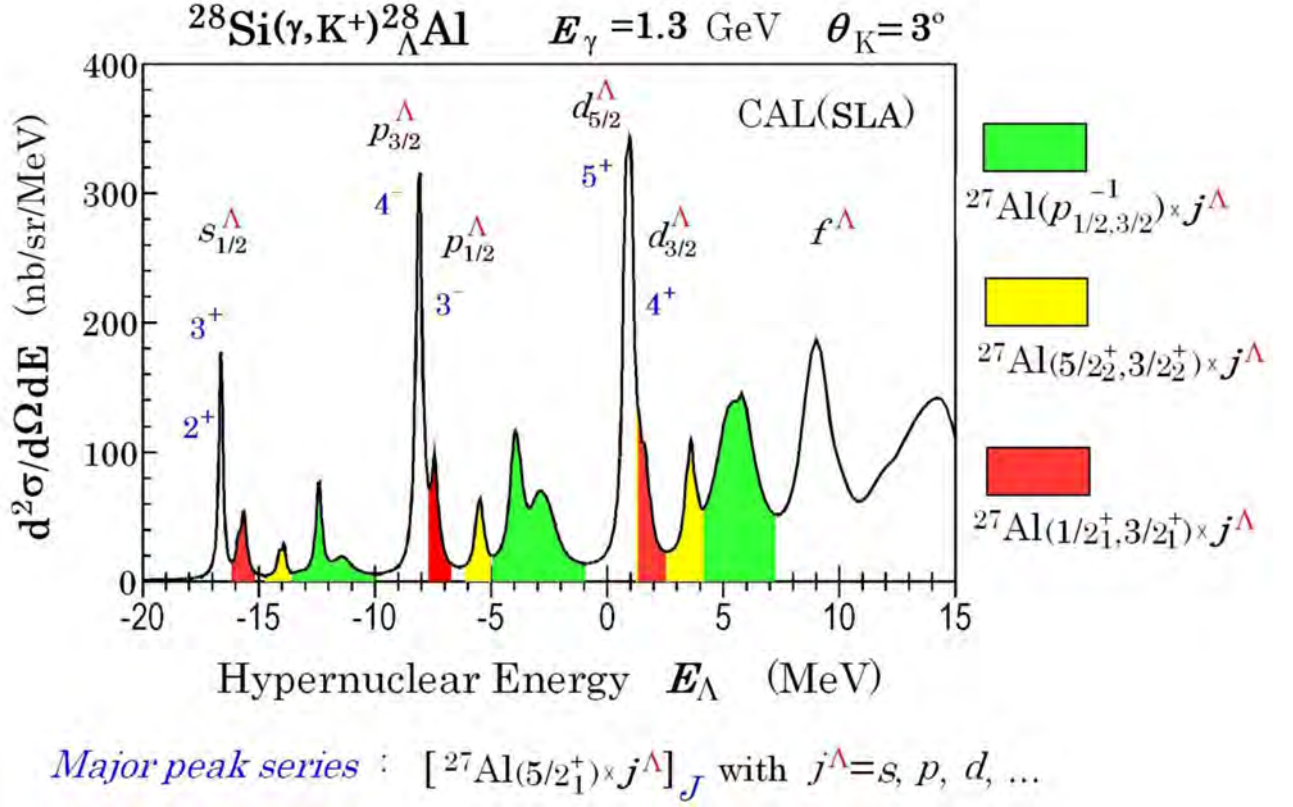


Figure 5.25: Shell model calculation of $^{28}_{\Lambda}\text{Al}$ with DWIA adopting SLA amplitude at $E_{\gamma} = 1.3 \text{ GeV}$ and $\theta_{K^+} = 3^{\circ}$ [37]. The energy resolution is assumed as 0.3 MeV (FWHM).

perimental results (Fig. 5.26). The excitation energy of the p_{Λ} state ($10.73 \pm 0.02 \pm 0.33 \text{ MeV}$) is about 2.2 MeV higher than the weighted average (8.56 MeV) of calculated ones for 4^- and 3^- states. On the other hand, the obtained energy spacing between p_{Λ} and d_{Λ} states ($8.66 \pm 0.03 \pm 0.39 \text{ MeV}$) is consistent with the calculation (8.84 MeV) within error. For cross sections, experimental results tend to be smaller than the calculation. Especially, the cross section of the d_{Λ} state is much smaller than the calculation though the peak significance is not enough to draw a quantitative conclusion.

The reason for the deeper s_{Λ} bound state of $^{28}_{\Lambda}\text{Al}$ than $^{28}_{\Lambda}\text{Si}$ is not understood so far. It seems that a similar tendency is seen in $^{12}_{\Lambda}\text{B}$ and $^{12}_{\Lambda}\text{C}$; the B_{Λ} value of $^{12}_{\Lambda}\text{B}$ s_{Λ} state is 0.6 MeV larger than that of $^{12}_{\Lambda}\text{C}$. Systematic studies of various Λ hypernuclei in a wide mass region is necessary.

peak no.	Experimental results		Theoretical prediction			
	Ex [MeV]	$(d\sigma/d\Omega) _{1^\circ-13^\circ}$ [nb/sr]	J^π	Ex [MeV]	$(d\sigma/d\Omega) _{1^\circ-13^\circ}$ [nb/sr]	
					SLA	KMAID
# 1	0.0	$79 \pm 5.7 \begin{smallmatrix} +30 \\ -37 \end{smallmatrix}$	$2^+, 3^+$	0	92.1	71.76
# 2	$10.73 \pm 0.02 \pm 0.33$	$125 \pm 7.5 \begin{smallmatrix} +47 \\ -58 \end{smallmatrix}$	4^-	8.32	134.9	117.5
			3^-	8.92	91.3	58.5
# 3	$19.39 \pm 0.03 \pm 0.39$	$47 \pm 6.4 \begin{smallmatrix} +18 \\ -44 \end{smallmatrix}$	5^+	16.63	148.4	135.1
			4^+	18.21	139.1	89.9

Table 5.15: Comparison of obtained excitation energies and cross sections with theoretical calculations for $^{28}_{\Lambda}\text{Al}$ for the virtual photon energies of $1.3 < E_\gamma < 1.6$ GeV corresponding to the present experiment.

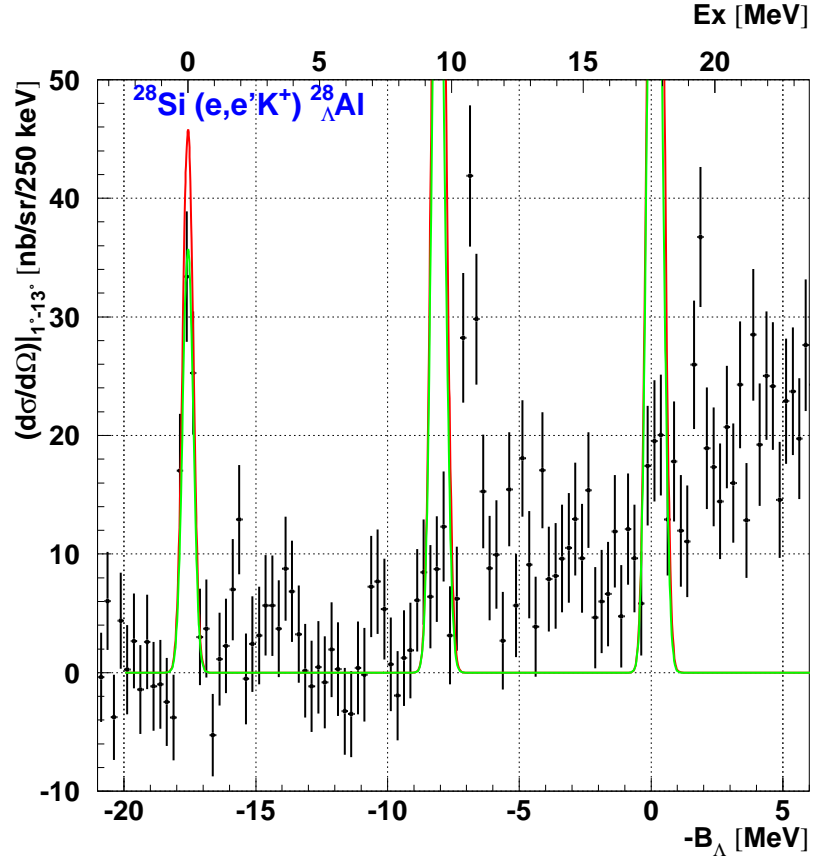


Figure 5.26: Missing mass spectrum of $^{28}_{\Lambda}\text{Al}$ with theoretical calculations. Red and green curves represent calculations based on the SLA and KMAID models, respectively, with an energy resolution of 470 keV (FWHM).

5.3.3 Spectroscopy of ${}^7_{\Lambda}\text{He}$

Results

${}^7_{\Lambda}\text{He}$ is one of the neutron-rich hypernuclei which are suitable to be studied by the $(e, e'K^+)$ reaction since a proton is converted into a Λ hyperon in this reaction. The binding energy of this hypernucleus has been studied from the emulsion data by Juric *et al.* in 1970s [31]. However, they could not obtain a reliable binding energy of the ${}^7_{\Lambda}\text{He}$ ground state due to insufficient statistics (Fig. 5.27). The first generation hypernuclear spectroscopy experiment, E89-009, also studied this hypernucleus [26]. Although a bump structure at $-B_{\Lambda}=7$ MeV was reported, the ground state peak was not observed.

In the E01-011 experiment, the first ${}^7_{\Lambda}\text{He}$ spectroscopy experiment with sufficient statistics was successfully performed. One major peak which is interpreted as $[(p_{1/2})_p^{-1}(s_{1/2})_{\Lambda}]$ state is observed. Similar to other hypernuclei, the binding energy and cross section were obtained by a Gaussian fitting after subtracting accidental background (Fig. 5.28 and Fig. 5.29). The experimental result is summarized in Tab. 5.16 and Tab. 5.17.

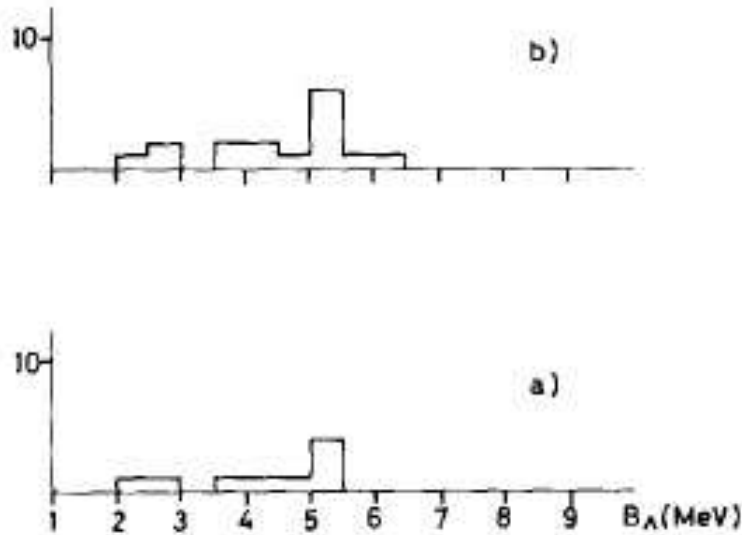


Figure 5.27: Emulsion data of ${}^7_{\Lambda}\text{He}$ [31]. The top figure represents all the world data. The experimental result in Juric's paper is shown in the bottom.

Peak No.	$-B_{\Lambda}$ [MeV] \pm (stat.) \pm (sys.)	Ex [MeV] \pm (stat.) \pm (sys.)	FWHM [MeV]
# 1	$-5.68 \pm 0.03 \pm 0.22$	0	0.63 ± 0.12

Table 5.16: Obtained binding energy and width for the ${}^7_{\Lambda}\text{He}$ spectrum.

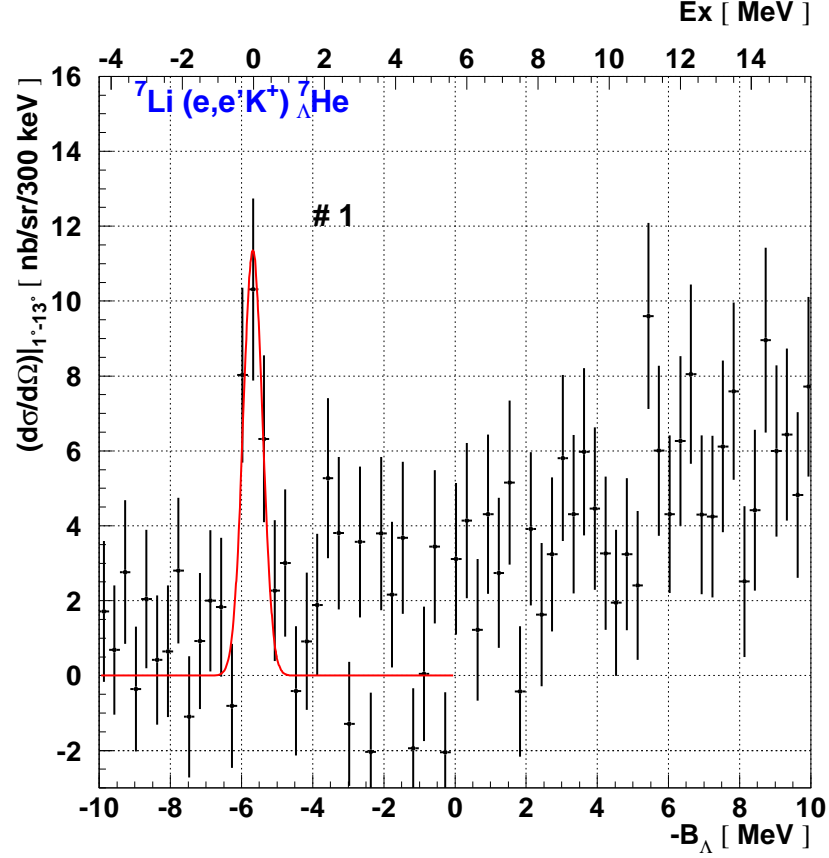


Figure 5.28: Missing mass spectrum for ${}^7_{\Lambda}\text{He}$. The vertical axis represents the differential cross section.

Peak No.	$(d\sigma/d\Omega) _{1^\circ-13^\circ}$ [nb/sr] \pm (stat.) \pm (sys.)	$\sigma_{1^\circ-13^\circ}$ [nb] \pm (stat.) \pm (sys.)
# 1	$26 \pm 2.7^{+9.9}_{-9.9}$	$0.40 \pm 0.04^{+0.15}_{-0.15}$

Table 5.17: Results of the fitting for ${}^7_{\Lambda}\text{He}$ spectrum. The definition of two kinds of systematic errors is described in Sec. 5.2.

Comparison with theoretical calculations

A charge symmetry breaking (CSB) effect in the hypernuclear systems of ${}^4_{\Lambda}\text{H}$ and ${}^4_{\Lambda}\text{He}$ has been studied by taking $\Lambda\text{N}-\Sigma\text{N}$ coupling into account [77]. Recently, the level structures of the $T = 1$ isotriplet hypernuclei with mass number $A = 7$ (${}^7_{\Lambda}\text{He}$, ${}^7_{\Lambda}\text{Li}$ and ${}^7_{\Lambda}\text{Be}$) were calculated by Hiyama *et al.* in an $\alpha + \Lambda + \text{N} + \text{N}$ four-body cluster model [78]. They introduce a phenomenological CSB interaction with a one range Gaussian form :

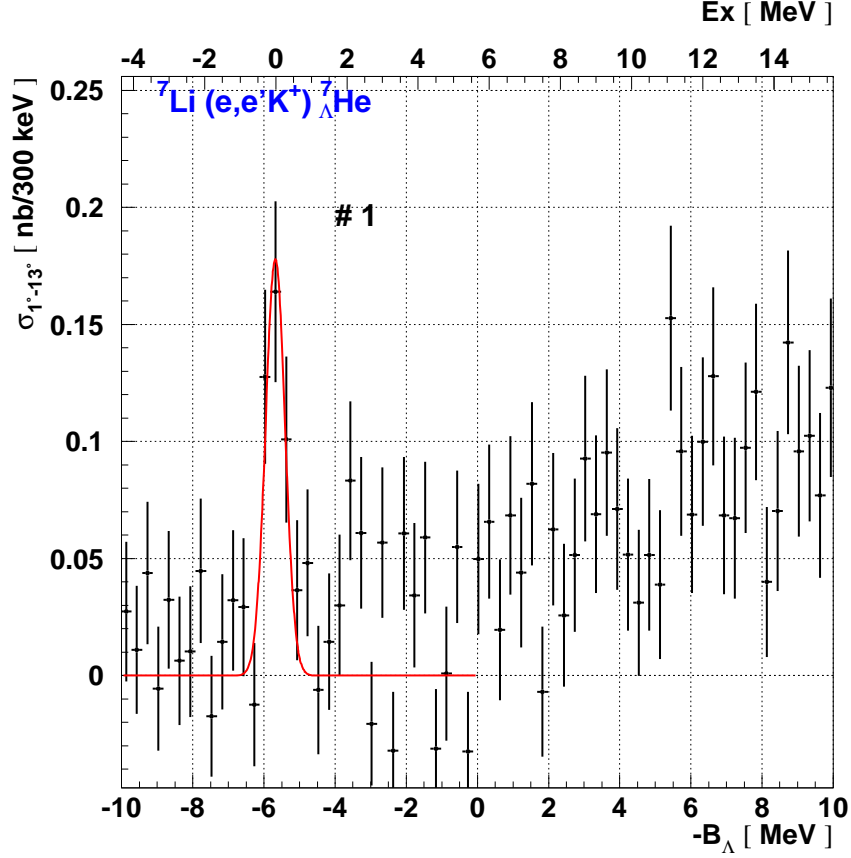


Figure 5.29: Missing mass spectrum for ${}^7_{\Lambda}\text{He}$. The vertical axis represents the total cross section.

$$\begin{aligned}
 V_{\Lambda N}^{\text{CSB}}(r) = & -\frac{\tau_z}{2} \left[\frac{1+P_r}{2} (v_0^{\text{even,CSB}} + \boldsymbol{\sigma}_{\Lambda} \cdot \boldsymbol{\sigma}_N v_{\sigma_{\Lambda} \cdot \sigma_N}^{\text{even,CSB}}) e^{-\beta_{\text{even}} r^2} \right. \\
 & \left. + \frac{1-P_r}{2} (v_0^{\text{odd,CSB}} + \boldsymbol{\sigma}_{\Lambda} \cdot \boldsymbol{\sigma}_N v_{\sigma_{\Lambda} \cdot \sigma_N}^{\text{odd,CSB}}) e^{-\beta_{\text{odd}} r^2} \right], \quad (5.5)
 \end{aligned}$$

which includes spin-independent and spin-spin parts. The parameters $v_0^{\text{even,CSB}}$ and $v_{\sigma_{\Lambda} \cdot \sigma_N}^{\text{even,CSB}}$ are determined phenomenologically so as to reproduce the measured ground state (0^+) and excited state (1^+) of ${}^4_{\Lambda}\text{H}$ and ${}^4_{\Lambda}\text{He}$. In the four-body calculation of ${}^4_{\Lambda}\text{H}$ and ${}^4_{\Lambda}\text{He}$, the effects of the odd-state interactions are found to be negligibly small and their strengths cannot be determined. Therefore, they took $v_0^{\text{odd,CSB}}=0$ and $v_{\sigma_{\Lambda} \cdot \sigma_N}^{\text{odd,CSB}}=0$.

The measured binding energy of $-5.68 \pm 0.03 \pm 0.22$ MeV for the ${}^7_{\Lambda}\text{He}$ ground state is bound deeper than the theoretical calculation of -5.36 MeV (Fig. 5.30), where the CSB effect is not included. On the other hand, the binding energy is calculated to be -5.16 MeV with the CSB effect, which is 0.52 MeV less bound than the

experimental result and inclusion of the CSB effect makes the discrepancy larger. As discussed above, the odd-state interaction is not included in this calculation. This experimental result will play an important role for further understanding of the CSB effect.

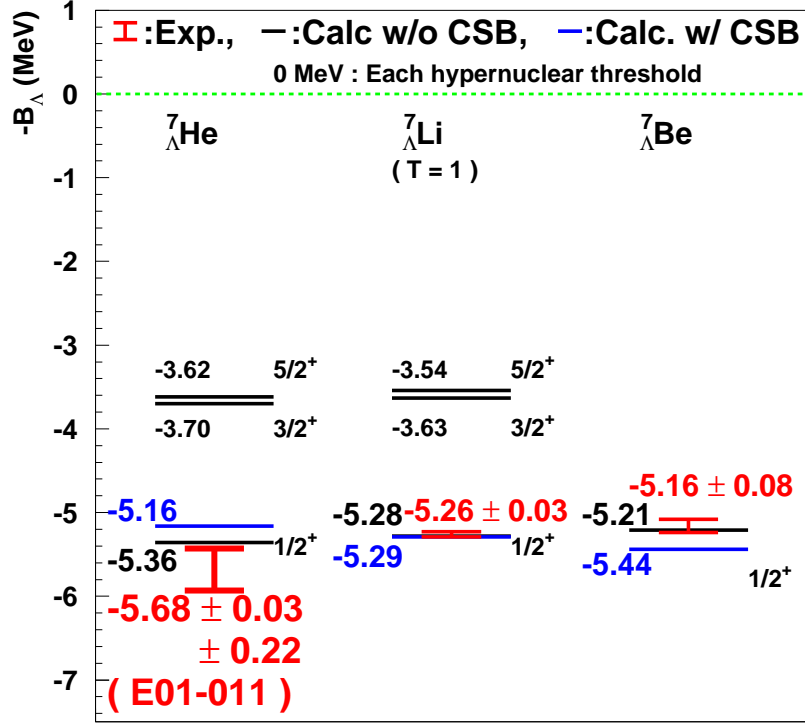


Figure 5.30: Comparison of the binding energy of ${}^7_{\Lambda}\text{He}$ with those of ${}^7_{\Lambda}\text{Li}(T=1)$ and ${}^7_{\Lambda}\text{Be}$.

The cross section of the ${}^7_{\Lambda}\text{He}$ ground state is calculated by Sotona *et al.* [40]. Similar to other hypernuclei, the cross section was averaged over the experimental acceptance. The experimental results and the theoretical calculations are summarized in Tab. 5.18. The theoretical calculations are superimposed on the experimental results (Fig. 5.32). The measured cross section of $26 \pm 2.7^{+9.9}_{-9.9}$ nb/sr tends to be larger than the calculation, although the systematic errors are large.

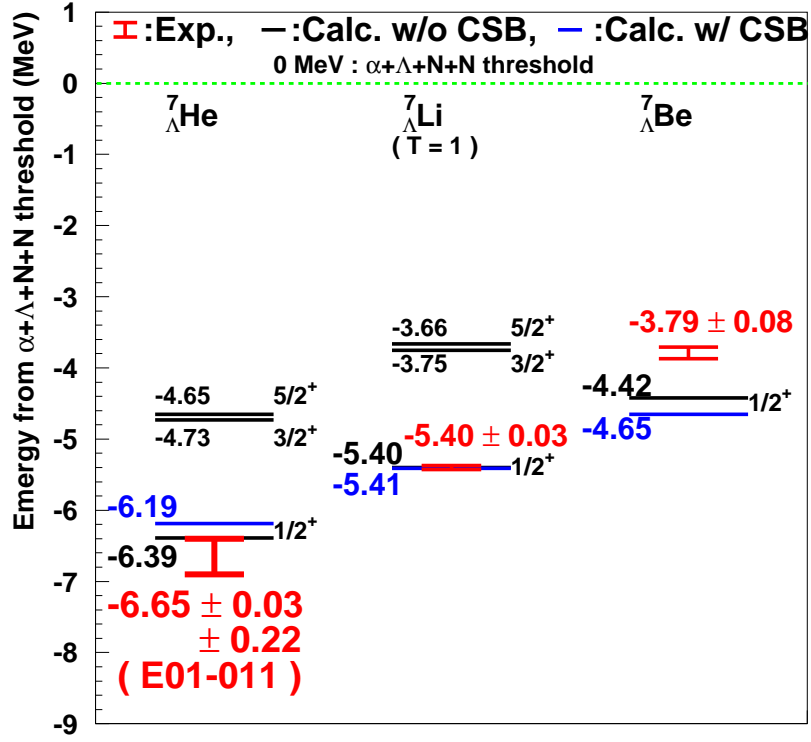


Figure 5.31: The same as Fig. 5.30 but plotted in the energy from $\alpha+\Lambda+N+N$.

	Experimental results		Theoretical prediction			
peak no.	-B $_{\Lambda}$ [MeV]	(d σ /d Ω) $_{1^{\circ}-13^{\circ}}$ [nb/sr]	J $^{\pi}$	-B $_{\Lambda}$ [MeV]	(d σ /d Ω) $_{1^{\circ}-13^{\circ}}$ [nb/sr]	
					SLA	KMAID
# 1	-5.68 \pm 0.03 \pm 0.22	26 \pm 2.7 $^{+9.9}_{-9.9}$	1/2 $^{+}$	-5.36 [78]	13.2	9.7

Table 5.18: Comparison of obtained excitation energies and cross sections with theoretical calculations for ${}^7_\Lambda\text{He}$ for the virtual photon energies of $1.3 < E_\gamma < 1.6$ GeV corresponding to the present experiment.

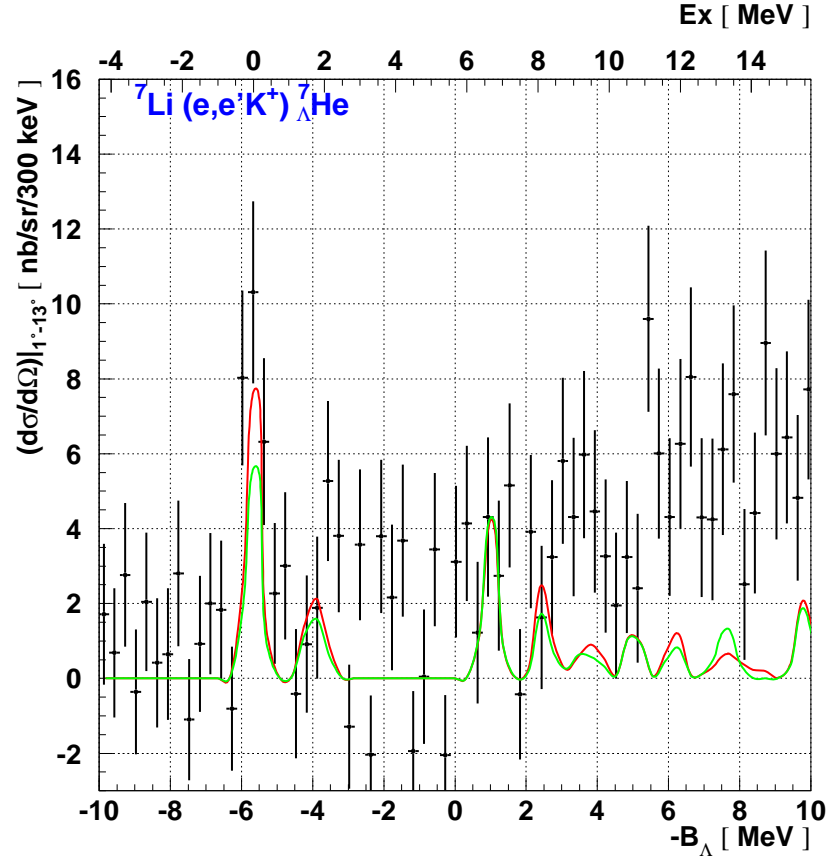


Figure 5.32: Missing mass spectrum of ${}^7_\Lambda\text{He}$ with theoretical calculations. Red and green curves represent calculations based on the SLA and KMAID models, respectively, with an energy resolution of 470 keV (FWHM).

Chapter 6

Summary and conclusion

The second generation hypernuclear spectroscopy using the $(e, e'K^+)$ reaction was successfully performed in JLab's Hall C in 2005. Both high statistics and high resolution were achieved thanks to new characteristic configurations of the experimental setup. 1) The High resolution Kaon Spectrometer (HKS) with a large acceptance was newly designed and constructed. 2) The detection angle of scattered electron was optimized and the scattered electron spectrometer was vertically tilted by 8 degrees to suppress background electrons (Tilt method). These new configurations allowed a high luminosity and data on various targets were successfully taken.

$p(e, e'K^+)\Lambda/\Sigma^0$ with CH_2 target

The transfer matrices of the two spectrometers were calibrated with the well-known masses of Λ and Σ^0 hyperons as both spectrometers had new optics features. By using masses of Λ , Σ^0 and detailed simulation data, the linearity and systematic errors of the above obtained binding energies and cross sections were evaluated.

$^{28}\text{Si}(e, e'K^+)_{\Lambda}^{28}\text{Al}$

With the $(e, e'K^+)$ reaction, the first sd -shell hypernucleus, $^{28}_{\Lambda}\text{Al}$, was successfully measured. Two prominent peaks were observed and interpreted as the states with a Λ hyperon bound in the s and p orbits. It was found that the ground state ($-B_{\Lambda} = -17.57 \pm 0.02 \pm 0.24$ MeV) is more deeply bound and the energy spacing between the s_{Λ} and p_{Λ} states is larger, compared to the mirror symmetric hypernucleus $^{28}_{\Lambda}\text{Si}$ and the shell model prediction. The current framework of hypernuclear theories cannot explain these differences quantitatively, though a similar tendency can be seen for the $^{12}_{\Lambda}\text{B}$ and $^{12}_{\Lambda}\text{C}$ ground states. Further investigation is necessary theoretically as well as experimentally. The success of $^{28}_{\Lambda}\text{Al}$ spectroscopy has opened a door to heavier hypernuclei with the $(e, e'K^+)$ reaction.

$^{12}\text{C}(e, e'K^+)_{\Lambda}^{12}\text{B}$

In the spectrum of $^{12}_{\Lambda}\text{B}$, two major peaks which are interpreted as the states with a Λ bound in s and p -orbits were observed. The obtained binding energies for the s_{Λ} state of $-11.40 \pm 0.01 \pm 0.14$ MeV and the energy spacing between the s_{Λ} and p_{Λ} states were in agreement with those obtained in our first generation experiment (E89-009), the Hall A experiment (E94-107) and the theoretical calculation with

DWIA. In the present study, the width of the s_Λ peak is narrower than that of the p_Λ peak, which does not agree with the result of E94-107 but is consistent with the γ -ray data that determined a small splitting of the ground state doublet of $^{12}_\Lambda\text{C}$. The obtained cross sections for these major peaks were consistent with the shell model calculations.

$^7\text{Li}(e, e'K^+)^7_\Lambda\text{He}$

A neutron-rich hypernucleus, $^7_\Lambda\text{He}$, was studied with sufficient statistics for the first time. The binding energy of the ground state was determined as $-B_\Lambda = -5.68 \pm 0.03 \pm 0.22$ MeV reliably. Recently, a charge symmetry breaking (CSB) effect was theoretically studied for the $A=7$, $T=1$ isotriplet Λ hypernuclei by a detailed four-body cluster model. The calculation, assuming a naive CSB interaction which was introduced to reproduce the $A=4$ hypernuclear masses, gives a smaller B_Λ value than the measured one. The present result provides new information on the charge symmetry breaking effect in the ΛN interaction.

Figure 6.1 summarizes the measured binding energies from this work and for other hypernuclei.

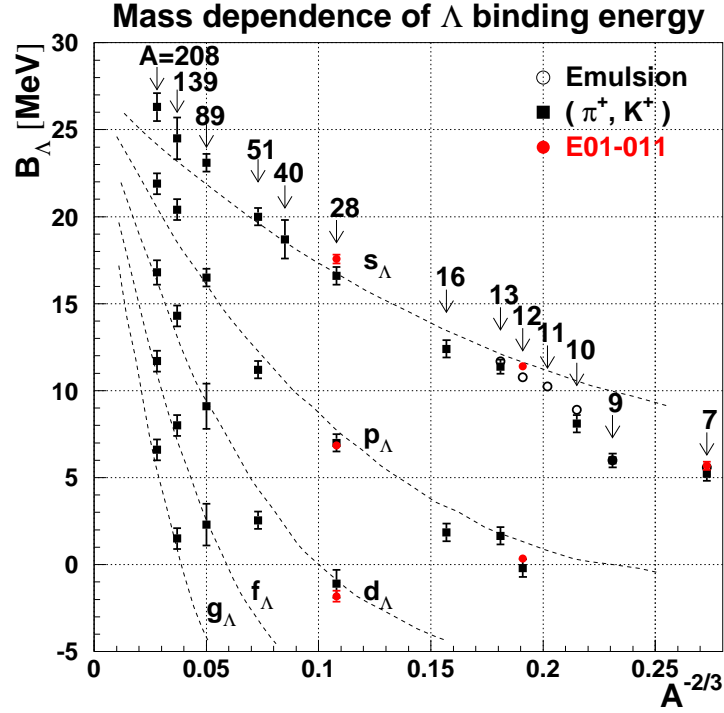


Figure 6.1: Updated Mass dependence of a Λ hyperon binding energy shown in Fig. 1.2. The results of a present study are plotted in red.

The present study firmly established the high quality $(e, e'K^+)$ hypernuclear spectroscopy developing new experimental techniques and elaborate analysis procedures. It is complementary to the spectroscopy with hadron beams such as pions

and kaons and has a great advantages of realizing Sub-MeV resolution and determining absolute hypernuclear binding energies. Together with the physics results summarized above, $(e, e'K^+)$ reaction spectroscopy will be a powerful tool for the systematic spectroscopic study of Λ hypernuclei with high precision in the future.

Acknowledgement

I would like to thank all members of the E01-011 collaboration and people in JLab for their great efforts to perform the present study.

I would like to express my sincere gratitude to Prof. O. Hashimoto for giving me an opportunity to participate this challenging experiment. A lot of advises and suggestions based on his wide experience helped me any time. I would like to express my sincere appreciation to Prof. Satoshi. N. Nakamura for the great support and encouragement. He always gave me an exact advise and guided me to complete this thesis. I am deeply grateful to Prof. H. Tamura who provide me not only the physics but also the experimental techniques. His lecture of the noise reduction was very helpful during the experiment. I would like to appreciate to Dr. Y. Fujii and Dr. T. Maruta for their worthful advises on the data analysis. I would like to thank Dr. T. Miyoshi and Prof. M. Sumihama for their great efforts to perform the experiment. I would like to appreciate Prof. T. Takahashi for his contribution to drift chamber R&D and development of the TUL system. I would like to thank Dr Y. Sato for his contribution based on his experience of the first generation hypernuclear spectroscopy experiment. I would like to express my deep gratitude to Prof. S. Kato who designed the HKS optics. I would like to express my appreciation to Prof. I. Sugai for the preparation of an enriched isotopically ^{28}Si target. I would like to express my acknowledgement to Prof. T. Motoba and Prof. E. Hiyama for giving me a lecture of the latest theoretical calculations and a lot of comments on the experimental results. I would like to express my thanks to Prof. K. Maeda and Prof. J. Shirai for their reviews and advises on this thesis.

I would like to express my special appreciation to Dr. Y.Okayasu for his great efforts to the experiment. He especially worked on the simulation for the Tilt method, water cherenkov counter, TUL, optics calibration, efficiency estimation and so on. Without his contributions and powers, this study was not completed. He always supported and guided me as for not only physics but also my normal activities. Thanks to him, I could enjoy a comfortable life in Virginia with many unforgettable memories, such as his good cooking, the thigh, Elvis' hairpiece and so on. I would like to express my gratitude to Mr. D.Kawama for his contribution to the experiment. I believe his experience will be a great advantage for the analysis of the third generation hypernuclear experiment.

I am sincere grateful to Prof. Ed. V. Hungerford, Prof. L. Tang and Prof. J. Reinhold for their great leaderships and guidance to the experiment. I would like to express my appreciation to Dr. S. A. Wood who taught me the entire experimental system in JLab Hall C, especially the DAQ system, and revised this thesis. I would

like to express my thanks to Dr. D. Abbott and Dr. Ed. Jastrzembski for their supports to establish the DAQ system with the F1TDC. I would like to express my gratitude to Dr. L. Yuan who especially worked on the optics calibration and gave me a lecture of the detailed concepts and procedures gently at any time. I want to thank Dr. L. Cole, Dr. V. M. Rodriguez, Dr. P. Bartlin, Dr. S. Tomislav and Dr. A. Daniel for their supports and kindnesses.

I really appreciate Dr. M. Ukai, Dr. T. Koike, Dr. M. Kaneta, and Dr. K. Miwa for their great advises. They always gave me a fresh philosophy. I am grateful to Mr. B. Beckford who revised this thesis. I want to express my acknowledgement to Ms. N. Kawamura, Ms. M. Shimaya and Mr. N. S. Chiga for their special supports to my research.

Finally, I am extremely thankful to my world's best family.

Appendix A

Mass values

Particle masses used in the present study are summarized in Tab. A.1 [79].

Item	Mass [MeV/c ²]
Electron	0.511
K ⁺	493.677
proton	938.272
neutron	939.565
Λ	1115.683
Σ^0	1192.642

Table A.1: Particle masses used in the present study [79].

A nuclear mass, $M_N(A, Z)$, can be calculated as [58]

$$M_N(A, Z) = M_A(A, Z) - Z \times M_e + B_{el}(Z), \quad (\text{A.1})$$

where N, Z, A and M_e represent the number of neutrons, the number of protons, the mass number and the electron mass, respectively. The approximation formula of the total binding energy of all removed electrons, $B_{el}(Z)$, is given by

$$B_{el}(Z) = 14.4381Z^{2.39} + 1.55468 \times 10^{-6}Z^{5.35} \text{ [eV]} \quad (\text{A.2})$$

Nuclear masses used in the present study are summarized in Tab. A.2.

Item	Mass [MeV/c ²]
Atomic mass unit	931.494
⁶ He	5605.537
⁷ Li	6533.834
¹¹ B	10252.548
¹² C	11174.864
²⁷ Al	25126.506
²⁸ Si	26053.195

Table A.2: Nuclear masses used in the present study [58].

Appendix B

Spectroscopic factor

Spectroscopic factors (S-factor) for proton pick-up reactions on ${}^7\text{Li}$, ${}^{12}\text{C}$ and ${}^{28}\text{Si}$ nuclei are summarized in this chapter.

J^π	Ex (MeV)	S-factor of ${}^{28}\text{Si}(d, {}^3\text{He}){}^{27}\text{Al}$	S-factor of ${}^{28}\text{Si}(t, {}^4\text{He}){}^{27}\text{Al}$
$5/2^+$	0.00	7.50	6.80
$1/2^+$	0.84	1.00	1.40
$3/2^+$	1.01	1.10	1.00
$5/2^+$	2.73	1.20	0.80
$3/2^+$	2.98	<0.80	—
$1/2^+$	3.68	<0.04	—
$1/2^-$	4.05	3.60	2.80
$5/2^+$	4.41	0.70	1.00
$3/2^+$	5.16	2.00	—

Table B.1: Relative spectroscopic factor of ${}^{28}\text{Si}(d, {}^3\text{He}){}^{27}\text{Al}$ reaction at $E_d = 34.4$ MeV [80, 81] and ${}^{28}\text{Si}(t, {}^4\text{He}){}^{27}\text{Al}$ reaction at $E_t = 23.8$ MeV [82].

J^π	Ex (MeV)	S-factor ${}^{12}\text{C}(p, 2p){}^{11}\text{B}$	S-factor of ${}^{12}\text{C}(d, {}^3\text{He}){}^{11}\text{B}$	S-factor of ${}^{12}\text{C}(e, e'p){}^{11}\text{B}$
$3/2^-$	0.00	2.00	2.98	1.72
$1/2^-$	2.12	0.37	0.69	0.26
$5/2^-$	4.44	0.15	—	—
$3/2^-$	5.02	1.08	0.31	0.20
$1/2^+$	6.79	0.25	—	—

Table B.2: Relative spectroscopic factor of ${}^{12}\text{C}(p, 2p){}^{11}\text{B}$ reaction at $E_p = 98.7$ MeV [83], ${}^{12}\text{C}(d, {}^3\text{He}){}^{11}\text{B}$ reaction at $E_d = 52$ MeV [84] and ${}^{12}\text{C}(e, e'p){}^{11}\text{B}$ reaction at $300 < E_e < 500$ MeV [85].

J^π	Ex (MeV)	S-factor ${}^7\text{Li}(t,\alpha){}^6\text{He}$	S-factor of ${}^7\text{Li}(e,e'p){}^6\text{Li}$
0^+	0.00	1.08	0.42
2^+	1.79	—	0.16

Table B.3: Relative spectroscopic factor of ${}^7\text{Li}(t,\alpha){}^6\text{He}$ reaction at $E_t = 38$ MeV [86], ${}^7\text{Li}(e,e'p){}^6\text{Li}$ reaction at $E_e = 329.7, 454.7$ MeV [87].

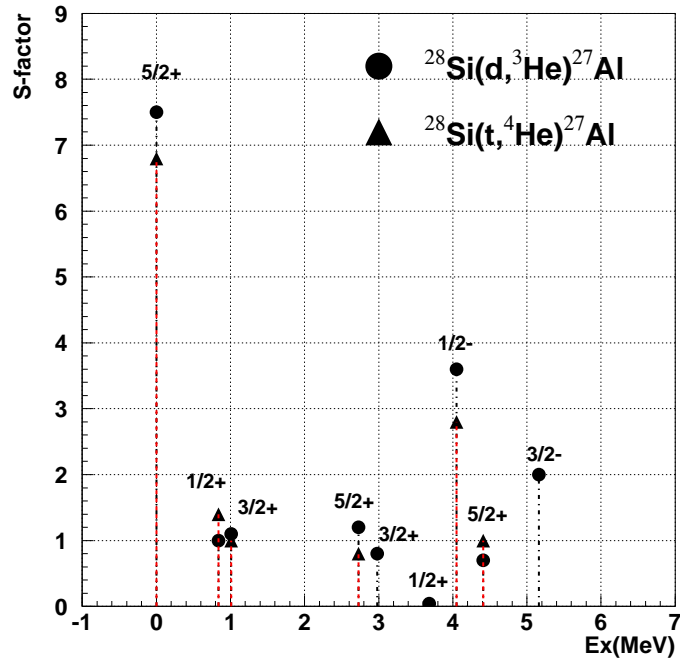


Figure B.1: Spectroscopic factor of proton pickup for ${}^{28}\text{Si}$ [80–82].

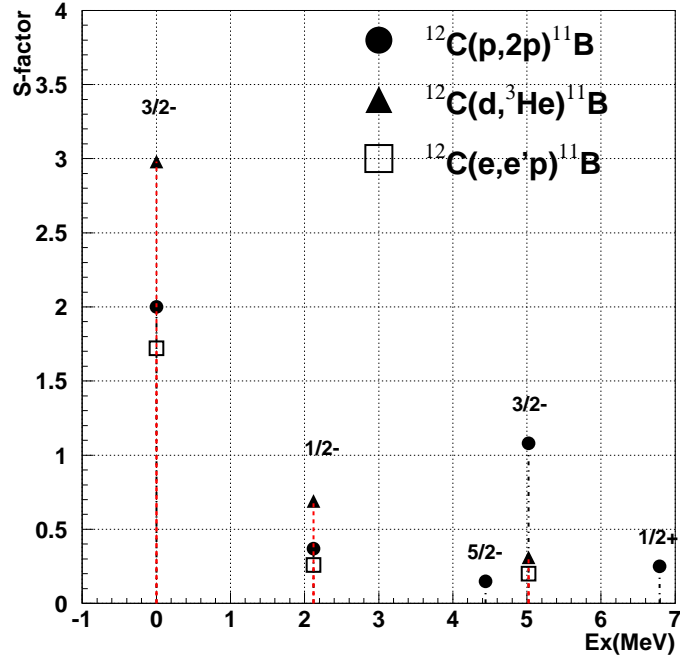


Figure B.2: Spectroscopic factor of proton pickup for ^{12}C [83–85].

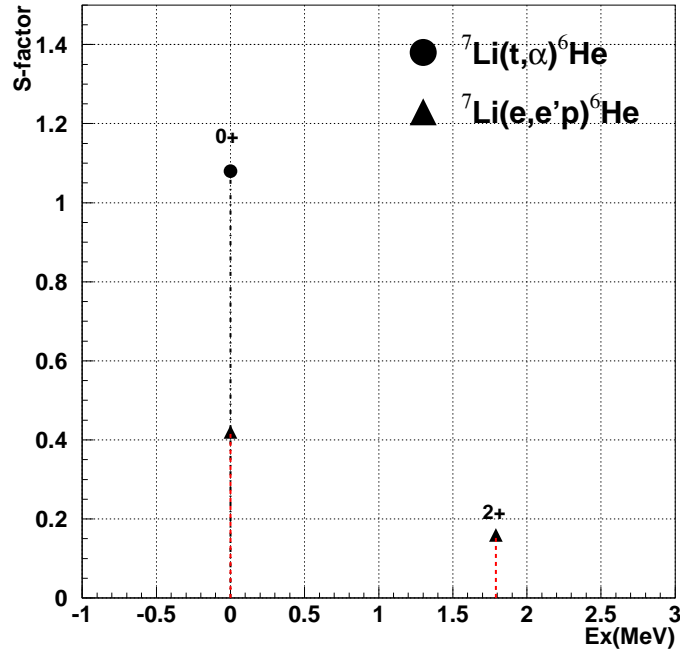


Figure B.3: Spectroscopic factor of proton pickup for ^7Li [86, 87].

Appendix C

Isotopically enriched ^{28}Si target

A natural ^{28}Si target (^{28}Si : 92.2%, ^{29}Si : 4.7%, ^{30}Si : 3.1%) was used for the $^{28}\text{Si}(\pi^+, \text{K}^+)_{\Lambda}$ spectroscopy [3, 21]. A high intensity electron beam in the present study enabled us to use the thin target. Thus, the isotopically enriched ^{28}Si target was prepared by the high intensity vibrational powder plating (HIVIPP) method [53].

Figure C.1 shows a schematic process of HIVIPP method for enriched ^{28}Si target. The ^{28}Si powder was placed in the quartz tube closed by two plate-type electrodes made of Cu. The bottom plate was grounded and the top plate was at a positive voltage of some kilo volts. As the supplied voltage was gradually increased, quantities of ^{28}Si powder were accelerated toward upper plate. In this way, the vibrational motion was established, which resulted in the deposition of a metal layer on both electrodes. After the plating, a protective coating of wax was applied to avoid cracking the deposit during removal of the backing. Then the Cu backings could be removed by chemically dissolving them in a dilute solution of HNO_3 . Finally, the electron wax was also removed with an isopropyl-alcohol solution.

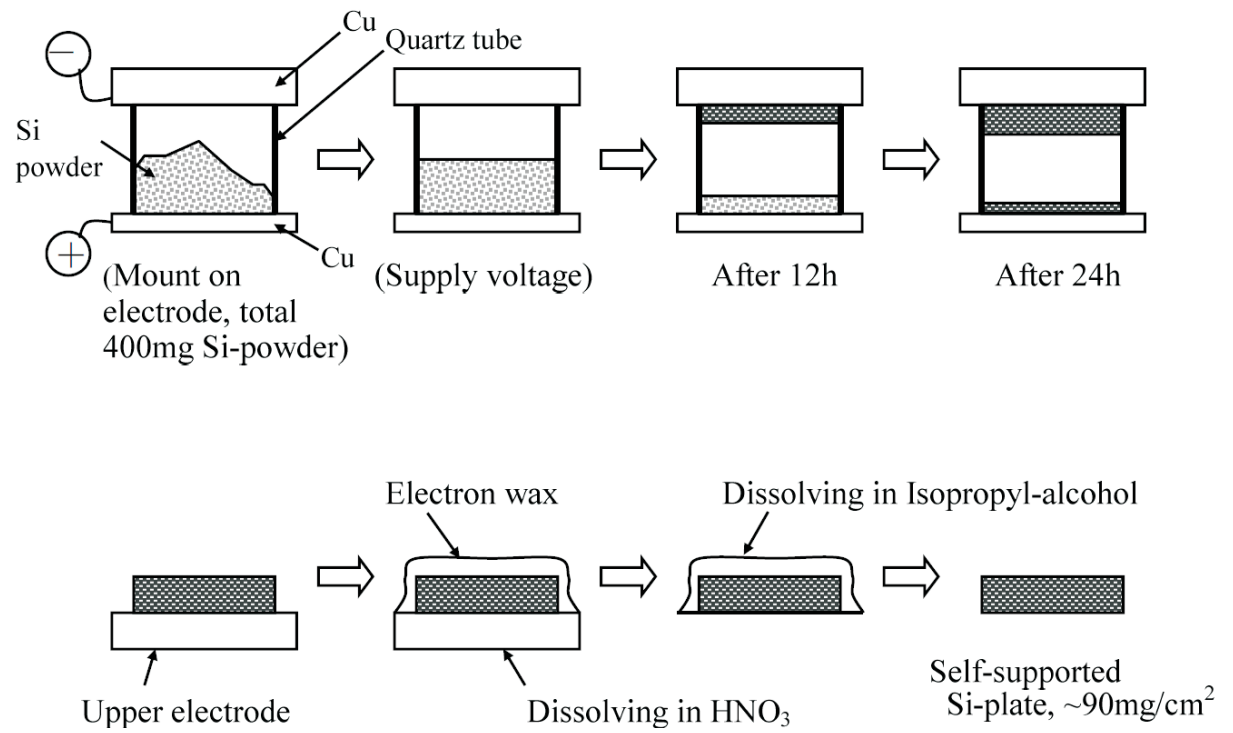


Figure C.1: Schematic process for the preparation of enriched ^{28}Si target [53].

Appendix D

List of the data point of $^{12}_{\Lambda}\text{B}$

Table D.1: List of the data point of the $^{12}_{\Lambda}\text{B}$ spectrum shown in Fig. 5.14. The quoted values of $-B_{\Lambda}$ represent the centers of bins.

$-B_{\Lambda}$ (MeV)	$\overline{(d\sigma/d\Omega)} _{1^{\circ}-13^{\circ}}$ (nb/sr)	Stat. error (nb/sr)	$-B_{\Lambda}$ (MeV)	$\overline{(d\sigma/d\Omega)} _{1^{\circ}-13^{\circ}}$ (nb/sr)	Stat. error (nb/sr)
-19.907	-0.691	1.262	-16.157	0.178	1.290
-19.757	0.580	1.317	-16.007	-0.504	1.263
-19.607	-0.144	1.282	-15.857	0.020	1.310
-19.457	0.025	1.297	-15.707	1.070	1.362
-19.307	-0.872	1.250	-15.557	1.198	1.373
-19.157	2.147	1.454	-15.407	-1.079	1.240
-19.007	-0.750	1.228	-15.257	1.211	1.388
-18.857	0.218	1.299	-15.107	1.461	1.379
-18.707	0.986	1.360	-14.957	0.113	1.290
-18.557	1.092	1.351	-14.806	1.100	1.363
-18.407	-1.280	1.196	-14.656	3.255	1.515
-18.257	-0.294	1.277	-14.506	0.039	1.314
-18.107	2.126	1.436	-14.356	-2.356	1.112
-17.957	2.251	1.461	-14.206	2.939	1.488
-17.807	-0.796	1.236	-14.056	0.320	1.319
-17.657	2.133	1.411	-13.906	1.282	1.397
-17.507	0.143	1.298	-13.756	1.227	1.396
-17.357	-1.961	1.139	-13.606	0.971	1.348
-17.207	-0.150	1.284	-13.456	-0.359	1.258
-17.057	1.281	1.371	-13.306	2.667	1.481
-16.907	-0.383	1.250	-13.156	2.096	1.420
-16.757	-1.119	1.189	-13.006	1.149	1.375
-16.607	-1.194	1.189	-12.856	2.701	1.472
-16.457	3.755	1.531	-12.706	4.549	1.597
-16.307	-0.946	1.253	-12.556	0.114	1.329

$-B_\Lambda$ (MeV)	$\overline{(d\sigma/d\Omega)} _{1^\circ-13^\circ}$ (nb/sr)	Stat. error (nb/sr)	$-B_\Lambda$ (MeV)	$\overline{(d\sigma/d\Omega)} _{1^\circ-13^\circ}$ (nb/sr)	Stat. error (nb/sr)
-12.406	0.090	1.302	-6.706	2.161	1.482
-12.256	3.111	1.500	-6.556	1.179	1.370
-12.106	1.142	1.386	-6.406	0.085	1.294
-11.956	2.628	1.477	-6.256	1.950	1.440
-11.806	8.464	1.823	-6.106	1.946	1.429
-11.656	14.515	2.093	-5.956	0.195	1.306
-11.506	20.161	2.359	-5.806	1.813	1.430
-11.356	26.481	2.582	-5.656	0.541	1.326
-11.206	15.544	2.138	-5.506	2.155	1.455
-11.056	10.948	1.945	-5.356	4.337	1.587
-10.906	7.028	1.728	-5.206	3.837	1.556
-10.756	1.275	1.406	-5.056	6.872	1.754
-10.606	3.590	1.509	-4.906	4.976	1.650
-10.456	4.332	1.580	-4.755	4.642	1.582
-10.306	4.816	1.607	-4.605	4.157	1.571
-10.156	2.458	1.480	-4.455	3.083	1.524
-10.006	3.084	1.507	-4.305	1.004	1.392
-9.856	5.079	1.616	-4.155	3.622	1.532
-9.706	2.892	1.511	-4.005	0.807	1.371
-9.556	1.452	1.388	-3.855	2.921	1.508
-9.406	3.650	1.541	-3.705	0.561	1.328
-9.256	3.078	1.526	-3.555	-1.857	1.166
-9.106	1.909	1.421	-3.405	1.512	1.412
-8.956	7.994	1.783	-3.255	1.827	1.428
-8.806	6.649	1.709	-3.105	3.066	1.491
-8.656	6.039	1.693	-2.955	2.748	1.481
-8.506	0.838	1.335	-2.805	3.072	1.539
-8.356	1.762	1.435	-2.655	3.448	1.537
-8.206	-0.313	1.295	-2.505	0.927	1.352
-8.056	2.191	1.432	-2.355	3.399	1.532
-7.906	1.439	1.415	-2.205	3.269	1.506
-7.756	0.025	1.303	-2.055	0.828	1.350
-7.606	2.665	1.498	-1.905	4.723	1.618
-7.456	4.775	1.623	-1.755	5.344	1.650
-7.306	-0.666	1.240	-1.605	3.650	1.559
-7.156	2.531	1.486	-1.455	5.790	1.672
-7.006	1.761	1.436	-1.305	10.669	1.952
-6.856	-1.643	1.186	-1.155	8.830	1.832

$-B_\Lambda$ (MeV)	$\overline{(d\sigma/d\Omega)} _{1^\circ-13^\circ}$ (nb/sr)	Stat. error (nb/sr)	$-B_\Lambda$ (MeV)	$\overline{(d\sigma/d\Omega)} _{1^\circ-13^\circ}$ (nb/sr)	Stat. error (nb/sr)
-1.005	7.644	1.773	4.545	7.400	1.776
-0.855	13.194	2.068	4.695	6.017	1.720
-0.705	16.030	2.206	4.845	7.960	1.815
-0.555	14.716	2.144	4.995	5.825	1.702
-0.405	25.565	2.582	5.146	10.535	1.947
-0.255	15.999	2.185	5.296	4.518	1.624
-0.105	14.379	2.114	5.446	9.795	1.911
0.045	10.114	1.919	5.596	6.312	1.725
0.195	10.496	1.943	5.746	8.233	1.833
0.345	5.215	1.643	5.896	7.016	1.762
0.495	6.259	1.707	6.046	9.368	1.883
0.645	8.093	1.795	6.196	8.078	1.817
0.795	9.518	1.872	6.346	6.949	1.779
0.945	9.990	1.908	6.496	9.836	1.908
1.095	8.979	1.831	6.646	6.584	1.723
1.245	7.944	1.817	6.796	7.419	1.787
1.395	8.658	1.838	6.946	7.487	1.815
1.545	6.930	1.766	7.096	11.609	1.987
1.695	6.732	1.728	7.246	7.842	1.777
1.845	4.827	1.627	7.396	10.515	1.957
1.995	7.021	1.758	7.546	7.687	1.801
2.145	5.407	1.674	7.696	9.009	1.898
2.295	6.654	1.736	7.846	10.482	1.936
2.445	7.177	1.744	7.996	10.685	1.966
2.595	7.648	1.804	8.146	7.865	1.823
2.745	8.834	1.856	8.296	8.074	1.819
2.895	7.786	1.802	8.446	7.910	1.822
3.045	8.302	1.824	8.596	10.493	1.956
3.195	8.381	1.831	8.746	9.542	1.891
3.345	5.080	1.643	8.896	9.986	1.927
3.495	4.184	1.596	9.046	11.393	2.007
3.645	6.004	1.717	9.196	10.752	1.982
3.795	7.058	1.752	9.346	9.384	1.884
3.945	6.743	1.737	9.496	8.675	1.832
4.095	8.158	1.819	9.646	7.219	1.788
4.245	7.611	1.800	9.796	8.871	1.862
4.395	7.352	1.777	9.946	5.862	1.699

Appendix E

List of the data point of $^{28}_{\Lambda}\text{Al}$

Table E.1: List of the data point of the $^{28}_{\Lambda}\text{Al}$ spectrum shown in Fig. 5.21. The quoted values of $-B_{\Lambda}$ represent the centers of bins.

$-B_{\Lambda}$ (MeV)	$\overline{(d\sigma/d\Omega)} _{1^{\circ}-13^{\circ}}$ (nb/sr)	Stat. error (nb/sr)	$-B_{\Lambda}$ (MeV)	$\overline{(d\sigma/d\Omega)} _{1^{\circ}-13^{\circ}}$ (nb/sr)	Stat. error (nb/sr)
-20.875	-0.382	3.763	-14.625	5.674	4.243
-20.625	6.043	4.130	-14.375	5.660	4.234
-20.375	-3.767	3.582	-14.125	3.710	4.078
-20.125	4.372	4.049	-13.875	8.761	4.375
-19.875	0.247	3.764	-13.625	6.851	4.262
-19.625	2.674	4.007	-13.375	3.239	4.101
-19.375	-1.424	3.753	-13.125	0.163	3.962
-19.125	2.594	3.973	-12.875	-1.143	3.850
-18.875	-1.157	3.743	-12.625	0.451	3.886
-18.625	-0.976	3.742	-12.375	-0.830	3.882
-18.375	-2.475	3.721	-12.125	1.934	3.989
-18.125	-3.789	3.622	-11.875	0.288	3.953
-17.875	17.037	4.773	-11.625	-3.254	3.655
-17.625	33.396	5.509	-11.375	-3.496	3.641
-17.375	25.262	5.205	-11.125	0.387	3.916
-17.125	3.010	4.069	-10.875	-0.166	3.951
-16.875	3.721	4.122	-10.625	7.248	4.267
-16.625	-5.265	3.486	-10.375	7.678	4.398
-16.375	1.141	3.915	-10.125	5.367	4.256
-16.125	2.259	3.991	-9.875	0.704	3.945
-15.875	6.995	4.281	-9.625	-1.945	3.767
-15.625	12.899	4.606	-9.375	1.225	4.016
-15.375	-0.529	3.839	-9.125	1.875	4.035
-15.125	2.409	4.033	-8.875	6.091	4.326
-14.875	3.126	4.111	-8.625	8.469	4.439

$-B_\Lambda$ (MeV)	$\overline{(d\sigma/d\Omega)} _{1^\circ-13^\circ}$ (nb/sr)	Stat. error (nb/sr)	$-B_\Lambda$ (MeV)	$\overline{(d\sigma/d\Omega)} _{1^\circ-13^\circ}$ (nb/sr)	Stat. error (nb/sr)
-8.375	6.397	4.352	-1.125	4.744	4.316
-8.125	8.735	4.443	-0.875	12.095	4.688
-7.875	12.317	4.646	-0.625	9.634	4.535
-7.625	3.147	4.144	-0.375	5.824	4.387
-7.375	6.235	4.395	-0.125	17.452	5.042
-7.125	28.230	5.474	0.125	19.544	5.100
-6.875	41.895	5.955	0.375	20.023	5.095
-6.625	29.812	5.522	0.625	12.905	4.728
-6.375	15.276	4.804	0.875	17.809	5.054
-6.125	8.806	4.403	1.125	11.962	4.713
-5.875	9.958	4.582	1.375	11.073	4.710
-5.625	2.688	4.112	1.625	25.959	5.407
-5.375	15.452	4.805	1.875	36.737	5.892
-5.125	5.663	4.366	2.125	18.927	5.129
-4.875	18.071	4.907	2.375	17.346	5.003
-4.625	9.109	4.517	2.625	14.450	4.874
-4.375	3.878	4.227	2.875	20.712	5.158
-4.125	17.070	4.895	3.125	15.982	5.020
-3.875	7.888	4.420	3.375	24.279	5.343
-3.625	8.157	4.439	3.625	12.839	4.844
-3.375	9.621	4.544	3.875	28.487	5.548
-3.125	10.521	4.631	4.125	19.226	5.163
-2.875	12.942	4.754	4.375	25.036	5.418
-2.625	9.630	4.589	4.625	24.166	5.384
-2.375	15.392	4.871	4.875	14.579	4.891
-2.125	4.639	4.259	5.125	22.892	5.289
-1.875	6.000	4.342	5.375	23.720	5.384
-1.625	6.631	4.399	5.625	19.740	5.090
-1.375	11.917	4.752	5.875	27.617	5.544

Appendix F

List of the data point of ${}^7_\Lambda\text{He}$

Table F.1: List of the data point of the ${}^7_\Lambda\text{He}$ spectrum shown in Fig. 5.28. The quoted values of $-B_\Lambda$ represent the centers of bins.

$-B_\Lambda$ (MeV)	$\overline{(d\sigma/d\Omega)} _{1^\circ-13^\circ}$ (nb/sr)	Stat. error (nb/sr)	$-B_\Lambda$ (MeV)	$\overline{(d\sigma/d\Omega)} _{1^\circ-13^\circ}$ (nb/sr)	Stat. error (nb/sr)
-9.874	1.715	1.878	-2.371	-2.032	1.580
-9.574	0.685	1.724	-2.071	3.792	2.046
-9.274	2.764	1.915	-1.771	2.161	1.941
-8.974	-0.356	1.666	-1.471	3.684	2.031
-8.673	2.047	1.849	-1.170	-1.941	1.599
-8.373	0.417	1.728	-0.870	0.048	1.796
-8.073	0.650	1.761	-0.570	3.440	2.045
-7.773	2.803	1.940	-0.270	-2.051	1.605
-7.473	-1.099	1.618	0.030	3.118	2.020
-7.173	0.921	1.819	0.330	4.140	2.070
-6.873	2.001	1.886	0.630	1.219	1.890
-6.573	1.829	1.855	0.930	4.310	2.129
-6.273	-0.808	1.654	1.231	2.745	2.008
-5.972	8.022	2.340	1.531	5.152	2.188
-5.672	10.310	2.428	1.831	-0.423	1.742
-5.372	6.321	2.231	2.131	3.919	2.047
-5.072	2.272	1.880	2.431	1.627	1.915
-4.772	3.004	1.969	2.731	3.238	2.056
-4.472	-0.408	1.725	3.031	5.809	2.220
-4.172	0.917	1.836	3.331	4.310	2.113
-3.872	1.887	1.899	3.631	5.976	2.232
-3.571	5.269	2.136	3.932	4.462	2.170
-3.271	3.805	2.037	4.232	3.264	2.046
-2.971	-1.287	1.660	4.532	1.945	1.953
-2.671	3.571	2.015	4.832	3.240	2.032

$-B_\Lambda$ (MeV)	$(d\sigma/d\Omega) _{1^\circ-13^\circ}$ (nb/sr)	Stat. error (nb/sr)
5.132	2.409	1.991
5.432	9.603	2.480
5.732	6.003	2.267
6.032	4.311	2.105
6.333	6.265	2.261
6.633	8.048	2.394
6.933	4.297	2.119
7.233	4.244	2.160
7.533	6.119	2.288
7.833	7.591	2.366
8.133	2.510	2.013
8.433	4.414	2.146
8.734	8.959	2.465
9.034	6.002	2.287
9.334	6.432	2.297
9.634	4.821	2.211
9.934	7.717	2.398

Reference

- [1] H. Bando, T. Motoba and Y. Yamamoto, *Phys. Rev.* **C31**, p. 265 (1985).
- [2] A. Likar, M. Rosina and B. Povh, *Z. Phys.* **A324**, 35 (1986).
- [3] O. Hashimoto and H. Tamura, *Prog. Part. Nucl. Phys.* **57**, 564 (2006).
- [4] T. A. Rijken, V. G. J. Stoks and Y. Yamamoto, *Phys. Rev.* **C59**, 21 (1999).
- [5] M. Danysz and J. Pniewski, *Phil. Mag.* **44**, 348 (1953).
- [6] M. A. Faessler *et al.*, *Phys. Lett.* **B46**, 468 (1973).
- [7] W. Bruckner *et al.*, *Phys. Lett.* **B55**, p. 107 (1975).
- [8] W. Bruckner *et al.*, *Phys. Lett.* **B62**, p. 481 (1976).
- [9] W. Bruckner *et al.*, *Phys. Lett.* **B79**, p. 157 (1978).
- [10] R. Bertini *et al.*, *Phys. Lett.* **B83**, p. 306 (1979).
- [11] R. Bertini *et al.*, *Nucl. Phys.* **A360**, p. 315 (1981).
- [12] R. Bertini *et al.*, *Nucl. Phys.* **A368**, p. 365 (1981).
- [13] R. E. Chrien *et al.*, *Phys. Lett.* **B89**, p. 31 (1979).
- [14] M. May *et al.*, *Phys. Rev. Lett.* **47**, 1106 (1981).
- [15] A. Bamberger *et al.*, *Phys. Lett.* **B36**, 412 (1971).
- [16] A. Bamberger *et al.*, *Nucl. Phys.* **B60**, 1 (1973).
- [17] C. Milner *et al.*, *Phys. Rev. Lett.* **54**, 1237 (1985).
- [18] P. H. Pile *et al.*, *Phys. Rev. Lett.* **66**, 2585 (1991).
- [19] M. Akei *et al.*, *Nucl. Phys.* **A534**, 478 (1991).
- [20] T. Hasegawa *et al.*, *Phys. Rev. Lett.* **74**, 224 (1995).
- [21] T. Hasegawa *et al.*, *Phys. Rev.* **C53**, 1210 (1996).
- [22] S. Ajimura *et al.*, *Nucl. Phys.* **A639**, 93 (1998).

- [23] H. Hotchi *et al.*, *Phys. Rev.* **C64**, p. 044302 (2001).
- [24] H. Tamura *et al.*, *Phys. Rev. Lett.* **84**, 5963 (2000).
- [25] T. Miyoshi *et al.*, *Phys. Rev. Lett.* **90**, p. 232502 (2003).
- [26] L. Yuan *et al.*, *Phys. Rev.* **C73**, p. 044607 (2006).
- [27] D. J. Millener, C. B. Dover and A. Gal, *Phys. Rev.* **C38**, 2700 (1988).
- [28] Y. Yamamoto, H. Bando and J. Zofka, *Prog. Theor. Phys.* **80**, 757 (1988).
- [29] D. E. Lansky and Y. Yamamoto, *Phys. Rev.* **C55**, 2330 (1997).
- [30] C. M. Keil, F. Hofmann and H. Lenske, *Phys. Rev.* **C61**, p. 064309 (2000).
- [31] M. Juric *et al.*, *Nucl. Phys.* **B52**, 1 (1973).
- [32] D. H. Davis, *Nucl. Phys.* **A547**, 369c (1992).
- [33] C. B. Dover Invited talk at Int. Symp. on Medium Energy Physics, Beijing, China, Jun 23-27, 1987.
- [34] T. Motoba, M. Sotona and K. Itonaga, *Prog. Theor. Phys. Suppl.* **117**, 123 (1994).
- [35] M. W. Ahmed *et al.*, *Phys. Rev.* **C68**, p. 064004 (2003).
- [36] T. Motoba, *Int. J. Mod. Phys.* **A24**, 2091 (2009).
- [37] T. Motoba *et al.*, *Sendai2008, Strangeness in nuclear and hadronic system* , p. 178.
- [38] C. W. Leemann, D. R. Douglas and G. A. Krafft, *Ann. Rev. Nucl. Part. Sci.* **51**, 413 (2001).
- [39] C. E. Hyde, W. Bertozzi and J. M. Finn, (1985), In *Newport News 1985, Proceedings, Continuous Electron Beam Accelerator Facility* 532-551. (see Conference Index).
- [40] M. Sotona, *private communication* .
- [41] J. E. Spencer and H. A. Enge, *Nucl. Inst. Meth.* **49**, p. 181 (1967).
- [42] Y.-S. Tsai, *Rev. Mod. Phys.* **46**, p. 815 (1974).
- [43] M. Q. Tran *et al.*, *Phys. Lett.* **B445**, 20 (1998).
- [44] S. M. Seltzer and M. J. Berger, Energy Loss Straggling of Protons and Mesons: Tabulation of the Vavilov Distribution, in *Studies in Penetration of Charged Particles in Matter*, 1964.

- [45] J. J. W. Lightbody and J. S. O'Connell, *Computers in Physics* **2**, p. 57 (May 1988).
- [46] H. Yamazaki *et al.*, *Phys. Rev.* **C52**, 1157 (1995).
- [47] E. Miyata *et al.*, *Nucl. Instrum. Meth.* **A459**, 157 (2001).
- [48] M. Nomachi and S. Ajimura, Serial data link on advanced tca back plane *Real Time Conference, 2005. 14th IEEE-NPSS* June 2005.
- [49] E. Jastrzembski, D. Abbott, W. Heyes, R. MacLeod, C. Timmer and E. Wolin, The jefferson lab trigger supervisor system *Real Time Conference, 1999. Santa Fe 1999. 11th IEEE NPSS* 1999.
- [50] V. Gyurjyan *et al.*, Jefferson lab data acquisition run control system *Proc. CHEP04* 29 September 2004.
- [51] *F1 TDC User's Manual V1.1*, (23 Apr. 2004).
- [52] C. Yan *et al.*, *Nucl. Instrum. Meth.* **A365**, 46 (1995).
- [53] I. Sugai, Y. Takeda and H. Kawakami, *Nucl. Instrum. Meth.* **A561**, 38 (2006).
- [54] Y. Fujii *et al.*, *Nucl. Phys.* **A721**, 1079 (2003).
- [55] S. N. Nakamura *et al.*, *Nucl. Phys.* **A754**, 421 (2005).
- [56] M. Carl *et al.*, *Nucl. Instrum. Meth.* **A527**, 301 (2004).
- [57] A. Bezaguet, C. Geles, S. Reucroft, G. Marini and G. Martellotti, *Nucl. Instrum. Meth.* **158**, 303 (1978).
- [58] G. Audi, A. H. Wapstra and C. Thibault, *Nucl. Phys.* **A729**, 337 (2002).
- [59] Bowen *et al.*, *Phys. Rev. D* **7**, 22 (1973).
- [60] R. W. Bland *et al.*, *Nucl. Phys.* **B13**, 595 (1969).
- [61] Bugg *et al.*, *Phys. Rev.* **168**, 1466 (1968).
- [62] G. Giacomelli *et al.*, *Nucl. Phys.* **B20**, 301 (1970).
- [63] K. Abe *et al.*, *Phys. Rev.* **D11**, 1719 (1975).
- [64] W. M. Yao *et al.*, *J. Phys.* **G33**, 1 (2006).
- [65] J. J. LeRose *et al.*, *Nucl. Phys.* **A804**, 116 (2008).
- [66] Y. Ma, *Ph.D thesis* (2009).
- [67] L. Yuan, *Ph.D thesis* .

- [68] K. Itonaga, T. Motoba, O. Richter and M. Sotona, *Phys. Rev.* **C49**, 1045 (1994).
- [69] K. Itonaga, T. Motoba and H. Bando, *Prog. Theor. Phys.* **84**, 291 (1990).
- [70] S. Cohen and D. Kurath, *Nucl. Phys.* **73**, 1 (1965).
- [71] S. Cohen and D. Kurath, *Nucl. Phys.* **A101**, 1 (1967).
- [72] P. G. Roos, S. M. Smith, V. K. C. Cheng, G. Tibell, A. A. Cowley and R. A. J. Riddle, *Nuclear Physics A* **255**, 187 (1975).
- [73] Y. Yamamoto and H. Bando, *Prog. Theor. Phys.* **73**, 905 (1985).
- [74] T. A. Rijken, P. M. M. Maessen and J. J. de Swart, *Nucl. Phys.* **A547**, 245c (1992).
- [75] T. Mizutani, C. Fayard, G. H. Lamot and B. Saghai, *Phys. Rev.* **C58**, 75 (1998).
- [76] T. Mart and C. Bennhold, *Phys. Rev.* **C61**, p. 012201 (2000).
- [77] A. Nogga, *Nucl. Phys.* **A754**, 36 (2005).
- [78] E. Hiyama, Y. Yamamoto, T. Motoba and M. Kamimura, *Phys. Rev.* **C80**, p. 054321 (2009).
- [79] C. Amsler *et al.*, *Phys. Lett.* **B667**, p. 1 (2008).
- [80] B. H. Wildenthal and E. Newman, *Phys. Rev.* **167**, 1027 (1968).
- [81] H. E. Gove *et al.*, *Nucl. Phys. A* **116**, p. 369 (1968).
- [82] J. D. Sherman *et al.*, *Nucl. Phys. A* **257**, p. 45 (1976).
- [83] F. Ajzenberg-Selove, *Nuclear Physics A* **433**, 1 (1985).
- [84] G. Mairle and G. J. Wagner, *Nuclear Physics A* **253**, 253 (1975).
- [85] A. E. L. Dieperink and P. K. A. Huberts, *Ann. Rev. Nucl. Part. Sci.* **40**, 239 (1990).
- [86] N. M. Clarke, *Journal of Physics G: Nuclear and Particle Physics* **18**, p. 917 (1992).
- [87] L. Lapikas, J. Wessling and R. B. Wiringa, *Phys. Rev. Lett.* **82**, 4404 (1999).